Title

QUANTITATIVE ASSESSMENT OF PULMONARY DISEASE USING LOW-DOSE COMPUTED TOMOGRAPHY

Author

Zhao, Yixiao

Publication Date

2021

UNIVERSITY OF CALIFORNIA,

IRVINE

QUANTITATIVE ASSESSMENT OF PULMONARY DISEASE USING LOW-DOSE COMPUTED TOMOGRAPHY

DISSERTATION

submitted in partial satisfaction of the requirements

for the degree of

DOCTOR OF PHILOSOPHY

in Electrical Engineering

by

Yixiao Zhao

Dissertation Committee:
Professor Sabee Molloi, Chair
Professor Min-Ying Lydia Su
Professor Matthew Brenner

2021

DEDICATION

To

Dr. Sabee Molloi

for his unwavering support, inspiration, and encouragement over the years.

TABLE OF CONTENTS

LIST OF FIGURES

LIST OF TABLES

ACKNOWLEGEMENTS

Foremost, I would like to express my deep and sincere gratitude to my advisor Prof. Sabee Molloi for the continuous support of my Ph.D. study and research, for giving me the opportunity to do research on the topic of quantitative assessment of pulmonary disease using low-dose computed tomography. His guidance helped me in all the time of research and writing of this dissertation. His motivation, encouragement, enthusiasm, patience and immerse knowledge deeply inspired me. It was a great privilege and honor to work and study under his guidance.

Besides my advisor, I would like to thank the rest of my committee: Prof. Min-Ying Lydia Su and Prof. Matthew Brenner, Prof. Frothjof Kruggel and Prog. Gultekin Gulsen, for their insightful comments, thoughtful questions, and encouragement.

My sincere thanks also goes to Dr. Andrew Hernandez and Prof. John Boone from University of California, Davis, for offering me the collaborative opportunity on the project of airway measurement using a high-resolution computed tomography.

I thank all my fellow lab mates in Dr. Molloi’s Imaging Physics Laboratory: Dr. Logan Hubbard, Shant Malkasian, Dr. Pablo Abbona, Christina Leung, Nile Luu, Dale Black. In particular, I am grateful to Logan and Shant, for enlightening me the first glance of research and helped me throughout the research.

Last but not least, I extremely grateful to my parents for their love, caring and sacrifices for educating and preparing me for my future. I am very much thankful to my lover Damian, for his love, understanding and continuing support to compete this research work.

CURRICULUM VITAE

Yixiao Zhao

Department of Electrical Engineering
University of California, Irvine

EDUCATION

University of California, Irvine
- Ph.D. - Electrical & Computer Engineering (2021, Expected)

University of Florida
- M.S. - Electrical & Computer Engineering, major in Signal & System (2015)

Harbin Institute of Technology
- B.S. - Electrical Engineering, Department of Automatic Test and Control (2012)
- B.A. - Advertising, Department of Media Technology and Art (2012)

HONORS & AWARDS

- *2013* Achievement Awards of University of Florida
- *2013* National Scholarship for Graduate students
- *2013* 10th 'Century Cup' Technology Invention Competition Second Prize
- *2011* Meritorious Winner of Mathematical Contest in Modeling/Interdisciplinary Contest in Modeling
- 2010 National People's Scholarship

ARTICLES IN PEER-REVIEWED JOURNAL PAPERS

1. Abbona P, **Zhao Y**, Hubbard L, Malkasian S, Flynn B, Molloi S. Absolute cerebral blood flow: assessment with a novel low-radiation-dose dynamic CT perfusion technique in a swine model. (In Review, Journal of Neuroradiology)
2. **Zhao Y**, Molloi S. Quantification of Airway Dimensions using an Integrated-Intensity Based Technique: A Phantom Study. (In Review, European Radiology)
3. **Zhao Y,** Hernandez AM, Boone JM, Molloi S. Quantification of Airway Dimensions using a High-Resolution CT Scanner: A Phantom Study. Med Phys. 2021 Jul 20.
4. Hubbard L, Malkasian S**, Zhao Y**, Abbona P, Molloi S. Combining perfusion and angiography with a low-dose cardiac CT technique: a preliminary investigation in a swine model. Int J Cardiovasc Imaging 37, 1767–1779 (2021).
5. **Zhao Y**, Hubbard L, Malkasian S, Abbona P, Molloi S. Two-volume Dynamic CT Pulmonary Perfusion: Contrast Timing Optimization (*In Review*)
6. **Zhao Y**, Hubbard L, Malkasian S, Abbona P, Molloi S. Dynamic Pulmonary CT Perfusion using first-pass analysis technique with only two volume scans: Validation in a Swine Model. *PLoS ONE. 2020 Feb 15(2): e0228110.*

7. Hubbard L, Malkasian S, **Zhao Y,** Abbona P; Molloi S. Low-Radiation-Dose Stress Myocardial Perfusion Measurement Using First-Pass Analysis Dynamic Computed Tomography: A Preliminary Investigation in a Swine Model. *Invest Radiol.* 2019 Dec ;54: 774–780.
8. Hubbard L, Malkasian S, **Zhao Y,** Abbona P; Molloi S. Timing optimization of low-dose prospective dynamic computed tomography perfusion acquisition: validation in a swine model. *Eur Radiol Exp.* 2019; 3(1):16
9. Hubbard L, Malkasian S, **Zhao Y**, Abbona P, Molloi S. Contrast-to-noise ratio optimization in coronary computed tomography angiography: validation in a swine model. *Acad Radiol. 2018; 26(6).*

CONFERENCES & PRESENTATIONS

1. **Zhao Y**, Hubbard L, Malkasian S, Molloi S. Quantification Of Perfusion Defect Distal To Pulmonary Embolism Using Computed Tomography Angiography: Validation In A Swine Model. RSNA, 2021. [Oral]
2. **Zhao Y,** Luu, N.K., Molloi S. Low-dose Dynamic Pulmonary CT Perfusion Using Only Two Volume Scans. RSNA, 2021. [Oral]
3. Hubbard L, Malkasian S, **Zhao Y,** Abbona P; Molloi S. Motion-Immune Dynamic CT Myocardial Perfusion. JCCT. 2021 July;15(4): S29.
4. Hubbard L, Malkasian S, **Zhao Y,** Abbona P; Molloi S. Timing Optimization of Coronary CT Angiography Acquisition. JCCT.2021 July;15(4): S17-S18.
5. **Zhao Y**, Hubbard L, Malkasian S, Abbona P, Molloi S. Contrast Timing Optimization for a Two-Volume Dynamic CT Pulmonary Perfusion Technique. AAPM, 2020, WE-C-TRACK 1-3. [Oral]
6. **Zhao Y**, Hubbard L, Malkasian S, Abbona P, Molloi S. An Optimal Timing Protocol for Improved CT Pulmonary Angiography. AAPM, 2020, SU-E-TRACK 1-7. [Oral]
7. Flynn B, **Zhao Y**, Hubbard L, Malkasian S, Abbona P, Molloi S. Validation of a Two-Volume Dynamic CT Renal Perfusion Technique. AAPM, 2020, WE-C-TRACK 1-4. [Oral]
8. Abbona P, **Zhao Y**, Hubbard L, Malkasian S, Flynn B , Molloi S. Absolute Cerebral Blood Flow Assessment with Novel Low-Dose Whole Brain Dynamic CT Perfusion Technique. Stroke, 51:ATP89, 2020.
9. Molloi S, **Zhao Y**, Hubbard L, Malkasian S, Zhao Y, Abbona P. Quantification of pulmonary blood flow using low-dose computed tomography. *World Congress on Medical Physics and Biomedical Engineering*, Prague, Czech Republic, 2018.
10. Molloi S, Hubbard L, Malkasian S**, Zhao Y**, Abbona P. Dynamic myocardial perfusion measurement using low-dose computed tomography.*World Congress on Medical Physics and Biomedical Engineering*, Prague, Czech Republic, 2018.
11. **Zhao Y**, Brewington C., Nordeck S, Hubbard L, Malkasian, S, Leung C, Abbona P, and Molloi S. Comparison of Novel Whole Nodule First Pass Analysis versus Standard Maximum Slope Model in the Detection of Lung Malignancies using Low-Dose CT Perfusion. RSNA, 2018. [Poster].

12. Hubbard L, Malkasian S, **Zhao Y**, Abbona P, Molloi S. Submillisievert Dynamic CT Perfusion for Quantitative Assessment of Coronary Artery Disease. *Abstract 2018-A-547-SCCT: J Cardiovasc Comput Tomogr*. 2018.
13. **Zhao Y,** Hubbard L, Malkasian S, Abbona P, Molloi S.Pulmonary Blood Flow Measurement Using Low-Dose Computed Tomography. *Med Phys.* 2017 Jun; 44(6):3300
14. Yu S, You X, Jiang X, Ou W, Zhu Z, **Zhao Y,** C. L. Philip Chen, Tang, Y. Generalized Kernel Normalized Mixed-Norm Algorithm: Analysis and Simulations. *Neural Information Processing. ICONIP*. Lecture Notes in Computer Science, vol: 9490. 2015.
15. **Zhao Y,** Yu S, Wu J, Han L, Chen Z, Yang X, Zhao, B. Data-Driven Bridge Detection in Compressed Domain from Panchromatic Satellite Imagery. *ISNN,* Macau, 2014. [Oral]
16. Yu S, **Zhao Y,** Mou Y, Wu J, Han L, Yang X, Zhao, B. Content-Adaptive Rain and Snow Removal Algorithms for Single Image. *ISNN*, Macau, 2014. [Oral]
17. Yu S, Fan Z, **Zhao Y,** Zhao K, Wu D. Quantized Kernel Least Mean Mixed-Norm Algorithm. *12th IEEE ICSP*, Hang Zhou, China, 2014. [Oral]
18. Lu H, **Zhao Y,** Yu S, Zhao B, Li J, Wu J. A General Solution for Multi-thread based Multisource Compressed Video Surveillance System. *ICSPAC*, Wuhan, China, 2014. [Oral]
19. **Zhao Y,** Han L, Yang S, Tang L. Scene-based Adaptive Iteration Bad Pixel Dynamic Correction Algorithm for Infrared Focal Plane Arrays. *3rd EMEIT*, Sep. 2013, pp. 1084-1068
20. Wu J, Li J, Lu H, **Zhao Y,** Tang L, Zhao, B. Face Recognition Based on LBP and Extreme Learning Machine. *ITCA*, Sep. 2013, pp. 3526-3529.
21. Li J, Tang L, **Zhao Y.** FWT-DCT Feature Based Face Authentication. *IET* International Conference on Radar, Xi’an, China, Apr. 2013.
22. **Zhao Y,** Wu J, Yang X, Tang L. Research on Band Interference Correction for Multi-CCD Hyper-spectral Image. *Computer Engineering and Applications*, 2013, 49(S3): 466-470.
23. **Zhao Y,** Yang X, Wang Y, Repeater Coordination Optimize Modeling and Analysis——Base on Cellular. *IC.*

ABSTRACT OF THE DISSERTATION

QUANTITATIVE ASSESSMENT OF PULMONARY DISEASE USING LOW-DOSE COMPUTED TOMOGRAPHY

By

Yixiao Zhao

Doctor of Philosophy in Electrical Engineering

University of California, Irvine, 2021

Professor Sabee Molloi, Chair

Various lung disorders can lead to respiratory failure that causes significant morbidity and mortality, such as pulmonary thromboembolic disease, obstructive airway disease, and lung cancer. At present, computed tomography (CT) imaging of the chest plays a vital role in identifying distinct patterns between pulmonary diseases with varied clinical presentations. Pulmonary embolism (PE) is the third most common cardiovascular disease after cardiac infarction and stroke. While CT pulmonary angiography (CTPA) has become the first-choice imaging technique for including and excluding PE, it can only provide the morphological severity of PE without the physiological assessment regarding the pulmonary blood flow circulation. Hence, it is essential to understand physiological and pathophysiological mechanisms of pulmonary disorders via the assessment of pulmonary perfusion. Unfortunately, existing contrast-enhanced dynamic CT pulmonary perfusion techniques are limited by their unacceptable high radiation dose, systematic estimation bias, and limited scan coverage in the quantification of absolute perfusion for the entire lung, precluding their widespread clinical use. As such, there is a clinical necessity to develop an accurate, low-dose, whole-lung dynamic CT perfusion technique at a low radiation dose in

conjunction with the CTPA image. Such a technique should be capable of providing a comprehensive assessment with both morphological and physiological information and potentially improve the diagnosis and management of pulmonary diseases at early stages.

This dissertation tackles all these limitations of existing dynamic CT perfusion techniques. An accurate, low-dose, quantitative pulmonary CT-based technique incorporating CT pulmonary angiography and CT perfusion acquisition was developed, validated, and equipped for clinical translation. Such a comprehensive CT technique can accurately measure the absolute whole-lung perfusion on a voxel-by-voxel basis and evaluate regional perfusions on a lobar basis, while simultaneously providing the CTPA within a single contrast injection at a reduced effective radiation dose. Therefore, the morphological and physiological assessment of pulmonary disease is feasible using a single low-dose CT examination, making the CT-based evaluations of pulmonary diseases more reliable, accessible, and impactful to patients in need.

Chapter 1 Introduction

1.1 Research Background

Pulmonary Thromboembolic disease

Among life-threatening cardiovascular conditions, pulmonary embolism (PE) is the third most common cardiovascular disease after cardiac ischemic syndromes and stroke. (1–3). An earlier report estimated that the annual incidence of PE is approximately 100,000 cases in the United States , while the true incidence of PE remains uncertain as many cases are undiagnosed (4–6).

Pulmonary embolism (PE) occurs when a thrombus or multiple thrombi migrate from the systemic circulation to the pulmonary vasculature. From the clinical standpoint, PE shares risk factors with deep vein thrombosis (DVT) as they are both regarded as a consequence of venous thromboembolism (7). The diagnosis of PE has been challenging as the presentation of PE is often variable, non-specific, and can be completely asymptomatic at times (8). Patients with suspected PE should be evaluated efficiently as early as possible for the management of therapeutic strategies to reduce morbidity and mortality (9–11).

Pulmonary arterial hypertension

Pulmonary arterial hypertension (PAH), a chronic and progressive disease of pulmonary vasculature, is characterized by fibrotic and proliferative changes in the pulmonary arterioles, leading to endothelial and smooth muscle proliferation and dysfunction, inflammation and thrombosis (12–14). Without therapy, the increase in pulmonary vascular resistance and subsequent pulmonary arterial pressure may cause inexorable right ventricular failure, functional decline, and ultimately death. Even with increased physician awareness and rapid development of therapies in recent years, PAH remains difficult to diagnose and refractory to therapy(15).

Chronic Obstructive Pulmonary disease (COPD)

Chronic obstructive pulmonary disease (COPD) is a leading cause of morbidity and mortality with an estimation of three million deaths worldwide every year (16,17). In general, COPD refers to several lung conditions such as emphysema and chronic bronchitis, which lead to increased airway resistance and airflow obstruction. Tobacco smoking is the main cause of COPD universally (18). Despite advances in lung imaging enabled a more detailed visualization of airway and lung parenchyma abnormalities, the high prevalence and difficulty in early-stage diagnosis of COPD make it become more severe with time(19).

Pulmonary Perfusion Imaging

The lung performs multiple functions including gas exchange, regulation of blood pressure, hemostasis, as well as inflammatory and immunologic reactions in the systemic circulation (20). The process of gas exchange requires the ventilation, passive diffusion across the alveolar surface and pulmonary perfusion to be cooperatively regulated (21). Hypoxemia and carbon dioxide retention can be observed in various pulmonary diseases, resulting in the mismatch of ventilation and perfusion in the lung (22). The balance between pulmonary perfusion and ventilation varies depending on the physiopathology of different types of pulmonary diseases. Therefore, the assessment of regional pulmonary perfusion pattern change is essential to understand multiple physiological and pathophysiological mechanisms and to evaluate various types of pulmonary diseases or disorders(23). So far, multiple perfusion imaging modalities have been qualitatively and quantitatively used to evaluate pulmonary perfusion.

Single photon emission computed tomography (SPECT)

SPECT is currently one of the major clinical ventilation/perfusion lung scintigraphy, which has been frequently performed in the diagnosis of pulmonary embolism (24). Such radionuclide scanning requires the injection of ^{99m}Tc labelled macroaggregated albumin for arterial sampling, resulting in exposure to ionizing radiation (24). SPECT imaging is also limited by its low spatial and temporal resolution, soft tissue attenuation and motion artefacts.

Magnetic resonance imaging (MRI)

MRI allows for the assessment of capillary level tissue perfusion without risk from ionizing radiation (25). The dynamic first-pass contrast-enhanced perfusion MRI allows the quantitative assessment in pulmonary perfusion in academic and clinical settings(26–28). This technique measures regional pulmonary blood flow (PBF), pulmonary blood volume (PBV) and mean transit time (MTT) within the entire lung on 3-dimentional sequences. Nevertheless, the MRI perfusion is still limited by three main factors: the low signal due to low proton density, the rapid signal decay due to susceptibility differences between multiple air-tissue interfaces, and the mis-registrations caused by cardiac and respiratory motions (29,30).

CT-based perfusion imaging

The advent of computed tomography (CT) imaging techniques has enabled better visualization and quantification of pulmonary diseases such as pulmonary embolism, chronic obstructive pulmonary disease (31,32) and lung cancer (33–35). With the capability of imaging regional pulmonary blood volume by multidetector CT in the late 1990's, dynamic first-pass contrast-enhanced perfusion CT examination has been clinically implemented for improved structural and functional assessment of pulmonary nodules, thromboembolism, and therapeutic effect (36–38).

The development of dual-energy CT enabled the differentiation between different contrast materials (i.e. iodine or xenon) and lung parenchyma for assessment of regional perfusion or ventilation in pulmonary vascular diseases (39,40). Various dual-energy CT techniques such as dual x-ray sources, dual-layer detectors, or fast kilovoltage-switching methods have made it possible to obtain or reconstruct the two registered high-energy and low-energy x-ray image series(41–43). The basic principle of dual-energy CT involves material decomposition based on attenuation differences at the high- and low-energy x-ray spectra(44). As a three-component system, the lung consisting of air, soft tissue, and iodine, the additional iodine component can be derived to each voxel using the CT data acquired at both energy levels(45–47). However, several factors including low signal-to-noise ratio(SNR), mis-registration between the two image datasets are identified as limitations of these techniques (48).

CT pulmonary angiography (CTPA)

In the last decades, computed tomography pulmonary angiography (CTPA) has become the first-line imaging choice for the structural analysis of the pulmonary vasculature due to its high diagnostic accuracy, wide availability, and low invasiveness (49–51). Recent technical advances in CT have made the management of patients with suspected PE more prompt, safer, and well-standardized. The resolution has allowed for more sensitive PE diagnosis in subsegmental pulmonary arteries (2-3mm in diameter) (52,53).

1.2 Motivation

Existing dynamic CT perfusion techniques have several major drawbacks in the quantitative pulmonary perfusion measurement (54–58). First, despite that the number of detector rows has been increased by 4 to 64-detector row CT systems after clinical implementation of MDCT, most of CT perfusion techniques are still limited by its small scan ranges (38,55–57).

several small volumes-of-interest (VOIs) have been used to monitor the contrast enhancement change over the lung parenchyma at different time points (38,55–57). Unfortunately, the use of small VOIs may lead to the contrast material loss during the measurement period due to its short contrast pass time (<1 sec), resulting in a systematic bias of underestimation. Second, a large number of consecutive acquisitions is needed to apply a mathematical model for the first-pass perfusion measurement, such as the maximum slope model (MSM) and the de-convolutional model. As a result, a high radiation dose is generated per dynamic CT perfusion examination, along with the motion misregistration artifacts caused by a long breath-hold time (33–35,57,59–61). These limitations have hampered the widespread use of existing dynamic CT for assessment of pulmonary disease.

The purpose of this dissertation is to develop a low-dose, first-pass, dynamic CT perfusion technique for the quantification of pulmonary perfusion using only two prospectively acquired volume scans. A 320-slice CT scanner with 16 centimeters of cranio-caudal coverage was used to enlarge compartment size to encompass the entire lobe, fundamentally improving the perfusion measurement accuracy by preventing the contrast outflow during the measurement period as compared to the small VOIs (62,63). In addition, by significantly reducing the temporal sampling rate of the dynamic CT perfusion to two volume scans, it is possible to use a fast helical scan mode to acquire the pre- and post- contrast-enhanced images of the entire lung parenchyma for the whole-lung, first-pass perfusion measurement. Furthermore, by using an optimal contrast-specific timing protocol, the second volume scan of the CT perfusion scans can be acquired at the maximal arterial contrast enhancement and serve as the CT angiography; thus, anatomical and physiological assessment of pulmonary disease may be feasible with a single contrast injection. Lastly, given the simultaneous acquired CTPA data, automatic delineation of vessel-specific perfusion territories was determined, enabling further assessment of regional CT perfusion measurement on a lobar basis. As a result, by integrating the dynamic CT perfusion and CTPA into a single CT examination, the radiation and contrast dose can be dramatically reduced while providing a comprehensive morphological and physiological assessment of multiple pulmonary diseases. The accuracy, reproducibility and feasibility of such technique were investigated in this dissertation for the translation to clinical practice.

1.3 Dissertation Structure

The organization of this dissertation is summarized as follows:

Chapter 2 evaluates the accuracy of a low-dose first-pass analysis (FPA) CT pulmonary perfusion technique in comparison to fluorescent microsphere measurement as the reference standard. The theory of the FPA pulmonary perfusion technique as described in this chapter.

Chapter 3 develops and validates an optimal timing protocol for a low-radiation-dose CT pulmonary perfusion technique using only two volume scans. The contrast time-to-peak delay between the two volume scans was empirically correlated to one-half of contrast injection time and a specific dispersion delay. Using the optimal timing protocol, simulated two-volume prospective dynamic CT perfusion technique was assessed as compared to the previous validated retrospective FPA perfusion technique

Chapter 4 compares the image quality of CT pulmonary angiography (CTPA) using the proposed patient-specific timing protocol to the standard fixed-delay timing protocol, using retrospective CT pulmonary arterial enhancement with multiple volume scans as the reference standard. The patient-specific timing protocol is developed to improve CTPA image quality, both quantitatively and subjectively, and further reduce the contrast volume for CTPA while maintaining adequate diagnostic image quality.

Chapter 5 validates an automated minimum-cost path (MCP) technique to accurately calculate the subtended lung tissue distal to a PE using the CTPA image. The application of the MCP technique for pulmonary lobar segmentation is also implemented.

Chapter 6 validates a whole-lung, first-pass analysis perfusion technique with only two prospectively acquired scans, using either volume scan mode or helical scan mode. The reproducibility of the prospective, two-volume perfusion technique is also evaluated. Both global and regional lung perfusions are quantitatively compared.

Chapter 7 quantitatively assesses the small airway dimensions using both high-resolution CT and conventional normal-resolution CT for better assessment of airway obstructive diseases. The accuracy and limitations of measurements are evaluated at different dose levels using an airway phantom.

Chapter 8 assesses the accuracy of a new integrated intensity-based technique and a standard full-width half-maximum method for quantifying small airway dimensions. Such a technique can fundamentally overcome the partial volume effect caused by the spatial resolution in small airway assessment.

Chapter 9 concludes the dissertation and gives the future prospective for clinical translation of the low-dose pulmonary computed tomography.

Chapter 2 Validation of Dynamic Pulmonary Computed Tomography Perfusion using First-Pass Analysis Technique Against Quantitative Microsphere Perfusion Measurement

Abstract

The aim of this chapter was to evaluate the accuracy of a low-dose first-pass analysis (FPA) CT pulmonary perfusion technique in comparison to fluorescent microsphere measurement as the reference standard. The first-pass analysis CT perfusion technique was validated in six swine (41.7 ± 10.2 kg) for a total of 39 successful perfusion measurements. Different perfusion conditions were generated in each animal using serial balloon occlusions in the pulmonary artery. For each occlusion, over 20 contrast-enhanced CT images were acquired within one breath (320 x 0.5mm collimation, 100kVp, 200mA or 400mA, 350ms gantry rotation time). All volume scans were used for maximum slope model (MSM) perfusion measurement, but only two volume scans were used for the FPA measurement. Both MSM and FPA perfusion measurements were then compared to the reference fluorescent microsphere measurements. As a result, the mean lung perfusion of MSM, FPA, and microsphere measurements were 6.21 ± 3.08 ($p = 0.008$), 6.59 ± 3.41 ($p = 0.44$) and 6.68 ± 3.89 ml/min/g, respectively. The MSM (P_{MSM}) and FPA (P_{FPA}) perfusion measurements were related to the corresponding reference microsphere measurement (P_{MIC}) by $P_{MSM} = 0.51P_{MIC} + 2.78$ ($r = 0.64$) and $P_{FPA} = 0.79P_{MIC} + 1.32$ ($r = 0.90$). The root-mean-square-error for the MSM and FPA techniques were 3.09 and 1.72 ml/min/g, respectively. The CT dose index for MSM and FPA techniques were 138.7 and 8.4mGy, respectively. To conclude, the first-pass analysis technique can accurately measure regional pulmonary perfusion and has the potential to reduce the radiation dose associated with dynamic CT perfusion for assessment of pulmonary disease.

Introduction

The advent of quantitative computed tomography (CT) imaging techniques has enabled better evaluation of pulmonary disease. Multidetector CT has previously been used for detection of emphysema (52,53) and the development of the dual-energy CT has improved the differentiation between different contrast materials (i.e. iodine or xenon) and lung parenchyma for assessment of regional perfusion or ventilation (39,40). With the capability of imaging regional pulmonary blood volume, CT has been clinically implemented, thus contributing to assessment for pulmonary embolism, chronic obstructive pulmonary disease (31,32) and lung cancer(33–35).

Despite positive correlation with microsphere perfusion measurement, existing dynamic CT perfusion techniques have been hampered by a number of limitations (54–58). First, CT perfusion techniques such as the maximum slope model (MSM), derive pulmonary blood flow by monitoring the contrast enhancement over time using several small volumes-of-interest (VOIs) (57). However, this approach can be limited by short contrast transit time (<1 sec) through the small VOIs, which are inherently subject to contrast material loss from the small compartments over the measurement period. Second, curve-fitting is performed on these time-series data, which requires a large number of consecutive acquisitions for pulmonary blood flow measurement leading to high radiation dose and motion misregistration artifacts (33–35,57,59–61).Thus, the limitations of the existing perfusion models have hampered the widespread use of dynamic CT for assessment of pulmonary disease.

The purpose of this study was to validate a new low-dose dynamic CT perfusion technique based on first-pass analysis (FPA) for perfusion measurement in a swine model, with the MSM technique also implemented for comparison. The FPA CT perfusion technique has previously been validated for myocardial perfusion measurement in phantom and animal studies (64–66) and addressed the underestimation of the flow measurement by imaging the whole heart within each cardiac cycle. The use of the whole organ as the perfusion compartment allows adequate time for image acquisition and contrast accumulation before contrast exits the perfusion compartment(62,63). By increasing the perfusion compartment within the spatial domain, it is possible to reduce the temporal sampling to a minimum of only two time points for FPA measurement. The central hypothesis is that pulmonary perfusion can be accurately measured with the CT FPA technique using only two volume scans, as compared to fluorescent microsphere perfusion method as the reference standard(67).

Material and Methods

Ethics Statement and General methods

The experimental protocol was approved by the Institutional Animal Care and Use Committee (IACUC, Protocol Number: AUP-18-191) at University of California, Irvine. All studies were performed under isoflurane anesthesia, and all efforts were made to minimize suffering.

Each swine was housed in a single cage in the vivarium and food was withdrawn but water was provided for 12 hours before the study. A total of six swine (41.7 ± 10.2 kg, male, Yorkshire) were used for validation of the FPA technique with fluorescent microsphere perfusion measurements. A standard MSM dynamic CT perfusion technique was also used for comparison. All experimental data were successfully acquired between June 2016 and July 2017 and analyzed between September 2016 and December 2018. All authors conducted the experiments and data acquisition. Three authors (Y.Z., L.H., S. Malkasian.) with more than 3 years of medical imaging research experience conducted the data analysis. One author (P.A.) with 19 years of clinical radiology experience, helped with the intubation, anesthesia, catheters placement and other interventional procedures.

First-Pass Analysis (FPA) Theory

In this study, the entire lung or lobe was used as the first-pass compartment in the pulmonary perfusion measurement. The FPA technique measures the accumulation of iodine mass ($M_c(t), mg$) within the perfusion compartment (63,68), as represented by:

$$M_c(t) = \int_0^t [Q_{in}(t)C_{in}(t) - Q_{out}(t)C_{out}(t)]dt \qquad (2.1)$$

where $M_c(t)$ is the accumulated iodine mass (mg) within the compartment; $Q_{in}(t), Q_{out}(t)$ are the inflow and outflow for the compartment (ml/min); $C_{in}(t), C_{out}(t)$ are the incoming and outgoing concentration of iodine (mg/ml).

<u>For pulmonary flow measurement</u>, the accumulation of contrast mass is only caused by pulmonary circulation. Assuming no contrast material outflow from the measurement compartment over the measurement period, ***Eq 2.1*** can be simplified as:

$$M_c(t) = \int Q_P(t)C_{pa}(t)dt \qquad (2.2)$$

where $Q_P(t)$ is the pulmonary blood flow, $C_{pa}(t)$ is the iodine concentration (mg/ml) within the pulmonary artery.

By taking derivative on both sides of ***Eq 2.2***, the pulmonary flow ($Q_{ave}, ml/min$) is given by:

$$Q_{ave} = \frac{1}{C_{in\_ave}} \frac{\Delta M_c}{\Delta t} \qquad (2.3)$$

where ΔM_c is the overall contrast mass change within the compartment over the measurement period (Δt), C_{in_ave} is the average input concentration of pulmonary artery.

In this study, twenty dynamic CT volume scans were acquired for the MSM technique, but only two volume scans were systematically chosen for the FPA perfusion technique. Specifically, the first volume acquisition (V1) was chosen as the contrast started to enter the compartment with a threshold of 80 HU above the background blood pool enhancement, and the second volume scan (V2) was chosen near the peak of the pulmonary arterial input function as shown in **Figure 2.1.** Hence, the lung tissue compartment time attenuation curve (TAC) was used to calculate the change in the integrated contrast mass ($\boldsymbol{\Delta M_c}/\Delta \boldsymbol{t}$) between the first (V1) and second (V2) volume scans for the blood flow ($\boldsymbol{Q_{ave}}$, $\boldsymbol{ml/min}$) measurement (**Eq. 2.3)**. The average incoming contrast material concentration ($\boldsymbol{C_{in\_ave}}$, $\boldsymbol{mg/ml}$) was estimated using the two volume scans from the arterial input function (AIF) in the pulmonary artery (66).

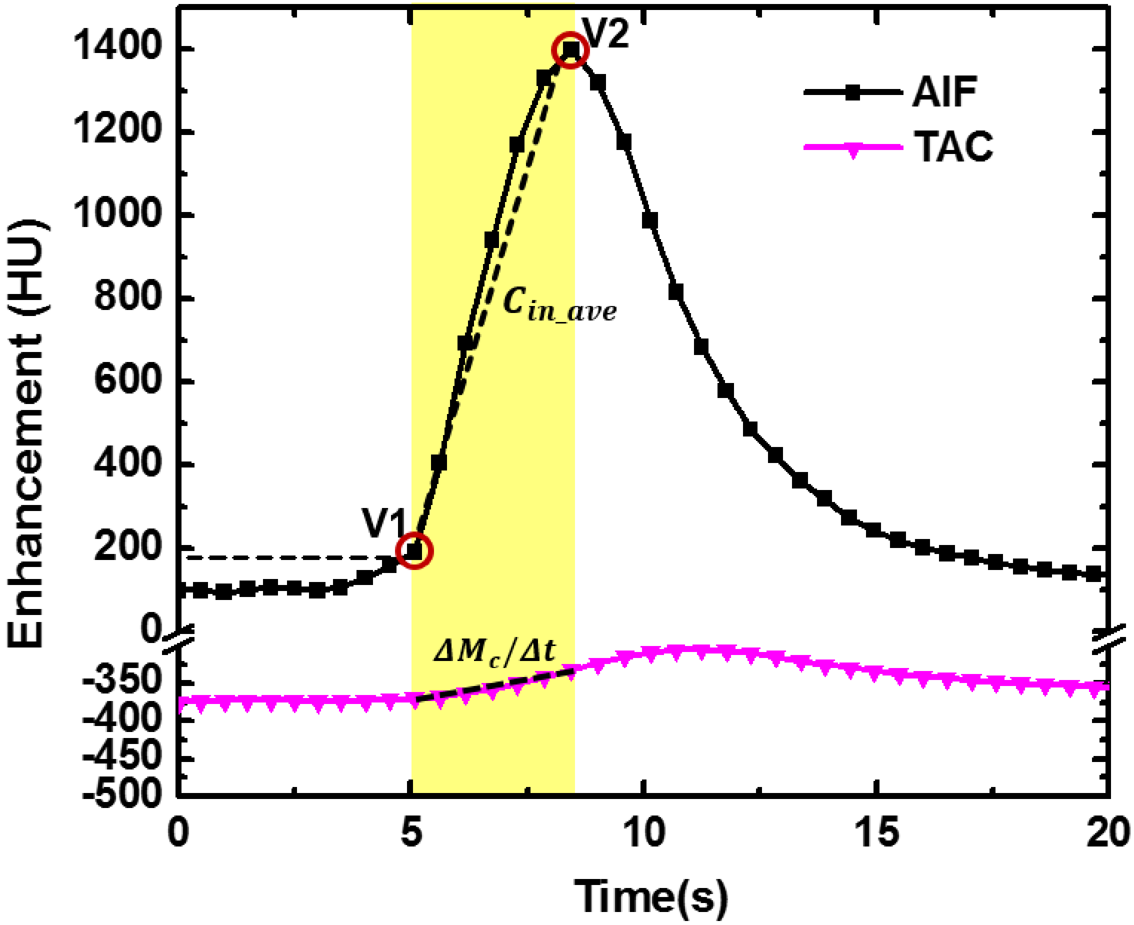

Figure 2.1 The first-pass analysis acquisition protocol.

The lung tissue compartment time attenuation curve (TAC) was used to calculate the change in the integrated contrast mass ($\Delta M_c/\Delta t$) between the first (V1) and second (V2) volume scans. The pulmonary arterial input function (AIF) was used to estimate the average input concentration (C_{in_ave}) between V1 and V2. The first volume scan (V1) was acquired with a threshold of 80 HU above the background blood pool enhancement.

Voxel-by-voxel Blood Flow Normalization

Since the contrast concentration change ($\Delta \boldsymbol{HU}$) within the entire compartment is approximately proportional to the contrast material mass change, i.e. the average pulmonary flow ($\boldsymbol{Q_{ave}}$), the voxel-by-voxel contrast concentration change ($\Delta \mathrm{HU}_{\mathrm{x,y,z}}$) can be used to estimate pulmonary blood flow on a voxel-by-voxel basis ($\boldsymbol{Q_{P_{x,y,z}}}, \boldsymbol{ml/min}$) as:

$$\boldsymbol{Q_{P_{x,y,z}}} = \boldsymbol{Q_{ave}} \frac{\Delta \boldsymbol{HU_{x,y,z}}}{\Delta \boldsymbol{HU}} \tag{2.4}$$

Voxel-by-voxel Perfusion Normalization

The pulmonary blood flow is normalized to tissue mass to account for its spatial heterogeneity. The fraction of non-air tissue ($\boldsymbol{T_f}$, %) is calculated from the non-contrast enhanced image V1 with decomposition of the pure soft tissue (greater than 50 HU) and air (less than -1000 HU) (55,69). The mass of each voxel ($\boldsymbol{M_{x,y,z}}$) is the product of tissue fraction ($\boldsymbol{T_f}$), voxel size ($\boldsymbol{Voxel_{x,y,z}}, \boldsymbol{cm^3}$) and the non-air tissue density (1.04 $\boldsymbol{g/cm^3}$) (69) as:

$$\boldsymbol{T_f} = \frac{\boldsymbol{HU_{x,y,z}} - \boldsymbol{HU_{Air}}}{\boldsymbol{HU_{Tissue}} - \boldsymbol{HU_{Air}}} \tag{2.5}$$

$$\boldsymbol{M_{x,y,z}} = \boldsymbol{T_f} \times \boldsymbol{Voxel_{x,y,z}} \times 1.04 \tag{2.6}$$

where $\boldsymbol{HU_{x,y,z}}$ represents the Hounsfield unit number per each voxel in V1 image, $\mathrm{HU_{Tissue}}$ = 50 HU, $\mathrm{HU_{Air}} = -1000\mathrm{HU}$. $\boldsymbol{M_{x,y,z}}$ is the tissue mass per voxel in gram, $\boldsymbol{T_f} \geq 1$ is set as 1.

The ultimate voxel-by-voxel pulmonary perfusion ($\boldsymbol{P_{P_{x,y,z}}}, \boldsymbol{ml/min/g}$) is derived as:

$$\boldsymbol{P_{P_{x,y,z}}} = \frac{\boldsymbol{Q_{P_{x,y,z}}}}{\boldsymbol{M_{x,y,z}}} \tag{2.7}$$

Animal Preparation

Each swine was premedicated via intramuscular injection of Telazol (4.4mg/kg), Ketamine (2.2 mg/kg), and Xylazine (2.2 mg/kg), intubated (Mallinckrodt, tube 6.0/6.5/7.0, Covidien, Mansfield, MA), then ventilated (Surgivet, Norwell, MA, and Highland Medical Equipment, Temecula, CA) with 1.5-2.5% Isoflurane (Baxter, Deerfield, IL) to maintain anesthesia. Under ultrasound guidance (9L Transducer, Vivid E9, GE 145 Healthcare), four introducer sheaths (AVANTIR, Cordis Corporation, Miami Lakes, FL) were placed in the left jugular vein (intravenous contrast injection), left femoral vein (intravenous fluid and drug administration), right femoral vein (intravenous microsphere injection), and the right femoral artery (mean arterial pressure monitoring), respectively. Two more introducer sheaths were placed in the right jugular vein for the insertion of a pulmonary arterial Swan-Ganz-balloon catheter and for reference microsphere blood withdrawal catheters. Specifically, under fluoroscopic guidance, the Swan-Ganz catheter was placed distally in the left-caudal lobe pulmonary artery branch for induction of balloon occlusion. An additional pulmonary arterial catheter was placed proximally in the left main pulmonary arterial trunk for blood sample withdrawal for microsphere perfusion measurement. Several perfusion conditions were then induced by inflating a balloon in several different locations in the left caudal lobe. ECG, mean arterial pressure (mmHg), end-tidal CO2 (mmHg), and O2 saturation (%) were monitored and recorded. After the final acquisition, each animal was euthanized with 10 cc of saturated KCL under deep anesthesia and both lungs were resected without draining the blood for tissue sample extraction.

Reference Fluorescent Microsphere Perfusion Measurement

Figure 2.2 shows a summary of data acquisition protocol. The protocol includes vascular access using fluoroscopy, dynamic CT acquisition, microsphere measurement, and postmortem tissue processing. Immediately before each CT perfusion acquisition, one color of fluorescent-labeled microspheres (NuFLOW™, IMT Laboratories, Lawrence, KS) was diluted and injected into the vena cava. A reference blood sample was then withdrawn using a syringe pump at

10ml/min via a pulmonary arterial catheter proximal to the balloon occlusion (GenieTouch; Kent Scientific, Torrington, Conn). The pump was turned on 5 seconds prior to the microsphere injection and was run for a total of 2 minutes. A total of 5 to 8 different color microspheres were used for each animal. Each color of microsphere was used for an independent CT perfusion acquisition. After all acquisitions were completed, the animal was euthanized, and 6 to 8 tissue samples (approximately 10g per sample) were excised from different lobes of both lungs. Microsphere (15.5±1.10µm in diameter) analyses were conducted independently by IMT Laboratories (67).

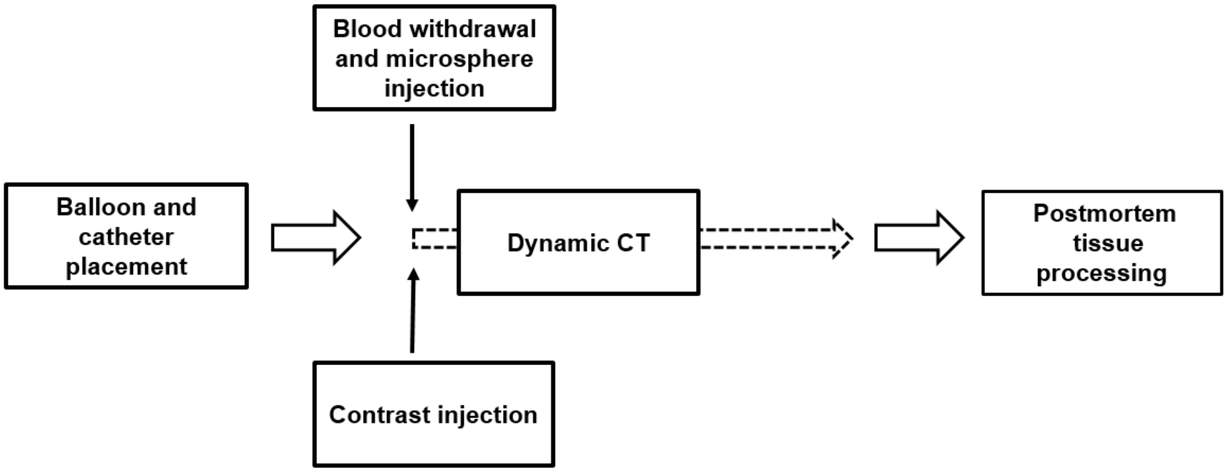

Figure 2.2 Data acquisition protocol timeline.

The protocol includes vascular access using fluoroscopy, dynamic CT acquisition, microsphere measurement, and postmortem tissue processing. The contrast and microsphere injections were made before the continuous dynamic CT scan. The blood sample withdrawal was started 5 seconds prior to the microsphere injection and lasted for two minutes.

CT Scanning Protocol

Each animal was first positioned supine, head first through the gantry (320-slice Aquilion One, Canon Medical Systems, Tustin, CA), and a localization scan was performed with a 16-cm z-coverage to include the balloon placed in the base of the lung. Balloon occlusion was then induced followed by contrast (0.5 or 1 ml/kg, Isovue 370, Bracco Diagnostics, Princeton, NJ) and saline chaser (0.25 or 0.5 ml/kg) injection at 5 ml/s (Empower CTA, Acist Medical Systems, Eden Prairie, MN). For each occlusion, the ventilator was turned off to simulate a breath hold, and ECG-gated volume acquisitions were acquired at functional residual capacity for approximately 20 seconds (100kVp, 200mA or 400mA, 0.35s rotation time, 320 x 0.5 mm collimation, FOV: 240-400mm). Detailed injection and scan parameters are summarized in **Table 2.1**. Dynamic CT perfusion acquisition was repeated approximately every 20 minutes. All volume acquisitions were reconstructed using 360 degree projection data using a soft tissue kernel (FC07) with a 0.5-mm slice thickness and an adaptive iterative dose reduction 3D (AIDR 3D) reconstruction algorithm. The CT dose index ($\boldsymbol{CTDI_{vol}^{32}}$) was recorded and the size-specific dose estimate (SSDE) was also calculated to account for the small effective chest diameter of the swine used in the study(70,71). In combination with the chest conversion factor, the effective dose for perfusion measurement with the FPA technique was also estimated (72).

Table 2.1 Acquisition Protocols and Dose Metrics for the FPA and MSM perfusion measurement.

Number of Samples (N)	Contrast (ml/kg)	FPA Perfusion (mGy)		MSM Perfusion (mGy)	
		$CTDI_{vol}^{32}$	SSDE	$CTDI_{vol}^{32}$	SSDE
200 mA (N = 2)	1	8.2	17.4	138.7	285.8
400 mA (N = 4)	0.5	26.3	54.2	434.1	894.3

Note.— $\boldsymbol{CTDI_{vol}^{32}}$ is the CT dose index for a 32 cm diameter body dosimetry phantom, SSDE is the size-specific dose estimate based on the effective diameter of the swine in the study (conversion factor : 2.06). Noted that the listed CT dose index for the FPA technique with only 2 volume scans.

FPA Perfusion Measurement

Dynamic volume acquisitions were first registered to a single coordinate system by applying a GPU-based affine and deformable registration algorithm (73). The volume-of-interest was then placed in the pulmonary artery to derive the pulmonary arterial input function **(AIF, Figure 2.1 1**). For pulmonary flow measurement, only two volume scans (V1 and V2) were systematically selected from the AIF, where V1 was defined as the first volume scan at 80 HU above the baseline blood pool enhancement as the indication of contrast arrival time, and V2 was defined as the peak of the AIF (**Figure 2.1**). Lung segmentation (lung parenchyma in the FOV) was conducted based on V1. The contrast mass change ($\Delta \boldsymbol{M_c}$) in the lung parenchyma and the average arterial input concentration ($\boldsymbol{C_{in\_ave}}$) were used to derive the pulmonary blood flow (***Eqs.2.1-2.3***). Finally, to calculate perfusion, the average blood flow was normalized to each voxel (***Eq. 2.4***) and the non-air tissue mass for each voxel was calculated based on V1 (***Eqs. 2.5–2.6***). The final pulmonary perfusion per voxel was calculated as the voxel flow normalized by voxel mass (***Eq.2.7***).

To derive regional pulmonary perfusion measurements for the validation of microsphere measurements, digital segmentations (ViTAL Images; Canon Medical Systems) were made by a chest radiologist (P.A.) with 19 years of clinical experience, to correspond with the excised tissue samples used for the reference microsphere perfusion measurements. Anatomical landmarks were used as a guide for correspondence between excised tissue samples and digital segmentation. Blood vessels were excluded by excluding voxels greater than 100 HU (52,74). The average CT perfusion within each digital segment was compared to the corresponding reference fluorescent microsphere perfusion measurement.

MSM Perfusion Measurement

Maximum slope model (MSM) perfusion data were generated using a standard commercial software (ViTAL Images, CT Body Perfusion 4D, Dual-Input Lung Workflow). After automatic registration, small regions-of-interest (ROIs) were placed within the pulmonary trunk and lung parenchyma to generate arterial input functions and tissue attenuation curve, respectively. A parametric pulmonary perfusion map (ml/min/100ml) was then generated. The perfusion maps were rescaled into ml/min/g by using the same mass distribution map

($\boldsymbol{M_{x,y,z}}, \boldsymbol{g/ml}$, ***Eq.2.6***) as the FPA perfusion measurement. Regional perfusion measurements were also averaged using the same regional segmentations as the FPA measurement.

Statistical Analyses

For all microsphere perfusion measurements (including all tissue samples under all perfusion conditions), the combined variance within each subject was compared with the combined variance of measurements between subjects with intra-cluster correlation. To evaluate the performance of the FPA and MSM techniques, linear regression (Pearson's r) and Bland-Altman analyses were performed as compared to the reference fluorescent microsphere perfusion measurements. The root-mean-square error (RMSE) (mean prediction error between the measurement and the gold standard measurement), the root-mean-square deviation(RMSD) (mean prediction error between the measurement and the line of best fit in the regression analysis) and Lin's concordance correlation coefficient (75) (concordance between the measurement and the gold standard measurement) were also determined. Student's t-tests were used to assess mean differences of the FPA and MSM techniques with the reference microsphere perfusion measurements. Statistical software (SPSS, version 22, IBM, Armonk, NY) was used for all statistical analyses.

<u>Results</u>

Vitals and Statistics

The FPA CT perfusion technique was validated in six swine (41.7 ± 10.2 kg) for a total of 44 perfusion measurements. Five acquisitions were excluded from the dataset since reference microsphere measurements were not available. Among the 39 successful perfusion measurements, 287 segments from different lobes of both left and right lungs (7 segments per animal on average) were used in the data analysis, as shown in **Table 2.2**.

The overall heart rate and mean arterial pressure during all the CT perfusion acquisitions were 94.7 ± 18.9 bpm and 68.8 ± 22.8 mmHg, respectively. The intra-cluster correlation was calculated to be r = 0.19, indicating negligible correlation within intra-cluster measurements and statistical independence (76). The effective sample size was found to be 28, showing that 28 independent individual subjects were equivalently used in this study (77).

Lung Mass Validation

The average CT-measured lung mass and the actual ex-vivo mass were 455.4 g (372.5 – 496.0 g) and 434.3 g (347.2 – 487.4g), respectively (p=0.20, RMSE=38.2g).

Qualitative Validation

No significant image quality differences were found between images acquired using 400 and 200mA. Representative FPA and MSM pulmonary perfusion maps under 4 different balloon occlusion conditions acquired at 400 mA are shown in **Figures 2.3** and **2.4**. Additional FPA pulmonary perfusion maps with and without balloon occlusion acquired at 200 mA are shown in **Figure 2.5**.

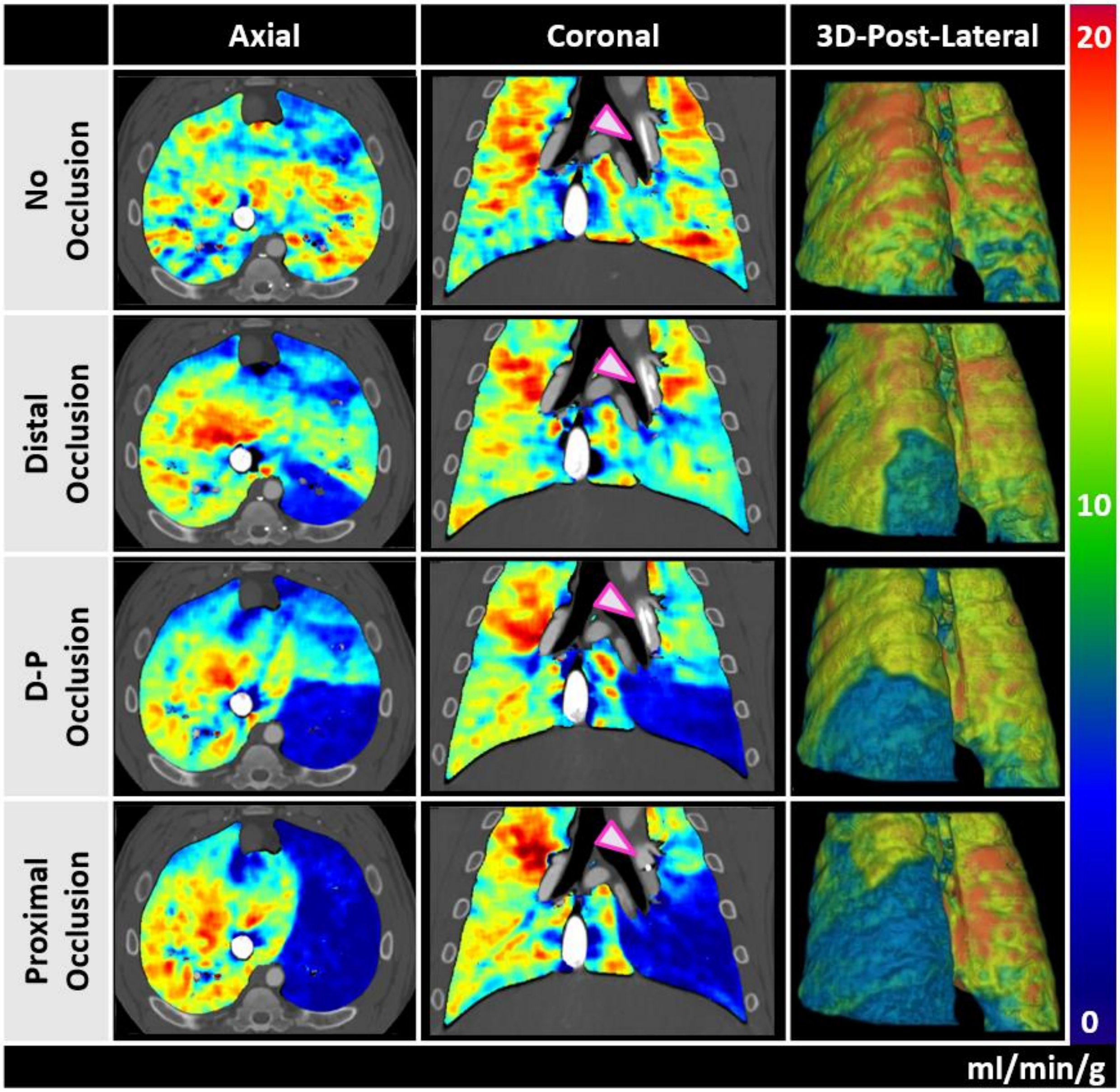

Figure 2.3 FPA pulmonary perfusion maps for different balloon occlusions acquired at 400mA.

Axial, coronal, and 3D posterior-lateral views in the presence of no occlusion (first row), a distal occlusion (second row), a distal-to-proximal occlusion (third row) and a proximal occlusion (fourth row) are shown. The arrows indicate the location of the balloon for each occlusion. The color bar indicates perfusion in the range of 0-20 ml/min/g.

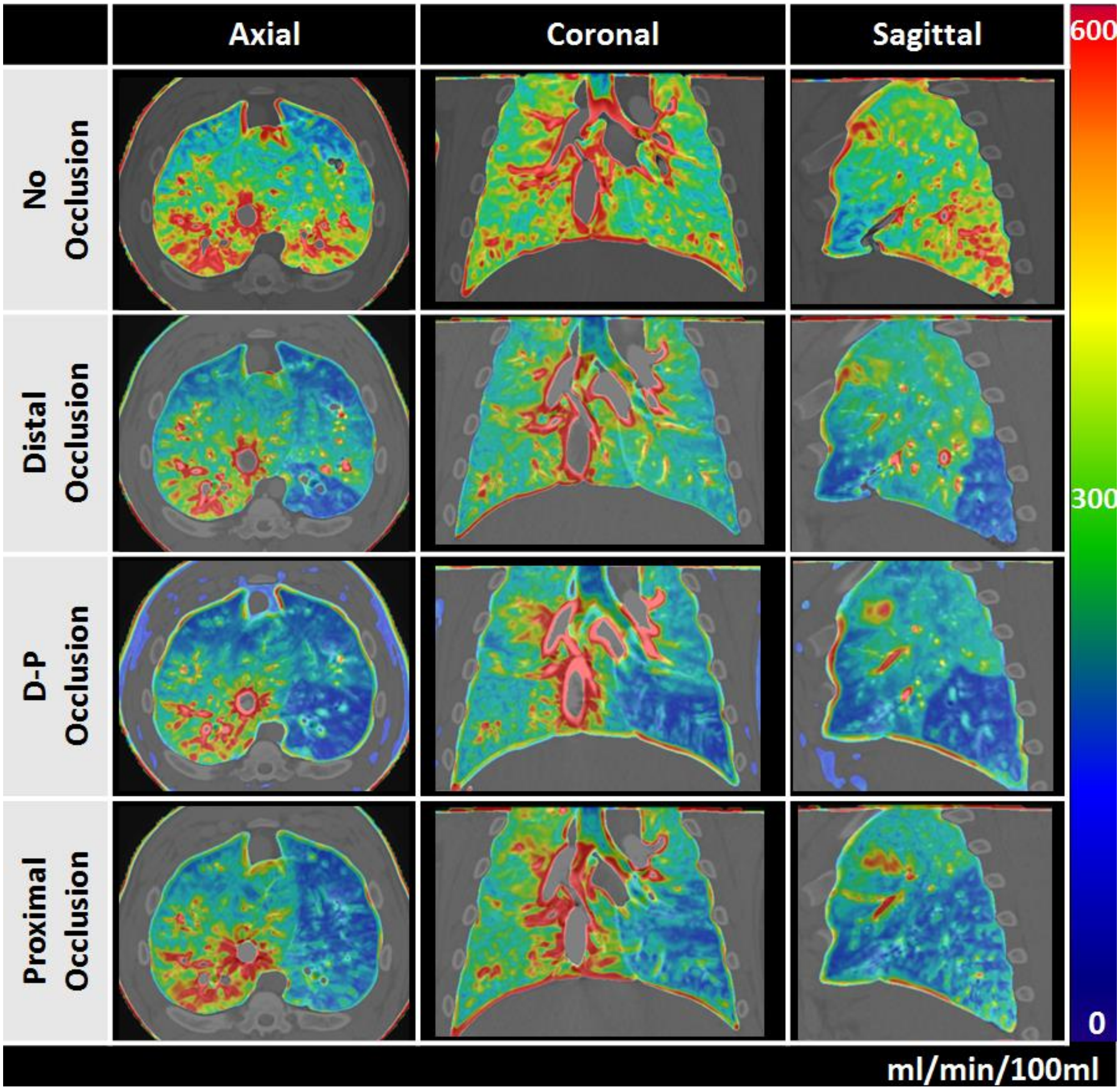

Figure 2.4 MSM pulmonary perfusion maps for different balloon occlusions acquired at 400mA.

Axial, coronal, and sagittal views in the presence of no occlusion (first row), a distal occlusion (second row), a distal-to-proximal occlusion (third row) and a proximal occlusion (fourth row) are shown. The arrows indicate the location of the balloon for each occlusion. The color bar indicates perfusion in the range of 0-600 ml/min/100ml.

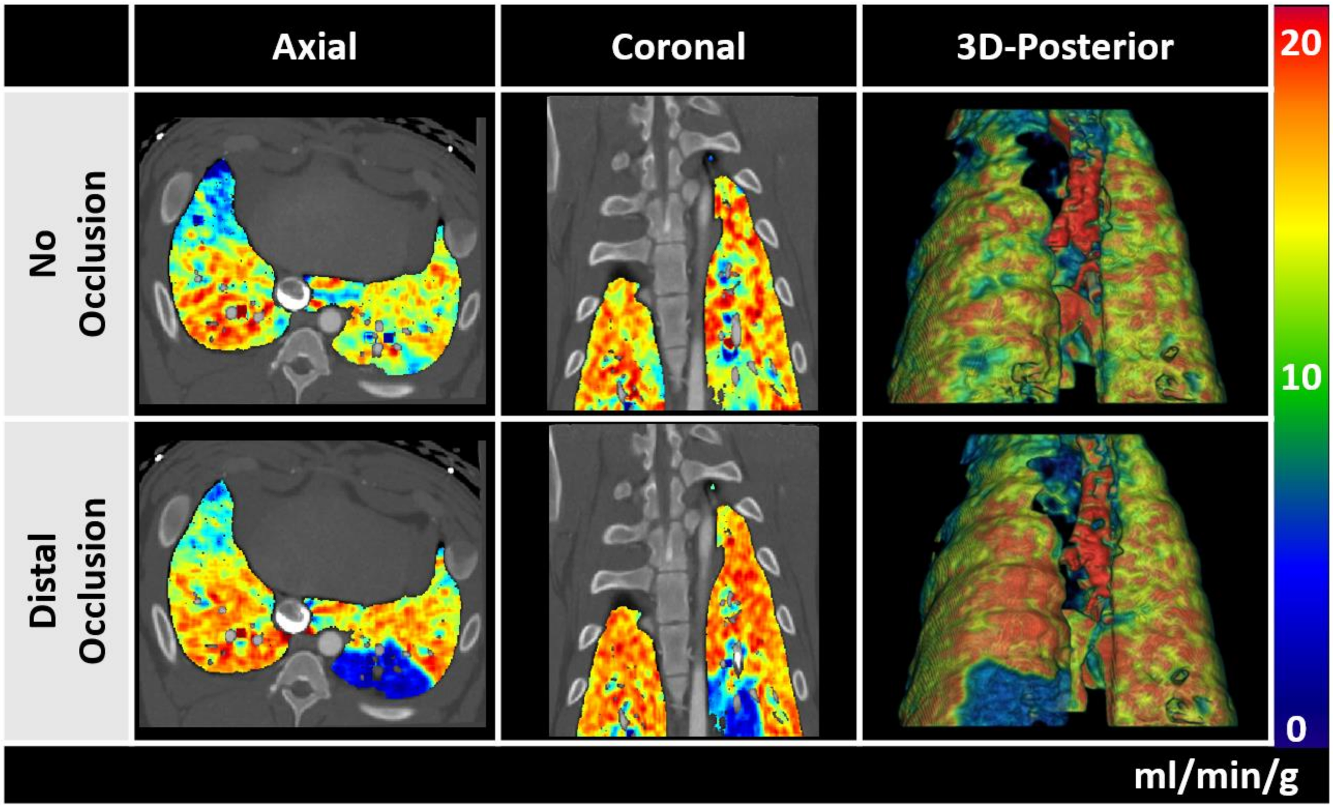

Figure 2.5 FPA pulmonary perfusion maps for different balloon occlusions at 200mA.

Axial, coronal, and 3D posterior views in the presence of no occlusion (first row) and a distal occlusion (second row) are shown. The color bar indicates perfusion in the range of 0-20 ml/min/g. Images were acquired at 200 mA.

Quantitative Analysis

For all segments combined, the mean lung perfusion of the FPA and MSM techniques were 6.59 ± 3.41 (p = 0.44) and 6.21 ± 3.08 (p = 0.008) ml/min/g, respectively, while the mean microsphere perfusion was 6.68 ± 3.89 ml/min/g. Detailed pulmonary perfusion comparisons (n = 287) are summarized in **Tables 2.2** and **2.3**. Since the balloon occluded the arterial branch in the left caudal lobe, a reduction in perfusion can be found in the occluded regions in the left caudal anterior lobe (n = 39, FPA: 4.65 ± 2.98 vs. microsphere: 4.55 ± 2.95 in ml/min/g) and left caudal posterior lobe (n = 28, FPA: 2.76 ± 3.57 vs. microsphere: 2.17 ± 3.37 in ml/min/g) as compared to the other lobes. Except for the occluded regions, the mean perfusion values gradually decreased from the caudal lobe to the cranial lobe, indicating the change in the lung perfusion by gravitational effects, as shown in **Table 2.2**. Significant differences from the middle lobes, cranial lobes are mainly caused by the beam hardening artifacts by the contrast in vena cava and heart.

Table 2.2 FPA and MSM mean pulmonary perfusion versus reference microsphere mean perfusion.

		Microsphere	**FPA**		**MSM**	
	Number of Samples	Reference Perfusion (ml/min/g)	CT Perfusion (ml/min/g)	P-value ($\alpha < 0.05$)	CT Perfusion (ml/min/g)	P-value ($\alpha < 0.05$)
	n	Mean ± SD	Mean ± SD		Mean ± SD	
Right Lung	**155**	**7.49 ± 3.51**	**7.40 ± 2.82**	**0.513**	**7.08 ± 2.78**	**0.128**
Right Cranial Lobe	12	6.79 ± 4.45	5.93 ± 3.36	0.038*	4.03 ± 1.91	0.005*
Accessory Lobe	39	7.88 ± 2.47	7.97 ± 4.67	0.776	8.23 ± 2.62	0.537
Right Middle Lobe	39	5.80 ± 2.60	6.44 ± 1.91	0.013*	7.32 ± 2.48	0.004*
Right Caudal Anterior Lobe	39	8.95 ± 2.79	8.49 ± 1.88	0.174	6.93 ± 1.80	<0.001*
Right Caudal Posterior Lobe	19	7.62 ± 5.24	7.04 ± 4.81	0.023*	6.64 ± 3.81	0.036*
Left Lung	**132**	**5.71 ± 4.09**	**5.63 ± 3.78**	**0.542**	**5.22 ± 3.16**	**0.037***
Left Cranial Lobe	12	4.45 ± 2.21	4.22 ± 2.54	0.583	4.28 ± 2.58	0.728
Left Middle Lobe	27	7.76 ± 1.97	7.25 ± 2.27	0.126	7.97 ± 2.67	0.787
Left Caudal Superior Lobe	26	9.72 ± 4.26	9.14 ± 3.45	0.156	6.71 ± 2.61	<0.001*
Left Caudal Anterior Lobe	39	4.55 ± 2.95	4.65 ± 2.98	0.701	4.63 ± 2.03	0.814
Left Caudal Posterior Lobe	28	2.17 ± 3.37	2.76 ± 3.57	0.001*	2.28 ± 2.44	0.055
Both Lungs	**287**	**6.68 ± 3.89**	**6.59 ± 3.41**	**0.440**	**6.21 ± 3.08**	**0.008***

Note.— SD: Standard Deviation.

1. The mean perfusion values are the average perfusion values of each lobe sample, the SD values are the perfusion value variations from the same sample, not the measurement errors.
2. The P-values are calculated by the paired-samples t-test statistics. The larger P-values indicate higher similarity between the two groups of data.
3. * Denotes mean CT perfusion values that are significantly different from reference microsphere perfusion values.

Table 2.3 FPA and MSM pulmonary perfusion regression versus reference microsphere perfusion.

Technique	Slope	Intercept	Pearson r	CCC	RMSE (ml/min/g)	RMSD (ml/min/g)
FPA						
Right Lung (n = 155)	0.69* (0.63, 0.76)	2.22* (1.68, 2.77)	0.85* (0.80, 0.89)	0.83* (0.77, 0.88)	1.81	0.87
Left Lung (n = 132)	0.85* (0.79, 0.91)	0.78* (0.34, 1.22)	0.92* (0.89, 0.94)	0.92* (0.88, 0.94)	1.61	0.58
Both Lungs (n = 287)	0.79* (0.75, 0.84)	1.32* (0.98, 1.67)	0.90* (0.87, 0.92)	0.89* (0.86, 0.91)	1.72	1.50
MSM						
Right Lung (n = 155)	0.36 (0.24, 0.47)	4.42 (3.49, 5.36)	0.45 (0.30, 0.57)	0.43 (0.29, 0.56)	3.38	2.48
Left Lung (n = 132)	0.59 (0.51, 0.68)	1.83 (1.24, 2.44)	0.77 (0.69, 0.84)	0.74 (0.65, 0.81)	2.69	2.05
Both Lungs (n = 287)	0.51 (0.44, 0.58)	2.78 (2.24, 3.33)	0.64 (0.57, 0.71)	0.62 (0.54, 0.69)	3.09	2.38

Note.—Data in parentheses are 95% confidence intervals. CCC: concordance correlation coefficient, RMSD: root-mean-square deviation, RMSE: root-mean-square error.

* Denotes FPA perfusion regression parameters that are significantly different than MSM perfusion regression parameters, as indicated by non-overlap of each 95% confidence interval, respectively.

FPA perfusion measurements (P_{FPA}) were related to the reference fluorescent microsphere measurements (P_{MIC}) by $P_{FPA}=0.79P_{MIC}+1.32$ (r = 0.90), with a concordance correlation coefficient (CCC) of 0.89, a root-mean-square deviation (RMSD) of 1.50 ml/min/g and a root-mean-square error (RMSE) of 1.72 ml/min/g (**Figure 2.6a**). MSM perfusion measurements (P_{MSM}) were related to reference fluorescent microsphere perfusion measurements by $P_{MSM}=0.51P_{MIC}+2.78$ (r = 0.64), with a CCC of 0.62, RMSD of 2.38 ml/min/g and RMSE of 3.09 ml/min/g (**Figure 2.6c**). Both FPA and MSM measurements had a downward trend in the Bland-Altman plot (**Figures 2.6b** and **2.6d**), but the MSM technique showed worse correspondence at higher perfusion measurements. With respect to the two different tube currents, the overall measurement error was slightly lower for high tube currents as compared with the low tube currents. Specifically, for 400mA data, the RMSE and RMSD for the FPA technique were 1.37 and 1.29 ml/min/g, for the MSM technique were 2.69 and 2.14 ml/min/g, respectively. For 200 mA data, the RMSE and RMSD for the FPA technique were 2.34 and 1.92 ml/min/g, for the MSM technique were 3.87 and 2.87 ml/min/g, respectively.

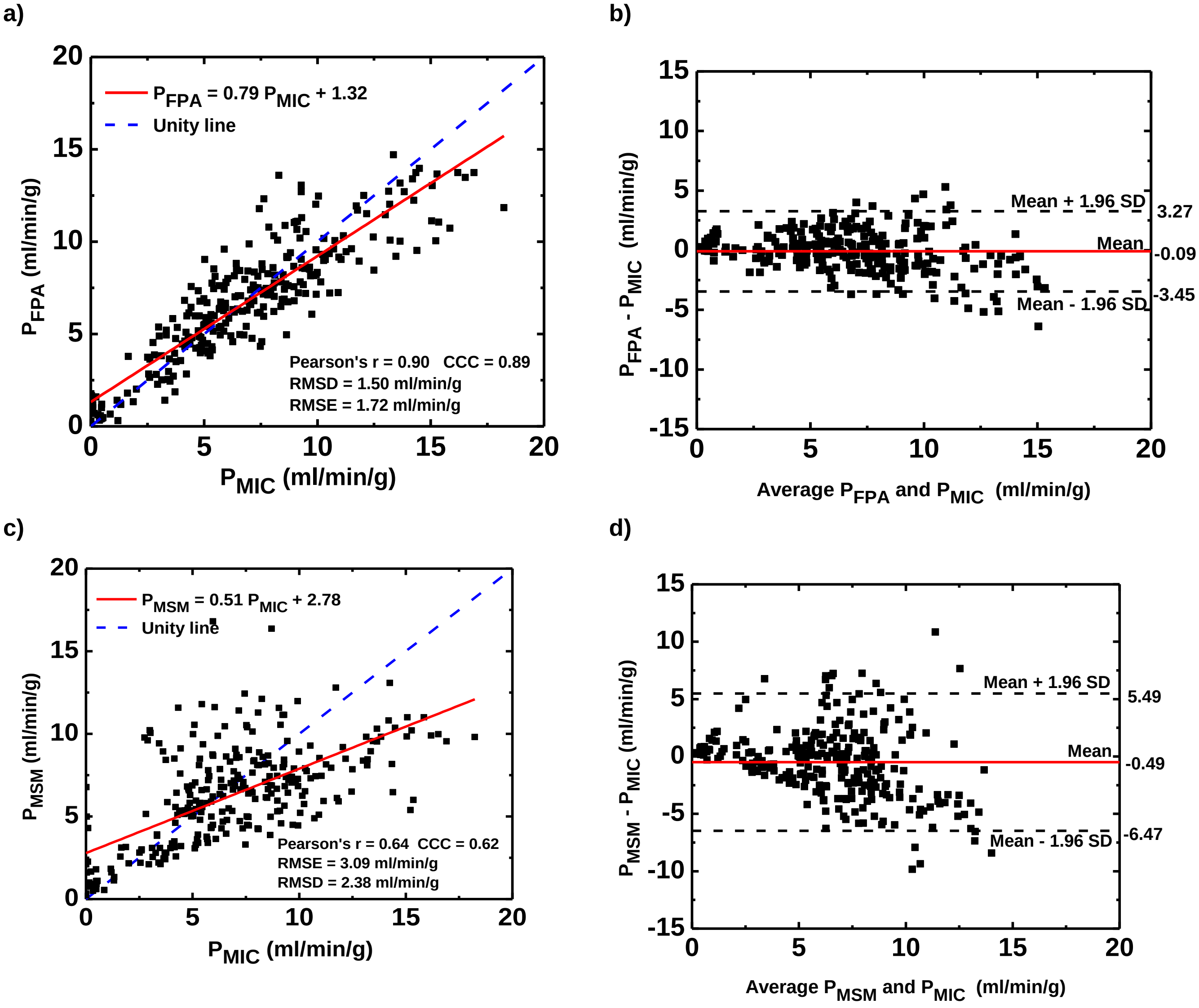

Figure 2.6 Quantitative analysis of FPA and MSM perfusion measurements versus reference fluorescent microsphere perfusion measurements.

(a,c) Regression analysis comparing the results of two perfusion measurements to the reference standard perfusion measurements. (b,d) Bland-Altman analysis was performed for both techniques, with the limits of agreement. P_{FPA}: FPA perfusion measurements, P_{MIC}: Reference fluorescent microsphere measurements, P_{MSM}: MSM perfusion measurements
RMSD = root-mean-square deviation, RMSE = root-mean-square error, CCC = concordance correlation coefficient.

The repeatability analysis of the FPA and MSM perfusion measurements are shown in **Figure 2.7**. Two repeated contrast injections were made in two animals with the same occlusion. The interval between the two acquisitions, the average change in heart rate and blood pressure were 15 minutes, 2.18% and 12.75%, respectively. The results of the first (P_{T1}) and the second (P_{T1}) measurements were related by $P_{T1\_FPA} = 0.94\ P_{T2\_FPA} + 0.32$ (r = 0.99, RMSE: 0.60 ml/min/g, RMSD: 0.17 ml/min/g) for the FPA technique and $P_{T1\_MSM} = 1.08\ P_{T2\_MSM} – 0.54$ (r = 0.97, RMSE: 0.86 ml/min/g, RMSD: 0.23 ml/min/g) for the MSM technique (**Figures 2.7a** and **2.7c**). The repeatability for FPA and MSM measurements had negligible bias and lower variability (**Figures 2.7b** and **2.7d**) as compared to the accuracy measurements (**Figure 2.6**).

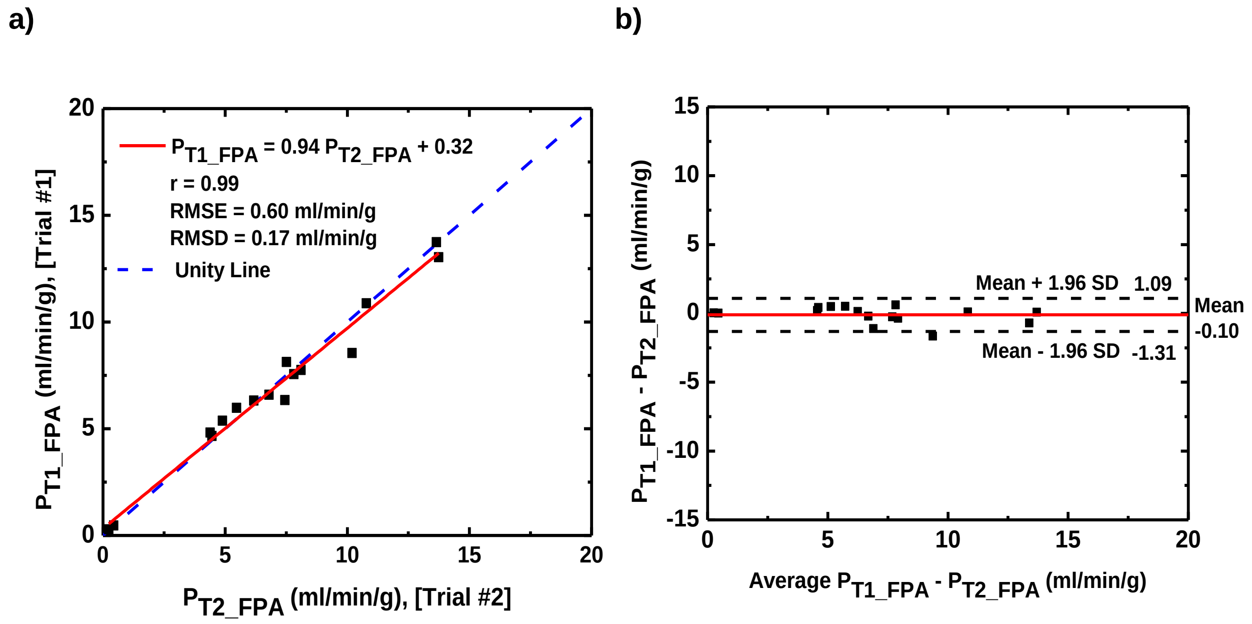

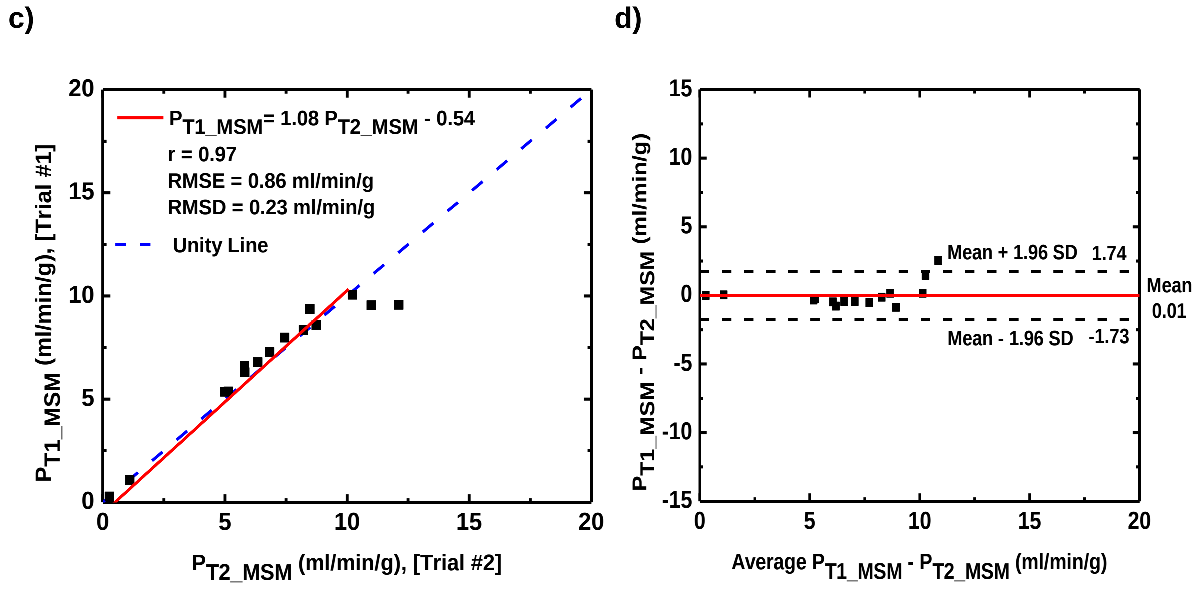

Figure 2.7 Repeatability analysis of FPA and MSM perfusion measurements.

Two repeated contrast injections were made in two animals under the same perfusion condition. (a,c) Regression analysis comparing the result of the Trial #1 to Trial #2 using the FPA and MSM perfusion measurements. (b,d) Bland-Altman analysis was performed for both techniques, with the limits of agreement.
P_{T1_FPA} , P_{T2_FPA}: FPA perfusion measurements, P_{T1_MSM} , P_{T2_MSM}: MSM perfusion measurements.
RMSD = root-mean-square deviation, RMSE = root-mean-square error.

Dose estimation

For the retrospectively acquired perfusion images at 200mA, the CT dose index for the MSM techniques was 138.7mGy. For the FPA technique, if the two volume scans were acquired prospectively, the CTDI would have been 8.4mGy. All other dose metrics are reported in **Table 2.1**.

Discussion

The results indicate that the FPA technique can accurately measure pulmonary perfusion on a voxel-by-voxel basis as indicated by the good agreement with reference fluorescent microsphere perfusion measurement. The FPA technique also has high precision for repeated perfusion measurements. Furthermore, the pulmonary perfusion measurement can be made using only two volume scans, indicating significant potential for dose reduction with its prospective implementation. Moreover, the second volume acquisition for the pulmonary perfusion measurement could potentially be used for CT pulmonary angiography; hence, the FPA technique has the potential to provide anatomical and physiological assessment of lung disease following a single contrast injection, while also reducing the radiation dose, although further validation is still necessary.

Previously reported MSM techniques (56–58) use small regions-of-interest (ROIs) for perfusion measurements, resulting in underestimation of the perfusion due to the problem of contrast loss during the measurement time. Our results agree with previous reports showing the underestimation of the MSM technique, especially at higher perfusion rates. Deconvolution-based techniques have been used to resolve the underestimation issue by estimating the venous contrast outflow over the measurement time (78,79). However, these techniques require the entire contrast-pass curve and involve high radiation doses. On the other hand, for the proposed FPA technique, the expansion of the compartment size to encompass the whole lobe enables the possibility of measuring blood flow using only two volume scans and minimizes the problem of contrast loss over the measurement time, improving the accuracy of the perfusion measurement.

Apart from the measurement accuracy, the prospective implementation of the FPA technique with two-volume scan is the most critical issue to be solved in reducing the radiation dose. A prospective timing protocol for FPA technique has recently been reported for the optimal capture of the two-volume scans at the base and peak of the aortic enhancement (80). It was shown that V1 can be acquired based on a bolus-tracking technique and V2 can be acquired after a pre-defined time-to-peak delay based on contrast injection time interval. A robust relation between the contrast injection time and the aortic enhancement time-to-peak delay was investigated to predict V2 timing, which can be further studied for the pulmonary system. A previous report has shown that accurate perfusion measurements can be made using the FPA technique for different timing protocols of the first (V1) and second (V2) volume scans (34). Furthermore, a diluted test-bolus technique(81) was also reported to prospectively determine the timing for the two-volume scans, however, with slightly increased contrast and radiation dose. By injecting the same amount of diluted contrast as the actual contrast bolus, the contrast arrival timing (V1) and maximal enhancement timing (V2) can be monitored and used for the prospective FPA volume scans(81).

The breath-hold difficulty is another limitation in clinical practice due to the length of time required for image acquisition. Previously reported dynamic CT perfusion techniques (33–35,40,56,57,59,79,82) require sampling most of the contrast pass curve with a large number of volume acquisitions for approximately 30 seconds. Images are often acquired during shallow breathing, resulting in major motion artifacts. Fortunately, given the unique two-volume sampling protocol of the FPA technique, its prospective implementation will only require a short breath hold of approximately 10 seconds. The relatively short breath-hold time is expected to substantially reduce the motion misregistration artifacts and make the FPA technique more feasible for patients with lung disease.

The effective radiation dose of dynamic CT perfusion techniques for volume CT scanners with equivalent 16-cm detector has been reported to be in the range of 4.55-50mSv (33–35,57,59–61), using a continuous dynamic volume scanning mode. If implemented prospectively, the effective radiation dose for the two-volume FPA technique is expected to be approximately 3.98mSv at 200mA using the SSDE and a chest conversion factor of 0.014mGy·cm (72). Future studies are necessary to optimize the radiation dose associated with the FPA technique, including optimization of tube current, beam energy, and other scanning parameters. Nevertheless, significant potential exists for radiation dose reduction in the proposed dynamic FPA CT perfusion technique.

Limitations

Despite improvements in quantitative pulmonary perfusion, our study had limitations. Firstly, the comparison between the physical tissue samples and the corresponding digital segmentations is challenging. Potential errors were minimized using anatomical landmarks for improved registration during the regional segmentation process. Larger physical sample sizes could help to reduce the measurement variation caused by spatial misregistration and motion. Secondly, images were acquired at a relatively high tube current, which is not necessary for accurate perfusion measurement. Therefore, additional radiation dose optimization studies will be required. Thirdly, highly attenuating contrast material in the vena cava, heart, and aorta generated significant streaking artifacts that impacted all adjacent lobes. These artifacts potentially degrade the CT perfusion measurement accuracy and precision. Further contrast dose reduction and the use of beam hardening correction algorithms (83,84) can be helpful in reducing such artifacts. Fourthly, the z-axis range was limited to 16 cm, which is smaller than the range necessary for whole lung imaging in human subjects. However, using an individual lobe as the compartment would be sufficient for the FPA model. Finally, image quality degradation is expected in the periphery of the scan range. However, this effect was difficult to quantify since all the measurements were made at approximately the same distance from the iso-center.

Conclusions

The proposed FPA technique can provide pulmonary perfusion measurement using two volume scans. In summary, the first-pass analysis technique for pulmonary perfusion measurement was validated in a swine model and has the potential to reduce the radiation dose associated with dynamic CT perfusion for assessment of pulmonary disease.

Chapter 3 Prospective Acquisition Timing Protocol for the Two-Volume Dynamic CT Pulmonary Perfusion Technique

Abstract

The aim of this chapter is to develop and validate an optimal timing protocol for a low-radiation-dose CT pulmonary perfusion technique using only two volume scans. A total of 24 swine (48.5±14.3 kg) underwent contrast-enhanced dynamic CT. Multiple contrast injections were made under different pulmonary perfusion conditions, resulting in a total of 147 complete pulmonary arterial input functions (AIF). Using the AIFs, an optimal timing protocol for acquisition of two volume scans was developed for the first-pass CT perfusion technique. Specifically, the first volume scan was obtained at the base of the AIF using the bolus-tracking; the second volume scan was obtained at the peak of the AIF using a time-to-peak relation derived by regression analysis. Additionally, a subset of 14 swine with 60 CT acquisitions were used to validate the optimal timing protocol. The prospective perfusion measurements using the two-volume scans, were quantitatively compared to the retrospective perfusion measurements using the entire AIF with t-test, linear regression, and Bland-Altman analysis. The CT dose index ($\mathrm{CTDI}_{\mathrm{vol}}^{32}$) and size-specific dose estimate (SSDE) of the two-volume perfusion technique were also determined. As a result, the pulmonary artery time-to-peak (T_{PA}) can be related to one-half of the contrast injection duration($\frac{T_{Inj}}{2}$) by $T_{PA} = 1.06\frac{T_{Inj}}{2} + 0.90$ (r=0.97). With such timing protocol, simulated prospective two-volume perfusion measurements (P_{PRO}) were related to the retrospective measurements (P_{RETRO}) by $P_{PRO} = 0.87P_{RETRO} + 0.56$ (r=0.88). The $\mathrm{CTDI}_{\mathrm{vol}}^{32}$ and SSDE of the two-volume CT technique were estimated to be 28.4 and 47.0mGy, respectively. In conclusion, the optimal timing protocol can enable an accurate, low-radiation-dose two-volume dynamic CT perfusion technique.

Introduction

Computed tomography (CT) has enabled the non-invasive quantification of pulmonary perfusion allowing for the assessment of pulmonary embolism and pulmonary hypertension (56,60,85–87). Existing dynamic CT perfusion techniques require the entire contrast pass curve over many cardiac cycles for perfusion measurement, resulting in high radiation dose (55–58,60). Moreover, the pulmonary perfusion measured by such techniques is known to be underestimated due to the use of small tissue volumes for measurement (59,66,66,88). Although dual-energy CT iodine map is also used to depict pulmonary perfusion defects, it has limited contrast-to-noise ratio and cannot provide absolute pulmonary blood flow (89–92). Hence, an accurate, low-dose dynamic CT perfusion technique is necessary for improved physiological assessment of pulmonary disease.

Fortunately, previous studies have demonstrated that accurate cardiac and pulmonary perfusion measurement is feasible with a first-pass analysis (FPA) technique using only two volume scans (65,66,93): one at the base (V1) and one at the peak (V2) of the arterial input function (AIF). Nevertheless, these prior validations required the entire AIF curve and retrospectively down-sampled to two volume scans for blood flow measurement. Hence, a timing protocol for the true prospective implementation of two-volume FPA technique remains necessary, where such protocol can also account for different hemodynamic conditions and cardiac outputs (94–97).

Thus, the purpose of this study was to develop an optimal timing protocol for the prospective two-volume FPA dynamic CT pulmonary perfusion technique. The central hypothesis is that the time-to-peak relation between the two volume scans, V1 and V2, can be predicted using one-half of contrast injection time and an empirically derived dispersion delay. Finally, using the optimal timing protocol, the accuracy of the two-volume prospective FPA dynamic CT perfusion technique was assessed as compared to the previously validated retrospective FPA perfusion technique (93).

Materials and Methods

General Method

The study was approved by the Institutional Animal Care and Use Committee (IACUC, Protocol Number: AUP-18-191). A total of 24 male Yorkshire swine (48.5±14.3 kg) were used with 154 contrast injections, where seven were excluded due to injection failures (**Figure 3.1**). In total, 147 successful contrast injections were used to retrospectively develop an optimal timing protocol for the two-volume perfusion technique (**Figure 3.1**). The time-to-peak delay between V1 and V2 was then predicted using the contrast injection duration and a dispersion delay. Finally, using the predicted time-to-peak, prospective acquisition of V1 and V2 was simulated in a subset of fourteen swine, where the accuracy of the two-volume prospective technique was compared to the previously validated retrospective perfusion measurement (93). All experimental data was prospectively acquired by all authors between March 2016 and December 2017 and was retrospectively analyzed between June 2018 and July 2019.

Animal Preparation

All 24 swine were premedicated with Telazol (4.4 mg/kg), Ketamine (2.2 mg/kg) and Xylazine (2.2 mg/kg) then intubated (Mallinckrodt, tube 6.0 - 8.0 mm, Covidien, Mansfield, MA). Anesthesia was maintained with 1.5% - 2.5% Isoflurane (Baxter, Deerfield, IL) in oxygen via mechanical ventilation (Surgivet, Norwell, MA, and Highland Medical Equipment, Temecula, CA). Two femoral venous and one femoral arterial introducer sheaths (5-Fr AVANTIR, Cordis Corporation, Miami Lakes, FL) were placed for intravenous contrast medium injection, fluid and drug administration, and arterial pressure monitoring, respectively. An introducer sheath and

Swan-Ganz catheter were then placed into a distal pulmonary arterial branch, via the jugular vein, under fluoroscopic guidance for the eventual induction of balloon occlusion. The cardiac output was varied by producing the balloon occlusion in the left caudal lobe at different locations of the pulmonary artery. At the conclusion of each experiment, all animals were euthanized with saturated KCl.

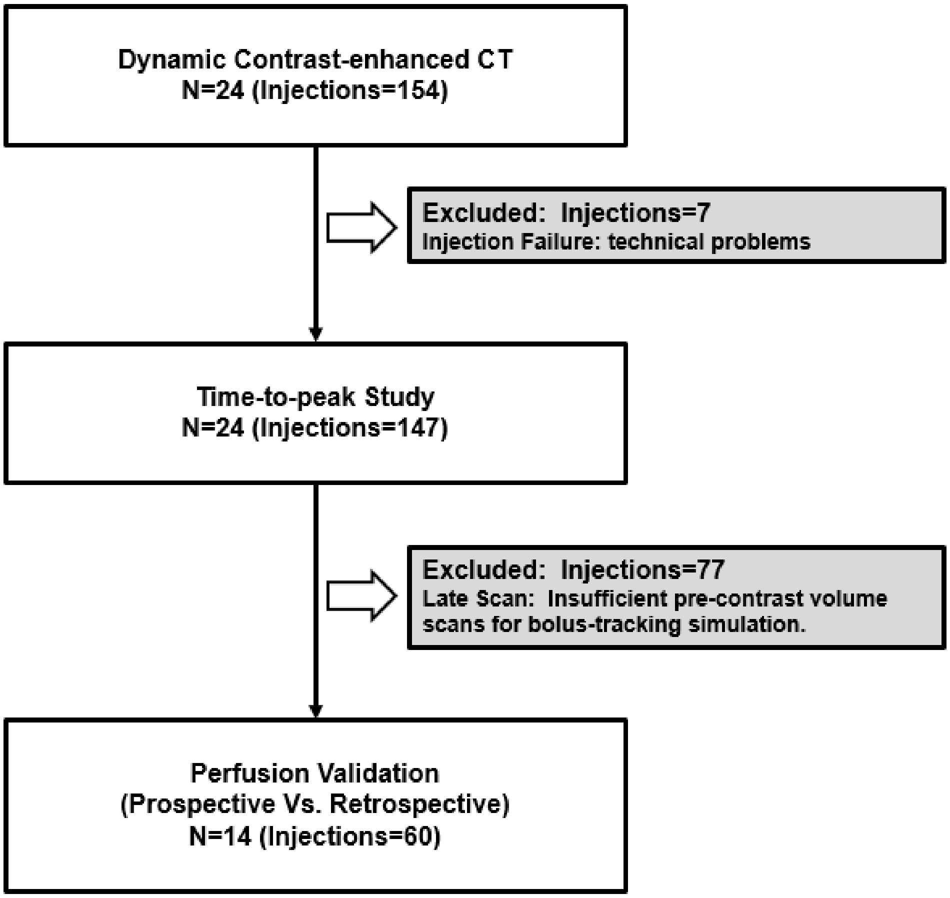

Figure 3.1 Flowchart and inclusion criterions of the study.
N = number of swine.

CT Imaging Protocol

Contrast material (Isovue 370, Bracco Diagnostics, Princeton, NJ) was injected followed by a saline chaser (Empower CTA, Acist Medical Systems, Eden Prairie, MN). Different injection rates and volumes were used as shown in **Table 3.1**. ECG-gated dynamic scanning was then performed with a 320-slice CT scanner (Aquilion One, Canon America Medical Systems, Tustin, CA) for approximately 30 cardiac cycles during a ventilator-controlled inspiratory breath hold. The following scan parameters were used: tube voltage, 100 kV; tube current, 200mA; detector collimation, 320 x 0.5 mm; volume scanning mode; gantry rotation time, 0.35 seconds; slice thickness, 0.5 mm; scan field-of-view, 240-400 mm; voxel raster, 512×512; and a FC07 soft tissue reconstruction kernel with AIDR3D iterative reconstruction. A 20-minute time delay was used between all acquisitions to allow for adequate contrast material recirculation and redistribution.

Table 3.1 Contrast injection protocols.

Injection Protocols (N = Number of swine)	**Iodine dose per body weight (ml/kg)**	**Saline Flush (ml/kg)**	**Injection rate (ml/s)**
Protocol A (N = 20)	1	0.5	5
Protocol B (N = 10)	0.5	0.25	5
Protocol C (N = 5)	0.5	0.25	10
Protocol D (N = 5)	0.25	0.125	10

Bolus Characterization and Time-to-Peak Delay Estimation

Bolus tracking is commonly used to detect the contrast arrival time within a region of interest in a monitoring artery. A fixed time delay is then used to estimate the time to peak of the contrast bolus. In this study, we will use a patient-specific time to peak estimation. Prior to recirculation phase of the contrast agent bolus passage, the geometry of the arterial input function (AIF) is predominantly determined by the contrast bolus injection geometry and the bolus dispersion within the circulatory system, given a short contrast injection duration (< 15 seconds) (94,98). Specifically, the initial rectangular geometry of an undiluted contrast bolus injection will dilute and disperse into a contrast pass curve, where the area under the curve remains conserved and the width of the curve remains proportional to the amount of the contrast volume injected at a fixed rate (96,99,100). Moreover, despite contrast mixing and hemodynamic perturbation, the dispersion of the bolus primarily occurs at its temporal edges or tails; hence, the center of the AIF has the maximal contrast attenuation. As such, we investigated the possibility of relating one-half the contrast bolus injection time ($\boldsymbol{T_{Inj}/2}$) and the time-to-peak delay ($\boldsymbol{T_P}$) of the AIF (**Figure 3.2**). In this study, such a relation was derived using the known contrast injection duration and the time-to-peak delay from the AIF, as described in **Eq. 3.1**. An empirically derived dispersion delay (D_x) was also introduced to describe the degree of the contrast bolus mixing. Such a factor is proportional to the physical distance between the contrast injection site and vessel of interest used for the AIF generation (80).

$$T_P = \alpha \times \frac{T_{inj}}{2} + D_x \qquad (3.1)$$

where $\boldsymbol{\alpha}$ is the coefficient of the relation between one-half the injection time ($\boldsymbol{T_{Inj}/2}$) and the time-to-peak ($\boldsymbol{T_P}$), $\boldsymbol{D_x}$ is the dispersion delay.

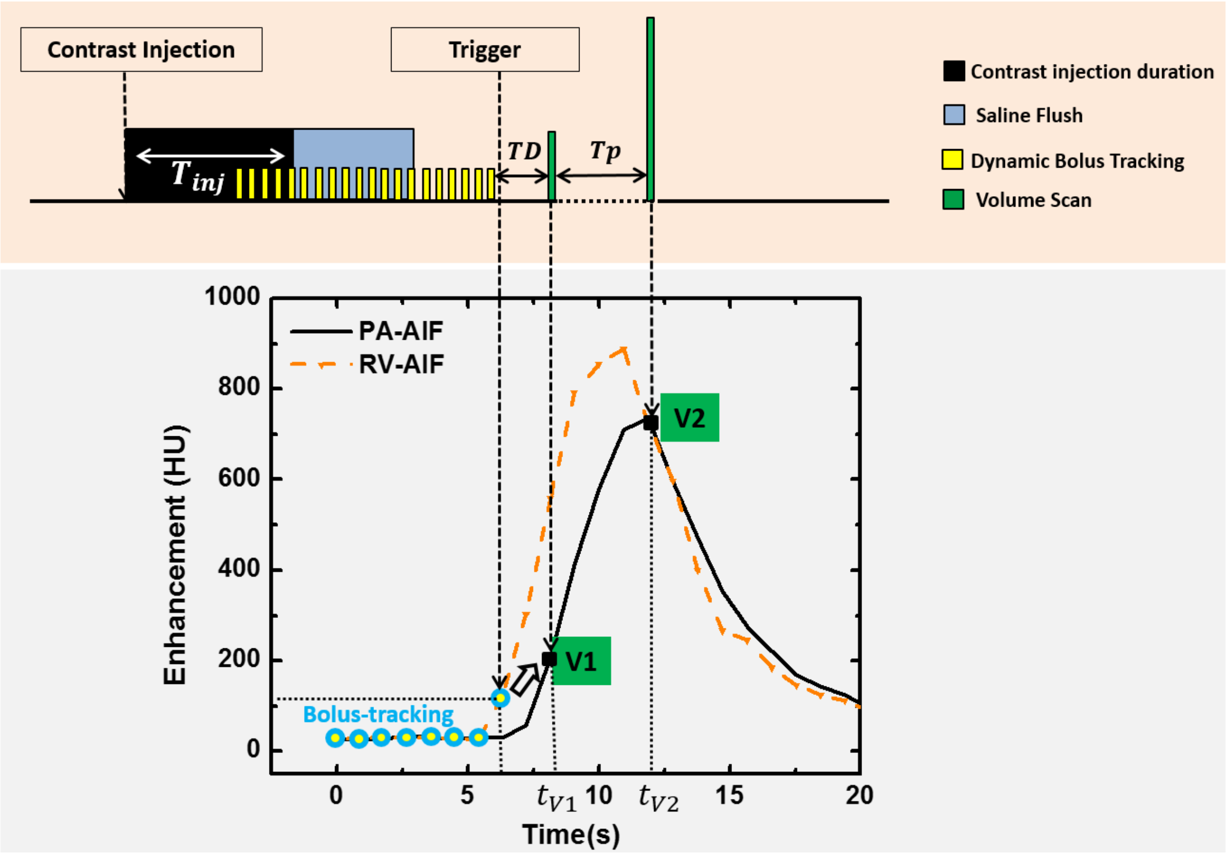

Figure 3.2 Prospective imaging protocol and the corresponding arterial input functions.
Top, imaging protocol. $\boldsymbol{T_{inj}}$ is the contrast injection duration, $\mathbf{TD}$ is the scanner-specific transition delay (2s), and $\boldsymbol{T_P}$ is the pre-defined time-to-peak delay. Bottom, right ventricle (RV) and pulmonary artery (PA) arterial input functions (AIF). $\boldsymbol{t_{V1}}$ and $\boldsymbol{t_{V2}}$ are the acquisition times for the first volume scan (V1) and the second volume scan (V2). The baseline volumes used to emulate the bolus-tracking are shown in blue circles.

Data Pre-Processing

The images from each contrast-enhanced CT acquisition were first registered using a non-rigid algorithm (73). Regions-of-interest were placed in the right ventricle, pulmonary artery, and descending aorta to generate arterial input functions (AIFs). Next, a gamma-variate fitting (LSQCurveFit; Matlab 2013a, MathWorks) was performed on each dataset to generate smooth continuous AIF curves. Next, the 3D lung parenchyma was semi-automatically segmented using a standard commercial software (ViTAL Images, Lung CT, Pulmonary Analysis Workflow; Canon Medical Systems) and was used for the whole-lung FPA perfusion measurement. Further, 3D-segmentted binary masks of approximately 800-1400 mm^3 were generated to measure regional perfusion. In summary, nine segments were assessed for each animal, including one segment for the left cranial lobe, left lingula lobe, right cranial lobe, right middle lobe, accessory lobe, and two segments for the left and right caudal lobes.

Optimal Retrospective Protocol

Using the continuous AIF curve by the gamma variate fitting, the optimal acquisition timing for the baseline volume scan (V1) was defined as the peak of the second derivative, indicating arrival of the bolus in the vessel of interest. The optimal acquisition timing for the second volume scan (V2) was then defined as the true peak of the gamma variate fit. The time-to-peak delay between V1 and V2 was then computed and then averaged over multiple acquisitions in each animal. The average time-to-peak delay was related to one-half of the contrast injection time through regression analysis for both pulmonary artery and descending aorta.

Prospective Protocol Simulation

Bolus-tracking (SureStart, Aquilion One, Canon Medical Systems, Tustin, CA) was simulated for the prospective acquisition of the first volume scan (V1) at the base of the pulmonary artery AIF. Given a minimal allowable scanner-specific transition delay (TD) between the trigger and the start of the scan(17), the monitoring region-of-interest was placed in the right ventricle (RV) instead of the pulmonary artery. Further, only the RV AIFs with at least three pre-contrast images were used to reproduce the bolus-tracking (**Figure 3.1**), where the average contrast enhancement of the first three pre-contrast images was defined as the baseline enhancement of the blood pool. Multiple offset thresholds above the baseline, e.g. 40, 60, 80, 100, 120 and 140 HU, were compared to optimize the acquisition of V1. In addition, the second volume scan (V2) was automatically chosen using the predicted time-to-peak delay that was defined in **Eq. 3.1**. Hence, the prospective timing protocol simulation is summarized in **Eq. 3.2** and **Eq. 3.3** as:

$$t_{V1} = t_{trigger} + TD \qquad (3.2)$$

$$t_{V2} = t_{V1} + T_P \qquad (3.3)$$

where $\boldsymbol{t_{V1}}$ and $\boldsymbol{t_{V2}}$ are the acquisition times of the V1 and V2, $\boldsymbol{t_{trigger}}$ is the triggering time determined by bolus-tracking in RV, $\boldsymbol{TD}$ is the scanner-specific transition delay (*2s* for our scanner), and $\boldsymbol{T_P}$ is the predicted time-to-peak delay (**Eq. 3.1)**.

Two-volume FPA CT Perfusion Measurement

First-pass analysis used for blood flow measurement as described in the previous chapter (63,68). Assuming no contrast outflow over the measurement period ($[t_{V1}, t_{V2}]$), the whole-lobe compartment is used to calculate the integrated contrast mass change of tissue ($\boldsymbol{\Delta M_c / \Delta t}$) between V1 and V2, and the average input contrast concentration ($\boldsymbol{C_{in}}$) (**Figure 3.3**). Thus, the blood flow ($\boldsymbol{Q_{ave}}$) measurement is represented by (66,93):

$$Q_{ave} = \frac{1}{C_{in}} \frac{\Delta M_c}{\Delta t} \qquad (3.4)$$

where C_{in} is the average input concentration, $\Delta M_c/\Delta t$ is the rate of contrast mass change between t_{V1} and t_{V2}, $\Delta t = t_{V2} - t_{V1}$. The cardiac output is estimated by the total blood flow to the lung. Finally, the regional perfusion of each 3D-segment is calculated and compared between the prospective and the reference retrospective FPA perfusion techniques, where the retrospective FPA was previously validated against fluorescent microspheres (93).

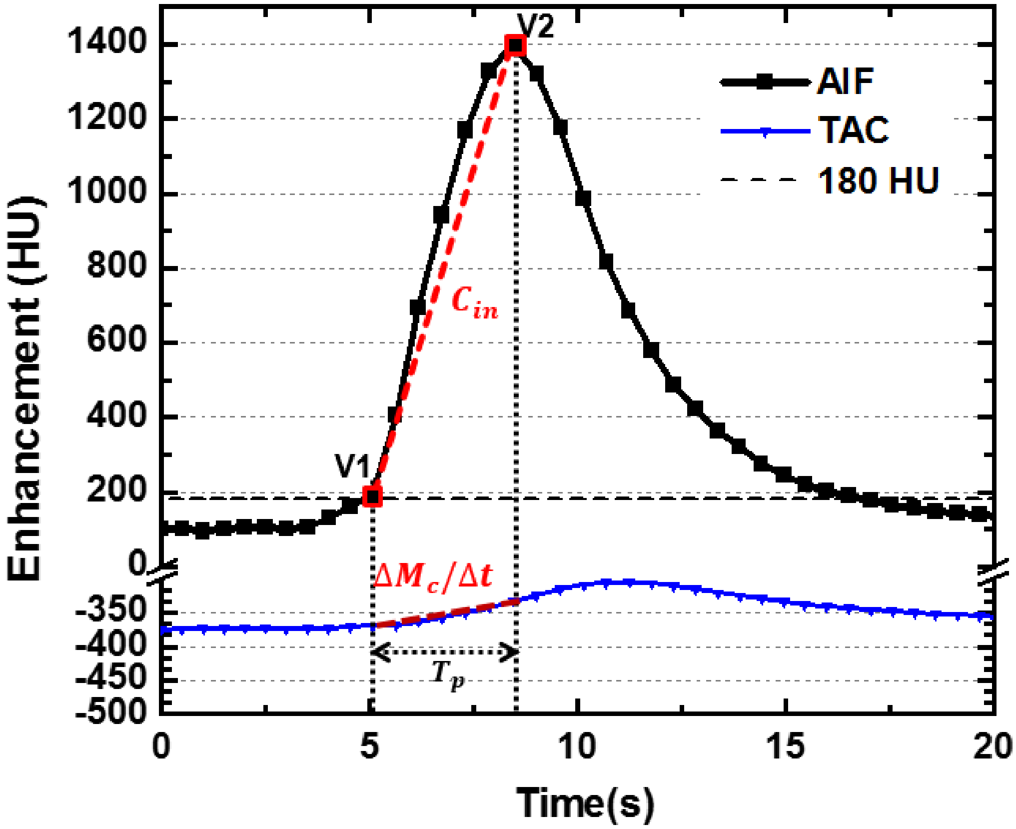

Figure 3.3 Two-volume FPA perfusion protocol.

The integrated contrast enhancement change ($\Delta M_c/\Delta t$) within the lung compartment is measured by the tissue time attenuation curve (TAC, blue line). The average input concentration ($\mathbf{C_{in}}$) is estimated from the pulmonary arterial input function (AIF, black line) at V1 and V2. $\mathbf{T_p}$ is the time-to-peak delay.

Radiation Dose

The CT dose index ($\mathrm{CTDI}_{\mathrm{vol}}^{32}$, mGy) and the dose-length product (DLP, mGy · cm) were recorded for each two-volume acquisition. Size-specific dose estimates(SSDE, mGy) were also calculated to account for the effective diameter of each swine (70).

Statistical Approach

For the time-to-peak estimation, the empirical time-to-peak delays in the pulmonary artery and descending aorta were related to one-half the contrast injection time through linear regression analysis, where the root-mean-square-error (RMSE) and root-mean-square-deviation (RMSD) of the function were also calculated. The V2 acquisition time and contrast enhancement determined by the prospective protocol simulation were then compared with the real peak time and the real peak enhancement using paired sample t-testing (SPSS, version 22, IBM, Armonk, NY). Finally, simulated prospective two-volume perfusion measurements were quantitatively compared to the corresponding retrospective perfusion measurements through regression, Bland-Altman, RMSE, RMSD, and Lin's concordance correlation coefficient (CCC).

Results

General Data and Radiation Dose Exposure

A total of 24 swine with an average weight of 48.5±14.3kg (25–91kg) and an average heart rate of 89.5±15.0 bpm was used for this study. In total, 147 successful injections were included for the time-to-peak prediction study (**Figure 3.1**). Overall, the contrast injection durations ranged from 2 to 15 seconds and the cardiac outputs ranged from1.4 to 5.1 L/min. The average $\mathrm{CTDI}_{\mathrm{vol}}^{32}$

and SSDE for each dynamic perfusion CT acquisition was 258.2 and 427.3mGy, respectively. For two-volume perfusion measurement, the $\mathrm{CTDI}_{\mathrm{vol}}^{32}$ and SSDE were calculated to be 28.4 and 47.0mGy, respectively.

Time-to-Peak Validation

The time-to-peak in the pulmonary artery (T_{PA}) and descending aorta (T_A) were related to one-half the contrast injection time by $T_{PA} = 1.06\frac{T_{Inj}}{2} + 0.90$ (r=0.97, RMSE=0.44s, RMSD=0.41s) and $T_A = 1.14\frac{T_{Inj}}{2} + 1.91$ (r=0.96, RMSE=0.82s, RMSD=0.59s), respectively (**Figure 3.4**). The intercepts correspond to organ-specific dispersion delays (D_x in **Eq. 3.1**). In the prospective pulmonary perfusion study, $\alpha = 1$ and $D_x = 1$ were chosen for **Eq. 3.1**.

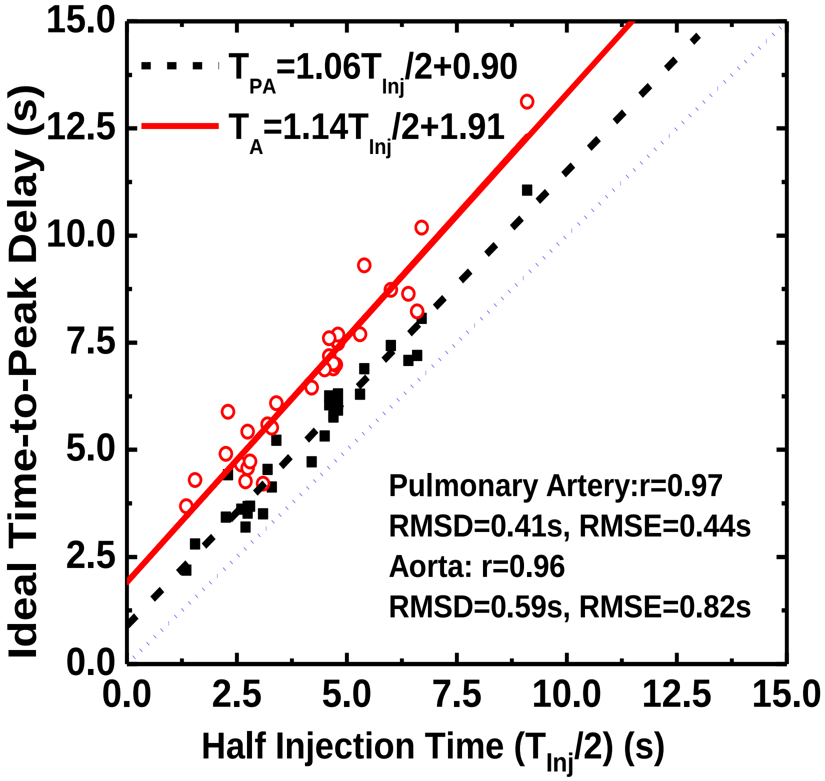

Figure 3.4 Time-to-peak delays in the pulmonary artery and descending aorta.
Gamma-fit ideal time-to-peak delays were compared to the one-half injection time. Pulmonary arterial time-to-peak (black) and the aortic time-to-peak (red) are shown with different interceptions (dispersion factor). Gamma fit time-to-peak (T_{PA}, T_A) is defined as the time between the peak of the second derivative of the

gamma fit and the true peak of the gamma fit, respectively. T_{Inj}: contrast injection time; RMSE: root-mean-square-error; RMSD: root-mean-square-deviation; r: Pearson correlation coefficient.

Prospective Protocol Simulation

A total of 60 CT acquisitions from 14 swine were used for the prospective perfusion measurements with bolus-tracking simulation. For each of the triggering offsets, the pulmonary artery enhancement and acquisition time of the simulated volume scans were compared to the optimal volume scans, as shown in **Table 3.2** and **Table 3.3**. To acquire V1 at a relatively low contrast enhancement, the triggering offset of 60HU in the RV was used in this prospective perfusion validation.

Table 3.2 Simulated Prospective Acquisition Time versus Optimal Acquisition Time.

Triggering Offsets (HU)	V1			V2		
	Time Difference (s)	**RMSE**	**P-value**	**Time Difference (s)**	**RMSE**	**P-value**
40	0.61 ± 0.61	0.86	<0.05	-0.61 ± 0.98	1.16	<0.05
60	0.87 ± 0.66	1.03	<0.05	-0.34 ± 0.96	1.02	<0.05
80	1.05 ± 0.66	1.24	<0.05	-0.17 ± 0.90	0.91	**0.252**
100	1.20 ± 0.69	1.37	<0.05	-0.03 ± 0.85	0.85	**0.921**
120	1.38 ± 0.72	1.56	<0.05	0.16 ± 0.83	0.84	0.056
140	1.53 ± 0.77	1.70	<0.05	0.31 ± 0.82	0.88	<0.05

Note-: The “Time Difference” shows the time difference between each bolus-tracking simulation and the optimal acquisition timing. The optimal acquisition timing is obtained from the gamma variate fitting AIF curve, where V1 at the second derivative peak of AIF and V2 at the AIF peak. RMSE: Root mean square error.

Table 3.3 Simulated Prospective Enhancement versus Optimal Enhancement in the Pulmonary Artery.

Triggering Offsets (HU)	C_{V1}		C_{V2}		$C_{V2} – C_{V1}$
	Enhancement (HU)	**RMSE**	**Enhancement (HU)**	**RMSE**	**Difference (ΔHU)**
Optimal	**228.8 ± 92.5**	**/**	**963.1 ± 294.4**	**/**	**735.1 ± 240.0**
40	340.1 ± 151.9	161.0	923.1 ± 302.8	77.8	583.0 ± 295.5
60	389.1 ± 173.4	214.9	914.6 ±311.2	96.4	525.6 ± 337.8
80	422. 5 ± 172.4	237.7	915.3 ±316.2	97.8	493.6 ± 332.9
100	446.3 ± 183.2	255.9	914.9 ± 319.9	98.3	468.4 ± 334.5
120	486. 3 ± 187.4	300.0	900.0 ± 332.5	122.3	413.5 ± 357.5
140	514. 5 ± 190.5	325.3	891.4 ± 330.5	134.6	377.3 ± 364.0

Note-: The "Optimal Enhancement” in the pulmonary artery is the simulated result from the gamma variate fitting curve. Specifically, C_{V1} was calculated as the average enhancement within the PA region at the time of the second derivative peak, C_{V2} was the average enhancement within the PA region at the time of peak enhancement. The root-mean-square-error (RMSE) between each triggering protocol and the ideal enhancement was also calculated.

The change in contrast enhancements (**ΔHU**) between C_{V1} and C_{V2} is shown in the last column. P-values in all comparisons are less than 0.001. Blood flow is measured based on **ΔHU.** Therefore, it is best for C_{V1} to be as low as possible and C_{V2} to be as high as possible.

Two-Volume FPA CT Perfusion Measurement

The perfusion assessments were based on a 9-segment model with a total of 540 lung segments. The mean perfusion of the retrospective and the simulated prospective measurements were 8.43±4.54 ml/min/g and 7.84±4.47 ml/min/g ($p<0.001$), respectively. The simulated prospective FPA perfusion (P_{PRO}) were related to reference retrospective perfusion (P_{RETRO}) measurements by $P_{PRO}=0.87P_{RETRO}+0.56$ (Pearson's $r=0.88$, RMSD=0.85 ml/min/g, RMSE=2.29 ml/min/g), with a concordance correlation coefficient of 0.87 (**Figure 3.5a**). The corresponding Bland-Altman analyses is also displayed in **Figure 3.5b.** The linear regression results perfusion measurements for individual lobes are shown in **Table 3.4**. There is no evident bias between lobes except for a larger error in the accessory lobe caused by the highly attenuating iodine in the vena cava. Representative examples of prospective two-volume FPA perfusion maps and the V2 image for one acquisition are shown in **Figure 3.6**. The perfusion defect by the balloon occlusion can be found in the distal left caudal lobe.

(a) **(b)**

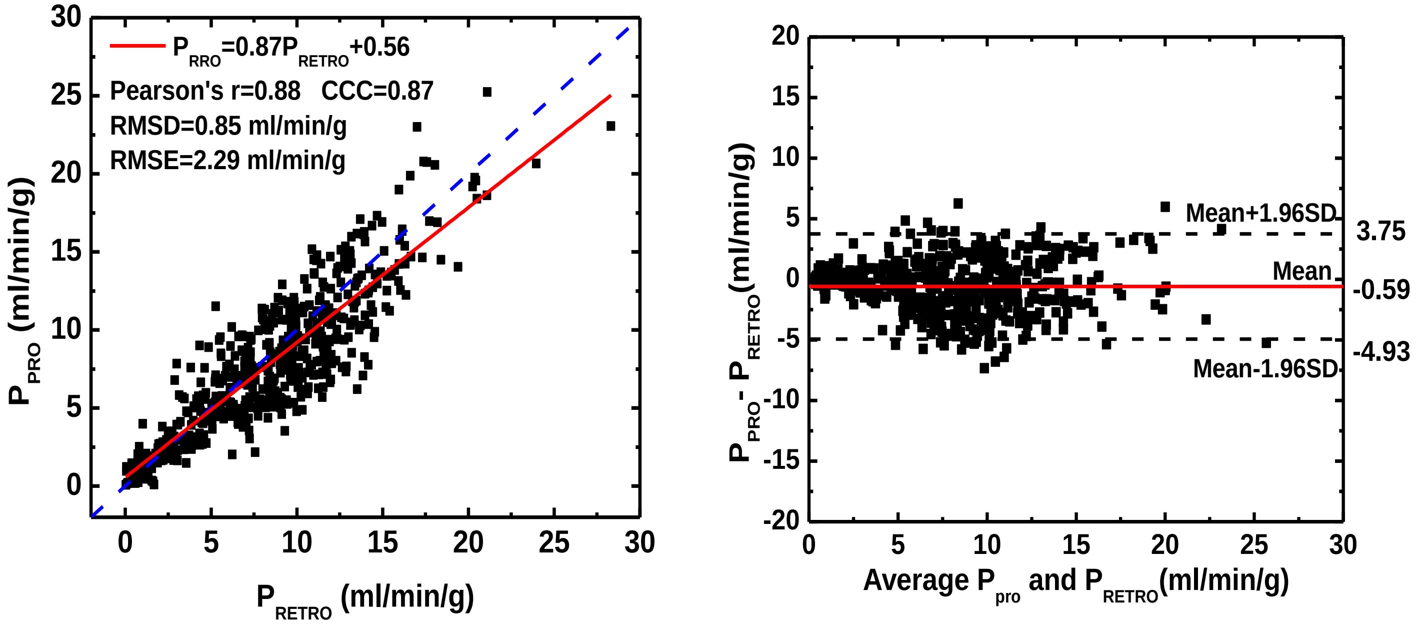

Figure 3.5 FPA prospective perfusion measurements versus reference retrospective perfusion measurements.

Regression analysis comparing the result of simulated two-volume prospective perfusion measurements (P_{PRO}) to the corresponding reference retrospective perfusion measurements (P_{RETRO}). Each data point represents an average of 3D perfusion region. For the retrospective assessment, the optimal V1 and V2 were selected at the base and peak of the AIF from the gamma fitting curve. For the prospective measurement, bolus-tracking simulation was conducted in the right ventricle within triggering threshold at 80 HU above the blood pool enhancement. (b) Bland-Altman analysis was performed with the limits of agreement.

CCC = concordance correlation coefficient, RMSD = root-mean-square deviation, RMSE = root-mean-square error, SD = standard deviation.

Table 3.4 Regression of Simulated Two-Volume Prospective FPA Perfusion versus Retrospective FPA Perfusion.

Segments (n)	Slope	Intercept	Pearson r	CCC	RMSE (ml/min/g)	RMSD (ml/min/g)	P-value
All (540)	**0.87** **(0.83, 0.90)**	**0.56** **(0.18, 0.93)**	**0.88** **(0.85, 0.89)**	**0.87** **(0.85, 0.89)**	**2.29**	**0.85**	**<0.001**
R_Cranial (60)	0.82 (0.66, 0.98)	1.13 (-0.42, 2.68)	0.81 (0.77, 0.83)	0.80 (0.77, 0.83)	2.23	0.83	0.051
R_Middle (60)	0.77 (0.62, 0.93)	0.91 (-0.26, 2.07)	0.80 (0.77, 0.83)	0.78 (0.75, 0.81)	2.19	0.90	0.019
R_Caudal (120)	0.91 (0.91, 1.00)	0.49 (-0.69, 1.66)	0.86 (0.83, 0.88)	0.85 (0.82, 0.87)	2.56	0.68	0.022
AL (60)	0.69 (0.53, 0.84)	1.90 (0.65, 3.16)	0.76 (0.72, 0.79)	0.74 (0.71, 0.78)	2.20	1.09	0.150
L_Cranial (60)	0.84 (0.69, 0.99)	0.87 (-0.69, 2.42)	0.82 (0.81, 0.86)	0.81 (0.78, 0.84)	1.87	0.85	0.036
L_Lingula (60)	0.80 (0.66, 0.93)	0.63 (-0.37, 1.64)	0.82 (0.79, 0.85)	0.81 (0.78, 0.84)	1.87	1.00	0.001
L_Caudal (120)	0.84 (0.77, 0.91)	0.50 (-0.10, 1.08)	0.92 (0.90, 0.93)	0.91 (0.89, 0.92)	2.31	1.08	0.003

Note.—Data in parentheses are 95% confidence intervals. P-value less than 0.05 indicate significant difference. CCC: concordance correlation coefficient, RMSD: root-mean-square deviation, RMSE: root-mean-square error.

AL: Accessory Lobe, R: right lung, L: left lung.

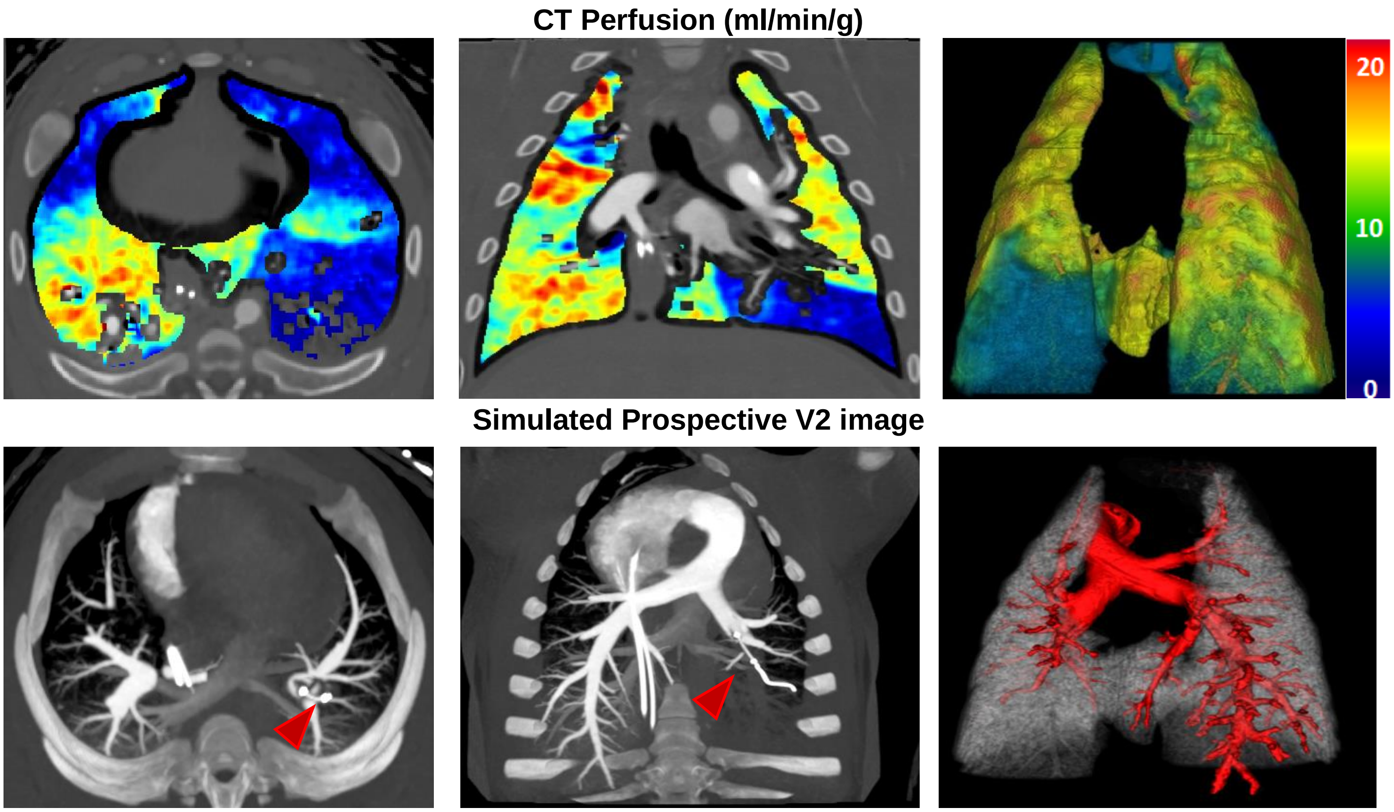

Figure 3.6 Two-volume dynamic CT perfusion maps and CT pulmonary angiography.
Top row: Axial, coronal, and 3D posterior views in the presence of balloon occlusions are shown. The color bar on the right indicates the perfusion in the range from 0 to 20 ml/min/g. Bottom row: Axial, oblique-corona, and 3D CT pulmonary angiogram generated from the corresponding V2 volume scan, displayed with a maximum intensity projection with slice thickness of 20mm. Red arrows indicate the angioplasty balloon.

Discussion

In this study, the time-to-peak delay of the pulmonary and aortic AIFs were evaluated in animals with a range of body weights (25–91 kg), contrast doses (20-100 mL), injection durations (2-15 seconds), and cardiac outputs (1.4-5.1 L/min). The results indicate that the injection duration is the most significant injection-related parameter impacting the bolus time-to-peak, particularly in the case of short contrast injection duration. Furthermore, the regional perfusion results indicate good correlation between the simulated prospective FPA measurements and the optimal retrospective FPA measurements. Such findings indicate that the proposed prospective timing protocol can potentially be used for accurate, prospective, two-volume FPA perfusion measurement.

Existing dynamic CT perfusion techniques, such as the maximum slope model and the deconvolution model, require the entire contrast pass curve for perfusion measurement resulting in a high effective radiation dose (7–9,13,15–17). Previous reports have shown that the reduction of temporal sampling frequency reduces the accuracies of these current techniques (101). Although previous reports have shown that the FPA technique can accurately measure the perfusion using only two volume scans as validated using microspheres (20,49), the prospective acquisition of the two volume scans is challenging. Given the findings of this paper, the prospective implementation of the two-volume perfusion technique can be achieved by the optimal timing protocol, enabling the accurate pulmonary perfusion measurement while substantially reducing the radiation dose.

In addition, our results demonstrate that the injection duration can be used to predict the time-to-peak for different injection rates and volumes, and are therefore in agreement with a previous report indicating that the scanning delay for the aortic peak is primarily affected by the injection duration (94). Such results may also have important implications for optimal CT pulmonary angiography (CTPA), as the optimal time-to-peak delay can be predicted using the contrast injection time interval. Although further validation remains necessary, the proposed time-to-peak prediction may result in an improved contrast opacification in CTPA and visualization of the vasculature.

Finally, previous studies have shown that pulmonary perfusion assessed with dual-energy CT (DECT) iodine density maps can be used for the clinical risk stratification of patients with acute pulmonary embolism (89,102). Another study reported that the use of DECT perfusion can be a better indicator for balloon pulmonary angioplasty in patients with chronic thromboembolic pulmonary hypertension (92). A different study has shown that subtraction CT has comparable diagnostic performance to DECT in detection of pulmonary embolism (90). However, both subtraction CT and DECT do not measure absolute perfusion. On the other hand, the proposed two-volume perfusion quantifies absolute perfusion (in ml/min/g). Quantitative absolute perfusion has the potential for improved assessment of the degree of perfusion defect. Hence, the dynamic two-volume perfusion technique can potentially be an alternative to the standard dynamic perfusion CT by providing functional assessment of pulmonary diseases, such as pulmonary embolism and chronic thromboembolic pulmonary hypertension, at a reduced radiation dose.

This study has several limitations. First, most of the swine used in the study were relatively small as compared to the average size of a patient. Additional studies may be necessary for larger patient sizes (> 90kg) to further validate the dispersion delay robustness. Second, retrospective FPA perfusion measurement was used for validation of the simulated prospective two-volume perfusion measurement. However, the accuracy of the retrospective FPA perfusion technique has previously been validated using fluorescent microspheres as the reference standard (93). Third, although the time-to-peak prediction has not been validated in patients with various cardiopulmonary conditions (such as acute pulmonary embolism, pulmonary hypertension, and heart failure), the prediction was tested following different levels of occlusion in the pulmonary artery of a swine model. Additionally, such timing protocol remained robust over a wide range of cardiac outputs. Fourth, since the scanner transition delay is manufacturer-specific, the bolus tracking trigger location and threshold have not been optimized for other CT scanners. A longer scanner transition delay after triggering may result in a late acquisition of V1. This could be a potential reason for the slight underestimation of perfusion using the simulated prospective two-volume protocol. Alternatively, the contrast arrival time can be pre-determined using a diluted test bolus acquisition (81), although the contrast and radiation dose will be slightly increased. The simulated pharmacokinetic global circulation models can also be helpful in prediction of contrast timing (97). Finally, the optimal prospective timing protocol was developed and assessed empirically (80); hence, the diagnostic performance of the two-volume FPA pulmonary perfusion technique with simultaneous CTPA (using the V2 volume scan), will require further studies.

Conclusion

An optimal timing protocol for a low-dose, two-volume dynamic CT pulmonary perfusion technique was retrospectively validated in 24 swine using pulmonary arterial AIF characterization and a first-pass analysis perfusion technique. Using dynamic bolus-tracking and time-to-peak delay estimation, the optimal timing protocol resulting in robust acquisition of the first volume scan at the base of the AIF and the second volume scan at the peak of AIF. Such finding enables a practical, low-dose, two-volume dynamic CT perfusion technique that may potentially act as a perfusion-based biomarker for stratifying the severity, prognosis, and follow-up in patients with pulmonary embolism and other pulmonary pathologies.

Chapter 4 A Patient-specific Timing Protocol for Improved Computed Tomography Pulmonary Angiography

Abstract

The aim of this chapter is to improve the image quality of CT pulmonary angiography (CTPA) using a patient-specific timing protocol as compared to the existing standard timing protocol, using retrospective CT pulmonary arterial enhancement with multiple volume scans as the reference standard. A total of 24 swine (48.5±14.3kg) underwent continuous contrast-enhanced dynamic CT acquisition over 30 seconds to capture the pulmonary arterial input function (AIF). Multiple contrast injections were made under different cardiac outputs (1.4-5.1L/min), resulting in a total of 154 AIF curves. The volume scan with maximal enhancement was retrospectively selected as the reference standard (group A). Two prospective CTPA protocols with bolus-tracking were then simulated using the AIF curve: one used a standard delay of 5 seconds (group B), while the other used a patient-specific delay based on one-half of the contrast injection duration (group C). The mean attenuation, signal-to-noise (SNR) and contrast-to-noise ratios (CNR) between the three groups were then compared using independent sample t-test. Subjective image quality scores were also compared using Wilcoxon-Mann-Whitney test. As a result, the mean attenuation of pulmonary arteries for group A, B and C were 870.1±242.5HU, 761.1±246.7HU and 825.2±236.8HU, respectively. The differences in the mean SNR and CNR between Group A and Group C were not significant (SNR: 65.2 vs. 62.4, CNR: 59.6 vs.56.4, both $p>.05$), while Group B was significantly lower than Group A ($p<.05$). In conclusion, the image quality of CT pulmonary angiography is significantly improved with patient-specific timing protocol, based on contrast injection duration, as compared with the standard timing protocol with a fixed delay. Such patient-specific timing protocol may be used to improve

CTPA image quality and further reduce the contrast volume for CTPA while maintaining adequate diagnostic image quality.

Introduction

Computed tomography pulmonary angiography (CTPA) is primarily used to detect suspected pulmonary embolism (PE) (103–108). While newer generation CT scanners have improved temporal resolution, contrast bolus timing of standard acquisition protocols with such scanners frequently miss the peak arterial contrast enhancement, leading to suboptimal image quality and reduced diagnostic accuracy (94,109,110). Hence, the optimization of CTPA contrast timing to provide adequate opacification of the pulmonary artery and its branches is highly relevant (104,111,112). Specifically, an accurate, robust timing protocol for patient-specific CTPA acquisition across a range of patients with varying hemodynamic states is essential (109,113,114).

The test bolus technique was the first known attempt to predict the proper scan timing of CTPA (115,116). Nevertheless, while it was shown to properly predict the contrast arrival time to the pulmonary circulation, it fails to predict the CTPA acquisition time at the peak of the pulmonary attenuation as the amount of contrast material used for a test bolus is much smaller than the amount needed for the diagnostic CTPA (80). Moreover, the need for additional contrast material, radiation dose, and operator interactions makes the test bolus less useful clinically. Alternatively, the bolus-tracking technique provides a better solution and has become the clinical standard for CTPA (80,109,116–121). Specifically, bolus tracking enables real-time monitoring of the contrast attenuation inside the sampling arterial vessel of interest for CTPA triggering. However, the time delay between triggering and acquisition remains largely unknown. Hence, standard CTPA protocols employ a fixed delay, without considering patient-specific parameters such as contrast injection volume and rate, body weight, and hemodynamic conditions. As a result, such protocols must also use a large volume of contrast material injected over a long period of time to increase the likelihood of good CTPA acquisition.

The purpose of this study was to assess the objective and subjective image quality of CTPA with a patient-specific timing protocol as compared to a standard timing protocol, using retrospectively acquired CTPA as the reference standard. Such patient-specific delay is determined by one-half of contrast injection duration plus a pre-defined dispersion delay. The central hypothesis was that the patient-specific timing protocol can yield images with higher contrast-to-noise ratio and better diagnostic image quality as compared to the standard protocol with a fixed delay.

Material and Methods

General Methods

The study was approved by the Institutional Animal Care and Use Committee (IACUC, Protocol Number: AUP-18-191) at University of California, Irvine. Twenty-four male Yorkshire swine (48.5±14.3kg) were used for the study. Following contrast injection, continuous dynamic CT data were acquired in all animals. Using the continuous CT images, bolus-tracking with two different prospective acquisition protocols was then simulated: a standard protocol with a fixed-delay between triggering and CTPA acquisition (group B), and a patient-specific protocol with a variable delay (group C) determined using one-half of the contrast injection duration plus a pre-defined dispersion factor. The objective and subjective image qualities of the two simulated prospective CTPA protocols were then compared to the maximal contrast attenuation of the continuous datasets (group A) as the reference standard. All experimental data were acquired between March 2016 and December 2017 and were analyzed between June 2018 and June 2019. All authors participated in the experimental design and data acquisition. YZ, LH and ShM had more than 3 years of medical imaging research experience and conducted the data analysis. PA is a radiologist with more than 15 years of clinical experience, helped with surgical and interventional procedures.

Animal Preparation

Each swine was premedicated with telazol (4.4mg/kg), ketamine (2.2mg/kg) and xylazine (2.2mg/kg), intubated (Mallinckrodt, tube 6.0-8.0mm, Covidien, Mansfield, MA) and mechanically ventilated (Surgivet, Norwell, MA, and Highland Medical Equipment, Temecula, CA). Anesthesia was maintained with 1.5%-2.5% isoflurane (Baxter, Deerfield, IL) and oxygen throughout the entire experiment. Catheters (5-Fr AVANTIR, Cordis Corporation, Miami Lakes, FL) were placed in the right femoral vein, left femoral vein and right femoral artery for intravenous contrast injection, fluid administration and pressure monitoring, respectively. Vital signs such as electrocardiogram (ECG), mean arterial pressure (mmHg), end-tidal CO2 (mmHg), and O2 saturation (%) were monitored every 15 minutes. At the end of each experiment, each animal was euthanized with saturated KCL under deep anesthesia.

CT Imaging Protocol

Each swine was imaged with a 320-slice CT scanner (Aquilion One, Canon America Medical Systems, Tustin, CA). First, a scout scan was obtained to correctly position the 16-cm cranio-caudal field-of-view for pulmonary arterial imaging. Iodinated contrast agent (Isovue 370, Bracco Diagnostics, Princeton, NJ) was then injected (0.5–1 ml/kg) at 5ml/s followed by a saline chaser (0.25-0.5ml/kg) at the same rate (Empower CTA, Acist Medical Systems, Eden Prairie, MN). ECG-gated volume scans were then acquired continuously during an inspiratory breath-hold over approximately 20 cardiac cycles. Multiple contrast injections were made under different cardiac outputs (1.4-5.1 L/min), resulting in a total of 154 acquisitions. Scan parameters were: tube voltage, 100 kVp; tube current, 200 mA; detector collimation, 320 x 0.5 mm; gantry rotation time, 0.35 second; field-of-view, 240-400mm. All images were reconstructed using a soft tissue kernel (FC07) with a 0.5-mm slice thickness and an adaptive iterative dose reduction 3D reconstruction algorithm.

Image Analysis and Reference Standard CTPA

The dynamic volumes were registered to a single coordinate system by applying a GPU-based affine and deformable registration algorithm (73). A region-of-interest (ROI) was then placed in the main pulmonary artery of each acquisition to generate the pulmonary arterial input function (AIF). In each case, the image volume at the peak attenuation of the pulmonary AIF was retrospectively selected and defined as the reference standard CTPA (group A).

Standard and Patient-specific Timing Simulation Protocols

For each acquisition dataset, two different prospective CTPA protocols were simulated. In each case, the pulmonary AIF was used for bolus-tracking based triggering. Specifically, for the standard protocol (group B), ‘triggering’ occurred when the AIF exceeded a threshold of 60 HU above the baseline blood pool enhancement while CTPA ‘acquisition’ occurred 5 seconds after triggering (**Figure 4.1a**). The baseline blood pool HU was defined as the mean HU of the first three non-enhanced samples of the AIF curve. For the patient-specific protocol (group C), triggering also occurred when the AIF exceeded 60HU above the baseline blood pool HU. However, CTPA acquisition occurred using a patient-specific delay after triggering (**Figure 4.1b**), where the patient-specific delay was predicted using the contrast injection duration and a pre-defined dispersion delay (80). Specifically, given a short injection time (<15s), with a fast injection rate (>4ml/s), and the absence of recirculation, the shape of the AIF curve is approximately normally distributed (94). Hence, the time-to-peak delay (t_{ttp}) can be linearly related to one-half of the total injection time ($\frac{\boldsymbol{t_{inj}}}{2}$) plus a dispersion delay (t_{dis}) that describes the degree of contrast dispersion occurring between the venous injection site and vessel or organ of interest. For the pulmonary artery, the patient-specific time-to-peak delay used in this study was calculated as one-half of the contrast injection time plus a 1 second of dispersion delay.

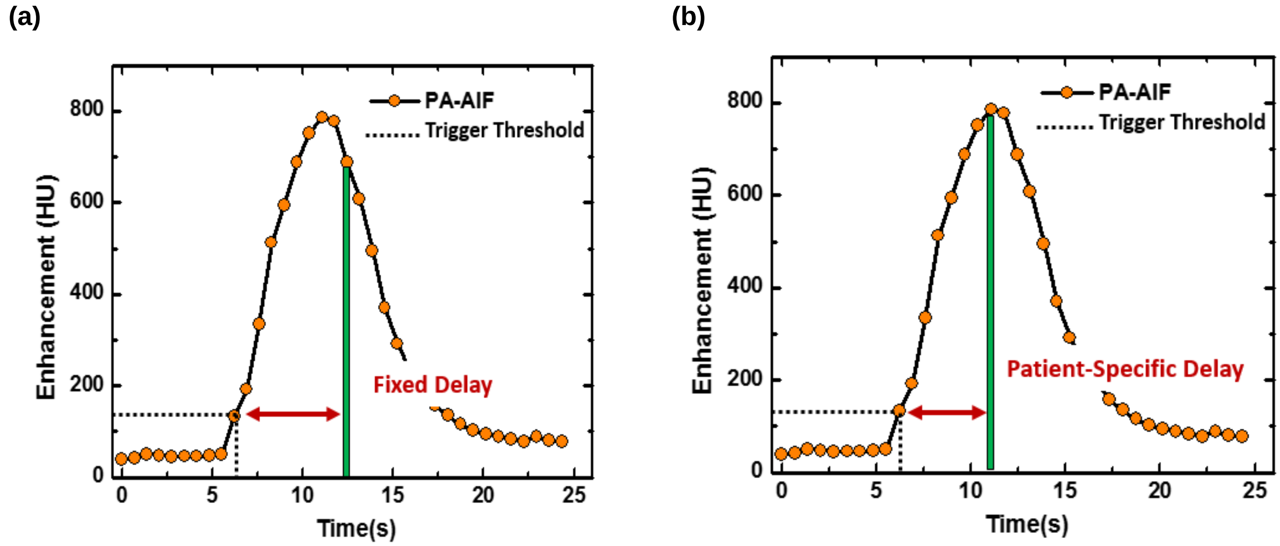

Figure 4.1 Prospective protocols for (a) standard fixed-delay timing protocol and (b) patient-specific timing protocol.

The arterial input function in the pulmonary artery trunk (PA-AIF) is shown and used to simulate bolus-tracking. For **(a)**, the CTPA volume scan is acquired 5 seconds after the triggering. For **(b)**, the CTPA volume scan is acquired after a patient-specific time delay. The patient-specific delay is derived from the one-half of injection duration plus a dispersion delay.

Objective Image Quality Assessment

To assess the level of arterial contrast enhancement achieved by each protocol, ROIs were placed in the main pulmonary artery (MPA), right pulmonary artery (RPA), left pulmonary artery (LPA), segmental arteries of the right upper lobe (RUL), right middle lobe (RML), right caudal lobe (RCL), left upper lobe (LUL), left lingula lobe (LLL), left caudal lobe (LCL), accessory lobe (AL), and sub-segmental arteries of the right caudal lobe (RCL_S) and left caudal lobe (LCL_S). In each case, the ROI was manually defined as a circular region ranging in size from $9cm^2$ for the MPA to $0.3cm^2$ for the sub-segmental arteries. The mean contrast enhancement within each vessel ROI was then calculated for group A, B and C. The signal-to-noise (SNR) and the contrast-to-noise (CNR) were also computed in each case. Specifically, three additional ROIs

(~ $3cm^2$) were drawn in artifact-free air region (anterior, left, and right, outside of the swine) and the average standard deviation in HU was defined as the background noise. The SNR of each vascular ROI was then determined as the ratio of the ROI contrast enhancement to the background noise. Two final ROIs (~ $2\mathrm{cm}^2$) were then placed in the paraspinal and subscapular muscles, and the average muscular contrast enhancement was determined. The CNR of each vascular ROI was then determined as the difference between the vascular and muscular contrast enhancement divided by the image noise.

Subjective Image Quality Assessment

Two independent blinded readers (P.A and V.B) assessed the overall subjective image quality of the pulmonary arteries for group A, B, and C, with a five-point Likert scale (111) (1=excellent , 2=good, 3=adequate, 4=poor, 5=non-diagnostic quality). Prior to reading the images from this study, 15 external CTPA images were first rated with the Likert score and discussed between the two readers. In the case of large disagreements between readers (score difference ≥ 3), the quality score was reevaluated and with the final score determined by a second joint-reading round.

Radiation Dose

For each acquisition, the CT dose index ($\mathrm{CTDI}_{\mathrm{vol}}^{32}$, mGy) and the dose-length product (DLP, mGy·cm) were recorded from the scanner dose summary log. Additionally, the effective diameter (ED) of each swine was calculated using the anteroposterior diameter (AD) and lateral diameter (LD) of the chest window ($ED = \sqrt{AD \times LD}$). Size-specific dose estimates (SSDE, mGy) were then calculated using a size-specific conversion factor (70).

Statistical Approach

All analyses were performed using IBM SPSS Statistics software (Version 22.0; Armonk NY). Quantitative variables were compared with mean ± standard deviation (SD) and 95% confidence intervals (CI). All objective and subjective image quality parameters were first verified to be normally distributed using skewness and kurtosis values and the Shapiro-Wilk test. The CT attenuations, SNR and CNR of all measurement vessels were then compared by independent-samples t tests. Additionally, the mean attenuations of different vessel generations were compared with Box-and -Whisker plot. In each case, a two-tailed p-value less than 0.05 is considered statistically significant. Subjective image quality was assessed between the two readers by rating the 12 pulmonary artery locations where the average score was calculated for each observer. The differences in rating scores across the study groups were then tested by the Wilcoxon-Mann-Whitney test. The inter-observer agreement of subjective image quality was evaluated with Cohen kappa value(***k***) with quadratic weighting (122). The kappa values were interpreted as: <0.20, poor agreement; 0.21–0.40, fair agreement; 0.41– 0.60, moderate agreement, 0.61–0.80, good agreement, and 0.81–1.00, excellent agreement.

Results

Vitals and CT Radiation Dose

Twenty-four swine were used in the study (body weight: 48.48±14.33 kg, heart rate 89.50±14.96 bpm) for a total of 154 independent contrast injections and acquisitions. The average dose for the continuous scan was 258.2mGy. For the simulated prospective CTPA acquisitions, the $\mathrm{CTDI}_{\mathrm{vol}}^{32}$ was calculated to be 9.4mGy, and the SSDE was estimated to be 17.8mGy.

Subjective Assessment

Overall subjective image quality between the two readers was in good agreement (Cohen quadratic weight ***k*** = 0.64, 95% CI: [0.47, 0.81]), as displayed in **Table 4.1**. There were no significant differences in image quality scores overall between the two readers (p=0.89). The largest disagreements were found between excellent (84.0% vs 65.1%) and good (10.8% vs 26.0%) image quality scores, while the maximum difference in image quality scores between readers was two points. The Likert scores from both readers were averaged and the group A, B, and C were compared. Significant differences were found between all three groups (p<.001), where the average subjective image quality score for each group was 1.24±0.42, 1.46±0.78 and 1.35±0.59, respectively.

Table 4.1 Subjective Image Quality Assessment.

	group A (n = 154)		group b (n = 154)		group C (n = 154)		Overall (n = 452)		
	Observer 1	**Observer 2**	**Observer 1**	**Observer 2**	**Observer 1**	**Observer 2**	**Observer 1**	**Observer 2**	**Both Observers**
1	141 (91.6%)	106 (68.9%)	119 (77.2%)	96 (62.3%)	128 (83.1 %)	99 (64.3%)	388 (84.0%)	301 (65.1%)	290 (62.8%)
2	9 (5.8%)	40 (26.0%)	23 (14.9%)	39 (25.3%)	18 (11.7%)	40 (26.0%)	50 (10.8%)	119 (26.0%)	136 (29.4%)
3	4 (2.6%)	8 (7.8%)	5 (3.2%)	13 (8.4%)	7 (4.5%)	14 (9.1%)	16 (3.5%)	35 (7.6%)	28 (6.06%)
4	0 (0.0%)	0 (0.0%)	4 (2.6%)	3 (1.3%)	0 (0.0%)	1 (0.6%)	4 (0.9%)	4 (0.9%)	4 (0.9%)
5	0 (0.0%)	0 (0.0%)	3 (1.9%)	3 (1.9%)	1 (0.6%)	0 (0.0%)	4 (0.9%)	3 (0.7%)	4 (0.9%)
Kappa value	**0.37**		**0.74**		**0.62**		**0.64**		
95% CI	**[nc, nc]**		**[0.62, 0.87]**		**[0.28, 0.96]**		**[0.47, 0.81]**		

Note.- Group A: Actual peak image from the retrospective arterial input function. Group B: The standard delay CTPA image. Group C: The patient-specific-delay CTPA image. The kappa values showed in the table are quadratic weighted values. CI: Confidence interval. NC: The quantity cannot be calculated. This was occurred when the data entries include a substantial proportion of zeros. 1 = excellent, 2 = good, 3 = adequate, 4 = poor, 5 = non-diagnostic quality.

Overall, a total of 462 CTPA images were assessed (154 images per group) and adequate image quality was achieved in 454 images (98.3%) (**Table 4.1**). For group A, all images were rated above adequate quality (100%) for both readers. For group B, the assessment showed excellent quality in 88 of 154 (57.1%), good quality in 50 of 154 (32.5%), adequate quality in 9 of

154 (5.8%), poor quality in 4 of 154 (2.6%), and non-diagnostic quality in 3 of 154 (1.9%). For group C, the assessment showed excellent quality in 96 of 154 (62.3%), good quality in 45 of 154 (29.2%), adequate quality in 12 of 154 (7.8%), and non-diagnostic quality in only one of 154 (0.6%). Representative examples of CTPA images in three different swine (body weights: 27kg, 55kg and 91kg) from each of study group are provided in **Figures 4.2, 4.3, and 4.4**.

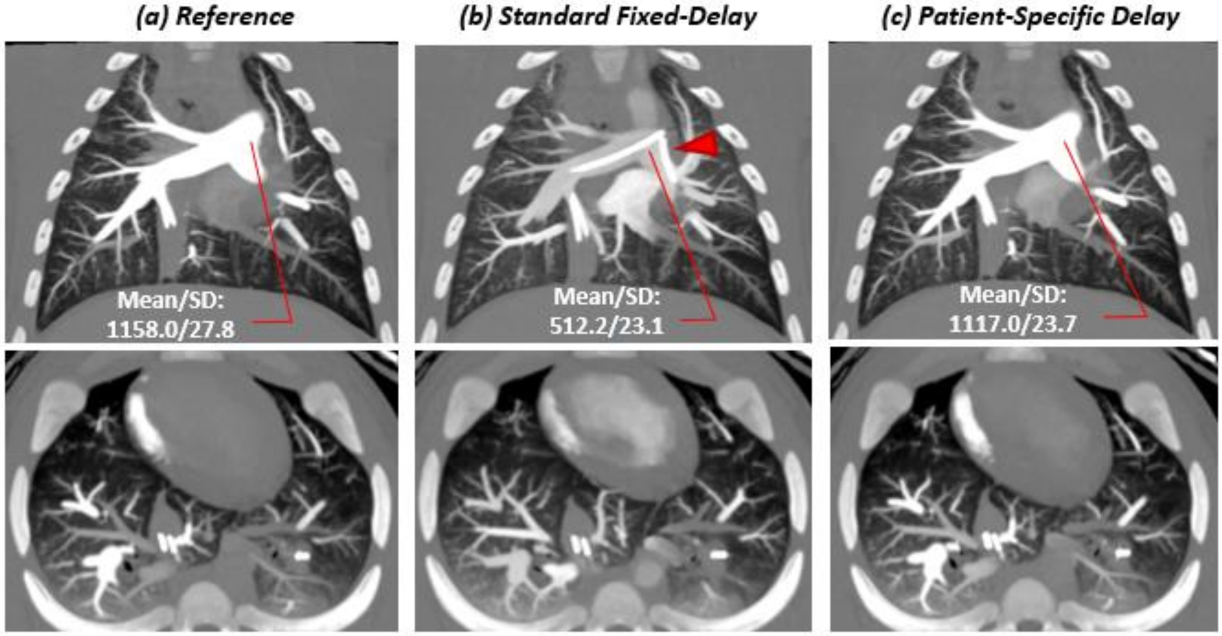

Figure 4.2 Images for a 27kg swine with an injection of 0.5 ml/kg contrast at a rate of 5 ml/s under balloon occlusion.

Contrast material–enhanced CT angiography (a) using retrospective peak from the pulmonary arterial input function (AIF); (b) with standard delay protocol; (c) with patient-specific timing protocol in a 10 mm maximum-intensity projection (MIP) image from both coronal and axial rendering ([window/level: 1600/500]. In the main pulmonary artery, The CT numbers for (a), (b) and (c) were 1158 HU, 512.2 HU and 1170 HU; the SNR were 134.1, 60.1 and 131.0; the CNR were 126.5, 50.9 and 121.9, respectively. For subjective image quality the scores were 1, 1, 1 respectively for reader 1, and were 1,2, 1 respectively for reader 2. Red arrows indicate the balloon catheter.

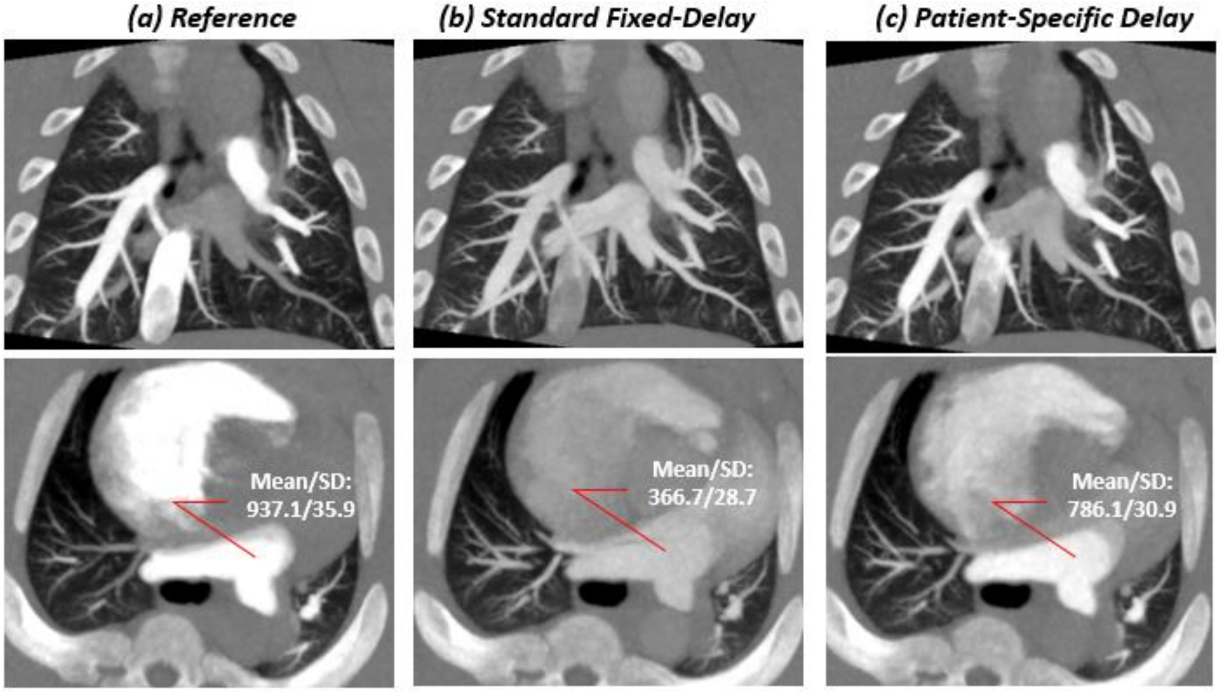

Figure 4.3 Images for a 55kg swine with an injection of 0.5 ml/kg contrast at a rate of 10 ml/s with no balloon occlusion.

Contrast material–enhanced CT angiography (a) using retrospective peak from the pulmonary arterial input function (AIF); (b) with standard delay protocol; (c) with patient-specific timing protocol in a 10 mm maximum-intensity projection (MIP) image from both coronal and axial rendering ([window/level: 1600/500]. In the main pulmonary artery, The CT numbers for (a), (b) and (c) were 937.1 HU, 366.7 HU and 786.1 HU; the SNR were 46.8, 18.3 and 39.2; the CNR were 43.4, 14.9 and 35.9, respectively. For subjective image quality the scores were 1, 2, 1 respectively for reader 1, and were 1,3, 1 respectively for reader 2.

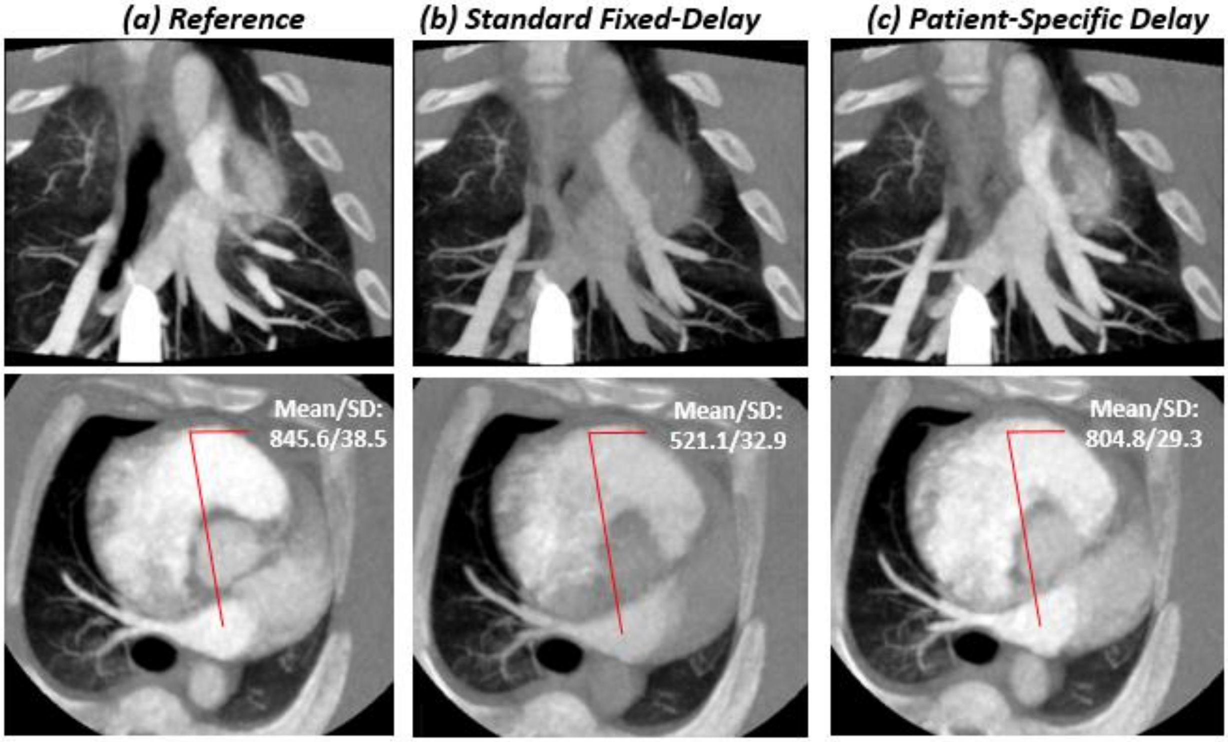

Figure 4.4 Images for a 91kg swine with an injection of 1 ml/kg contrast at a rate of 5 ml/s with no balloon occlusion.

Contrast material–enhanced CT angiography (a) using retrospective peak from the pulmonary arterial input function (AIF); (b) with standard delay protocol; (c) with patient-specific timing protocol in a 10 mm maximum-intensity projection (MIP) image from both coronal and axial rendering ([window/level: 1600/500]. In the main pulmonary artery, The CT numbers for (a), (b) and (c) were 845.6 HU, 521.1 HU and 804.8 HU; the SNR were 21.8, 13.4 and 20.7; the CNR were 19.6, 11.3 and 18.6, respectively. For subjective image quality the scores were 2, 3, 2 respectively for reader 1 and reader 2.

Objective Assessment

For each of CTPA images, the contrast enhancements of 12 pulmonary artery ROIs were measured, resulting in 5424 independent measurements in total. Overall, the mean contrast enhancement of all the pulmonary arteries for group A, B and C were 870 ± 244 HU, 826 ± 237 HU and 761 ± 247 HU, respectively. For each vessel ROI, no significant differences were found between group C and group A ($p = 0.15$), whereas significant differences were found between group B and group A ($p<.001$) except for the right caudal lobe artery, as illustrated in **Table 4.2**. The mean contrast enhancement of all pulmonary arteries from group B and group C were also compared to group A (reference), as depicted in **Figure 4.5**. In addition, at each pulmonary vessel generation, the differences between the three groups are shown in box plots (**Figure 6**). The largest contrast enhancement differences for group B and group C compared to group A were observed in the right and left main pulmonary artery, calculated as 154 HU (p<.001) and 67 HU (p=0.055), respectively (**Table 4.3**). The smallest contrast enhancement difference between group B and group C was observed in the lobar arteries at 60.6HU (p=0.025). For overall SNR and CNR, no significant differences were found between group A (SNR: 65.1±32.2; CNR: 59.6±30.8) and group C (SNR: 62.4 ± 32.0, p=0.444; CNR: 56.4 ± 30.3, p=0.421), but significant differences were found between group A and group B (SNR: 56.9 ± 30.4, p=0.020; CNR: 50.9±28.9, p=0.012) (**Table 4.3**). There were no differences in mean muscle contrast enhancement and background noise between groups (**Table 4.3**).

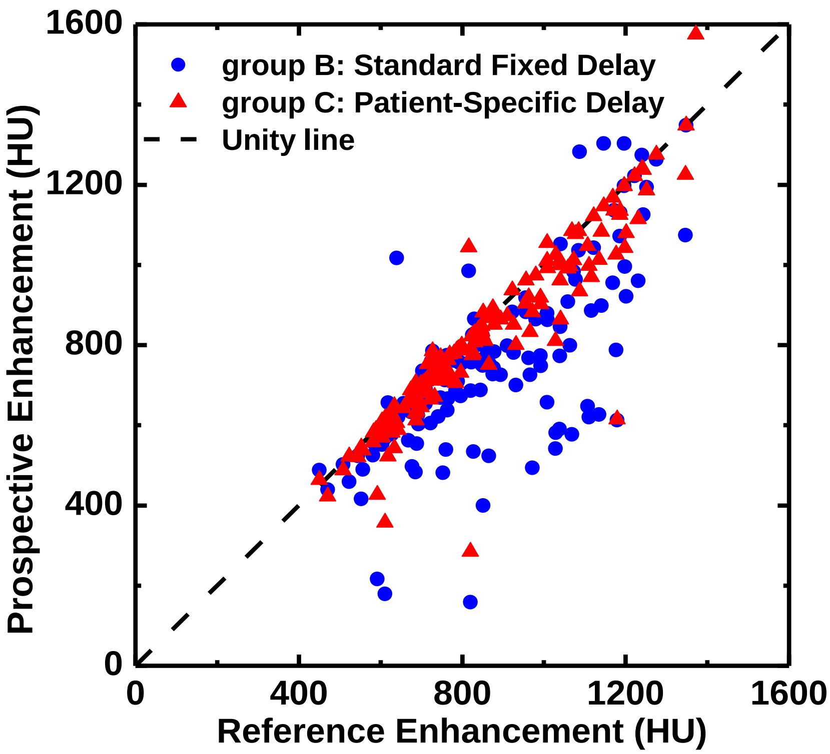

Figure 4.5 Overall mean contrast enhancements of all measurement locations in pulmonary arteries. Both simulated standard fixed delay (group B) and patient-specific delay (group A) CTPAs were compared to the retrospective reference peak (group A). Each point represents a mean contrast enhancement of the main pulmonary artery (MPA), right and left pulmonary artery (RPA, LPA), right upper lobe artery (RUL), right middle lobe artery (RML), right lower lobe artery (RLL), left upper lobe artery (LUL), left iliac artery (LIL), left lower lobe artery (LLL), assessor lobe artery (AL), right lower lobe segmental artery (RLL_S) and left lower lobe segmental artery (LLL_S). The black dash line is the unity line.

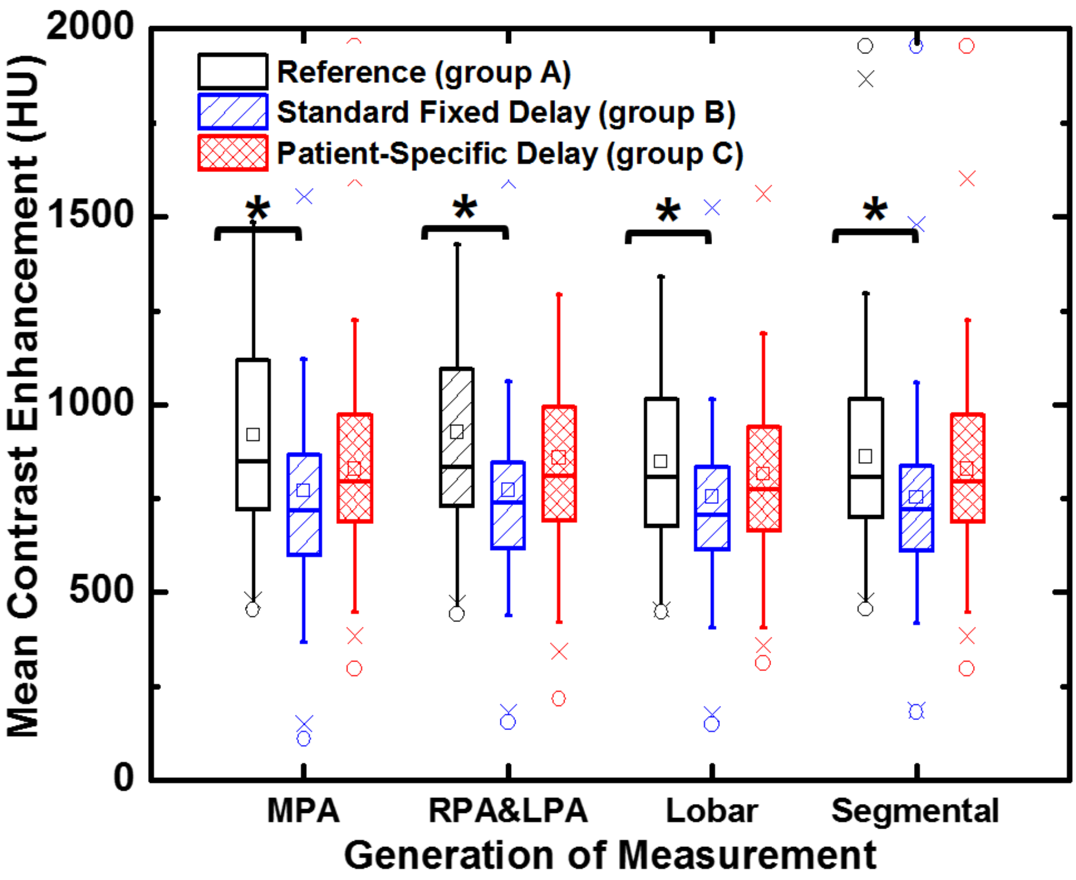

Figure 4.6 Box plot shows mean contrast enhancements (in Hounsfield units) in three study groups. Note that measurements are averaged within each generation, including the main pulmonary artery (MPA); mean of right and left pulmonary artery (RPA, LPA), mean of lobar artery (RUL, RML, RCL, LUL, LIL, LLL) and mean of segmental arteries (AL, RCL_S and LCL_S). The asterisk indicates the two boxes are significantly different.

Table 4.2 Contrast enhancement from twelve pulmonary arteries sub-regions.

Location	**group A**	**group B**			**group C**		
(HU)	**Mean ± SD [95% CI]**	**Mean ± SD [95% CI]**	**Difference**	**P-values**	**Mean ± SD [95% CI]**	**Difference**	**P-values**
MPA	920.1 ± 271.4 [877.6, 962.6]	772.3 ± 277.2 [731.2, 822.0]	-147.8	**<0.001**	861.0 ± 267.1 [812.4, 903.1]	-59.1	0.058
RPA	918.6 ± 267.4 [871.4, 958.8]	788.6 ± 276.2 [747.9, 837.4]	-130.0	**<0.001**	876.6 ± 263.6 [835.5, 917.7]	-40.6	0.163
LPA	932.8 ± 569.4 [840.6, 1025.0]	760.9± 268.6 [717.4, 804.4]	-171.9	**<0.001**	836.7 ± 258.5 [794.9, 878.5]	-91.6	0.059
RUL	846.4 ± 251.1 [805.7, 887.0]	760.0 ± 251.5 [719.3, 800.7]	-86.4	**0.001**	816.8 ± 242.3 [777.5, 856.0]	-29.6	0.290
RML	812.8 ± 224.4 [776.5, 849.1]	740.6 ± 357.6 [682.7, 798.5]	-72.2	**0.020**	783.5 ± 220.2 [747.9, 819.2]	-29.3	0.247
RCL	887.9 ± 261.6 [845.5, 930.3]	811.3 ± 504.6 [729.6, 893.0]	-76.6	0.062	850.0 ± 257.0 [808.3, 891.5]	-37.9	0.193
LUL	820.0 ± 244.9 [780.3, 859.6]	719.9 ± 239.4 [681.1, 758.7]	-100.1	**<0.001**	788.2 ± 242.1 [749.0, 827.4]	-31.8	0.260
LIL	831.3 ± 245.0 [791.6, 871.0]	744.1 ± 243.2 [706.1, 782.0]	-87.2	**0.001**	801.5 ± 238.2 [762.9, 840.1]	-29.8	0.300
LCL	869.4 ± 253.6 [828.3, 910.5]	758.3 ± 261.3 [716.0, 799.8]	-111.1	**<0.001**	828.0 ± 249.5 [787.6, 868.4]	-41.4	0.157
AL	826.6 ± 241.3 [787.7, 865.4]	723.6 ± 239.8 [684.7, 762.4]	-103.0	**<0.001**	792.2 ± 231.3 [754.8, 829.7]	-34.4	0.214
RCL_S	871.8 ± 257.8 [830.1, 913.5]	768.5 ± 247.8 [728.4, 808.6]	-103.3	**<0.001**	833.5 ± 249.5 [793.1, 873.9]	-38.3	0.199
LCL_S	875.1 ± 244.8 [835.4, 914.7]	772.6 ± 250.5 [733.2, 813.0]	-152.5	**<0.001**	840.5 ± 240.0 [801.7, 879.3]	-34.6	0.225

Note.- Group A: Actual peak image from the retrospective arterial input function. Group B: The fixe-delay CTPA image. Group C: The patient-specific delay CTPA image. Mean signal intensity are shown in mean ± standard deviation at each measurement location. CI = confidence intervals. HU = Hounsfield units. P-values less than 0.05 indicate the significant differences. MPA: main pulmonary artery; RPA: right pulmonary artery; LPA: left pulmonary artery; RUL: right upper lobe artery; RML: right middle lobe artery; RML: right middle lobe artery; RCL: right caudal lobe artery; LUL: left upper lobe artery; LIL: left ligula lobe artery; LCL: left caudal lobe artery; AL: accessory lobe artery; RCL_S: segmental artery in right caudal lobe; LCL_S: segmental artery in left caudal lobe.

Table 4.3 Objective Image Quality Assessments (Contrast enhancement, SNR, CNR) at different generations.

Measurement Generations		group A	group B		group C	
		(Mean ± SD)	**(Mean ± SD)**	**P-value**	**(Mean ± SD)**	**P-value**
Overall Pulmonary Artery	**SI (HU)**	870.1 ± 244.1	761.1 ± 246.7	**<0.001**	825.6 ± 238.8	0.152
	SNR	65.2 ± 32.2	56.9 ± 30.4	**0.020**	62.4 ± 32.0	0.444
	CNR	59.6 ± 30.8	50.9 ± 28.9	**0.012**	56.4 ± 30.3	0.421
MPA	**SI (HU)**	916.5 ± 271.5	776.6 ± 280.2	**<0.001**	858.0 ± 279.4	0.058
	SNR	69.2 ± 35.9	57.9 ± 32.7	**0.004**	64.7 ± 35.3	0.279
	CNR	63.6 ± 34.5	52.3 ± 31.4	**0.003**	59.1 ± 33.9	0.259
RPA & LPA	**SI (HU)**	926.7 ± 354.0	773.2 ± 267.3	**<0.001**	859.9 ± 265.3	0.055
	SNR	69.2 ± 40.2	57.8 ± 31.6	**0.004**	64.4 ± 33.2	0.231
	CNR	69.2 ± 35.9	52.2 ± 30.4	**0.003**	58.5 ± 31.6	0.213
Lobar Arteries	**SI (HU)**	848.5 ± 236.1	756.1 ± 250.0	**0.001**	816.7 ± 233.1	0.224
	SNR	63.5 ± 31.4	56.6 ± 30.1	**0.049**	61.4 ± 31.5	0.564
	CNR	57.9 ± 30.0	50.9 ± 28.7	**0.039**	55.8 ± 30.1	0.543
Segmental Arteries	**SI (HU)**	861.8 ± 239.4	755.8 ± 239.7	**<0.001**	828.0 ± 230.0	0.219
	SNR	64.4 ± 31.7	56.5 ± 30.0	**0.025**	62.2 ± 31.8	0.539
	CNR	58.9 ± 30.3	50.8 ± 28.8	**0.011**	56.6 ± 30.2	0.513
Muscle	**(HU)**	75.5 ± 15.5	77.1± 10.0	0.152	76.2± 11.2	0.277
Noise	**(HU)**	15.1 ± 5.3	14.7 ± 4.3	0.412	14.1 ± 5.8	0.248

Note.- Group A: Actual peak image from the retrospective arterial input function. Group B: The fixe-delay CTPA image. Group C: The patient-specific delay CTPA image. Mean signal intensity (SI), signal-to-noise ratio (SNR) and the contrast-to-noise ratio (CNR) are shown as mean ± standard deviation. HU = Hounsfield unit.

Discussion

The results indicate that the patient-specific timing protocol for CTPA produces significantly improved image quality as compared with the standard protocol with a fixed time delay. This was shown using objective image metrics such as contrast enhancement, CNR and SNR as well as subjective image quality for pulmonary arterial opacification at all generations.

Hence, if employed prospectively, there exists potential to improve CTPA image quality using the patient-specific timing protocol as compared to the standard protocol with a fixed delay. The patient-specific timing protocol was shown to be robust over a range of contrast injection volumes and durations. Such findings also agree with a previous report indicating that the aortic time-to-peak delay is primarily affected by the injection duration (7). Moreover, a prior study also showed the patient-specific timing-protocol can be used for a two-volume pulmonary perfusion technique, where the two-volumes are acquired at the base and peak of the AIF (80). Although further validation remains necessary, the patient-specific timing protocol has the potential to improve CTPA image quality.

It is important to point out that the results also indicate the potential for contrast volume reduction, while maintaining adequate image quality. Specifically, for a standard CTPA protocol, a high contrast dose (70~125 ml) is used for different size patients to ensure adequate contrast opacification is obtained (103,107,108,116,123,124). However, given the results from this study, a contrast dose of 0.5 ml/kg provided good diagnostic performance for the patient-specific protocol group, as the CTPA acquisition always occurred at or near the peak enhancement of the AIF curve. Hence, the patient-specific timing protocol can substantially reduce the contrast dose, although further validation in patients remains necessary.

A fixed bolus tracking threshold is currently used for CTPA image acquisition. A suitable triggering threshold is critical for acquisition of CTPA. In general, a low threshold may result in false-triggering prior to adequate contrast bolus arrival in the pulmonary vasculature, while a high threshold may lead to late acquisition with venous contamination. The current bolus tracking threshold varies between different CT scanners. The bolus tracking threshold in this study was calculated by adding a constant value to the patient-specific background. It is expected that a patient-specific bolus tracking threshold will be more robust for different patients.

Limitations

This study is not without limitations. First, all acquisitions were performed in swine, and not in patients. However, capturing the entire AIF curve is more feasible in animal studies, owing to the high radiation dose necessary to provide a true reference standard of the AIF peak. Second, the ‘prospective’ results were derived based on standard and patient-specific timing protocol simulations performed on the retrospective data; hence, future studies should also compare the prospective performance of the patient-specific timing protocol to the standard protocol. Further considerations of bolus tracking-based triggering and acquisition should also be addressed. Specifically, the location of the triggering ROI, the scan range, and the standard acquisition delay used by different CT scanners may all need to be considered by the patient-specific timing protocol. Third, objective image quality was only assessed down to segmental arterial generations; hence, more distal arterial generations may need to be assessed in future studies. Fortunately, significant differences were found in all measured vessel locations between patient-specific and fixed timing protocols, with higher subjective image quality obtained by the patient-specific timing protocol in the distal vessels. Fourth, radiation dose was not optimized in this study as the focus was to retrospectively develop and assess a patient-specific timing protocol for improved CTPA contrast opacification. Future studies should employ the patient-specific findings of this study prospectively, at which point radiation dose can truly be assessed. Additionally, the kilovoltage settings should be adjusted according to each patients' weight in future studies. Finally, the diagnostic performance using the patient-specific timing protocol requires further testing in patients with actual pulmonary pathologies such as the acute pulmonary embolism and chronic thromboembolic pulmonary hypertension.

Conclusion

The proposed patient-specific timing protocol has the potential to objectively improve contrast opacification in CTPA while also improving subjective image quality. Such improvements in image quality throughout successive pulmonary arterial generations may also improve the diagnostic accuracy and detection of small pulmonary embolisms compared to the standard CTPA protocols.

Chapter 5 Quantification of pulmonary perfusion territories using minimum-cost path assignment and Computed Tomography angiography

Abstract

Computed tomography pulmonary angiography (CTPA) is a first-line diagnostic technique used to assess patients with suspected pulmonary embolism (PE). PE risk stratification is necessary for optimal patient management. This chapter validated an automated minimum-cost path (MCP) technique to enable accurate calculation of the subtended lung tissue distal to a PE using CTPA. A Swan-Ganz catheter was placed in the segmental pulmonary artery of seven swine (body weight:42.6±9.6 kg) to produce different PE severity. A total of 33 PE conditions were generated, where the balloon tip was adjusted distally to proximally under fluoroscopic guidance via balloon inflation (balloon diameter: 2-4mm). Under each PE condition, CT pulmonary angiography and dynamic CT perfusion (CTP) scans were acquired using a 320-slice CT scanner after a 0.5 ml/kg of contrast material injection followed by a 0.25 ml/kg saline chaser. The pulmonary arterial tree was split into two segments based on the location of the occlusion and the MCP technique was used to assign the distal and proximal territories determined by the nearest supplied pulmonary arteries. The CTP data was used to generate the perfusion defect territory as the reference standard (RS). The accuracy of the MCP technique was evaluated by quantitatively comparing the MCP-derived PE-distal territories to the RS defect territories by linear regression, Bland-Altman analysis, and a paired sample t-test. The spatial correspondence was compared by Dice similarity coefficient and the minimum Euclidean distance. The MCP PE-distal territory masses ($Mass_{MCP}, g$) and the reference standard perfusion defect territory masses ($Mass_{RS}, g$) were related by $Mass_{MCP} = 1.02Mass_{RS} - 0.62\ g$ (r = 0.99, p=0.51). The mean Dice similarity

coefficient is 0.84. In conclusion, the territory distal to a PE can be accurately calculated using CTPA images. This technique can potentially be used for the PE risk stratification.

Introduction

With an estimated 100,000 deaths per year, pulmonary embolism (PE) remains the third common cause of cardiovascular death in the United States (4–6). Due to its high accuracy, wide availability, and low invasiveness, computed tomography pulmonary angiography (CTPA) has become the first-choice of imaging modality to confirm acute PE (49,50). Despite adequate diagnosis and treatment, the death rate after a diagnosis of acute PE is still 8%–15% (125,126). The risk-stratification of pulmonary embolism remains a challenge for emergency department physicians (127). Consequently, a quantification of PE severity would be of high value in risk-stratifying patients in order to provide prompt diagnostic strategies with appropriate disposition to further reduce the mortality rate.

Several CT obstruction indices have been used to describe the pulmonary arterial obstruction using CT angiography, such as the Miller index, Walsh index, and Qanadli index (128–131). Specifically, the Miller index comprises both subjective and objective scores, while the other two are pure objective scores that quantify only two factors: the total number of segmental branches under-perfused due to PE, and the degree of obstruction (partially or wholly occluded) (132,133). Additionally, the right/left ventricle ratio is commonly used as another CT indicator in the prognosis of acute PE, playing a critical role in identifying the massive PE from sub-massive PE (49,133–135). However, right ventricular dysfunction is unlikely to be identified in pulmonary arterial obstruction of less than 40% (136). To our knowledge, none of the existing CT obstruction indexes or CT indicators can provide spatial correspondence between the territory of emboli blocked tissue and the downstream arterial tree that may cause ischemia and infarction. Hence, a technique is critically needed to associate each tissue voxel and its specific supplying vessel.

With the minimum-cost path (MCP) technique, the amount of tissue subtended by a PE can be quantitatively determined, rather than computing the number of occluded distal vessels. Furthermore, the total mass of the distal PE territory can be quantified to add prognostic values in stratifying the PE severity using the CT angiography only without additional radiation dose.

Current regional quantitative analyses of the ventilation and perfusion CT scans are commonly evaluated on a zonal basis by subdividing the lung parenchyma into several equal-sized rectangular regions of interest, which are neither anatomic nor physiologic related (137–141). As the pulmonary arterial tree is independently distributed in each lobe, the MCP technique can be implemented to provide vessel-specific lobar segmentation by assigning every single lung parenchyma voxel to the specific lobar artery branch; thus, enabling the regional ventilation/perfusion evaluation on a lobar basis for different lung diseases.

The purpose of this chapter was to validate an automated minimum-cost path (MCP) technique to enable accurate voxel assignment of the subtended lung tissue distal to the pulmonary artery occlusion using pulmonary CT angiography. The central hypothesis is that PE-distal territory can be accurately calculated by the MCP technique using the CTPA image, as compared to the reference standard PE-distal perfusion defect territory using dynamic CT perfusion images. Hence, the minimum-cost path technique has the potential to improve the quantitative assessment of PE severity. The total tissue mass distal to the PE can be quantified to add prognostic values in stratifying the PE severity using only a CT angiogram without additional radiation dose..

Material and Methods

General Methods

All animal studies were approved by the Institutional Animal Care and Use Committee. Seven swine (42.6±9.6 kg, male, Yorkshire) were used for validation of the MCP technique, along with 33 CT acquisitions followed by the intravenous contrast injection. All experimental data was successfully acquired between 2016 and 2018 and analyzed between 2020 and 2021. All authors carried out the experiment and participated the data acquisition.

Animal Preparation

After an overnight fast with free access to water, seven domestic Yorkshire swine were premedicated via intramuscular injection of Telazol (4.4mg/kg), Ketamine (2.2 mg/kg), and Xylazine (2.2 mg/kg), intubated (Mallinckrodt, tube 6.0/6.5/7.0, Covidien, Mansfield, MA), then ventilated (Surgivet, Norwell, MA, and Highland Medical Equipment, Temecula, CA) with 1.5-2.5% Isoflurane (Baxter, Deerfield, IL) to maintain anesthesia. Each swine was monitored by electrocardiography, mean arterial pressure (mmHg), end-tidal CO_2 (mmHg), and O_2 saturation (%) during the experiment.

Under ultrasound guidance (9L Transducer, Vivid E9, GE 145 Healthcare), four introducer sheaths (AVANTIR, Cordis Corporation, Miami Lakes, FL) were placed in the left and right jugular veins, right femoral vein, and right femoral artery. Specifically, the left jugular vein was used for intravenous contrast injection. The right femoral vein was used for intravenous fluid and drug administration. The right femoral artery sheath was used for invasive blood pressure monitoring. Under fluoroscopic guidance, a 6-Fr Swan-Ganz catheter (Edwards, Edwards Lifesciences Corp, Irvine, CA) was placed in distal pulmonary artery via the right jugular vein. Several levels of PE conditions were generated, where the balloon tip was moved from distal to proximal regions of pulmonary artery via balloon inflation (balloon diameter: 2-4 mm). At the end of the experiment, each animal was euthanized with overdosed KCL.

CT Scanning Protocol

Each animal was first positioned supine, head first through the gantry of a 320-slice CT scanner (Aquilion One, Canon Medical Systems, Tustin, CA), and the caudal lung region was localized within a 16-cm z-axis coverage. After each PE induction, contrast (0.5 ml/kg, Isovue 370, Bracco Diagnostics, Princeton, NJ) and saline chaser (0.25 ml/kg) were intravenously administered via a dual-syringe injector at a rate of 5ml/s (Empower CTA, Acist Medical Systems, Eden Prairie, MN). Meanwhile, twenty ECG-gated dynamic CT volume scans were acquired during suspended respiration at the functional residual capacity at 100 kV and 200 mA (320 x 0.5 mm detector collimation, 320-400 mm scan field-of-view, 0.35s rotation time). Full projection CT data was reconstructed at 75% R-R interval using an adaptive iterative dose reduction 3D algorithm with a standard lung kernel FC07 (512×512 matrix, 0.5mm slice thickness and slice interval, 320-400 mm reconstruction field-of-view). The image with maximum contrast enhancement was used as the CTPA image to perform the MCP technique. Subsequent CT acquisitions were repeated at least 15 minutes apart to allow for adequate contrast clearance from the previous injection. The CT dose index (CTDI) and the dose-length product (DLP) were collected from the dose report sheet.

Minimum-Cost Path (MCP) Processing

The minimum–cost path (MCP) technique is based on the assumption that the lung parenchyma is perfused by its nearest arterial tree and microvascular bed (142). The MCP technique was implemented to determine the minimum distance between each voxel of the lung tissue and its supplying pulmonary artery. CT perfusion was used as the reference standard to validate the ‘perfused’ or ‘non-perfused’ territories under full arterial occlusion.

To validate the MCP technique, a single maximal contrast enhanced CT volume scan was selected from the dynamic volume scan series and used as the CTPA image. Next, the lung tissue and pulmonary artery segmentation were conducted on the CTPA using the Vitrea workstation (Pulmonary Analysis workflow, Vitrea fX version 7.7, Vital Images, Inc., Minnetonka, MN). Specifically, an automatic vessel selection tool was used and followed by a manual correction on vessel boundaries. Then, pulmonary artery centerlines and the lung tissue binary mask were extracted using in-house software developed by MATLAB® (R2019a; MathWorks Inc.). The coordinates of the Swan-Ganz balloon were marked. The vessel tree was then split into the proximal and distal segments, where the tissue supplied by the distal vessel tree is considered as the PE-related defect territory. The MCP algorithm was performed based on the lung tissue binary mask and the extracted pulmonary artery centerlines (143,144). Specifically, the centerlines were used as seed points to generate a distance map through the entire lung segment using a Fast-Marching algorithm (145). Using the distance map, the minimum–cost path from each tissue voxel to the artery centerlines was used to assign the voxel to its nearest supplying artery, resulting in the assignment of the 'PE-proximal' and 'PE-distal' for the entire lung. Additionally, the lung tissue mass of each territory was estimated by the product of the total territory volume, lung parenchymal tissue density (1.053 g/ml) and the non-air fraction of tissue (%) (93). The PE-distal mass-percent was defined as the PE-distal mass over the entire lung mass. The details of the MCP technique performed on a whole-lung segmentation is shown in **Figure 5.1**.

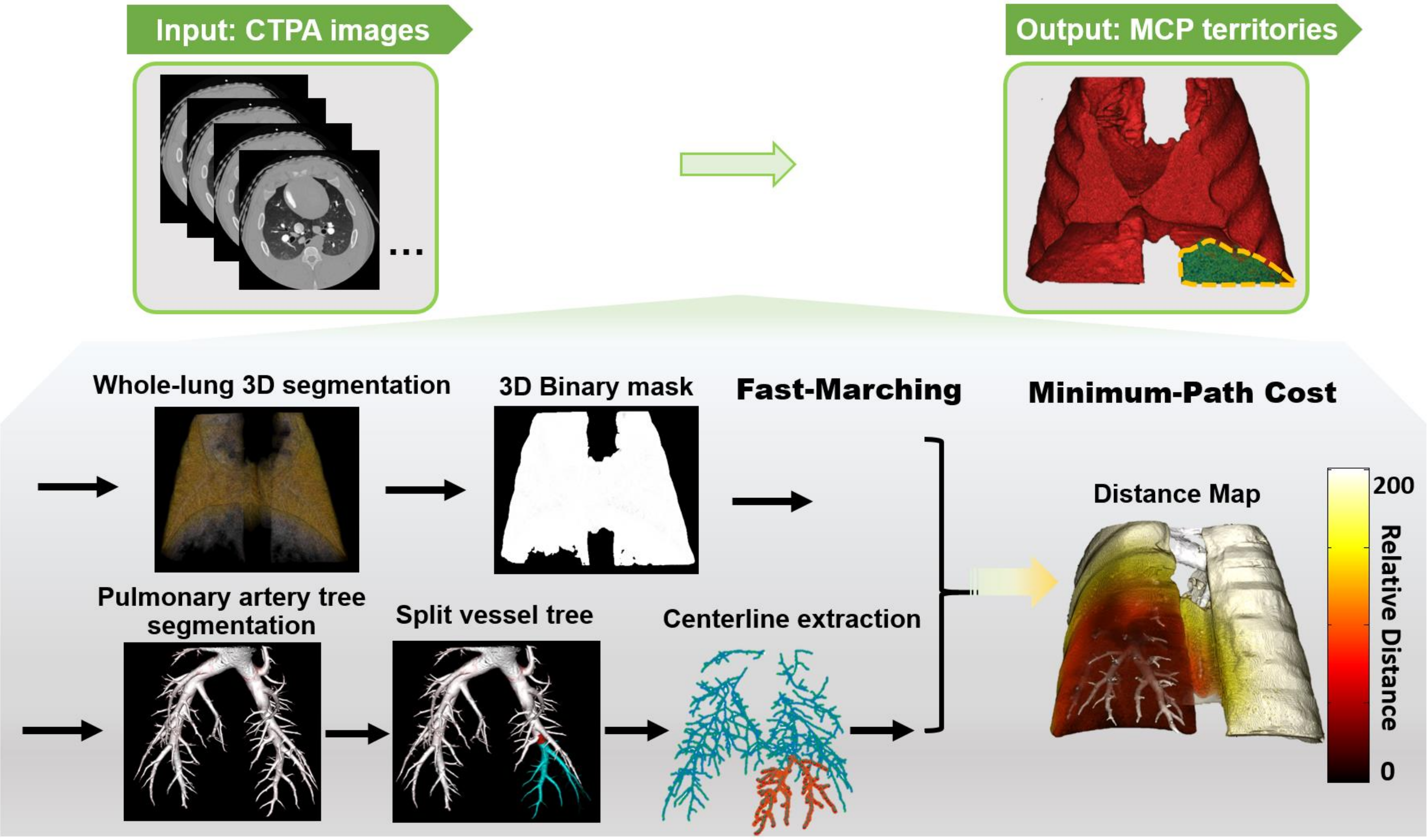

Figure 5.1 Minimum-cost path assignment technique.

The whole-lung segmentation and the pulmonary arterial tree segmentation was performed on the CTA image. The vessel tree was split based on the location of the end tip of the balloon. The vessel centerlines were extracted from the vessel segmentation. Using the vessel centerlines as seed points, distance maps through a whole-lung 3D binary mask were generated using the Fast-Marching algorithm.The distance maps were used to determine the minimum-cost path(MCP) of each tissue voxel to the non-PE related or PE-related artery, yielding MCP assignment territories.

(CTA=CT angiography, CTP=CT perfusion , MCP=minimum-cost path assignment.)

CT Perfusion technique and Reference Standard (RS)

Dynamic CT perfusion was used to determine the reference ‘perfused’ or ‘non-perfused’ territories. A previously validated two-volume, first-pass dynamic CT perfusion technique was used to calculate the pulmonary perfusion, resulting in a whole-lung three-dimensional perfusion map in ml/min/g (93). Then, a median filter was applied to the perfusion map, followed by automated region growing segmentation to extract the ‘perfused’ and ‘non-perfused’ territories.

Specifically, a seed point was placed within the perfusion defect region and iteratively grown into the whole lung tissue, with a cutoff value of 3 ml/min/g for determining the boundaries of the “non-perfused’ territory. As such, the entire lung volume resulted in two separate reference standard perfusion territories. The RS defect territory mass and perfusion defect mass-percent were calculated. A workflow of reference standard image processing steps is illustrated in **Figure 5.2**.

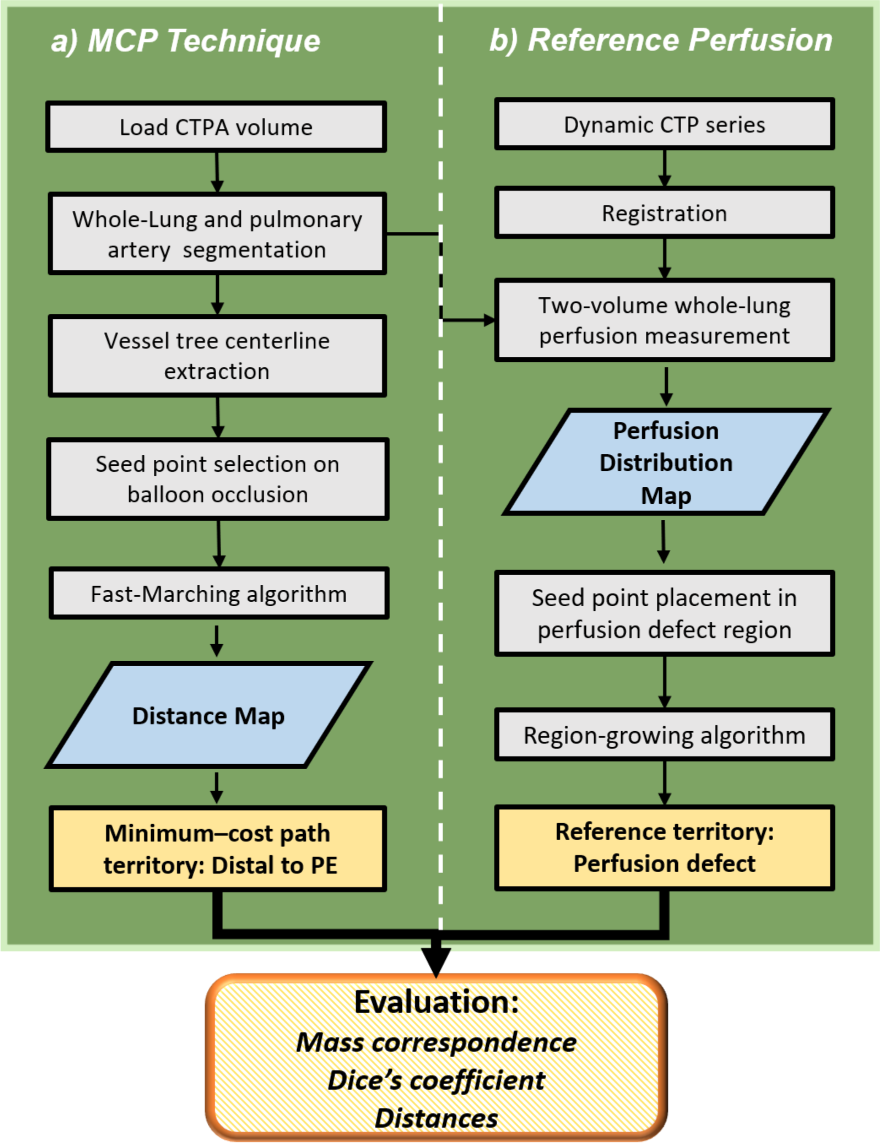

Figure 5.2 Image processing diagram.
(a) MCP assignment processing block.The whole-lung segmentation and the pulmonary arterial tree segmentation was performed on the CTPA image. The vessel tree was split based on the location of the balloon tip. The vessel centerlines were extracted from the vessel segmentation. Using the vessel centerlines as seed points, distance maps through a whole-lung 3D binary mask were generated using the Fast-Marching algorithm.The distance maps were used to determine the minimum-cost path(MCP) of each tissue voxel to the PE-proximal and PE-distal artery subtrees, yielding MCP assignment territories. (b)

Reference standard processing block. Dynamic CT acquisition was performed and a first-pass perfusion technique was used to generate the perfusion distribution map. A region-growing segmentation was performed within the perfsuion defect region to generate the reference standard territories.
(CTPA=CT pulmonary angiography, CTP=CT perfusion , MCP=minimum-cost path assignment.)

Lobar segmentation application

To implement the vessel-specific lobar segmentation, the subtree of each lobe is divided when bifurcating from either left pulmonary artery or right pulmonary artery, resulting in six lobar subtrees: left upper lobe (LUL), left lower lobe (LLL), right upper lobe (RUL), right middle lobe (RML), right lower lobe (RLL), and accessory lobe (AL), as shown in **Figure 3.3**. Using a whole-lung mask and centerlines of these trees, six separate distance maps were then generated. Each tissue voxel can be assigned to the specific lobar territory upon the shortest path to its arterial blood supply.

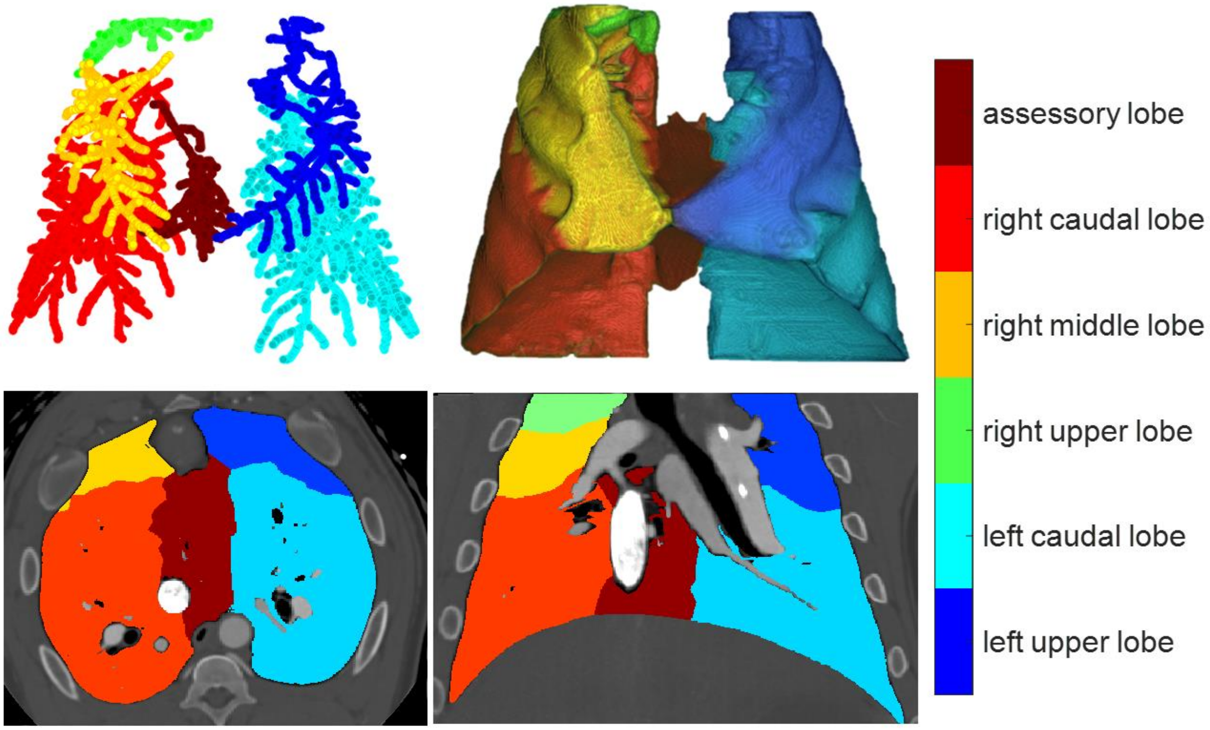

Figure 5.3 Lobar segmentation using the MCP technique.
Six lobar subtrees and the corresponding lobes including the left upper lobe (LUL), left lower lobe (LLL), right upper lobe (RUL), right middle lobe (RML), right lower lobe (RLL), and accessory lobe (AL) are shown with different colors.

Evaluation metrics

Both overlap-based and distance-based evaluation metrics were used for assessing the spatial correspondence between the distal MCP and RS defect territories (146,147). The three-dimensional image segmentations of each paired territories were compared. First, the Dice similarity coefficient (DSC) was used for evaluating the spatial overlap between two medical image segmentations (148,149). Specifically, the DCS computes for the number of overlap voxels divided by the total number of voxels of both volumes, ranging from 0 and 1. Second, boundary delineation is of importance in the dissimilarity measures. The Euclidean distance was used to measure the distance between the MCP territory boundary and RS territory “true” boundary. Specifically, the minimum distance was calculated for every point from one set to the nearest point in the other set, forming a distance metric. The maximum distance (MD) and average distance (AD) of the distance metric were determined. Generally, the MD is more sensitive to outliers than the AD. Thus, to further exclude possible outliners in a certain level, the distance can be defined to be the n^{th} quantile of distance, depending on the nature of the boundary datasets. The 90^{th} percentile distance and the 50^{th} percentile distance were reported as well.

Statistical Analysis

The mass and spatial correspondence were evaluated and compared between distal-PE territory by MCP and reference standard territory by perfusion defect. Statistical software (SPSS, version 22, IBM, Armonk, NY) was used for all statistical analyses. To evaluate the mass correspondence, the linear regression and Bland-Altman analyses were conducted, along with the Pearson’s r, adjusted R^2 (Adj. R^2), root-mean-square error (RMSE), root-mean-square deviation (RMSD) and Lin’s concordance correlation coefficient (75) being calculated. A paired sample t-test was used to determine the mean differences between the PE-distal mass and RS defect mass. A side-by-side histogram comparison of the mass-percent distribution using the MCP and RS were also performed. To evaluate the spatial correspondence, the Dice coefficient and Euclidean distance were computed between the PE-distal MCP and the reference standard defect territories, including the mean DSC, average distance, maximum distance, 90^{th} percentile distance, and 50^{th} percentile distance.

Results

General results

A total of seven swine (42.6±9.6 kg) were used for validation of the MCP technique. The average heart rate and mean arterial pressure during all the CT acquisitions were 90.7±17.8 beats per minute and 65.4±21.4 mmHg, respectively. A total of 33 successful contrast injections and CT imaging were made, resulting in 33 MCP and reference standard perfusion territory pairs. The average CT dose index (CTDI) for the single CTA image and dynamic CT perfusion images were 4.2 mGy and 138.7 mGy, respectively.

Qualitative Performance

A representative PE for one animal is shown in **Figure 5.4**, with the full artery occlusion in the left caudal lobe. The 20-mm maximum intensity projections (MIP) of the CTA image, pulmonary perfusion maps and MCP distance maps are shown in the axial, coronal, and posterior-lateral 3-D views (**Figure 5.4a**). The corresponding MCP PE-distal and RS defect territories are compared in **Figure 5.4b.** Further, the PE-distal tissue masses on each axial slice image are displayed for both techniques (**Figure 5.4c**).

An example of lobar segmentation using the MCP technique is also shown in **Figure 5.3**. Six lobar subtree centerlines and the vessel-specific lobar territories are shown with different colors.

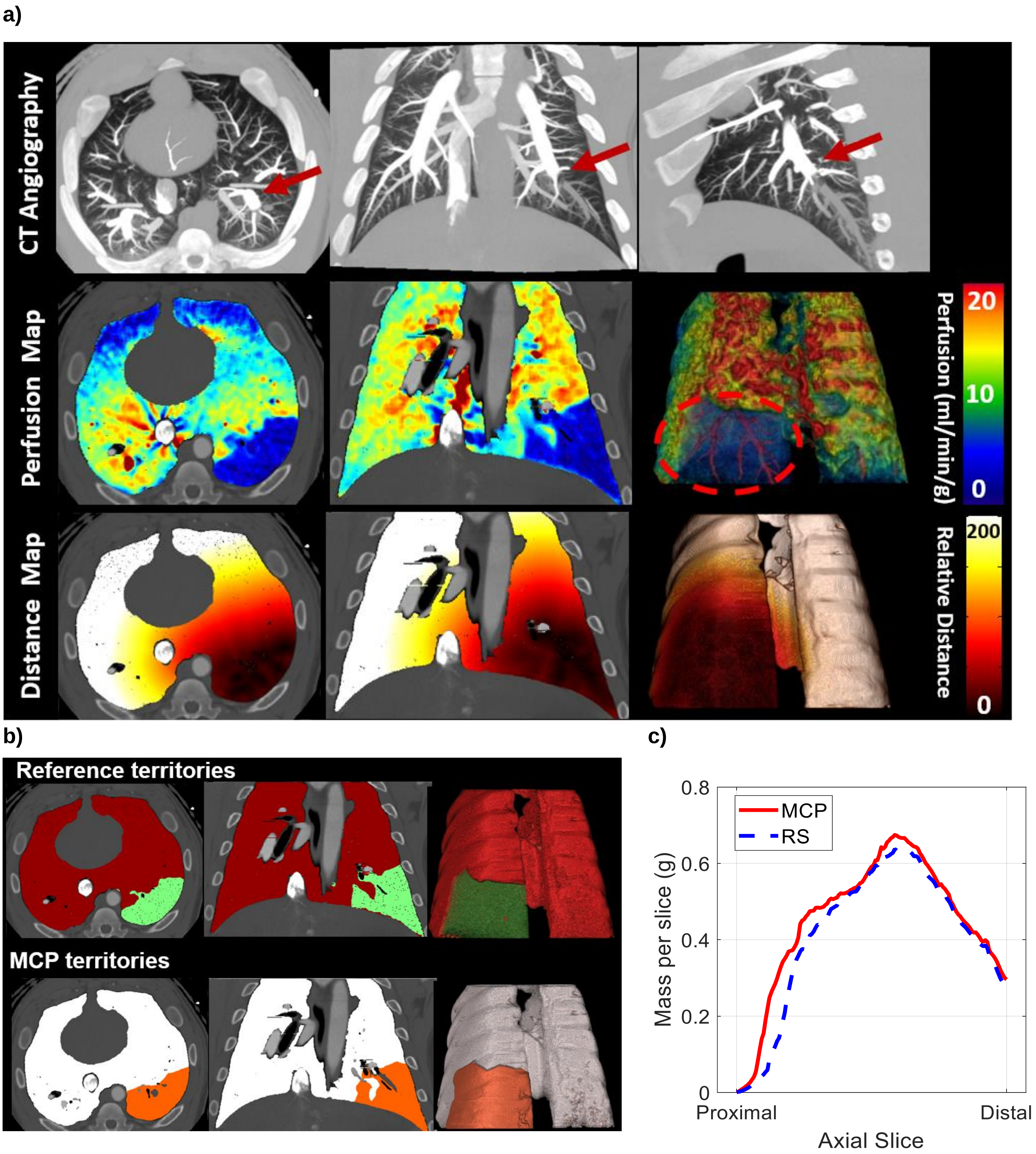

Figure 5.4 Qualitative results of the MCP and reference perfusion techniques.
a) The maximum intensity projection (MIP) of the CT angiography, the perfusion distribution map,and the MCP distance map are shown in axial, coronal and posterior 3-D volumetric views . The red arrows point to the balloon tip. Color bar indicate the perfusion in ml/min/g and the relative distance to the vessel centerlines .**b)** Axial, coronal and posterior 3-D volumetric views of MCP and reference standard territories are shown. **c)** Slice-by-slice analysis of the MCP and reference standard territories by comparing the PE-realated tiusse and the PE-related percentage mass at risk.

Mass Correspondence Evaluation

The average whole-lung tissue mass was 449.9±42.6 g. The average PE-distal mass of the RS and MCP territories were 47.2±35.7 g and 48.0 ± 37.1 g (p=0.42, **Table 5.1**), respectively. Using the linear regression analysis, the MCP PE-distal territory masses ($Mass_{MCP}$) and the RS defect perfusion territory masses ($Mass_{RS}, g$) were related by $Mass_{MCP} = 1.02Mass_{RS} - 0.62\ g$ (r = 0.99), with an Adjusted R^2 of 0.98, a concordance correlation coefficient (CCC) of 0.97, a root-mean-square error of 4.78 g, and a root-mean-square deviation of 4.67g (**Figures 5.5a, 5.5b and Table 5.2**). Moreover, **Figure 5.5c** shows mass-percent of tissue at risk for all PE conditions, where the number of different PE severity levels are compared between the RS and MCP techniques. The result indicates that more than half of the PE-distal territories have less than 10% of tissue at risk.

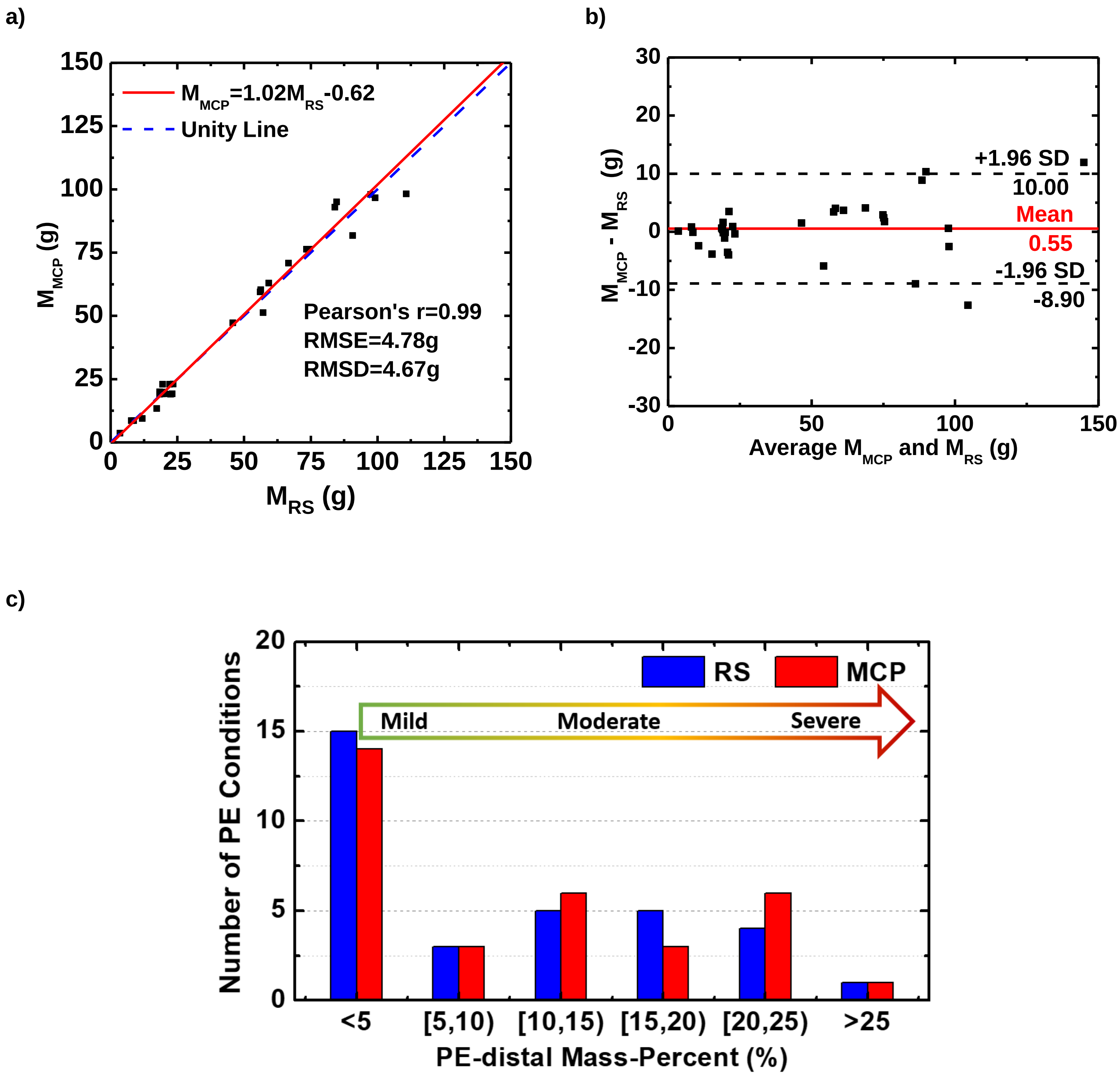

Figure 5.5 Mass correspondence evaluation.
a) Linear *Regression and b) Bland-Altman analysis comparing the MCP assigned defect tissue masses* (M_{MCP}) *and the reference standard perfusion defect tissue masses* (M_{RS}). c) Histogram of the *mass-percent at risk using the MCP and RS techniques.*

Table 5.1 Correspondence of MCP and reference standard coronary perfusion territories in PE-distal tissue mass and PE-distal mass percent.

Animal ID	Total Lung Mass	Defect Mass $(Mass_{RS})$	PE-distal Mass $(Mass_{MCP})$	Defect Mass-percent $(Percent_{RS})$	PE-distal Mass-percent $(Percent_{MCP})$
(Number of acquisitions)	*(g)*	*(g)*	*(g)*	*(%)*	*(%)*
Animal 1 (6)	429.2	16.3±7.5	17.2±7.9	3.8±1.8	4.0±1.8
Animal 2 (7)	469.7	70.3±20.6	75.6±22.4	15.0±4.4	16.1±4.78
Animal 3 (4)	496.0	101.1±34.0	100.8±42.8	20.4±6.9	20.3±8.6
Animal 4 (3)	409.8	39.9±44.1	34.9±40.7	9.8±10.8	8.5±9.9
Animal 5 (5)	483.7	33.6±27.7	35.5±29.6	6.9±5.7	7.3±6.1
Animal 6 (3)	372.5	69.7±1.3	85.4±5.8	18.7±1.1	22.9±1.5
Animal 7 (7)	481.2	20.1±1.9	19.1±0.1	4.2±0.4	4.0±0.1
Total (33)	**449.9±42.6**	**47.2±35.7**	**48.0±37.1**	**10.4±7.8**	**10.6±8.1**

Note.— Data expressed as mean mass ± standard deviation or mean mass-percent ± standard deviation.
MCP: Minimum-cost path technique; RS: reference standard perfusion technique.

Table 5.2 Linear regression analysis of MCP and reference standard perfusion PE-distal masses.

	PE-distal Mass
Slope	1.02 [0.98, 1.08]
Intercept (mm)	-0.62 [-3.76, 2.50]
Pearson’s r	0.99 [0.98, 1.00]
Adj. R^2	0.98
CCC	0.97 [0.95, 0.99]
RMSE	4.78
RMSD	1.04
P-value	0.51

Note.— For slope, intercept, Adj. R^2, CCC and r, 95% confidence intervals (CI) are presented as [CILower, CIUpper]. Adj. R^2=Adjusted R^2; CCC=concordance correlation coefficient; RMSE=root-mean-square error, RMSD=root-mean-square deviation). P-value less than 0.05 indicates significant difference.

Spatial correspondence Evaluation

Overall, the mean Dice similarity coefficient of all PE conditions was 0.84 ± 0.08. The average distance, maximum distance, 90^{th} percentile distance, and 50^{th} percentile distance between the distal MCP territories and RS-defect perfusion territories were 2.12 ± 1.03 mm, 22.77

± 10.78 mm, 6.37 ± 3.64 mm and 0.89 ± 0.63 mm, respectively. For the small PEs (distal mass-percent < 5%), the mean DSC is 0.79 ± 0.08, with an average minimum Euclidean distance of 2.34 ± 0.98 mm. Further MCP territory spatial correspondences regarding different levels of PE severity are detailed in **Figure 5.6** and **Table 5.3**.

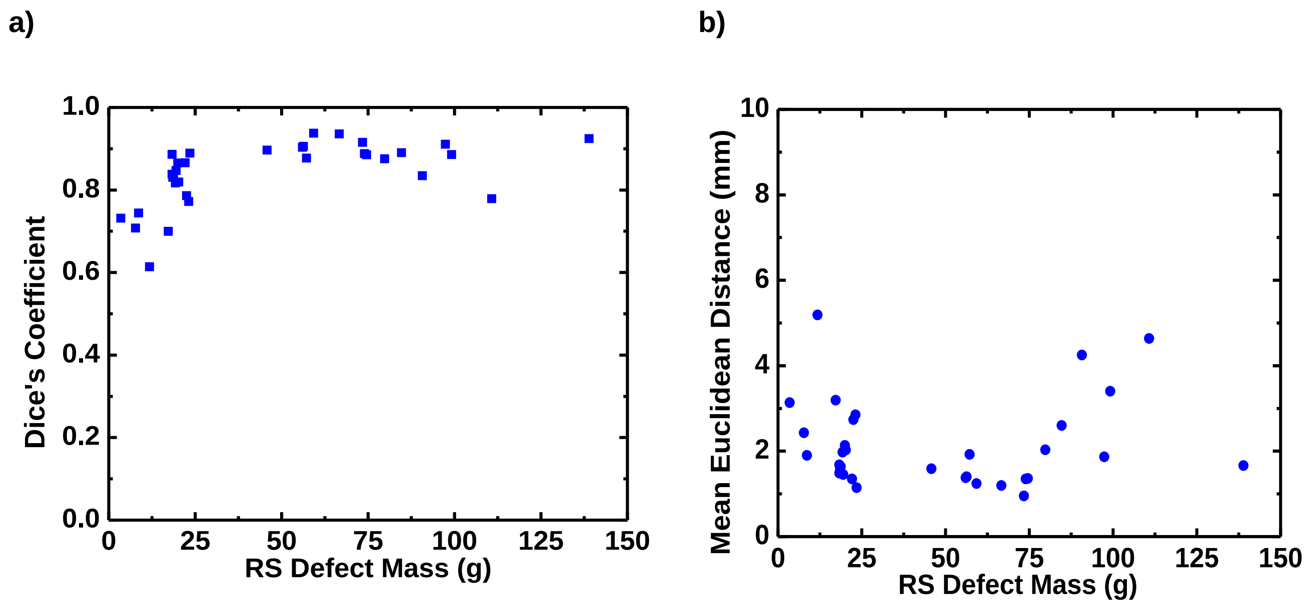

Figure 5.6 Dice's similarity coefficient and the mean Euclidean distance on the reference standard perfusion defect.

Table 5.3 Spatial correspondences of MCP and reference standard coronary territories in the PE-distal territory.

RS Distal Mass-percent (MP, %)	DSC	AD (mm)	MD (mm)	90^{th} percentile Distance (mm)	50^{th} percentile Distance (mm)
MP < 5	0.79 ± 0.08	2.34 ± 0.98	26.15 ± 7.94	6.80 ± 3.28	1.28 ± 0.52
5 ≤ MP <10	0.88 ± 0.02	1.36 ± 0.22	10.17 ± 5.94	3.81 ± 0.65	0.67 ± 0.58
10 ≤ MP <15	0.91 ± 0.03	1.43 ± 0.29	15.11 ± 3.42	4.69 ± 0.83	0.30 ± 0.48
15 ≤ MP < 20	0.90 ± 0.02	1.76 ± 0.63	24.60 ± 12.78	4.59 ± 1.47	0.13 ± 0.56
MP ≥ 20	0.86 ± 0.06	3.06 ± 1.49	31.63 ± 13.61	10..38 ± 5.14	0.94 ± 0.61

All	0.84 ± 0.08	2.12 ± 1.03	22.77 ± 10.78	6.37 ± 3.64	0.89 ± 0.63

Data expressed as mean ± standard deviation.
Note.— RS = reference standard, MP = Distal Mass-percent, DSC=Dice similarity coefficient, AD = average distance, MD = maximum distance.

Discussion

This chapter validated an MCP technique to quantify the tissue territory distal to a fully occluded PE using the perfusion defect territory as the reference standard. An excellent correlation was shown between the MCP distal mass and RS defect territory mass with a near-unity slope and negligible bias. The results indicate that the MCP technique can accurately quantify the distal-PE territory corresponding to the pulmonary arterial obstruction using the CTPA image; hence, this technique may potentially improve the PE-severity assessment of acute PE by quantifying the total mass of tissue at-risk caused by the PE. Further, the vessel-specific MCP can be applied to each of the lobar subtrees, yielding the lobar-basis territories over the entire lung for the assessment of the regional pulmonary ventilation and perfusion.

As CTPA has enabled the direct visualization of pulmonary emboli in the segmental and sub-segmental vessels, several CT angiography indexes have been studied to quantify the severity of arterial obstruction(128–131). The Miller index was initially proposed, consisting of an objective arterial obstruction score and a subjective evaluation for peripheral perfusion reduction(129). A full objective Walsh index that calculates the number of segmental vessels under-perfused due to the PE in segmental or larger vessels, has rarely been used in clinical practice due to computational complexity (130). Later, Qanadli et al. described a CT obstruction index with higher accuracy, which computes the value of the proximal clot site that equals to the number of segmental branches arising distally and a weighting factor of the obstruction degree (131). However, none of these CT-assessed parameters can directly reflect the embolus burden, especially for the distal PEs in segmental and subsegmental branches (4,5). To our knowledge, little consideration has been given to relate the amount of tissue subtended to the embolus location of the pulmonary artery. The MCP technique enables the assignment of every single voxel of the parenchyma to its supplying vessel; hence, the precise territory of lung parenchyma distal to the location of emboli can be delineated for better visualization and quantification.

Consequently, the total PE-related tissue mass (or mass percent) can potentially play a prognostic role in stratifying PE severity for improved patient outcomes.

In addition, the heterogeneity of the distribution of ventilation and perfusion can be observed in a variety of lung diseases, such as pulmonary embolism, chronic obstructive pulmonary disease, and lung cancer (137–141,150). As the lungs are anatomically and functionally separated into different lobes by lobar fissures, many diseases preferentially impact a particular lobe (150,151). Existing automatic lobe segmentation methods largely depend on the anatomy of healthy human lungs, including atlas-based (152,153), airway-guided (154), and deep learning-based algorithms(155). Unfortunately, these anatomical fissure-based segmentation algorithms can be susceptible to anatomical variations, particularly in human lungs that may have incomplete fissures (156,157). Moreover, as the deformation of lung anatomy may occur after coil treatment and lung volume reduction procedures, additional manual correction steps are required on the atlas to ensure accurate lobe segmentation for post-treatment CT analysis (141). Therefore, an automatic pulmonary lobar segmentation that does not rely on fissure visualization could improve assessment of the regional ventilation/perfusion mismatch and lung volume reduction. The vessel-specific MCP technique determines the lobar territories by assigning each voxel to its supplying vessel based on the shortest spatial distance, which is entirely independent of its borderlines. As the pulmonary arterial tree can be used for lobar assignment, such a technique can be robust over lung volume alteration and invisible fissures.

The present study has several limitations. First, the sample size of this animal study is relatively small. Further studies on a larger sample size with a wide range of patients under various pulmonary conditions are necessary. Second, in this validation study, the reference standard is the perfusion defect territory derived from dynamic CT perfusion measurement, rather than a direct intravascular contrast injection right at a PE location in a pulmonary artery branch. Any error from the CT perfusion measurement may appear as an error for the MCP technique.

Fortunately, a previous study has shown the high concordance of the two-volume first-pass CT perfusion measurements versus fluorescent microsphere measurements, laying a solid foundation for this work. Third, only fully occluded PE was induced in this study. It is known that both partial and full arterial obstruction have high presence in acute PE. As the perfusion technique served as the reference standard, only the total arterial obstruction can minimize the potential error from the perfusion measurement by thresholding an absolute low perfusion value for the validation purpose. The MCP technique is expected to quantify the territory for suspected PE, regardless of the partial or total occlusion in the clinical practice. Fourth, different levels of PE-distal mass-percent are not associated with the existing pulmonary artery obstruction indices and risk factors, such as the pulmonary arterial pressure and right ventricular function. Future studies will need to determine whether the mass-percent of the distal territory can be a substitute or better indicator for PE risk stratifications. Finally, the vessel-specific assignment for lobar segmentation has not been quantitatively validated in this study with a gold standard. The vessel-specific MCP assignment requires further investigation and evaluation with other existing automatic approaches.

Practical Application: This study validated an MCP technique for quantifying the PE-distal territory with the perfusion defect territory as the reference standard. Excellent mass and spatial correspondences were found between the MCP PE-distal and reference standard defect territories. The proposed MCP technique can accurately quantify the territory corresponding to the subtended tissue distal to a PE using a CTPA image; hence, such a technique may potentially improve the PE-severity assessment of acute PE by providing a mass-percent of tissue at-risk. In summary, the minimum-cost path technique was validated in a swine model to correlate the location of the pulmonary arterial obstruction to its under-perfused distal tissue at risk and has the potential to improve the stratification of pulmonary embolism severity.

Chapter 6 Accuracy and Reproducibility of the Prospective Two-volume Computed Tomography Perfusion Technique: Evaluation on Global and Regional Pulmonary Perfusion

Abstract

Existing dynamic CT perfusion (CTP) techniques are limited by the high radiation dose from multiple scans. The purpose of this chapter is to validate a low-dose, first-pass analysis (FPA) perfusion technique with only two volume scans and evaluate its reproducibility. Six Yorkshire swine (53.8±2.4 kg) were used in this validation study with 48 independent CTP acquisitions using a 320-slice CT scanner. Intravenous contrast material (370 mg/ml iodine, 0.5ml/kg) and saline chaser (0.5ml/kg) were injected at 5 ml/s for each CTP acquisition. For each swine, both retrospective and prospective dynamic CTP data were acquired. For the retrospective CTP acquisition, an average of twenty volume scans was acquired per acquisition for the CTP measurements and served as the reference standard. For the prospective CTP acquisition, only two volume scans were acquired, where the first low-dose (50 mA) volume scan was acquired before contrast injection and the second diagnostic (300 mA) volume scan was acquired following bolus-tracking in the main pulmonary artery with a time-to-peak delay calculated using the injection time interval. Two different scan modes were used in the prospective acquisition: a volume mode (16cm z-coverage, 0.35s rotation time) and a fast-pitch helical mode (25cm z-coverage, 2.5s scan time). All prospective CTP measurements were quantitatively compared to the reference standard CTP measurements using t-test and linear regression. The CT dose index for the retrospective, two-volume prospective, two-helical prospective CTP measurements were 184.8, 9.3, and 4.8 mGy, respectively. The prospective CTP measurements using the volume mode (P_{VOL}) and helical mode (P_{HEL}) were related to the reference CTP measurements by

$P_{VOL}=0.97P_{RETRO}+0.33$ ($r = 0.93$) and $P_{HEL}=1.01P_{RETRO}-0.94$ ($r=0.98$), respectively. In conclusion, the two-volume, first-pass CTP technique was validated in a swine model that can potentially be used for the assessment of pulmonary disease. This novel CTP technique enables dynamic whole-lung perfusion measurement with conventional 64-slice CT scanners using helical mode.

Introduction

Pulmonary perfusion scintigraphy, the first well-established non-invasive imaging modality for the diagnosis of pulmonary embolism (PE) and chronic thromboembolic pulmonary hypertension (CTEPH), has been widely used in clinical practice (158). Unfortunately, the perfusion imaging results are reported in terms of probabilities for the presence of PE, incapable of providing absolute lung perfusion measurement expressed in ml/min/g (2). A prompt diagnosis and treatment based on absolute CT perfusion measurement is critical for reducing the mortality rate(23,37,38).

Although CT techniques have been widely used in the assessment of pulmonary disease and lung cancer (159), concerns remain regarding high radiation exposure and accuracy. Conventional 64-slice or 128-slice detectors, as limited by the cranial-caudal coverage, only small volume-of-interest (VOIs) can be used to derive regional pulmonary blood flow, leading to an underestimation of the blood flow as the contrast exits the compartment way too soon due to the small compartment size (55,58). In addition, existing dynamic CT perfusion techniques require at least twenty volumes scans to fully measure the tissue contrast pass curve for perfusion measurement, e.g., the maximum slope model (MSM) and the de-convolution model, resulting in high radiation dose and potential motion artifacts (57–59,160). Consequently, such a high sampling rate at every cardiac cycle or every two seconds makes it impractical to perform a whole-lung dynamic perfusion measurement. By reducing the number of dynamic scans to a minimum of two scans, the expansion of the scan window is feasible by using a fast-pitch helical scan mode (scan time per whole-lung volume: 2~3 seconds). Given the extended compartment size and the minimized number of scans, the prospective two-volume perfusion technique can fundamentally overcome the limitations of current perfusion measurements, while significantly reducing the radiation dose; hence, enabling an assessment of whole-lung perfusion with improved accuracy and precision.

The purpose of this chapter was to validate a low-dose, first-pass, whole-lung CT perfusion technique using only two helical scans. The central hypothesis was that both global and regional perfusions can be accurately measured using only two helical scans, as compared with the reference standard perfusion that has been previously validated. The reproducibility of the two-volume prospective perfusion technique is also evaluated in this chapter.

<u>Material and Methods</u>

General Methods

All animal studies were approved by the Animal Care Committee and performed under guidelines for animal care. A total of six Yorkshire swine (53.8±2.4 kg) were used for the validation of a two-volume, whole-lung perfusion technique. For each swine, contrast-enhanced dynamic CT perfusion was first performed with over twenty volume scans and used for the retrospective perfusion measurement as a reference measurement. Then, the two-volume dynamic CT perfusion scan was performed, where the first non-contrast volume scan (V1) was acquired, followed by contrast injection, and the second volume scan (V2) was acquired after bolus tracking triggering and a pre-defined time-to-peak delay. Two scan modes, the volume scan mode and the fast-pitch helical scan mode, were used in the prospective acquisition and compared to the reference perfusion. The prospective acquisition was repeated one more time for precision evaluation. The same hemodynamic status was maintained between data acquisition for the two scan modes. The accuracy and precision of global and regional perfusion measurements were evaluated using linear regression and paired t-tests. All experimental data were successfully acquired between November 2020 and June 2021 and analyzed in the same time frame between and during studies. All authors were involved in data acquisition, and authors Y.Z. and N.L. conducted data analyses.

Animal Preparation

Each swine was initially induced with Telazol (4.4 mg/kg) and Xylazine (2.2 mg/kg). After intubation, anesthesia was maintained over the entire experiment via mechanical ventilation with 1.5–2.5% Isoflurane (Highland Medical Equipment, Temecula, CA and Baxter, Deerfield, IL). Two introducer sheaths (AVANTI®, Cordis Corporation, Miami Lakes, FL) were placed in left femoral vein and left jugular vein for intravenous fluid and contrast material administration, respectively. One more sheath was placed in the right femoral artery for invasive pressure monitoring. A urinary catheter was placed in the bladder for urine drainage. The oxygen saturation (%), end-tidal carbon dioxide (mmHg), heart rate (beats per minute), and mean arterial pressure (mmHg) were recorded every 15 minutes. At the conclusion of the experiment, animals were euthanized with saturated KCL under deep anesthesia and verified via ECG tracing.

Scanning Protocol

All CT examinations were performed using a 320-row detector CT scanner (Aquilion One, Canon Medical Systems, Tustin, CA) at our institution. Each animal was studied in a supine position and scanned from the top to bottom lung. For all scans, tube voltage was set at 100 kV, with the scan field-of view of 320 mm, and gantry rotation time of 0.35 seconds. Different tube currents were used for different scan protocols. For volume scan mode, 300mA(full-dose) was used for the retrospective and prospective V2 acquisitions, 90mA(low-dose) was used for the prospective V1 acquisition. For helical scan mode, 200mA (full-dose) was used for V2 acquisition, and 50mA (low-dose) was used for V1 acquisition. A collimation of 320 x 0.5 mm was used for the volume scan, while 64 x 0.5 mm was used for the fast-pitch helical scan mode with a pitch value of 1.481. For the retrospective acquisition, followed by intravenous contrast agents (0.5 ml/kg Isovue-370) and saline chaser (0.25 ml/kg) at an injection rate of 5 ml/s (Empower CTA, Acist Medical Systems, Eden Prairie, MN), breath-hold dynamic CT scans were acquired at the end-inspiration for approximately twenty cardiac cycles under ECG-gating. For the prospective acquisition, a low-dose non-contrast volume (or helical) scan was performed with breath-hold, followed by the contrast injection (same dose and rate), and the second full-dose volume (or helical) scan was initiated by bolus tracking within the pulmonary artery trunk to trigger data acquisition. A 10-minute delay was employed between acquisitions for contrast clearance. Full projection data was used for all volume (or helical) acquisitions, with a lung FC07 kernel using an adaptive iterative dose reduction 3D (AIDR 3D) reconstruction algorithm. The in-plane reconstruction was 512 x 512 pixels with a slice thickness of 0.5 mm, ending up with a 0.625 x 0.625 x 0.50 mm^3 voxel size. The CT dose index ($CTDI_{VOL}^{32}$, mGy), dose length product (DLP, mGy·cm) and size-specific dose estimates (SSDE, mGy) was recorded and computed for all CT acquisitions (70).

Retrospective and Prospective Two-volume Perfusion techniques

The average pulmonary blood flow was measured based on a first-pass, whole-lung compartment model, as previously described (65,66,93) . Prior to the contrast outflow from the entire compartment, the average pulmonary blood flow ($\boldsymbol{Q, ml/min}$) is proportional to the integrated contrast mass change ($\boldsymbol{\Delta M_c}$, mg), and normalized by the average arterial input concentration ($\boldsymbol{C_{in}}$, $\boldsymbol{mg/ml}$) and the total contrast accumulation time($\Delta\boldsymbol{t, s}$).

$$\boldsymbol{Q} = \frac{\boldsymbol{1}}{\boldsymbol{C_{in}}} \frac{\boldsymbol{\Delta M_c}}{\Delta \boldsymbol{t}} \qquad (6.1)$$

Then, the absolute perfusion in $ml/min/g$, was further normalized by the tissue mass on a voxel-by-voxel basis that accounts for the heterogeneity of tissue/air fraction (93) .

For the reference retrospective measurement, the two volume scans (V1 and V2) were systematically selected from the entire contrast pass curve, at approximately the base and peak of the pulmonary arterial enhancement, as shown in **Figure 6.1**(b). The accuracy of the reference retrospective perfusion measurement was previously validated versus fluorescent microsphere measurements in (93).

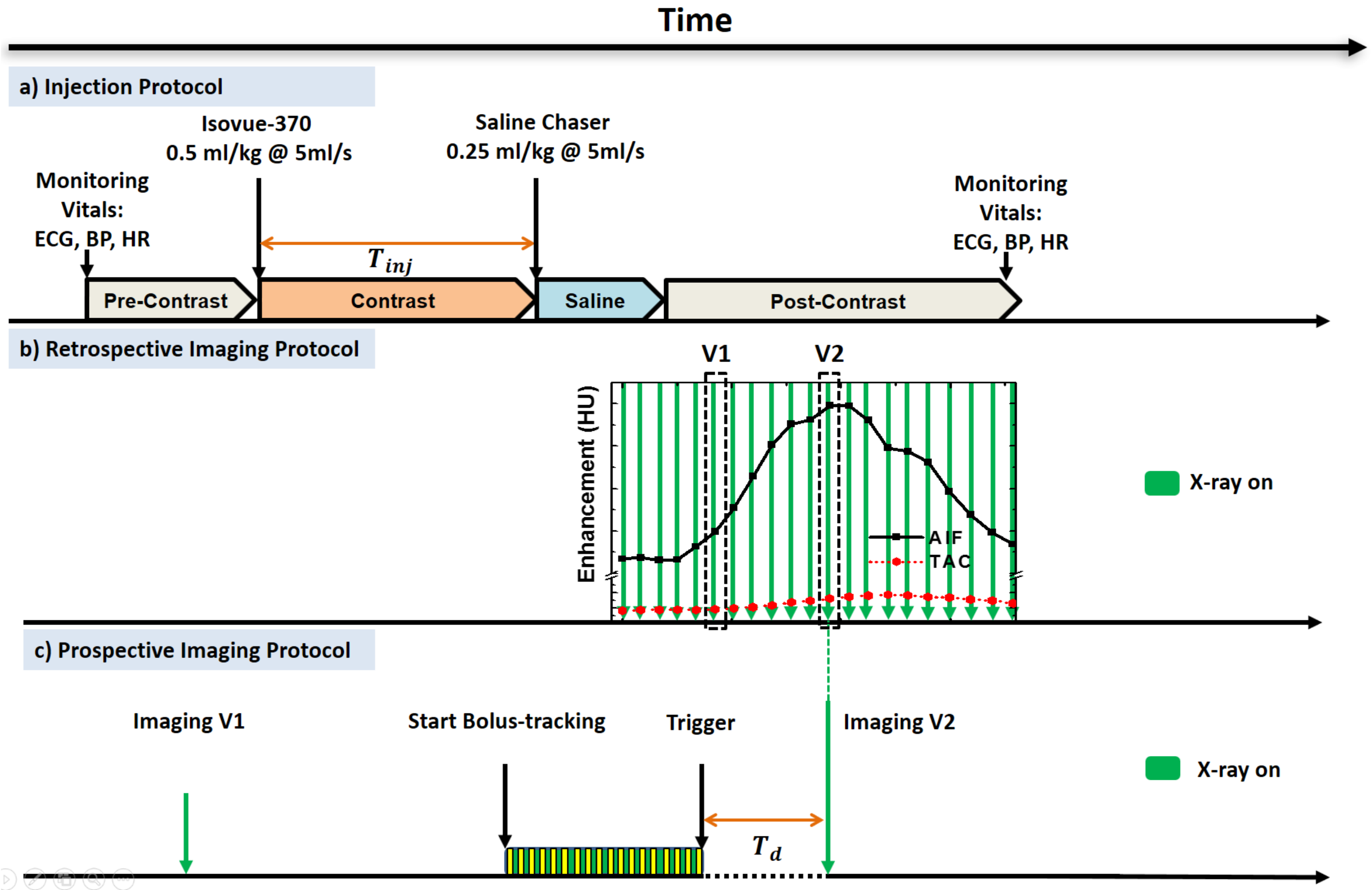

Figure 6.1 The timeline of the contrast injection, retrospective and prospective CT acquisition protocol. a) Injection protocol. Contrast-enhanced imaging, contrast was injected at 5ml/s followed by a saline chaser at the same rate. Dynamic imaging of the lung was then performed. b) Retrospective CT imaging protocol. The entire pulmonary arterial input function (AIF) and lung tissue time attenuation curve (TAC) was captured and used for perfusion measurement. c) Prospective CT imaging protocol. The first volume scan (V1) was acquired before contrast injection. The second volume scan (V2) was acquired at the maximal

enhancement of AIF using the bolus-tracking technique and a pre-defined time-to-peak delay. T_{inj}, contrast injection time; T_d, time-to-peak delay.

For the two-volume prospective measurement, the first volume (or helical) scan (V1) should be acquired prior to contrast arrival, and the second volume (or helical) scan (V2) should be acquired at the maximal arterial enhancement, as described in **Figure 6.1c**. Hence, V1 was acquired without contrast injection with a breath-hold at the maximal end-inspiration, and V2 was acquired following contrast injection with another breath-hold at full inspiration. Specifically, bolus-tracking (SureStart, Aquilion One, Canon Medical Systems, Tustin, CA) was performed using a 2-mm image window at the level of the pulmonary artery and triggered after the region-of-interest enhancement exceeded a threshold of 80 HU above the baseline blood pool enhancement (measured using the Scan &View image). Moreover, a time delay was set to ensure the second volume can be captured near the arterial enhancement peak for adequate contrast-to-noise ratio. Based on previously reported findings (80), this trigger-to-peak delay (T_d) can be related to one-half of the contrast injection time (T_{inj}) plus a dispersion delay ($\boldsymbol{d}$) to the pulmonary artery. As the helical scan time ranged from 1.8 to 2.3 seconds for a scan range of 210-260 mm, the time delay was set 1 second earlier than the volume scan, as summarized in Eq.2:

$$T_d = \begin{cases} T_{inj}/\mathbf{2} + \boldsymbol{d} & \text{volume scan mode} \\ T_{inj}/\mathbf{2} + \boldsymbol{d} - \mathbf{1} & \text{helical scan mode} \end{cases} \qquad (2)$$

where $\boldsymbol{d} = \mathbf{1}$ for pulmonary artery dispersion.

Image Processing

The procedure of image processing is shown in **Figure 6.2**. The two volume (or helical) scans, either systematically selected or prospectively acquired, were first registered using a deformable affine-based algorithm. Two volume-of-interests (VOIs), the entire lung parenchymal within the scan window, and a cylindrical pulmonary artery segment, were semi-automatically segmented using a Vitrea workstation (Vitrea fX version 7.7, Vital Images, Inc., Minnetonka, MN) and saved as two binary masks. Then, the integrated contrast mass change of the entire lung parenchyma and the average input concentration, as shown in ***Eq. 6.1***, were computed to yield a global lung perfusion measurement (MatLab 2021a, MathWorks, Natick, MA). Note that as the reference standard can only be acquired using the volume scan mode, a bounding box was set on the helical scan images regarding the same lung region to ensure a direct comparison in the accuracy assessment. Subsequently, using the lung segmentation mask, parenchyma voxels were divided into six lobar perfusion territories through a vessel-specific lobar segmentation based on a minimum-cost path technique(143), including the left upper lobe (LUL), left lower lobe (LLL), right upper lobe (RUL), right middle lobe (RML), right lower lobe (RLL) and accessory lobe (ALL) segments. The mean perfusion of each lobe was calculated for regional lung perfusion comparisons.

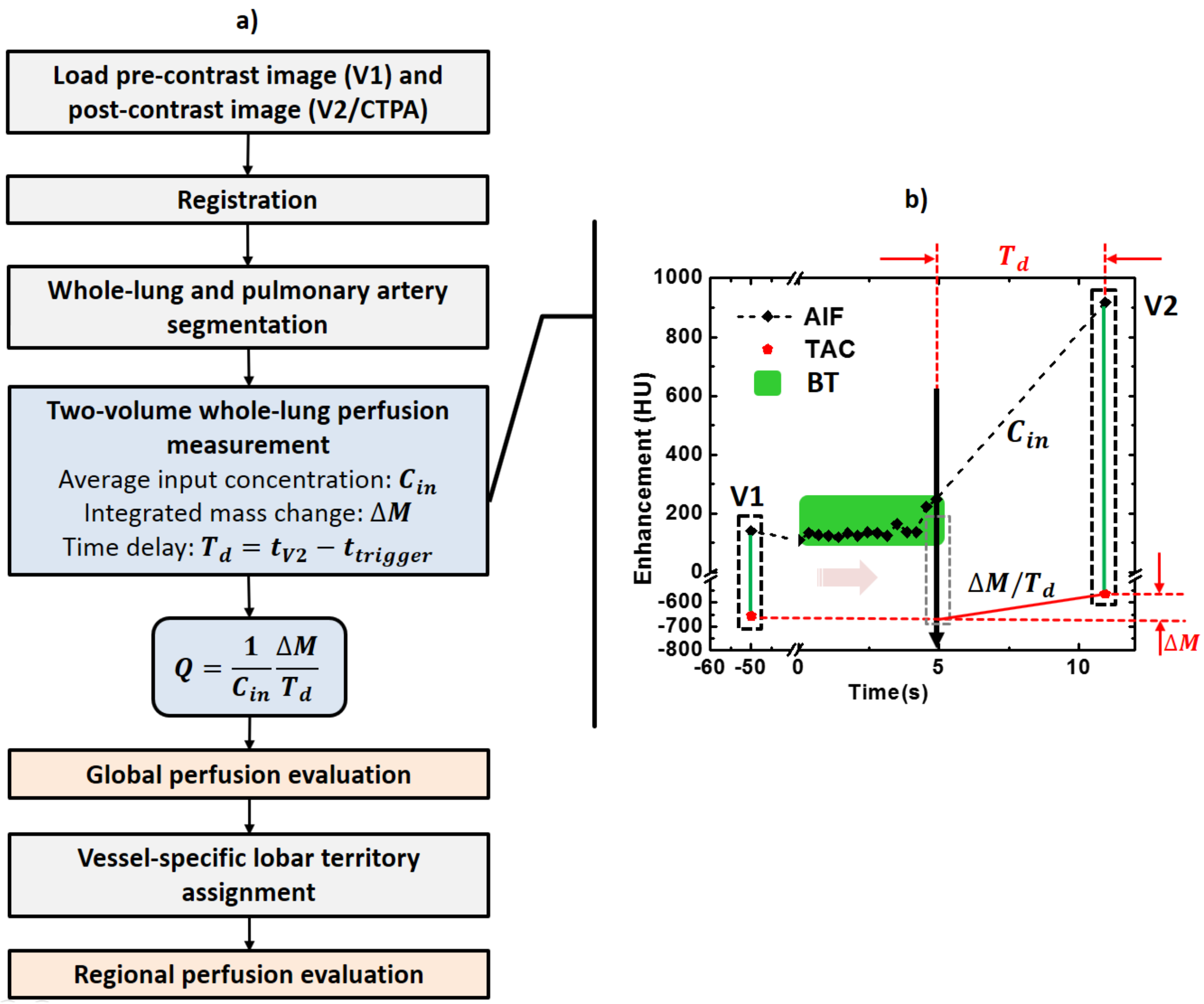

Figure 6.2 Image processing flowchart and prospective two-volume perfusion technique.
The first volume scan (V1) was acquired before contrast injection. The second volume scan (V2) was acquired after the bolus-tracking technique and a pre-defined time-to-peak delay.
(ΔM, integrated contrast mass change; T_d, time-to-peak delay; BT, bolus-tracking; AIF, arterial input function; TAC, time attenuation curve.)

Statistical Approach

The accuracy and precision of the two-volume prospective perfusion technique were evaluated for both volume and helical scan modes, using the global and regional perfusion measurements. The perfusion values were reported in mean ± standard deviation. With respect to the accuracy assessment, the prospective perfusion measurements were compared to the corresponding reference retrospective measurements by paired-sample t-test, linear regression, and Bland-Altman analysis. With respect to the precision assessment, two independent prospectively measured perfusion measurements were compared by paired-sample t-test, linear regression, and Bland-Altman analysis. P-values less than 0.05 indicate statistical significance. 95% confidence intervals of all fitting parameters were provided as well. Additionally, the root-mean-square-error (RMSE), root-mean-square deviation (RMSD), Pearson correlation coefficient (r), and Lin's concordance correlation coefficient (CCC) (75) were also computed. All statistical analyses were conducted using the SPSS software (Version 22, IBM Corporation, Armonk, NY).

Results

Vitals and Statistics

A total of six swine (53.8±2.4 kg) were used to validate the accuracy and reproducibility of the prospective, two-volume FPA perfusion technique. A total of 63 CT perfusion measurements were obtained, where only 15 acquisitions were excluded due to false triggering issues (2 cases), irregular heart rates (above 120 bpm, 9 cases), and severe respiratory motion artifacts (4 cases). Overall, 48 successful acquisitions were used in global and regional perfusion analyses. For the regional perfusion analysis, six three-dimensional lobar territories were used per animal, resulting in a total of 288 (48 x 6) regional segments in the evaluation. The average heart rate and mean arterial pressure throughout the CT perfusion acquisitions were 88.5 ± 19.3 bpm and 58.5 ± 17.7 mmHg, respectively.

Qualitative Analysis

Examples of perfusion maps acquired using the retrospective reference FPA technique, prospective two-volume FPA technique by the volume scan mode, and prospective two-volume FPA technique by the helical scan mode are displayed in axial, coronal, and three-dimensional volumetric images **(Figure 6.3)**. The blood flow measurements are represented by the absolute perfusion in ml/min/g, where red indicates high perfusion values, and blue indicates low perfusion values. Note that the helical scan mode shows the whole-lung perfusion map, while the volume scan mode can only show a limited section of the lung perfusion map with a 16-cm cranio-caudal coverage.

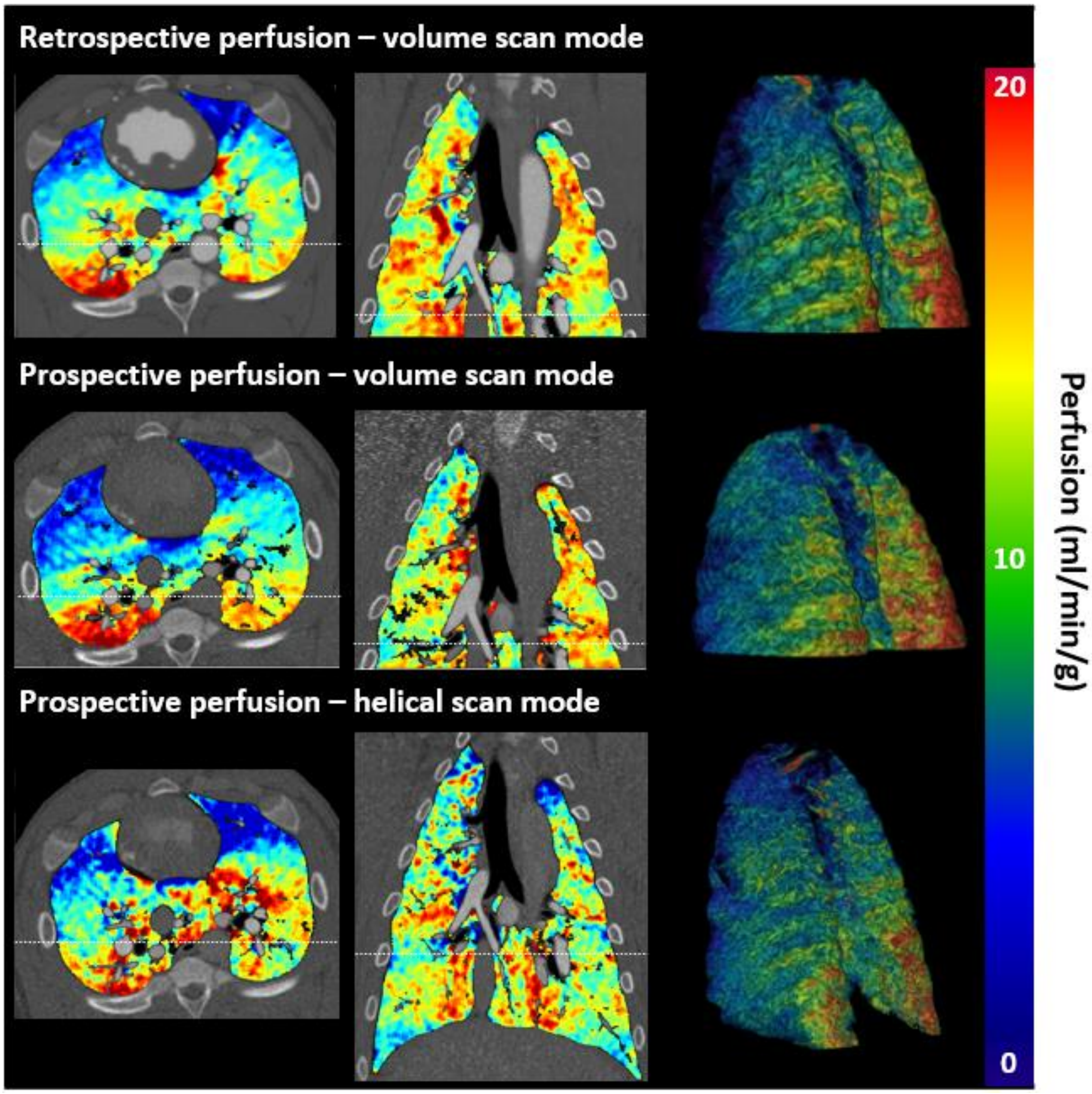

Figure 6.3 Qualitative perfusion maps with three scan protocols.
Top, reference retrospective perfusion map. Middle: prospective perfusion map using the volume scan mode. Bottom, prospective perfusion map using the helical scan mode. The bar on the right shows the abosulute perfusion measurement in *ml/min/g.*

Quantitative Analysis of Accuracy

Global Perfusion: The average global perfusions for the reference and prospective measurements of 15 volume scan pairs were 10.04±3.46 and 10.41±3.56 ml/min/g ($p=0.83$), and of 11 helical scan pairs were 10.15±3.52 and 9.43±3.65 ml/min/g ($p=0.01$), respectively (**Table 6.1**). Additionally, the prospective volume scan measurements (P_{VOL}) were related to the reference standard measurements by $P_{VOL}=0.97P_{RETRO}+0.33$ ($r = 0.93$), with a RMSD of 1.25 ml/min/g, and a RMSE of 1.04 ml/min/g, while the prospective helical volume scan measurements (P_{HEL}) were related to the reference standard measurements by $P_{HEL}=1.01P_{RETRO}-0.94$ ($r=0.98$), with a RMSD of 0.77 ml/min/g and a RMSE of 1.00 ml/min/g (**Figure 6.4a and Figure 6.5a, Table 6.1**). The mean differences of the global perfusion measurements using the volume and helical scan modes were 0.94 and -0.69 ml/min/g, respectively, where all measurements were within limits of agreement, as shown in **Figure 6.4b and Figure 6.5b.**

Table 6.1 Evaluation of accuracy of the perfusion measurement: Prospective measurement versus the reference retrospective measurement.

Lung Segments	Number of pairs (n)	Reference CT Perfusion (ml/min/g)	Prospective CT Perfusion (ml/min/g)	P-value ($\alpha < 0.05$)	RMSE (ml/min/g)
Volume Scan Mode					
Global Perfusion	15	10.04 ± 3.46	10.41± 3.56	0.83	1.25
Right Lung					
Right Upper Lobe	15	9.70 ± 3.29	10.50 ± 3.73	0.25	1.51
Right Middle Lobe	15	7.81 ± 2.45	7.28 ± 2.50	0.06	1.37
Right Caudal Lobe	15	14.54 ± 4.53	14.62 ± 4.62	0.33	1.37
Accessory Lobe	15	9.94 ± 3.19	10.47 ± 4.52	0.69	2.47
Left Lung					
Left Upper Lobe	15	8.78 ± 3.77	9.61 ± 4.72	0.29	1.43
Left Caudal Lobe	15	14.06 ± 5.43	14.94 ± 6.11	0.66	1.90
Helical Scan Mode					
Global Perfusion	11	10.15+3.52	9.43+3.65	0.01*	1.10
Right Lung					
Right Upper Lobe	11	10.36 ± 3.49	6.94 ± 2.34	0.00*	3.64
Right Middle Lobe	11	7.44 ± 2.46	6.77 ± 2.77	0.11	1.42
Right Caudal Lobe	11	14.22 ± 4.44	13.43 ± 4.67	0.38	2.17
Accessory Lobe	11	10.33 ± 3.60	9.85 ± 3.69	0.54	1.39
Left Lung					
Left Upper Lobe	11	8.66 ± 3.80	7.03 ± 3.46	0.00*	2.24
Left Caudal Lobe	11	13.75 ± 5.18	12.68 ± 4.92	0.16	2.33

Note.— SD: Standard Deviation.

1. The mean perfusion values are the average perfusion values of each lobe sample, the SD values are the perfusion value variations from the same sample, not the measurement errors.
2. The P-values are calculated by the paired-samples t-test statistics. The larger P-values indicate higher similarity between the two groups of data.
3. RMSE: root-mean-square error.

* Denotes mean CT perfusion values that are significantly different from reference perfusion values.

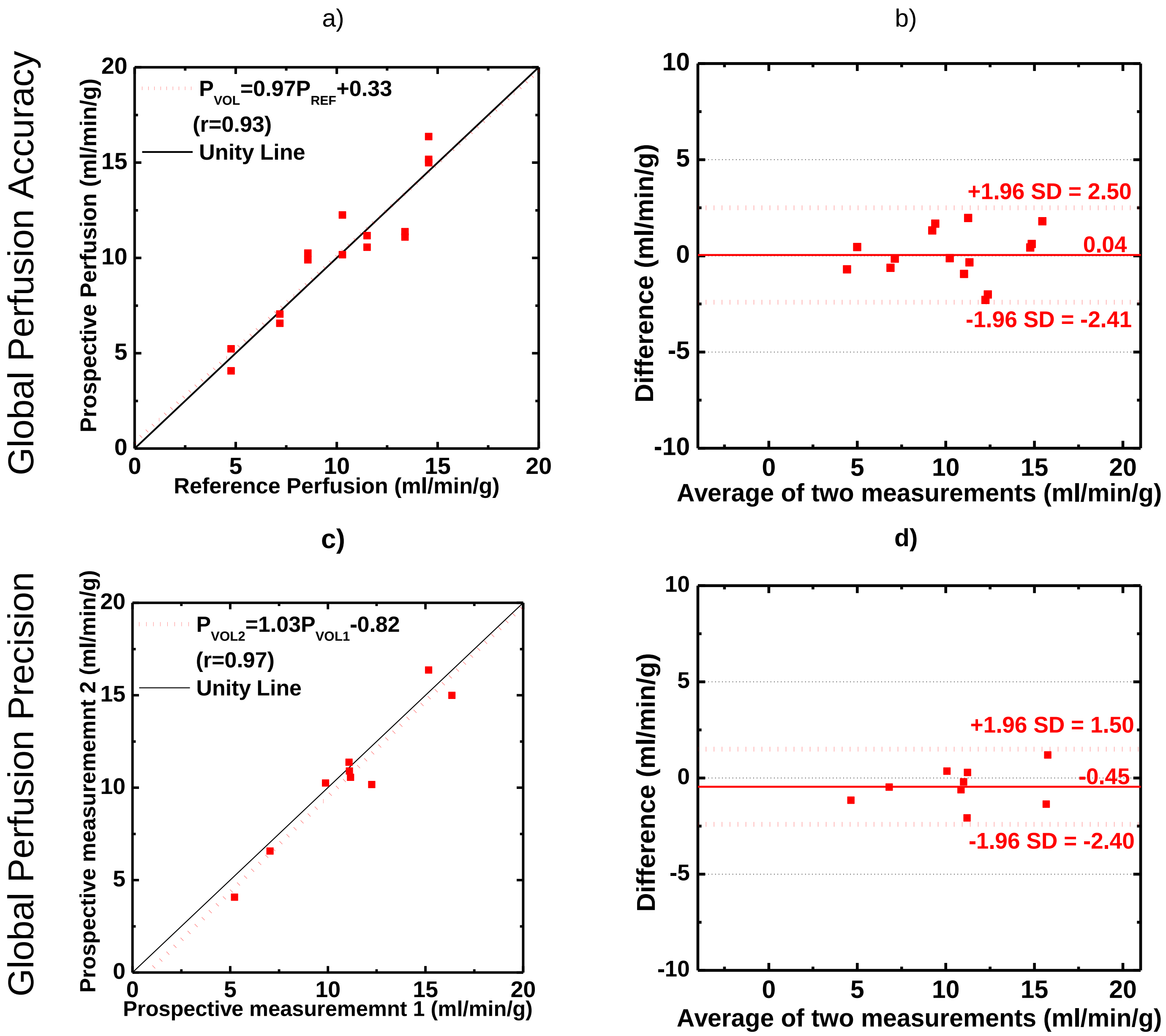

Figure 6.4 Linear regression and Bland-Altman analyses of the global perfusion using volume scan mode.

Top row) The perfusion measurements were compared between the prospective measurement and reference retrospective measurement for two scan modes. Bottom row) The perfusion measurements were compared between two prospective measurements for two scan modes.

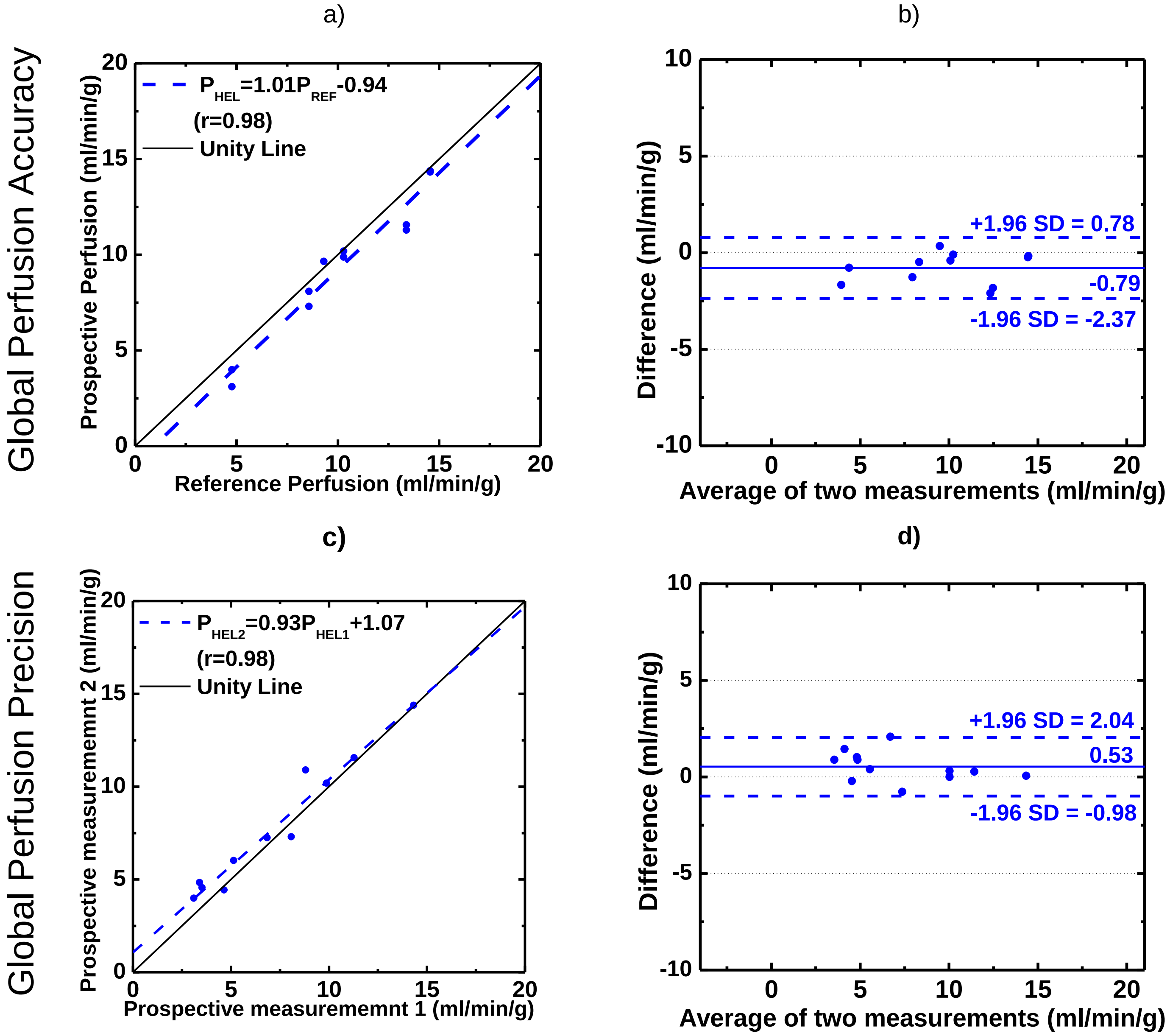

Figure 6.5 Linear regression and Bland-Altman analyses of the global perfusion using helical scan mode.

Top row) The perfusion measurements were compared between the prospective measurement and reference retrospective measurement for two scan modes. Bottom row) The perfusion measurements were compared between two prospective measurements for two scan modes.

Regional Perfusion: The mean regional perfusions of each lobar segment were calculated and compared between the reference standard, prospective volume scan measurements, and prospective helical scan measurements, as detailed in **Table 6.1**. For all lobar segments, no significant differences were found between the prospective volume scan measurements and the reference standard, while significant differences were found in the RUL and LUL between the helical scan prospective measurements and reference standard. A significantly higher RMSE of 3.64 ml/min/g was found in the RUL using the helical scan (**Table 6.1**).

Further, the overall prospective regional perfusion measurements were related to the reference standard by $P_{PRO}=1.04P_{RETRO}-0.38$ (r=0.94, RMSD=1.71 ml/min/g, RMSE= 1.72 ml/min/g) using the volume scan mode, and $P_{HEL} = 0.93P_{RETRO} -0.52$ (r=0.91, RMSD=1.92 ml/min/g, RMSE=2.32 ml/min/g using the helical scan mode (**Figures 6.6a and 6.6c, Table 6.1**). The linear regression parameters of overall regional perfusion measurements can be found in **Table 6.2**. Larger ranges of confidence intervals were found in the regional perfusion as compared to the global perfusion in both scan modes (**Figures 6.6b** and **6.6d**). No systemic bias (mean difference=0.11 ml/min/g) were found using the volume scan mode, while an underestimation of 1.27 ml/min/g was found using the helical scan mode in the overall regional perfusion measurements.

Table 6.2 Evaluation of linear regression parameters for accuracy. Prospective perfusion measurement versus reference perfusion measurement.

	Slope	Intercept	Pearson r	CCC	RMSE (ml/min/g)	RMSD (ml/min/g)
Volume scan mode						
Global (n = 15)	0.97 (0.75, 1.20)	0.33 (-2.14, 2.80)	0.93 (0.82, 0.97)	0.93 (0.81, 0.97)	1.25	1.25
Regional Overall (n = 90)	1.04 (0.962, 1.12)	-0.38 (-1.32, 0.56)	0.94 (0.85, 0.98)	0.93 (0.82, 0.97)	1.72	1.71
Helical scan mode						
Global (n = 11)	1.01 (0.842, 1.19)	-0.94 (-2.79, 0.91)	0.98 (0.92, 0.99)	0.96 (0.86, 0.99)	1.10	0.77
Regional Overall (n = 66)	0.93 (0.82, 1.04)	-0.52 (-1.78, 0.74)	0.91 (0.72, 0.97)	0.78 (0.67, 0.86)	2.32	1.92

Note.—Data in parentheses are 95% confidence intervals. CCC: concordance correlation coefficient, RMSD: root-mean-square deviation.

* Denotes prospective perfusion regression parameters that are significantly different from the retrospective perfusion regression parameters, as indicated by non-overlap of each 95% confidence interval, respectively.

Lobar Perfusion Accuracy

Volume scan mode

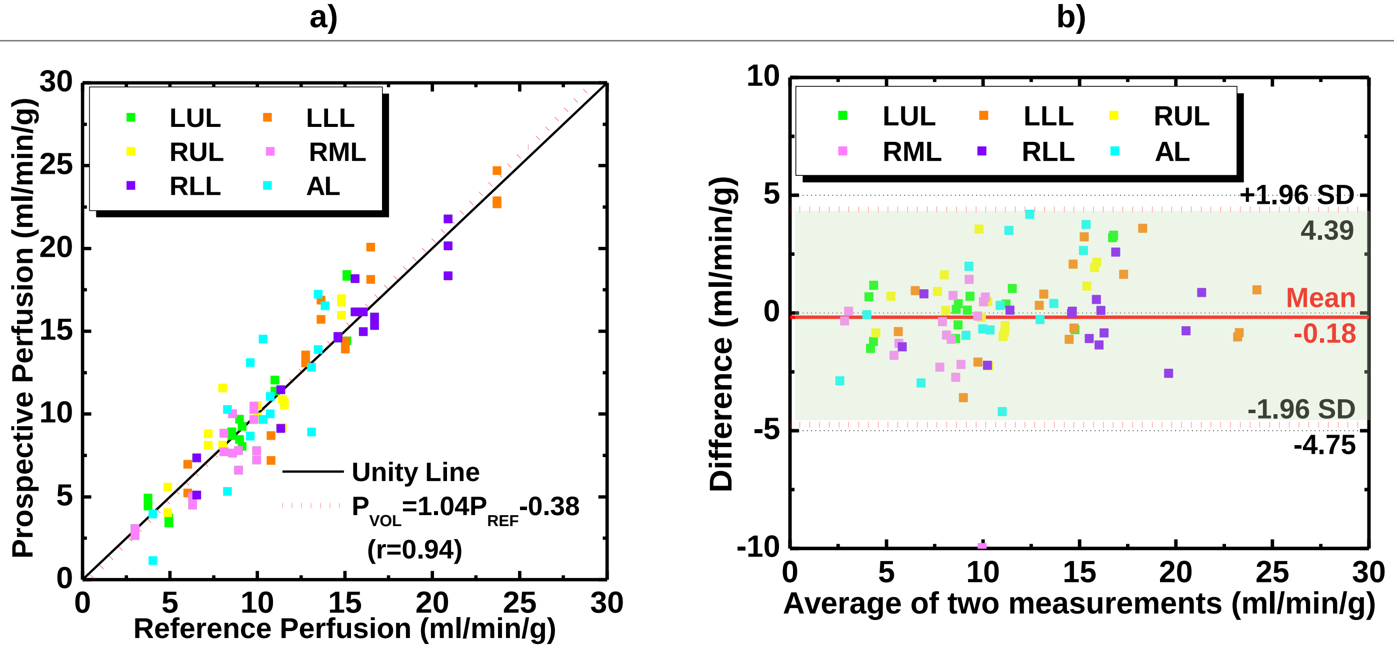
a) b)

Helical scan mode

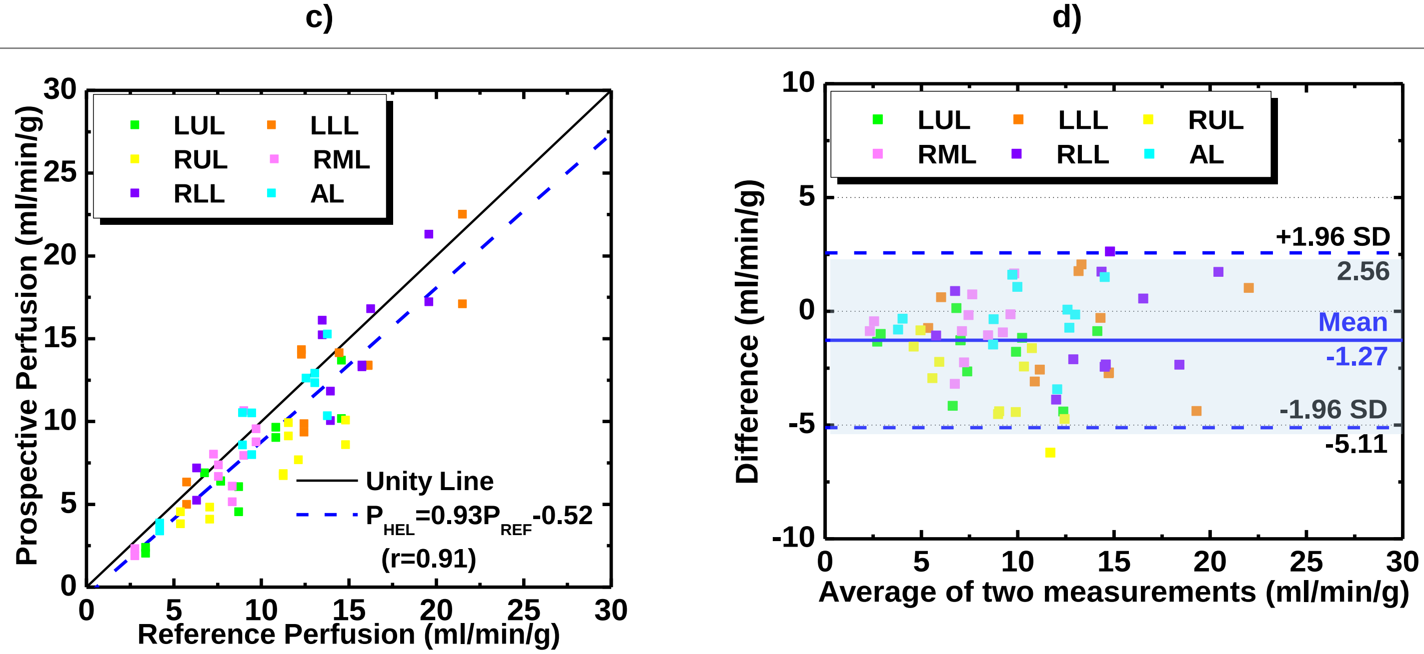
c) d)

Figure 6.6 The accuracy of the regional perfusion using linear regression and Bland-Altman analysis.

The regional perfuison measurements were compared between the prospective measurement and reference retrospective measurement using two scan modes. a) b) Volume scan mode, c) d) Helical scan mode.

Quantitative Analysis of Reproducibility

Global Perfusion: For the reproducibility of the prospective perfusion measurements, the average perfusions for the two paired sets were 11.03 ± 3.50 and 10.58 ± 3.75 ml/min/g (p=0.21) using the volume scan mode, and 7.19 ± 3.45 and 7.76 ± 3.49 ml/min/g (p=0.04) using the helical scan mode. Regression and Bland-Altman analyses of the global prospective measurements using volume scan and helical scan are shown in **Figures 6.4** and **6.5**, and detailed in **Tables 6.3** and **6.4.**

Table 6.3 Evaluation of reproducibility of the perfusion measurement. Prospective measurement 1 versus Prospective measurement 2.

Lung Segments	**Number of pairs (n)**	**Reference CT Perfusion 1 (ml/min/g)**	**Prospective CT Perfusion 2 (ml/min/g)**	**P-value (α < 0.05)**	**RMSE**
		Volume Scan Mode			
Global Perfusion	9	11.03 ± 3.50	10.58 ± 3.75	0.21	1.04
Right Lung					
Right Upper Lobe	9	11.37 ± 3.47	10.92 ± 3.66	0.39	1.46
Right Middle Lobe	9	7.96 ± 2.59	7.65 ± 2.18	0.43	1.09
Right Caudal Lobe	9	15.79 ± 4.38	15.08 ± 4.28	0.23	1.70
Accessory Lobe	9	11.28 ± 3.92	11.66 ± 4.72	0.76	3.41
Left Lung					
Left Upper Lobe	9	10.59 ± 5.15	10.14 ± 4.51	0.39	1.47
Left Caudal Lobe	9	15.53 ± 6.06	16.02 ± 5.74	0.32	1.39
		Helical Scan Mode			
Global Perfusion	11	7.19 ± 3.65	7.76 ± 3.49	0.04	1.00
Right Lung					
Right Upper Lobe	11	5.21 ± 2.43	5.75 ± 2.68	0.14	1.18
Right Middle Lobe	11	4.67 ± 2.53	4.94 ± 3.15	0.45	1.11
Right Caudal Lobe	11	10.06 ± 4.35	11.66 ± 4.78	0.00*	2.00
Accessory Lobe	11	7.04 ± 3.75	8.13 ± 3.76	0.17	2.56
Left Lung					
Left Upper Lobe	11	4.70 ± 3.05	5.10 ± 3.76	0.33	1.29
Left Caudal Lobe	11	9.26 ± 4.28	10.55 ± 5.32	0.03*	2.06

Note.— SD: Standard Deviation.

1. The mean perfusion values are the average perfusion values of each lobe sample, the SD values are the perfusion value variations from the same sample, not the measurement errors.
2. The P-values are calculated by the paired-samples t-test statistics. The larger P-values indicate higher similarity between the two groups of data.
3. RMSE: root-mean-square error.

* Denotes two perfusion measurements are significantly different.

Table 6.4 Evaluation of linear regression parameters for reproducibility. Prospective perfusion measurement 1 versus prospective perfusion measurement 2.

	Slope	Intercept	Pearson r	CCC	RMSE (ml/min/g)	RMSD (ml/min/g)
Volume scan mode						
Global (n = 9)	1.03 (0.78, 1.29)	-0.82 (-3.73, 2.09)	0.96 (0.87, 0.99)	0.95 (0.84, 0.99)	1.04	1.56
Regional Overall (n = 54)	0.92 (0.82, 1.03)	0.74 (-0.62, 2.10)	0.93 (0.76, 0.98)	0.93 (0.75, 0.98)	1.91	1.87
Helical scan mode						
Global (n = 11)	0.93 (0.78, 1.09)	1.07 (-0.17, 2.31)	0.98 (0.92 ,0.99)	0.96 (0.88, 0.99)	1.00	0.75
Regional Overall (n = 66)	1.11 (1.02, 1.21)	0.11 (-0.64, 0.86)	0.95 (0.39, 1.00)	0.92 (0.18, 0.99)	1.78	1.50

Note.—Data in parentheses are 95% confidence intervals. CCC: concordance correlation coefficient, RMSD: root-mean-square deviation.
* Denotes prospective perfusion regression parameters that are significantly different from the retrospective perfusion regression parameters, as indicated by non-overlap of each 95% confidence interval, respectively.

Regional Perfusion: Similarly, all mean perfusion values were compared between two prospective measurements on a lobar basis. For the volume scan mode, all lobes had p values greater than 0.05, suggesting insignificant differences between the two prospective measurements. For the helical scan mode, most of the lobes had insignificant differences from each other, except for the LLL and RLL (**Table 6.3**). The AL had a noticeably higher RMSE than all other lobar segments for both volume scan and helical scan prospective measurements (**Table 6.3**). Overall, good correlations were found between the two prospective measurements with less bias and variations as compared with the reference standard measurements (**Figure 6.7, Table 6.4**). The comparisons of the RMSE, RMSD and other regression parameters from all different lobes and whole lung are summarized in **Figure 6.8, Table 6.5, and Table 6.6**.

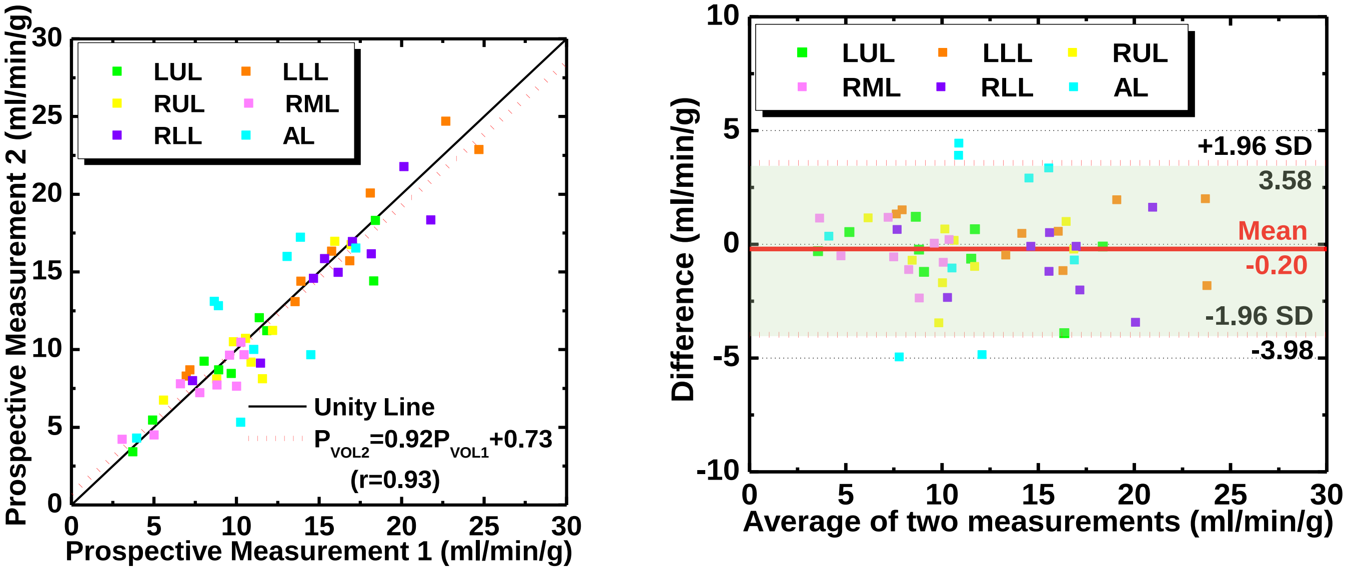

Helical scan mode

c)

d)

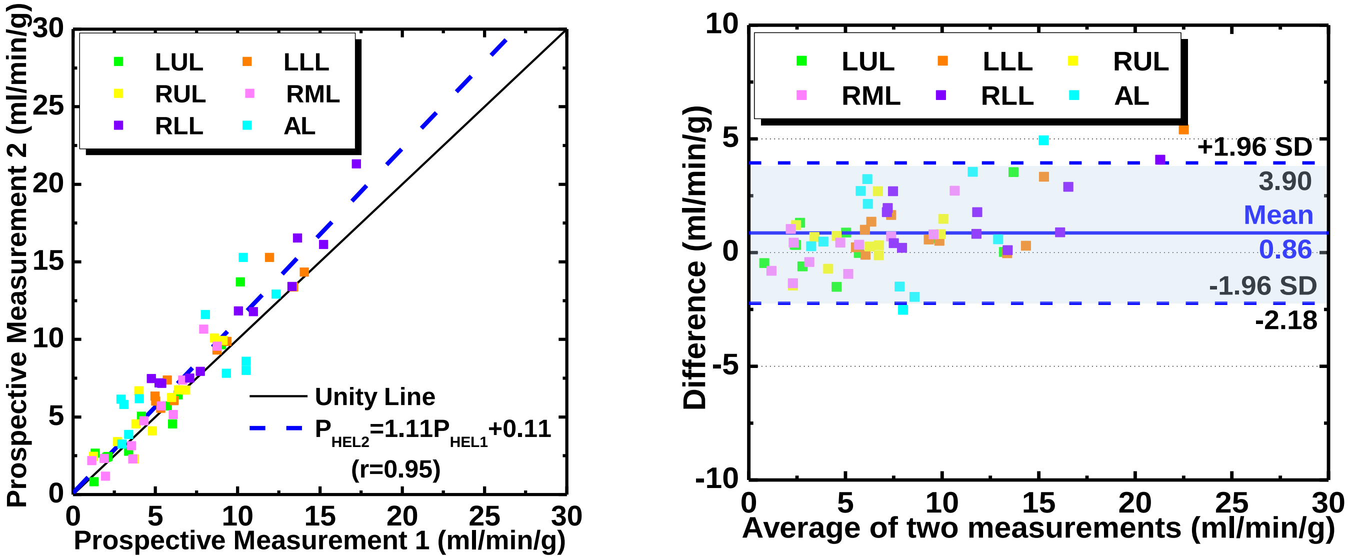

Figure 6.7 The reproducibility of the regional perfusion measurement using linear regression and Bland-Altman analysis.

The regional perfuison measurements were compared between the two prospective measurements using two scan modes. a) b) Volume scan mode, c) d) Helical scan mode.

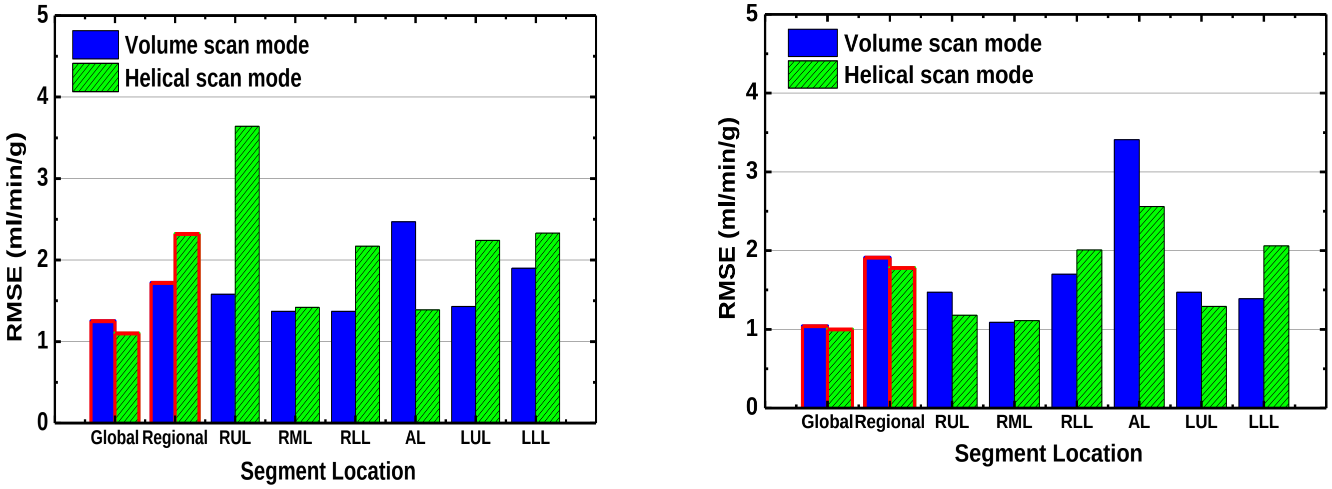

Figure 6.8 Comparisons of the RMSE of global and regional perfusion measurements.

Table 6.5 Evaluation of linear regression parameters for regional perfusion accuracy. Prospective perfusion measurement versus reference perfusion measurement.

	Slope	Intercept	Pearson r	CCC	RMSE (ml/min/g)	RMSD (ml/min/g)
			Volume Scan Mode			
Right Upper Lobe	1.03 (0.76, 1.30)	0.18 (-2.65, 3.00)	0.92 (0.79, 0.97)	0.89 (0.72, 0.96)	1.51	1.44
Right Middle Lobe	0.94 (0.62, 1.26)	-0.16 (-2.80, 2.47)	0.87 (0.68, 0.95)	0.85 (0.64, 0.94)	1.37	1.20
Right Caudal Lobe	0.98 (0.81, 1.16)	-0.10 (-2.84, 2.64)	0.96 (0.89, 0.98)	0.96 (0.89, 0.98)	1.37	1.20
Accessory Lobe	1.21 (0.74, 1.69)	-1.92 (-6.93, 3.09)	0.84 (0.61, 0.94)	0.78 (0.50, 0.92)	2.47	2.37
Left Upper Lobe	1.18 (0.99, 1.37)	-1.27 (-3.17, 0.62)	0.97 (0.91, 0.99)	0.92 (0.81, 0.97)	1.43	1.19
Left Caudal Lobe	1.03 (0.82, 1.24)	-0.24 (-3.49, 3.02)	0.95 (0.86, 0.98)	0.93 (0.82, 0.97)	1.90	1.88
			Helical Scan Mode			
Right Upper Lobe	0.61 (0.39, 0.84)	0.70 (-1.72, 3.12)	0.90 (0.70, 0.97)	0.50 (-0.04, 0.81)	3.64	0.98
Right Middle Lobe	0.99 (0.59, 1.40)	-0.64 (-3.79, 2.50)	0.88 (0.66, 0.96)	0.85 (0.58, 0.95)	1.42	1.25
Right Caudal Lobe	0.94 (0.57, 1.32)	0.19 (-5.28, 5.65)	0.89 (0.67, 0.96)	0.87 (0.63, 0.96)	2.17	2.07
Accessory Lobe	0.97 (0.66, 1.27)	0.05 (-3.21, 3.31)	0.92 (0.77, 0.98)	0.91 (0.75, 0.97)	1.39	0.27
Left Upper Lobe	0.86 (0.60, 1.12)	-0.54 (-3.01, 1.94)	0.93 (0.78, 0.98)	0.84 (0.56, 0.95)	2.24	1.23

Left Caudal Lobe	0.86 (0.56, 1.17)	0.88 (-3.53, 5.29)	0.91 (0.72, 0.97)	0.88 (0.66, 0.96)	2.33	1.98

Note.—Data in parentheses are 95% confidence intervals. CCC: concordance correlation coefficient, RMSD: root-mean-square deviation, RMSE: root-mean-square error.
* Denotes prospective perfusion regression parameters that are significantly different from the retrospective perfusion regression parameters, as indicated by non-overlap of each 95% confidence interval, respectively.

Table 6.6 Evaluation of linear regression parameters for regional perfusion precision. Prospective perfusion measurement 1 versus prospective perfusion measurement 2.

	Slope	Intercept	Pearson r	CCC	RMSE (ml/min/g)	RMSD (ml/min/g)
Volume Scan Mode						
Right Upper Lobe	0.96 (0.59, 1.34)	-0.05 (-4.52, 4.42)	0.92 (0.72, 0.98)	0.91 (0.70, 0.97)	1.46	1.38
Right Middle Lobe	0.76 (0.44, 1.08)	1.60 (-1.06, 4.26)	0.91 (0.69, 0.97)	0.88 (0.63, 0.97)	1.09	0.87
Right Caudal Lobe	0.91 (0.58, 1.23)	0.75 (-4.54, 6.04)	0.93 (0.76, 0.98)	0.92 (0.72, 0.98)	1.70	1.50
Accessory Lobe	0.80 (0.00, 1.60)	2.59 (-6.90, 12.09)	0.67 (0.15, 0.90)	0.65 (0.13, 0.89)	3.41	3.31
Left Upper Lobe	0.84 (0.63, 1.06)	1.24 (-1.27, 3.74)	0.96 (0.86, 0.99)	0.95 (0.82, 0.99)	1.47	1.19
Left Caudal Lobe	0.92 (0.73, 1.11)	1.68 (-1.48, 4.85)	0.97 (0.91, 0.99)	0.97 (0.89, 0.99)	1.39	1.22
Helical Scan Mode						
Right Upper Lobe	1.00 (0.66, 1.35)	0.51 (-1.44, 2.47)	0.91 (0.74, 0.97)	0.89 (0.68, 0.96)	1.18	1.05
Right Middle Lobe	1.18 (0.87, 1.49)	-0.57 (-2.20, 1.06)	0.94 (0.83, 0.98)	0.92 (0.75, 0.97)	1.11	0.99
Right Caudal Lobe	1.06 (0.85, 1.28)	0.98 (-1.34, 3.30)	0.97 (0.89, 0.99)	0.91 (0.72, 0.97)	2.00	1.17
Accessory Lobe	0.79 (0.33, 1.26)	2.55 (-1.11, 6.21)	0.79 (0.45, 0.93)	0.76 (0.38, 0.92)	2.56	2.20
Left Upper Lobe	1.17 (0.88, 1.46)	-0.39 (-2.01, 1.23)	0.95 (0.84, 0.98)	0.92 (0.77, 0.98)	1.29	1.13
Left Caudal Lobe	1.20 (0.94, 1.45)	-0.53 (-3.13, 2.06)	0.96 (0.88, 0.99)	0.91 (0.73, 0.97)	2.06	1.39

Note.—Data in parentheses are 95% confidence intervals. CCC: concordance correlation coefficient, RMSD: root-mean-square deviation, RMSE: root-mean-square error.
* Denotes prospective perfusion regression parameters that are significantly different from the retrospective perfusion regression parameters, as indicated by non-overlap of each 95% confidence interval, respectively.

Dose Estimation

The average scan length of the helical scan was 23.6 cm. The average CT dose index (CTDI) for the retrospective, prospective, and helical scan was 184.8, 9.3, and 4.8 mGy, respectively. The effective dose for the retrospective, prospective, and helical scan was calculated to be 53.8, 2.7, and 2.1 mSv, respectively. A detailed summary of the dose estimations and scan parameters can be found in **Table 6.7**.

Table 6.7 Scan parameter and dose estimation of the retrospective and prospective perfusion measurement.

	RETRO	**VOLUME**			**HELICAL**		
	Volume scans (n = 20)	V1 (n =1)	V2 (n =1)	V1+V2	V1 (n =1)	V2 (n =1)	V1+V2
Scan parameters							
Tube current (mA)	300	90	300	N/A	50	200	N/A
Tube voltage (kV)	100						
Detector collimation (mm)	320 × 0.5	320 × 0.5			64 × 0.5		
Dimension Measurements							
AP (cm)	24.2±1.0						
LAT (cm)	30.8±1.3						
Effective Diameter(cm)	27.3±0.8						
Z-length (cm)	16				23.64±1.35		
Dose Estimation							
CTDI (mGy)	184.8	2.1±0.2	7.2±0.2	9.3 ± 0.4	0.7±0.02	4.1±1.3	4.8 ± 1.3
SSDE (mGy)	240.0	2.71	9.4	12.01	0.91	5.4	6.3
DLP (mGy·cm)	3843.7	192.9			148.3		
Effective Dose (mSv)	53.8	2.7			2.1		

Note: AP = Anterior-Posterior, LAT = Lateral.

1. Effective diameter (ED) $ED = \sqrt{AP \times LAT}$
2. Size Specific Dose Estimate (SSDE): $SSDE = CTDI_{VOL}^{32} \times f_{size}^{32}$ where f_{size}^{32} is a value derived from the measured effective diameter for a 32cm phantom. In this case, the f_{size}^{32} was equal to 1.3.
3. Effective Dose $= DLP \times k$, where k is a coefficient derived for an adult. In this case, k = 0.014.

Discussion

The prospective two-volume, whole-lung CT perfusion technique using both volume and helical scan modes were validated against the reference standard retrospective perfusion measurements. The results suggest that both global and regional lobar perfusions were in good agreement with the corresponding reference standard measurements using both scan modes. For regional lobar perfusion analyses, near unity regression slopes and negligible biases were measured using the volume scan mode, while a slight underestimation was observed using the helical scan mode. Overall, the regional perfusion values distributed in a wide range from 0 to 30 ml/min/g, with an average root-mean-square error of 1.72 ml/min/g and 2.32 ml/min/g, using the volume and helical scan mode, respectively. Additionally, linear regression and agreement analysis results of the two prospective measurements indicate satisfying reproducibility of the two-volume prospective perfusion technique using both scan modes, with good correlation, negligible bias, and relatively small RMSE and RMSD. More importantly, the results of prospective helical scan measurements indicate that the accurate dynamic whole-lung perfusion measurement is feasible with the first-pass analysis technique using only two CT images. Lastly, the radiation dose of the prospective perfusion measurement using helical scan is as low as 2-3 mSv, which ultimately enables the clinical application of the whole-lung perfusion technique for the assessment of pulmonary disease.

Previous studies have used subtraction CT between the unenhanced and enhanced CT scan to show the iodine distribution for the detection of suspected PE (90,161,162). As there is no temporal information, the iodine map can only reflect the Hounsfield unit (HU) density differences in the lung parenchyma between the two scans, which lacks physiological information in terms of blood flow or perfusion. A first-pass kinetic model in conjunction with the temporal iodine concentration change estimation is required to provide perfusion measurement. Our two-volume, prospective CT perfusion technique minimized the number of volume scans required in a dynamic CT perfusion measurement to two scans and maximized the size of the perfusion compartment to encompass the entire lung parenchyma, as acquired by a fast helical scan. The expansion of the compartment size guarantees the most accurate and robust perfusion measurement as the iodine accumulation is calculated by integrating the change of HU in the entire lung as the compartment (163). Given that the contrast transit time within the entire lung is approximately five seconds, blood flow measurement can be completed before contrast starts to exit the compartment. Specifically, the first time point is determined by bolus-tracking on the atrial input vessel as an indication of contrast delivery; while the second time point is determined when the maximal enhancement reaches in arterial input vessel as an implication of contrast leaving. Such time-to-peak delay has been empirically related to the contrast injection duration and the fixed dispersion time in previous studies, demonstrating accurate and reliable time prediction over a wide range of body weights and cardiac outputs (80). Therefore, with the optimal timing protocol, the dynamic, whole-lung CT perfusion measurement is feasible with a first-pass analysis technique using only two helical scans.

Although satisfactory correlation and statistical bias were found in the global perfusion measurements, it is noticeable that the measurement variance increased in the lobar regional perfusion measurements. Potential contributors may lead to the measurement errors. First of all, blood flow fluctuations in the animals between paired acquisitions may still exist, albeit tight controls on ventilation, anesthesia, and hemodynamics monitoring. Second, motion artifacts may occur during the perfusion scan. Also, the two helical scans may be acquired in different cardiac phases due to the lack of electrocardiogram synchronization. In fact, a minimum of a 30-second breath-hold is usually required by the multi-volume dynamic scans (33–35,57,59–61), while the actual breath-hold time for the prospective two-volume scan is from the bolus-tracking triggering time to the second volume acquisition time. Generally, such delay lasts less than 10 seconds, which adequately prevents respiratory mis-registration and makes the technique more acceptable to patients with severe pulmonary diseases. In addition, the acquisition time of the peak enhancement volume scan is essential to the measurement accuracy. Therefore, the acquisition time after to the peak time may lead to underestimation, while prior to the peak time may suffer from inadequate contrast signal. As limited by the temporal resolution, the helical scan time is 2-3 seconds, which has to start before the peak and continue past the peak. As such, with the use of trigger-to-peak time (the scan time of the middle slice) in normalization, the HU change ($\Delta M/\Delta t$) from the early scanned slices is lower than it should be, which may explain the systematic underestimation bias from the helical scan mode, especially in the upper lobes as observed from the regional perfusion analyses. Finally, beam hardening artifacts due to contrast inflow are severe, particularly for the lobes adjacent to the heart and large vessels, resulting in increased error in the accessory, right and left middle lobes.

Other limitations are as follows. First, a small number of animals were used in this study. While multiple independent perfusion measurements were performed on each swine under various hemodynamic conditions, additional studies on a larger number of animals remain necessary. Second, the average animal weight is not equivalent to standard patient size. Although body-weight-adjusted contrast volume and time-to-peak delay were calculated in each experiment, automatic tube voltage and tube current modulation depending on patient BMIs should be used for a more optimal scan protocol. Third, the retrospective CT perfusion technique that served as the reference standard in the quantitative assessment may also be hampered by some inherent limitations of CT technique itself, such as the beam hardening artifacts, motion artifacts, etc. Fortunately, the retrospective FPA perfusion technique has been validated against fluorescent microsphere perfusion measurements with blood sample withdrawal and demonstrated high accuracy and precision (93). Nevertheless, further comparative studies with other perfusion imaging modalities may still be necessary as a follow up. Lastly, the two-volume prospective perfusion technique needs to be validated and assessed in patients with various cardiopulmonary conditions such as acute pulmonary embolism, pulmonary hypertension, as well as airway obstruction diseases.

Conclusion

The prospective two-volume, whole-lung CT perfusion technique was validated as compared with the reference standard perfusion measurements with two scan models. The results indicate that an accurate and reproducible dynamic whole-lung perfusion measurement is feasible with only two helical scans. Such prospective perfusion technique with helical scan mode ultimately enables a low-dose, whole-lung dynamic perfusion technique in the assessment of pulmonary disease.

Chapter 7 Quantification of Airway Dimensions using a High-Resolution Computed Tomography Scanner

Abstract

Small airways with inner diameters less than 2 mm are sites of major airflow limitations in patients with chronic obstructive pulmonary disease (COPD) and asthma. The purpose of this chapter is to investigate the limitations for accurate assessment of small airway dimensions using both high-resolution CT (HRCT) and conventional normal-resolution CT at low dose levels. To model the normal human airways from the 3rd to 20th generations, a cylindrical polyurethane phantom with 14 airway tubes of inner diameters (ID) ranging from 0.3 to 3.4 mm and wall thicknesses (WT) ranging from 0.15 to 1.6 mm was placed within an Anthropomorphic QRM-Thorax phantom. The Aquilion Precision (Canon Medical Systems Corporation) HRCT scanner was used to acquire images at 80, 100 and 120 kV using high resolution mode (HR, 0.25 mm x 160 detector configuration) and normal resolution mode (NR, 0.5 mm x 80 detector configuration). The HR data were reconstructed using 1024 x 1024 matrix (0.22 x 0.22 x 0.25 mm voxel size) and the NR data were reconstructed using a 512 x 512 matrix (0.43 x 0.43 x 0.50 mm). Two reconstruction algorithms (filtered back projection; FBP and an adaptive iterative dose reduction 3D algorithm; AIDR 3D) and three reconstruction kernels (FC30, FC52 and FC56) were investigated. The $CTDI_{vol}$ dose values ranged from 0.2 to 6.2 mGy. A refined automated full-width half-maximum (FWHM) method was used for the measurement of airway dimensions, where the density profiles were computed by radial oversampling using a polar coordinate system. Both ID and WT were compared to the known dimensions using a regression model, and the root-mean-squared-error (RMSE) and average error were computed across all 14 airway tubes. The results indicate that the ID can be measured within a 15% error down to approximately 0.8 mm and 2.0

mm using the HR and NR modes, respectively. The overall RMSE (and average error) of ID measurements for HR and NR were 0.10 mm (-0.70%) and 0.31 mm (-2.63%), respectively. The RMSE (and average error) of WT measurements using HR and NR were 0.10 mm (23.27%) and 0.27 mm (53.56%), respectively. The WT measurement using HR yielded a factor of two improvement in accuracy as compared to NR. In conclusion, high-resolution CT can provide more accurate measurements of airway dimensions as compared with normal resolution CT, potentially improving quantitative assessment of pathologies such as COPD and asthma. The high-resolution mode acquired and reconstructed with AIDR3D and the FC52 kernel provides most accurate measurement of airway dimensions. Low-dose high resolution measurements at dose level above 0.9 mGy can provide improved accuracy on both inner diameters and wall thicknesses compared to full dose normal resolution airway phantom measurements.

Introduction

Alteration of airway function is associated with airflow obstruction and inflammation in patients with chronic obstructive pulmonary disease (COPD) and asthma (164–169). Advanced computed tomography (CT) techniques have enabled noninvasive quantitative structural measurements of airway dimensions in the clinical settings for improving management of airway diseases (170–173). The CT-based quantification of airway in the segmental and sub-segmental airways have allowed better evaluation of the relationship between lumen narrowing and airflow impairment (164,166).

Despite accurate CT assessments of larger airways with thicker walls, the cross-sectional pathological features in small airways with internal diameters of less than 2 mm have shown to be more critical to airway function (172,174–177). Due to the spatial resolution limitations of CT techniques in the clinical setting, partial volume effects reduce measurement accuracy for both lumen diameters and wall thicknesses (175). Hence, the assessment of small airway dimensions up to the 6th generation (~2.5 mm in inner diameter) or higher generations remains challenging (164,178). Previous investigators have used paired inspiratory and expiratory CT lung scans as imaging biomarkers to allow for the assessment of functional small airways functions in patient with COPD (179). However, motion artifacts are the major limitation of the subtraction technique when applied with a voxel-by-voxel basis image co-registration method. Hence, an accurate, direct, and noninvasive approach to quantify small airway functions is absolutely needed.

A recently introduced clinical high-resolution CT (HRCT) scanner, the Aquilion Precision (Canon Medical Systems Corporation, Otawara, Japan), has approximately two times higher spatial resolution than normal resolution CT(180), enabling better visualization of small airway structures with clear details (181). The purpose of this study is to investigate the improvement of small airway assessment using the high-resolution (HR) mode (0.25 mm × 0.25 mm detector element size in the detector channel and row directions) and compare it with the normal resolution (NR) mode (0.5 mm × 0.5 mm). The central hypothesis of this study is that the HR mode produces more accurate measurements of the airway dimensions including both inner lumen diameter (ID) and the wall thickness (WT) than the NR mode, using the known tube sizes as the ground truth. The influence of various acquisition and reconstruction parameters were also evaluated to determine the optimal CT parameters for accurate measurement of airway dimensions.

MATERIALS AND METHODS

Airway Phantom

A 10 cm diameter cylinder composed of polyurethane foam mimicking the lung parenchyma was placed within an anthropomorphic chest phantom (QRM-Thorax phantom, Moehrendorf, Germany) as shown in **Figure 7.1**. The anthropomorphic phantom (300 mm x 200 mm x 100 mm; bore hole diameter 100mm) is used to simulate human tissues based on the density and X-ray attenuation characteristics of a human thorax. Fourteen silicone tubing (5 cm in length) of various sizes were embedded in the QRM-Thorax phantom. The tubing inner diameters (ID) ranged from 0.3 to 3.4 mm and the wall thickness (WT) ranged from 0.15 to 1.6 mm within 10% tolerance (Tubing T2001-T2014, Qosina, Ronkonkoma, NY, USA, **Figure 7.2**). This specific range of tube dimensions was chosen to mimic the human airway from the 3rd to the 20th generations of branching (178,182).

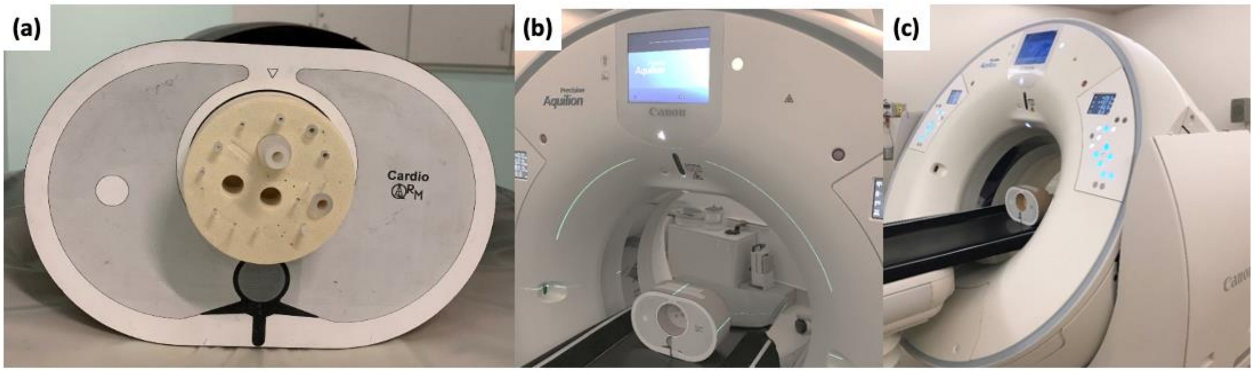

Figure 7.1 The phantom study experimental setup.

a) QRM-Thorax phantom with the embedded polyurethane foam cylinder with 14 airway tubes. b) The chest phantom placed perpendicularly to the scan slices. c) The chest phantom placed obliquely at a 30-degree gantry tilt angle to the scan slices.

Tube No.	T2001	T2002	T2003	T2004	T2005	T2006	T2007	T2008	T2009	T2010	T2011	T2012	T2013	T2014
ID (mm)	0.3	0.5	0.6	0.8	0.8	1	1.5	1.6	1.6	1.6	2	2.6	3.2	3.4
WT (mm)	0.15	0.2	0.3	0.45	1.58	0.6	0.25	0.4	0.8	1.6	0.6	1.15	1.6	0.6

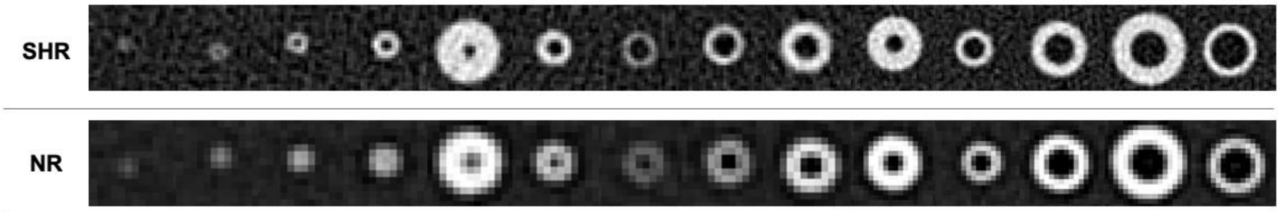

Figure 7.2 Comparisons of images of 14 airway tubes using super high-resolution (HR) and normal-resolution (NR) acquisitions on the Precision CT scanner.

Images were acquired at 6.2 mGy (120 kV, 91 mAs) and reconstructed with filter back projection using FC30 kernel. Window/Level: -300/1700 HU.

Phantom Imaging

The QRM-Thorax phantom with embedded airway phantoms were imaged on the Aquilion Precision HRCT scanner (Canon Medical Systems Corporation, Otawara, Japan). The center of the cylindrical phantom was placed at the isocenter of the scanner and separate scans were acquired with no gantry tilt and with a 30-degree gantry tilt angle as shown in **Figures 7.1b** and **7.1c**, respectively. Axial scans were acquired using both normal resolution “NR” mode (0.5 mm x 0.5 mm detector element sizes in the channel and row directions) and high resolution “HR” mode (0.25 mm x 0.25 mm). A 4 cm collimation width was used for both acquisitions (0.5 mm x 80 for NR; 0.25 mm x 160 for HR) with a 4 cm scan length (i.e. one table position). All acquisitions utilized the smallest focal spot size available on the system (0.4 mm x 0.5 mm) and a tube rotation time of 0.35 seconds. Scans were acquired at three tube potentials (80, 100, and 120 kV) and five CTDI_{vol} values for both HR and NR modes (6.2, 1.2, 0.9, 0.6 and 0.2 mGy). The combination of scan and reconstruction parameters are detailed in **Table 7.1**.

Table 7.1 Combinations of scan and reconstruction parameters.

Scan parameters

Scan mode	Tilt angle (degree)	Tube potential (kV)	Dose Level (mGy)				
HR	0	80		1.2	0.9	0.6	0.2
		100		1.2	0.9	0.6	0.2
		120	6.2	1.2	0.9	0.6	0.2
	30	120	6.2				
NR	0	80		1.2	0.9	0.6	0.2
		100		1.2	0.9	0.6	0.2
		120	6.2	1.2	0.9	0.6	0.2

Reconstruction parameters

Reconstruction algorithm	Reconstruction kernel
AIDR 3D	FC30
	FC52
	FC56
FBP	FC30
	FC52
	FC56

Note.— HR: High-resolution mode; NR: Normal-resolution mode. AIDR 3D: adaptive iterative dose reduction 3D algorithm; FBP: filtered back projection.

The HR data was reconstructed using 1024 x 1024 matrix (0.22 x 0.22 x 0.25 mm voxel size, 220 mm reconstructed field-of-view) and the NR data was reconstructed using a 512 x 512 matrix (0.43 x 0.43 x 0.50 mm, 220 mm reconstructed field-of-view). Two reconstruction algorithms (filtered back projection; FBP and an adaptive iterative dose reduction 3D algorithm; AIDR 3D) and three different reconstruction kernels (FC30, FC52 and FC56) were used for both scan modes.

Airway Measurements

For image pre-processing, commercial software (ViTAL Images, Lung CT, Pulmonary Analysis Workflow; Canon Medical Systems) was used for the semi-automatic segmentation of each airway phantom tube placed within the QRM-Thorax phantom. A 3D region-based vessel segmentation tool was first used by placing a seed point within the tube and growing to the neighboring pixels, followed by a manual correction of the segmentation.

Airway measurements were then obtained using in-house software developed in MATLAB® (R2019a; MathWorks Inc.). The image analysis was performed using the following six-step procedure (**Figure 7.3**):

1. Compute the centerline of each tube segment using a 3-D skeletonization algorithm (183), which constructs the skeleton model by 3-D digital filtering and thinning operations.
2. Perform a 3D curved planer reformation (CPR) on each tube segment along the centerline to generate longitudinal cross-sectional images perpendicular to the centerline.
3. Up-sample each cross-sectional image by a factor of ten using a linear bi-cubic interpolation algorithm (178,184) and convert the cartesian coordinates (x, y) to their polar coordinates equivalent (r, θ) (185,186).
4. Generate radial bins in the circumferential direction by sorting the pixels into equally spaced bins (radial bin size: 3 times the cross-sectional image pixel size) along theta ($\theta \epsilon [0, 2\pi]$, angular bin size: 0.1 rad, 62 bins) and average the values of each bin to generate the density profile along each theta.

5. Measure the ID and wall WT using the standard full-width half-maximum (FWHM) method by analyzing each of 62 density profiles and averaging the ID and WT measurements from all the profiles (178,184).
6. The final ID and WT dimensions were calculated by averaging the measurements from six axial images (HR: 0.25 mm × 6; NR: 0.5 mm × 6) along the z-axis.

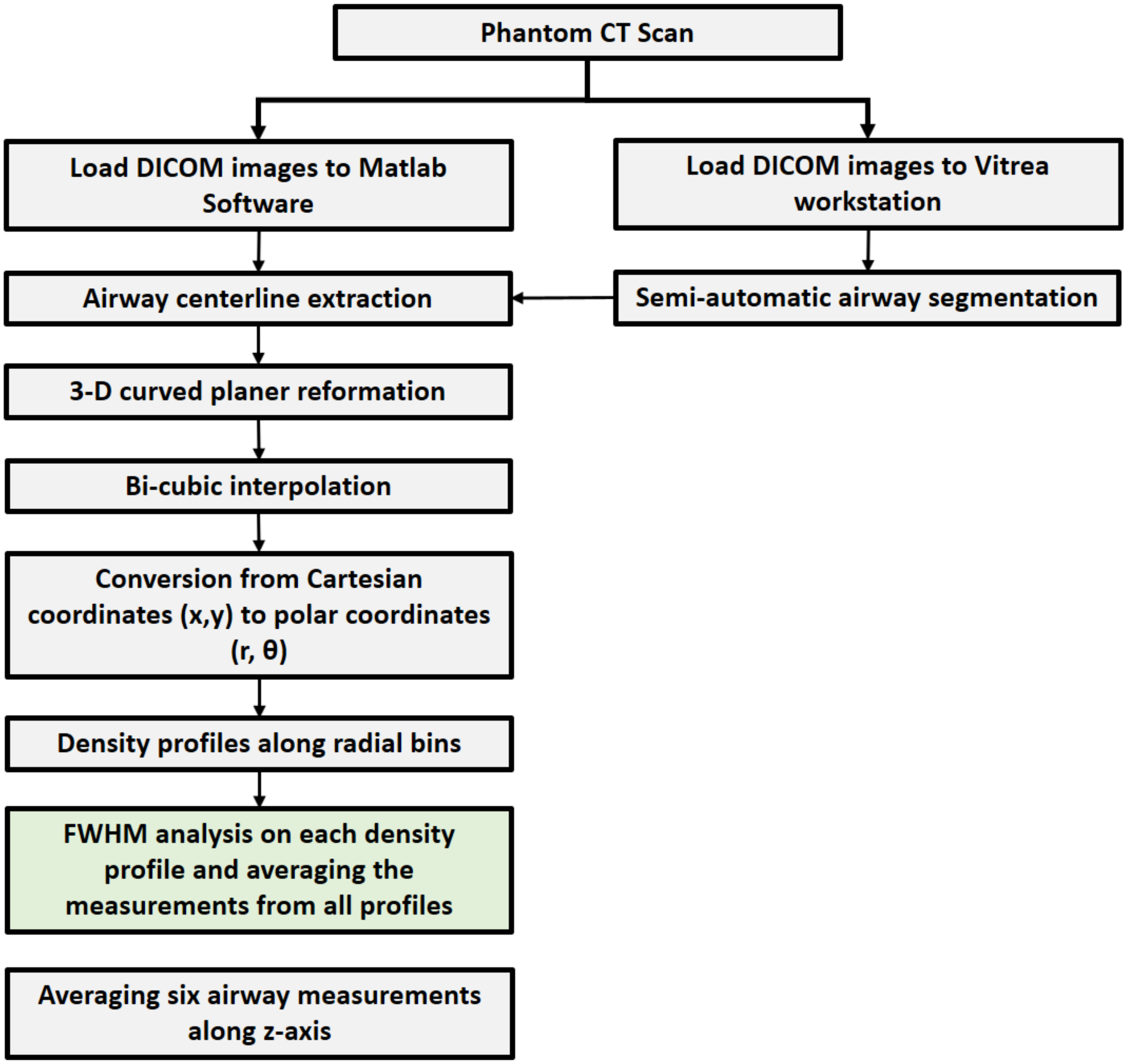

Figure 7.3 Schematic workflow diagram for the full-width half-maximum (FWHM) measurement approach.

Statistical Analysis

The mean and standard deviation (SD) of the ID and WT were calculated across six contiguous cross-sectional images centered at each tube along z-axis. The coefficient of variation (CV) was also calculated as the ratio of the mean and SD ($CV = \frac{SD}{Mean} \times 100\%$). To determine the effects of CT parameters on the airway dimension measurement, the error was calculated as the relative difference between the CT measurement size and the known tube size ($Error = \frac{(CT\_Measurement) - Actual}{Actual} \times 100\%$). The CT measurements were also compared with the known sizes using Mann Whitney U test (SPSS, version 22, IBM, Armonk, NY). Finally, the CT measurements were quantitatively compared to the known dimensions through regression, Bland-Altman, root-mean-square-error (RMSE) and root-mean-square-deviation (RMSD).

RESULTS

Overall Performance Evaluation

For CT images acquired by the HR mode at 120kV, 6.2 mGy, the mean CT value of the polyurethane foam and the silicone tube were -918 HU and 301 HU, respectively.

The ID and WT were evaluated for each of the airway phantoms using two scan modes and compared with the known phantom dimensions. **Figure 7.2** shows the phantom tube images acquired in NR and HR modes at a $\mathrm{CTDI}_{\mathrm{vol}}$ of 6.2 mGy and reconstructed with FBP using the FC30 kernel. For tubes with ID < 1.0 mm and WT < 0.5 mm, the airways within the airway tubes are not visible in NR mode, but can be clearly visualized in HR mode except for ID of 0.3 mm.

Performance metrics of the airway phantom dimensions determined from the CT images are shown in **Figure 7.4**. The mean, standard deviation, and error of each airway phantoms are summarized in **Table 7.2**. For ID measurements, the overall RMSE (mean error %) for HR and

NR were 0.10 mm (-0.70 %) and 0.31 mm (-2.63%), respectively. Larger errors were found using the NR mode when IDs were less than 2 mm (**Figure 7.4a, 7.4b**). For WT measurements, the HR measurements were related to the known measurements by W_{HR} = 0.86W_K + 0.16 (Pearson correlation coefficient, *r* = 1.00), with a RMSE of 0.10 mm, a RMSD of 0.05 mm and a mean error of 23.17%. NR WT measurements were related to the known measurements by W_{NR} = 0.68W_K + 0.35 (r=0.88), with a RMSE of 0.27 mm, a RMSD of 0.19 mm and a mean error of 52.56% (**Figure 7.4c, 7.4d**). Significant differences were found between the NR measured WT and the known WT (*p* = 0.03), while differences between the HR measured WT and the known WT were just outside our criterion for significance (*p* = 0.06). The detailed linear regression parameters, 95% intervals, RMSE, RMSD are listed in **Table 7.3**. The WT measurement using HR mode yielded a factor of two improvements in the accuracy (RMSE, RMSD and mean error) as compared to NR mode.

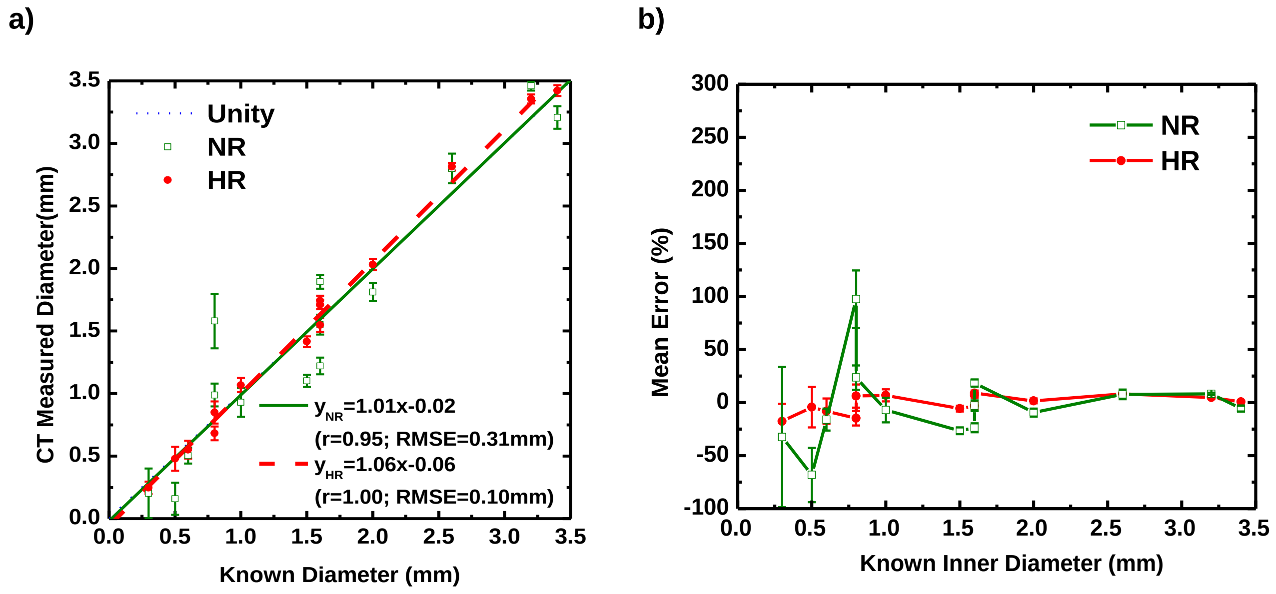

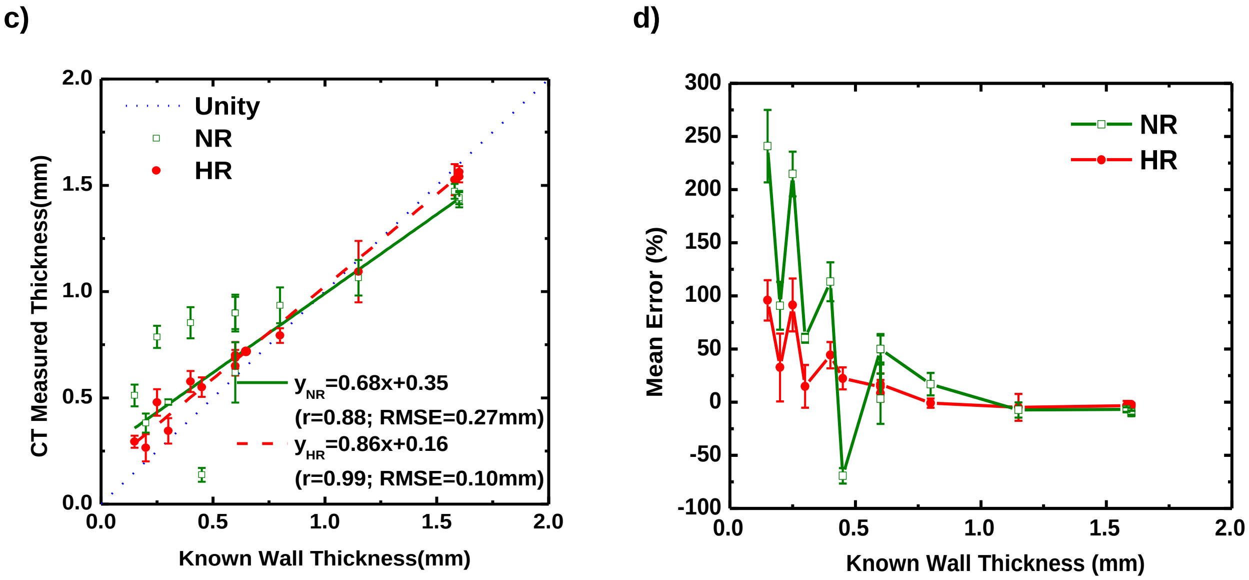

Figure 7.4 Linear regression and error results comparing high-resolution (HR) and normal-resolution (NR) scan modes.

(a,c): Inner diameter measurement; (b,d): Wall thickness measurement. The data shown in the graph were acquired at 120 kV, 260 mA, 6.2 mGy for each scan mode and reconstructed with all reconstruction methods and kernels. RMSE: Root mean square error.

Table 7.2 Comparisons of CT measured tube dimension using HR and NR modes.

ID: Inner diameter (mm)			
Tube No.	**Ref**	**HR mode**	**NR mode**
		Mean ± SD (%)	**Mean ± SD (%)**
T2001	**0.30**	0.25 ± 0.05 (-17.75)	0.20 ± 0.20 (-32.45)
T2002	**0.50**	0.48 ± 0.10 (-4.33)	0.16 ± 0.13 (-68.22)
T2003	**0.60**	0.55 ± 0.07 (-8.14)	0.50 ± 0.06 (-16.03)
T2004	**0.80**	0.68 ± 0.05 (-14.73)	1.58 ± 0.21 (97.44)
T2005	**0.80**	0.85 ± 0.09 (6.09)	0.99 ± 0.09 (23.53)
T2006	**1.00**	1.07 ± 0.06 (6.76)	0.92 ± 0.12 (-7.03)
T2007	**1.50**	1.42 ± 0.04 (-5.65)	1.10 ± 0.05 (-26.55)
T2008	**1.60**	1.55 ± 0.05 (-3.21)	1.22 ± 0.07 (-23.69)
T2009	**1.60**	1.71 ± 0.04 (6.86)	1.55 ± 0.08 (-3.03)
T2010	**1.60**	1.74 ± 0.04 (8.96)	1.89 ± 0.05 (18.38)
T2011	**2.00**	2.03 ± 0.05 (1.60)	1.81 ± 0.07 (-9.39)
T2012	**2.60**	2.81 ± 0.03 (8.21)	2.80 ± 0.12 (7.67)
T2013	**3.20**	3.36 ± 0.04 (4.86)	3.45 ± 0.04 (8.12)
T2014	**3.40**	3.42 ± 0.04 (0.64)	3.20 ± 0.09 (-5.65)
WT: Wall thickness (mm)			
T2001	**0.15**	0.29 ± 0.03 (95.80)	0.51 ± 0.05 (240.91)
T2002	**0.20**	0.27 ± 0.06 (32.65)	0.38 ± 0.04 (90.70)
T2007	**0.25**	0.48 ± 0.06 (91.42)	0.79 ± 0.05 (214.75)

T2003	**0.30**	0.34 ± 0.06 (14.88)	0.48 ± 0.01 (60.18)
T2008	**0.40**	0.58 ± 0.05 (44.21)	0.85 ± 0.07 (113.36)
T2004	**0.45**	0.55 ± 0.04 (22.34)	0.13 ± 0.03 (-69.30)
T2006	**0.60**	0.65 ± 0.05 (8.31)	0.62 ± 0.14 (3.24)
T2011	**0.60**	0.70 ± 0.06 (16.75)	0.90 ± 0.08 (49.95)
T2014	**0.60**	0.69 ± 0.04 (14.56)	0.90 ± 0.09 (49.81)
T2009	**0.80**	0.79 ± 0.03 (-0.86)	0.94 ± 0.08 (16.91)
T2012	**1.15**	1.09 ± 0.14 (-4.88)	1.07 ± 0.08 (-7.38)
T2005	**1.58**	1.53 ± 0.07 (-3.41)	1.47 ± 0.03 (-6.87)
T2010	**1.60**	1.56 ± 0.03 (-2.33)	1.43 ± 0.04 (-10.51)
T2013	**1.60**	1.54 ± 0.03 (-3.69)	1.44 ± 0.03 (-9.87)
Note.— The reference inner diameter and wall thickness (Ref) were listed in the manufacturer's manual. Images included were acquired at 260 mA, 120 kV, 91 mAs, 6.2 mGy CTDI$_{vol}$ and reconstructed with all reconstruction methods and kernels.			

Table 7.3 Linear regression parameters of CT measured airway dimensions using HR and NR modes.

Scan modes	**HR mode**		**NR mode**	
	ID [95% CI]	**WT [95% CI]**	**ID [95% CI]**	**WT [95% CI]**
Slope	1.06 [1.04, 1.07]	0.86 [0.84, 0.88]	1.01 [0.93,1.00]	0.68 [0.59, 0.76]
Intercept (mm)	-0.06 [-0.09, -0.03]	0.16 [0.14, 0.18]	-0.02 [0.16,0.1]	0.35 [0.28, 0.43]
Pearson’s r	1.00	0.99	0.95	0.87
Error (%)	-0.70	23.27	12.87	52.56
RMSE (mm)	0.10	0.10	0.31	0.27
RMSD (mm)	0.08	0.05	0.31	0.19
P-value	0.85	0.06	0.85	**0.03***

Note.— WT: wall thickness; ID: Inner diameter CI: Confidence Interval. p-value less than 0.05 indicates significant difference. Images included were acquired at 260 mA, 120 kV, 91mAs, 6.2 mGy.
The linear regression form: $\boldsymbol{Y_{measure}} = \boldsymbol{a} + \boldsymbol{bX_{true}}$, where the CT measured ID and WT (dependent variables) are related to the true ID and WT (explanatory variable), respectively.

Figure 7.5 shows the reliability of the airway measurements for the two scan modes using the coefficient of variations. The variability of the measurements was higher for the NR mode and especially dispersed for smaller ID and WT values due to the partial volume effects when compared with HR mode. In addition, the CV of ID was higher than WT in small tubes using the NR mode. ID measurements are not reliable below 0.8 mm for NR mode since the airway signal change is not detectable from its density profile due to the partial volume effects (**Figure 7.2)**.

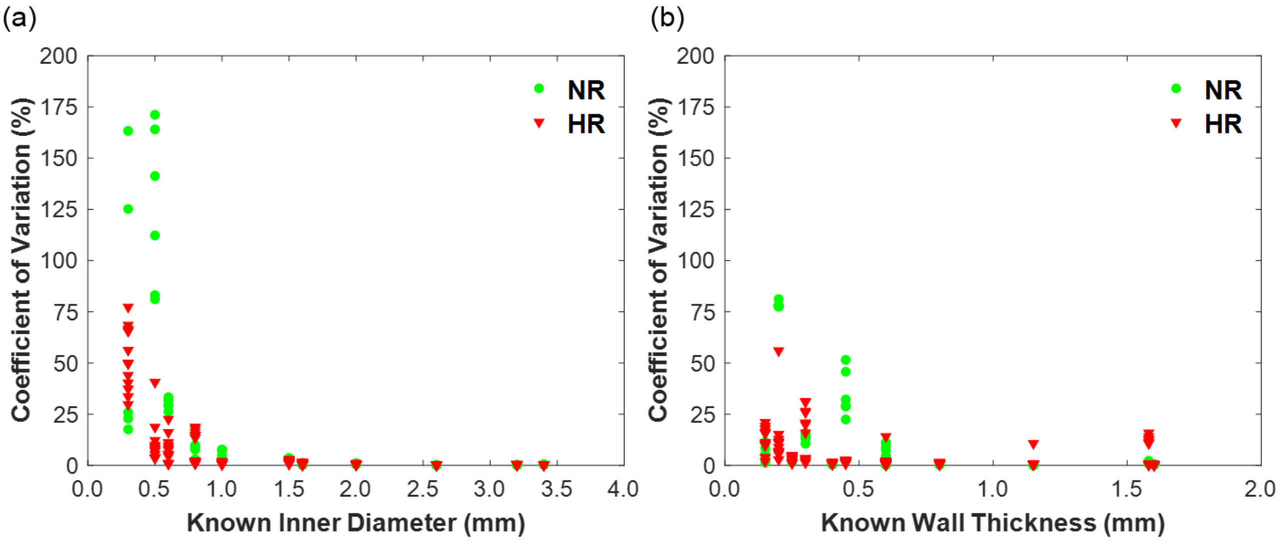

Figure 7.5 Reliability of tube dimension measurements using the HR and NR scan modes.

a) Inner diameter; b) wall thickness. Coefficient of variation (CV) is calculated from six independent realizations of each tube dimension by the mean and standard deviation. $CV = \frac{Standard\ Deviation}{Mean} \times 100\%$. Images included were acquired at 260 mA, 120 kV, 91mAs, 6.2 mGy.

Effects of CT parameters

Figure 7.6 shows box-plots of the mean error for the ID and WT measurements of the airway phantoms. Results are shown for HR and NR modes, various CTDI$_{vol}$ levels, tube potentials, reconstruction kernels, and gantry tilt angles.

The error decreased for HR mode as CTDI$_{vol}$ increased from 0.2 mGy to 6.2 mGy for both ID and WT measurements as shown in **Figure 7.6a** and **7.6b.** For NR mode, the mean error, RMSE, and RMSD was consistent across CTDI$_{vol}$ levels except for 0.2 mGy. At the highest dose level of 6.2 mGy, the RMSEs of ID and WT for the NR mode (ID: 0.31 mm; WT:0.27 mm) were at least two times greater than for the HR mode (ID: 0.10 mm; WT:0.10 mm). Furthermore, for the HR mode at 1.2 and 0.9 mGy, the RMSE (mean error) of ID were 0.16 mm (12.30%) and 0.17mm (10.63%) respectively, and the RMSE of WT were 0.19 mm (44.13%) and 0.20 mm (45.08%) respectively, indicating that low-dose HR measurements can provide improved accuracy on airway phantom measurements compared to the NR mode at the highest dose level (**Table 7.4**).

Table 7.4 Effect of the radiation dose using the HR and NR scan modes on inner diameter (ID) and wall thickness (WT) measurements.

Dose (mGy)			6.2	1.2	0.9	0.6	0.2
ID	HR	Error (%)	-0.99	12.30	10.63	12.38	28.15
		RMSE (mm)	0.10	0.16	0.17	0.19	0.40
		RMSD (mm)	0.09	0.15	0.15	0.18	0.25
	NR	Error (%)	12.87	13.60	13.54	10.21	29.92
		RMSE (mm)	0.31	0.29	0.28	0.29	0.37
		RMSD (mm)	0.31	0.29	0.28	0.28	0.31
WT	HR	Error (%)	23.27	44.13	45.08	71.96	130.52
		RMSE (mm)	0.10	0.19	0.20	0.31	0.58
		RMSD (mm)	0.05	0.11	0.12	0.19	0.30
	NR	Error (%)	52.56	61.90	62.12	70.74	93.10
		RMSE (mm)	0.27	0.29	0.29	0.32	0.40
		RMSD (mm)	0.19	0.20	0.18	0.20	0.25

Note.— Image data were acquired varied radiation dose and reconstructed with either FBP or AIDR 3D algorithm using three lung kernels. Error is the mean error across all 14 airway phantom measurements.

HR and NR performance at different tube potentials and a fixed dose level (1.2 mGy) are compared in **Figure 7.6c** and **7.6d**. For each scan mode, the differences in mean error are less than 10 % between any two tube potentials for ID and WT (**Table 7.5**).

Table 7.5 Effect of the tube potentials using the HR and NR scan modes on inner diameter (ID) and wall thickness (WT) measurements.

Tube Potential (kV)			120	100	80
ID	HR	Error (%)	12.04	9.96	14.89
		RMSE (mm)	0.16	0.15	0.18
		RMSD (mm)	0.15	0.15	0.16
	NR	Error (%)	3.62	6.47	0.72
		RMSE (mm)	0.30	0.29	0.28
		RMSD (mm)	0.29	0.28	0.28
WT	HR	Error (%)	43.59	48.84	39.96
		RMSE (mm)	0.20	0.21	0.17
		RMSD (mm)	0.12	0.13	0.11
	NR	Error (%)	66.52	60.71	58.48
		RMSE (mm)	0.31	0.29	0.28
		RMSD (mm)	0.19	0.19	0.18

Note.— Image data were acquired at 1.2 mGy and reconstructed with either FBP or AIDR3D algorithm using three lung kernels. Error is the mean error across all 14 airway phantom measurements.

The mean error was compared between the two reconstruction algorithms (AIDR3D and FBP) with the FC30 (soft), FC52 (medium) and FC56 (sharp) kernels at 6.2 mGy, as shown in **Figure 7.6e** and **7.6f**. The overall mean error using AIDR3D is slightly lower than FBP for HR and NR modes by 0.10% and 4.96% in ID measurements, and by 2.67% and 6.21% in WT measurements, respectively. For the HR mode, comparable results were found in WT and ID measurements between the FC30 and FC52 kernels, where a slight overestimation of 5% error was found in WT measurements using the FC56 kernel. The results indicate that AIDR3D with either FC30 or FC52 kernels can provide the least error in the airway measurement (**Table 7.6**).

Table 7.6 Effect of the reconstruction algorithms and kernels using the HR and NR scan modes on inner diameter (ID) and wall thickness (WT) measurements.

Algorithms			**AIDR 3D**			**FBP**		
Kernels			**FC30 (N = 2)**	**FC52 (N = 1)**	**FC56 (N = 1)**	**FC30 (N = 2)**	**FC52 (N = 1)**	**FC56 (N = 1)**
ID	**HR**	**Error (%)**	-1.52	1.15	-1.60	-0.95	0.74	-2.03
		RMSE (mm)	0.11	0.11	0.11	0.12	0.13	0.10
		RMSD (mm)	0.08	0.08	0.10	0.08	0.09	0.08
	NR	**Error (%)**	2.75	-0.48	6.11	-7.64	-9.14	-7.42
		RMSE (mm)	0.33	0.27	0.35	0.35	0.29	0.36
		RMSD (mm)	0.33	0.26	0.34	0.35	0.28	0.36
WT	**HR**	**Error (%)**	21.29	17.88	26.63	21.14	25.91	26.77
		RMSE (mm)	0.10	0.09	0.14	0.10	0.11	0.13
		RMSD (mm)	0.05	0.05	0.09	0.04	0.06	0.07
	NR	**Error (%)**	48.94	46.25	53.17	54.84	49.94	62.22
		RMSE (mm)	0.27	0.25	0.31	0.28	0.25	0.32
		RMSD (mm)	0.19	0.16	0.23	0.18	0.15	0.23

Note.— Image data were acquired at 6.2 mGy, 120 kV, 91mAsand reconstructed with either FBP or AIDR3D algorithm using three lung kernels. Error is the mean error across all 14 airway phantom measurements.

Last, for the HR mode, the differences in mean error between 0 and 30 degree gantry tilt angles were small (< 2%) with both ID and WT measurements, indicating that the measurements are robust to airway branches that are oriented with their centerline within 30 degrees of parallel to the z-axis of the scanner (**Table 7.7**).

Table 7.7 Effect of tilted-angle using the HR scan mode on inner diameter (ID) and wall thickness (WT) measurements.

Tilted angle (degree)		0	30
ID	**Error (%)**	-0.99	-0.41
	RMSE (mm)	0.11	0.10
	RMSD (mm)	0.09	0.08
WT	**Error (%)**	22.44	24.09
	RMSE (mm)	0.10	0.11
	RMSD (mm)	0.05	0.06

Note.— Image data were acquired at 6.2 mGy, 120 kV, 91mAsand reconstructed with either FBP or AIDR3D algorithm using three lung kernels. Error is the mean error across all **14 airway** phantom measurements.

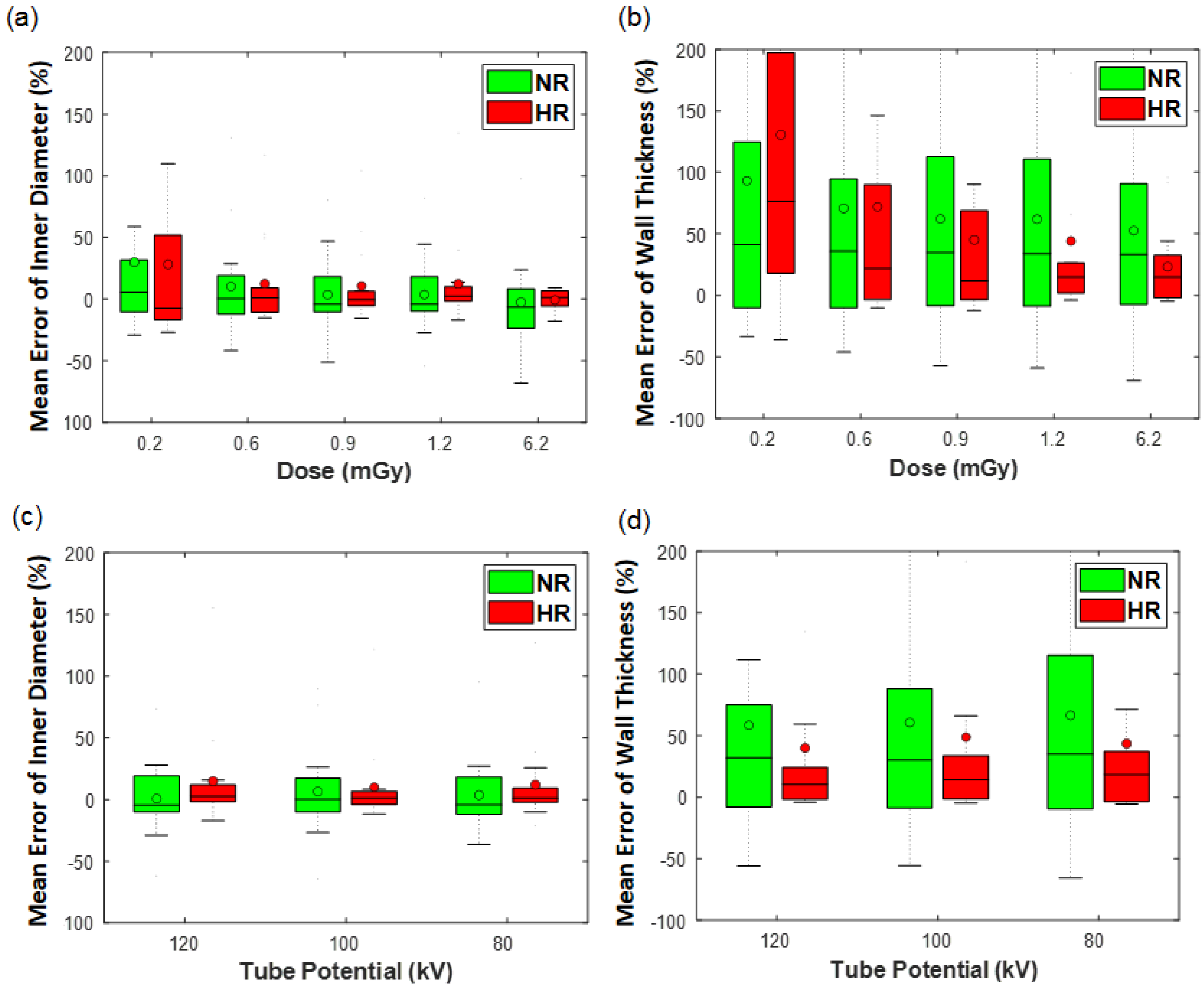

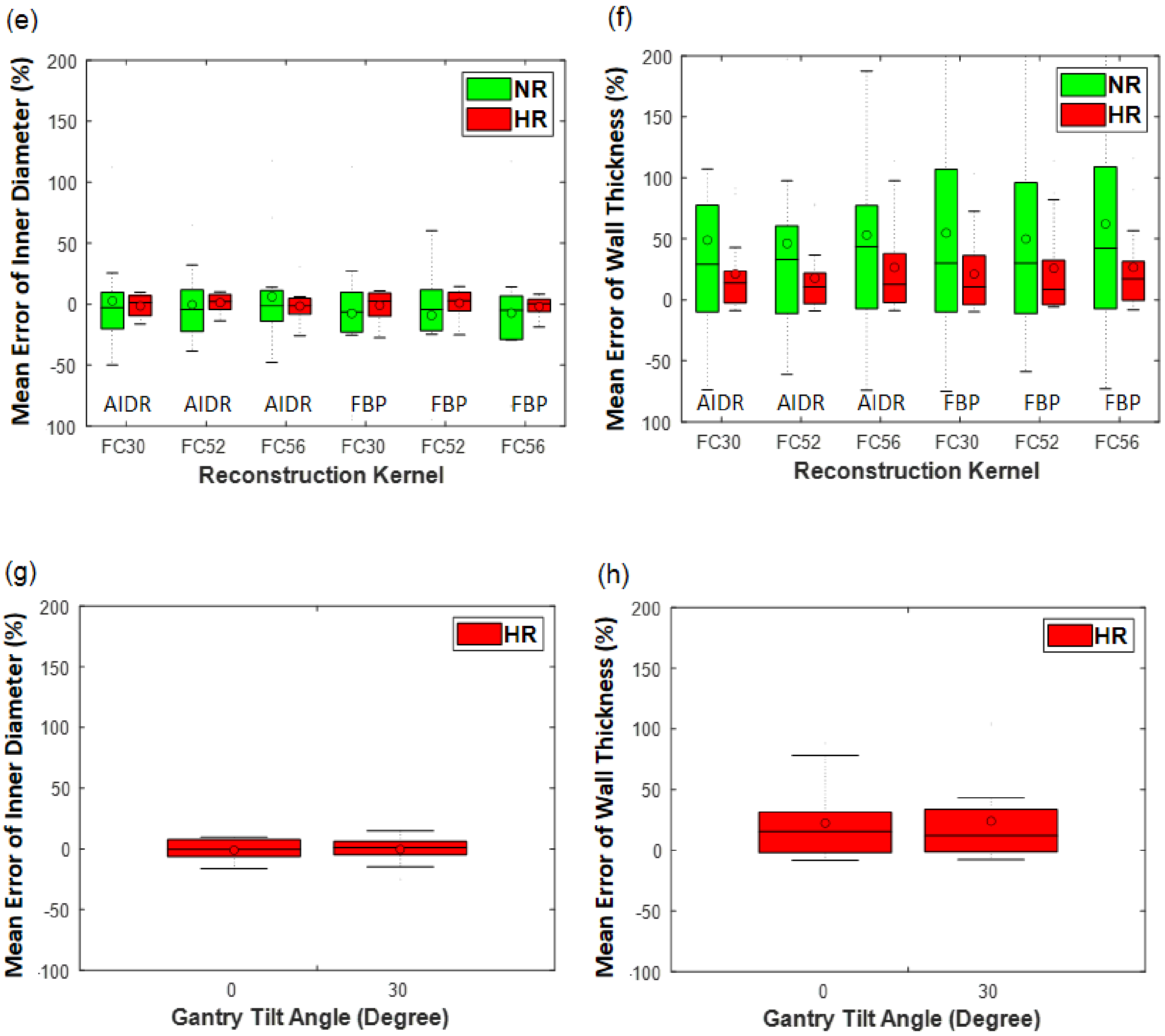

Figure 7.6 Comparison results for the mean error using HR and NR modes for various CTDIvol levels (a,b), tube potentials (c,d) and reconstruction algorithms (e,f).

The gantry tilt angle at 0 and 30 degrees were compared using HR mode only (g,h). Variations in the inner diameter (ID) are shown in (a,c,e,g) and wall thickness (WT) are shown in (b,d,f,h).
Note: (a-b) images were acquired at 3 tube potentials, 5 dose levels, 0° gantry tilt angle, and reconstructed with six reconstruction mode/kernel combinations for both scan modes. (c,d) images were acquired at 3 tube potentials,1.2 mGy, 0° gantry tilt angle, and reconstructed with six reconstruction mode /kernel combinations for both scan modes. (e,f) images were acquired at 120 kV, 6.2 mGy, 0° gantry tilt angle, and reconstructed with six reconstruction mode /kernel combinations for both scan modes. (g,h) images were acquired at 120 kV, 6.2 mGy, two tilt angles, and reconstructed with six reconstruction mode /kernel combinations for HR scan mode.

DISCUSSION

HR acquisitions on the HRCT scanner yields more accurate measurements of both ID and WT of the small airway phantoms (ID < 2 mm) compared to the NR mode. Although positive correlations were found with NR mode tube dimension measurements, the error was approximately twice as large as the error for HR mode (**Figure 7.4**). In addition, the results indicate that the ID can be measured within a 15% error down to approximately 1.3 mm and 2.5 mm using the HR and NR modes, respectively. Hence, HRCT can quantify smaller airways in HR mode with a more acceptable error rate.

To investigate the pathological lesions in patients with obstructive lung disease, histology results have shown the need for accurate assessment of airway remodeling in the smaller and more distal airways. Given that CT scanners have spatial resolution limitations, it is important to be aware of partial volume effects in the airway dimension measurements (178). Hence, phantom studies with known dimensions and compositions have been widely used to evaluate the influence of partial volume effects on the measurement of small sized targets. Unfortunately, tube dimensions provided in the previous studies were out of the range of airways with pathological features (IDs > 2 mm) (181,187–189). The present study focused on airway phantoms with luminal diameters ranging from 0.30 to 2.00 mm and wall thicknesses ranging from 0.15 to 1.00 mm. This wide range of sizes correspond to the major sites of airway obstruction from the 6th to 20th generation airways (182), and is therefore clinically relevant. Using a stationary airway phantom, our results demonstrate that there exists higher error for WTs less than 0.8 mm using NR mode as compared to the HR mode regardless of dose levels, tube potentials and reconstruction parameters used. The significant overestimation of WT was substantially reduced by a factor of two using HR mode with a slight increase in noise at the same CTDI_{vol} level. Additionally, photon-counting detector CT has been shown to have similar or improved image quality and spatial resolution compared to conventional HRCT systems using energy-integrating detectors. Photon-counting detector CT has been used to evaluate the visualization of fine structures in the lungs (190) , and the “Sharp” mode of the this system with smaller detector elements (150 microns) may further improve the quantification of small airway dimensions compared to conventional HRCT systems.

The present study also evaluated the effects of scanning and reconstruction parameters on airway measurement accuracy for both NR and HR modes. The findings suggest that WT has the greatest influence on airway dimension measurements. This is consistent with a previously-reported phantom study by Oguma *et al.* using conventional normal-resolution CT (178), which reported that a wall thickness of 0.5 mm had a high error (% err > 80%, inner diameter 3 mm) under any scanning parameters as the 0.5 mm was close to the size of detector of 0.5 mm. Using HR mode, the mean error of the 0.45 mm wall thickness was ~60% with the luminal diameter of only 0.8 mm. Second, the effects of radiation dose are relatively small using NR mode, which is consistent with previously-reported studies (178,187). For HR mode, the measurement error gradually increased as radiation dose decreased. These results indicate that the main source of error in airway measurements for NR mode is the spatial resolution, while image noise is the main source of error for HR mode. For the low dose lung cancer screening , the U.S. Centers for Medicare & Medicaid Services (CMS) required the CTDIvol of a standard-sized patient (height, 170 cm; weight, 70 kg) to be 3.0 mGy or less with adjustments for patients of different sizes (191). Our results indicate that the HR mode can provide adequate accuracy using low-dose CT on airway phantom measurements at 1 mGy. Additionally, AIDR3D performs better than FBP in terms of measurement error, and the sharpest kernel investigated (FC56) tends to increase the measurement error for both NR and HR resolution modes. Lastly, different matrix sizes and slice thicknesses were selected for the two scan modes with a fixed reconstruction FOV of 220 mm to take advantage of the resolution capabilities of HR mode with a 0.25 mm × 0.25 mm detector size compared to NR mode with a 0.50 mm × 0.50 mm detector size. The HR data was reconstructed with a 1024 x 1024 matrix (0.22 × 0.22 × 0.25 mm voxel size) and the NR data was reconstructed with a 512 x 512 matrix (0.43 × 0.43 × 0.50 mm voxel size). Reconstructing the HR data into a 512 x 512 matrix would not take advantage of the inherent resolution capabilities of HR mode for the 220 mm FOV utilized in this work.

This study has several limitations. First, the chest phantom is relatively small as compared with the normal range of patient sizes. It is expected that a larger phantom size would degrade image quality. However, a similar level of degradation is expected for both HR and NR images, thus preserving the relative advantage of the HR mode. Second, the airway phantom contains no motion artifacts, which may not reflect the human airway in vivo. In addition, for patients with airway obstructive diseases, the airway wall itself may be obscured with inflammation, which has similar CT number ranges as the wall itself. Therefore, future studies will need to be conducted on both healthy and diseased patients using HRCT. Third, the airway phantoms are all made of silicone, which the CT number (~300 HU) is slightly higher than the actual airway wall material (~100HU). Fourth, CT images were only reconstructed with the FBP and AIDR3D algorithms in this study. Although our results indicate that reconstruction kernel has a slight effect on the measurement accuracy, other algorithms such as the model-based iterative reconstruction algorithm (FIRST) may need to be further evaluated before its translation to clinical practice. Finally, the airway dimension measurements were only assessed with the FWHM method without providing the comparison results using other algorithms, such as the maximum-likelihood algorithms and deep-learning method, etc. However, as the measurement errors directly reflect the spatial resolution of the CT images, the FWHM method is appropriate and effective in the phantom validation study using high-resolution CT. Further evaluation using more advanced methods should be assessed with the high-resolution images in the future work.

CONCLUSION

High-resolution CT shows superior performance in the measurement of small airway lumen diameter and wall thickness with the improved accuracy and precision compared to normal resolution CT. The HR mode reconstructed with AIDR3D and the FC52 kernel provides the most accurate measurement of airway dimensions. The HRCT may potentially improve the quantitative analysis on the distal airways and further produce better understanding of airway remodeling in patients with COPD and asthma.

Chapter 8 Quantification of Airway Dimensions using an Integrated-Intensity Based Technique

Abstract

Alteration of small airway dimensions for airway diseases such as asthma and chronic obstructive pulmonary disease (COPD) has been shown to have a strong relation to airway function. This study assessed the accuracy of a new integrated intensity-based (IIB) technique and a standard full-width half-maximum (FWHM) method for quantifying small airway dimensions. To model human airway, tubing of inner diameters ranging from 0.3 to 3.4mm and wall thicknesses ranging from 0.15 to 1.6mm were fitted in a chest phantom. A semi-automated technique based on IIB was used to measure the inner diameter and wall thickness of the airway phantom. The IIB technique can overcome the partial volume effect caused by spatial resolution limitations. The IIB technique accounts for the partial volume effect by measuring the total HU intensity over the entire lumen rather than the number of voxels. The accuracy was evaluated for different imaging and reconstruction parameters as compared with the known airway dimensions using linear regression, t-test, root-mean-square-error (RMSE), and mean error. The results indicate that the inner diameter can be accurately measured (< 15% error) down to 0.5mm and 2mm with mean errors of 0.14mm (13.5%), and 0.18mm (27.7%) using IIB and FHWM methods, respectively. The mean RMSE for wall thickness measurements were 0.43mm and 0.11mm, using FWHM and IIB methods, respectively. In conclusion, the IIB technique enables accurate quantification of small airway dimensions, which can potentially be used for the assessment of airway diseases such as asthma and COPD.

Introduction

The alteration of airway function observed in chronic obstructive pulmonary disease (COPD) and asthma has been shown to be related to airway remodeling by using histological approaches (192–195). Anatomical feature changes in the airway lumen and wall area are associated with airflow obstruction and inflammation in patients with COPD (167,168,181,196,197). Advanced computed tomography (CT) techniques have enabled non-invasive quantitative structural measurements of airway dimensions in the segmental and sub-segmental levels and have been used for improving the management of airway disease (171,172,198). In addition, the objective CT-based quantification of airway dimensions is suitable in determining the status changes in longitudinal studies, such as comparing the airway remodeling before and after bronchial provocation test, evaluating the therapeutic interventions in chronic diseases, etc. (168,179,188,199,200).

Despite the accurate and sensitive evaluation of large airways, previous histological studies have shown that cross-sectional pathological features in small airways with internal diameters of less than 2 mm are especially critical to airway function (172,174,175,177,201). Due to the spatial resolution limitations and partial volume effects of current CT technology in clinical settings, a barrier remains for accurate measurement of the small airway dimensions up to the 6th generation or higher generations (178,181). Numerous studies have shown promising results for the measurement of airway dimensions to overcome spatial resolution limitations using volumetric X-ray CT images (170,171,174,184,201,202). The full-width-half-maximum (FWHM) method is a typical algorithm used in automatic 2-D airway measurements by casting a number of profile rays at different angles across the centroid of the airway (184). Unfortunately, the half-maximum ‘edges’ are difficult to define for small target sizes and varying target shapes. The point spread function (PSF) model-based method incorporating a Gaussian function was then developed to optimize the FWHM technique with maximum likelihood estimation of modeled airways (170,171,201,202). A newly proposed automatic attenuation profile matching (APM) method is able to improve the robustness of PSFs, allowing for accurate determination small airway dimensions down to 3 mm internal diameter and 0.6 mm wall thickness (174). However, such PSF models developed on a single CT system may not be generalizable for other CT systems, leading to variabilities and biases on airway measurements. An integrated Hounsfield unit (HU) based technique has been reported for quantification of coronary artery cross-sectional area that addresses some of these limitations (203,204).The key strength of the integrated-HU technique is that it overcomes the limitations of partial volume effects by measuring the total HU intensity over the entire lumen rather than the number of voxels for dimension measurement. Such a technique has the potential to account for partial volume effects in the assessment of the small airway dimensions.

The purpose of this chapter was to validate a semi-automatic and quantitative approach based on the integrated-HU technique for the quantification of small airway dimensions. The central hypothesis is that the airway dimensions, including the inner lumen diameter (ID) and the wall thickness (WT), can be accurately measured with the integrated-HU technique by using physical phantoms with known simulated airway sizes as the ground truth. The accuracy and influence of variable CT imaging and reconstruction parameters were also evaluated to determine the optimal CT parameters and measurement limitations for accurate measurement of airway dimensions using the integrated-HU method.

Material and Methods

Airway Phantom

The 10-cm diameter cylindrical polyurethane phantom consists of fourteen silicone tubes (Qosina, Ronkonkoma, New York, USA) that simulates airways, with various inner lumen diameters in a range of 0.3 – 3.4 mm and wall thicknesses in a range of 0.15 – 1.6 mm, was fitted in a chest phantom (Anthropomorphic Thorax Phantom, Quality Assurance in Radiology and Medicine, Moehrendorf, Germany) (**Figure 8.1**). The tube dimensions were chosen to mimic the human airway ranging from the 5th to the 20th generations of branching (178,182). The measured intensity of the background material used to simulate the lung parenchyma with emphysema was approximately -910 HU; the measured density of the artificial airway wall on CT images was approximately 350 HU. The actual dimension of the tubes was acquired from the product catalog and detailed specifications of airway tubes are presented in **Table 8.1**. The CT images of four representative airway tubes are shown in **Figure 8.2**.

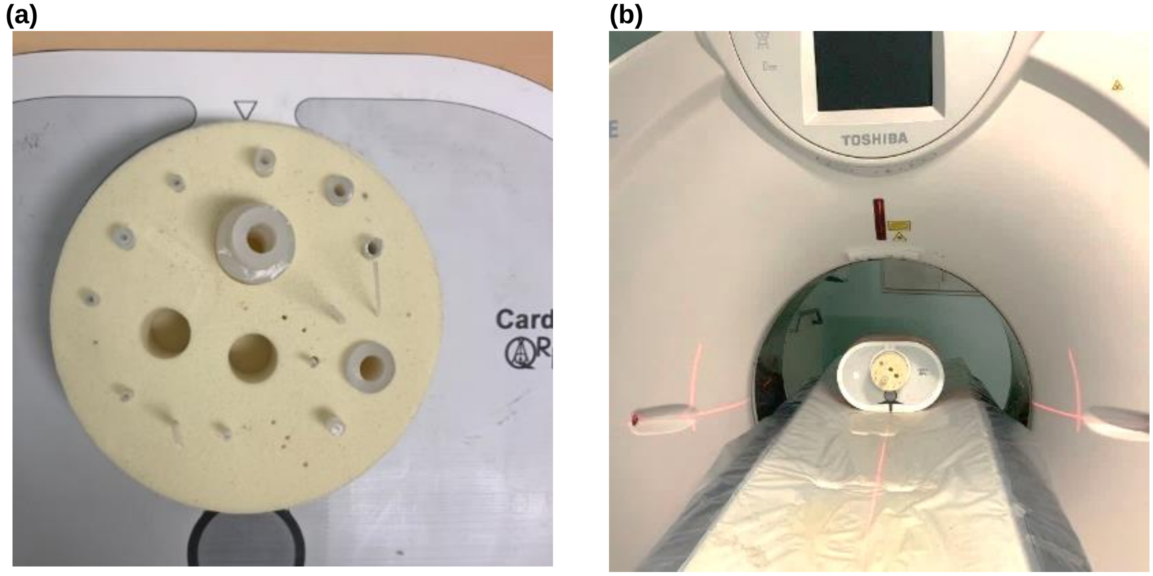

Figure 8.1 Airway Phantom Settings.

a) QRM-Thorax phantom with the embedded polyurethane foam cylinder with 14 airway tubes. b) The chest phantom placed perpendicularly to the scan slices inside the gantry.

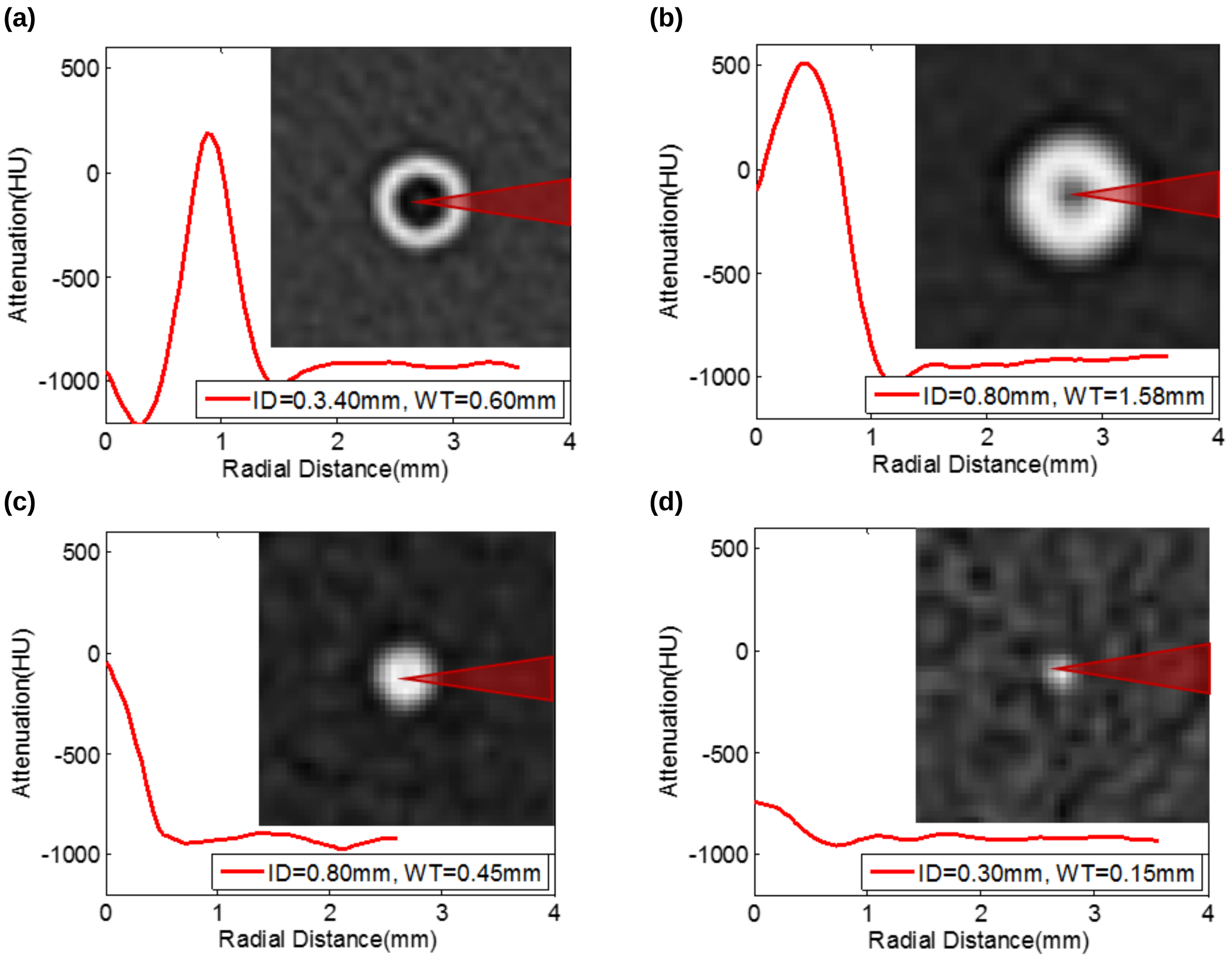

Figure 8.2 Profiles of representative tubes with partial volume effects.

Each profile is casting from the center of the tube. a) ID=3.4mm, WT=0.6mm(T2014). b) ID=0.8mm, WT=1.58mm (T2005). c) ID=0.8mm, WT=0.45mm T2004). d) ID=0.3mm, WT=0.15mm (T2001).

Table 8.1 Comparisons of CT measured airway dimensions using the integrated-based method (IIB) and FWHM with various tube sizes to the actual airway dimensions.

a) **Inner Diameter (ID)**

Tube No.	**Ref (mm)**	**IIB**	**FWHM**
		Mean ± SD (mm) (%)	
T2001	**0.30**	0.41 ± 0.13 (38.85)	0.61 ± 0.34 (103.08)
T2002	**0.50**	0.44 ± 0.09 (-11.70)	0.39 ± 0.19 (-22.53)
T2003	**0.60**	0.56 ± 0.06 (-7.29)	0.56 ± 0.10 (-6.33)
T2004	**0.80**	0.83 ± 0.09 (3.94)	1.29 ± 0.31 (61.01)
T2005	**0.80**	0.82 ± 0.07 (3.41)	1.13 ± 0.14 (41.72)
T2006	**1.00**	1.01 ± 0.16 (0.78)	1.00 ± 0.18 (0.10)
T2007	**1.50**	1.44 ± 0.14 (-3.90)	1.07 ± 0.10 (-28.93)
T2008	**1.60**	1.45 ± 0.07 (-9.60)	1.27 ± 0.09 (-20.61)
T2009	**1.60**	1.37 ± 0.08 (-14.64)	1.60 ± 0.08 (-0.17)
T2010	**1.60**	1.59 ± 0.03 (-0.41)	1.91 ± 0.05 (19.39)
T2011	**2.00**	1.78 ± 0.05 (-11.01)	1.85 ± 0.08 (-7.56)
T2012	**2.60**	2.61 ± 0.07 (0.30)	2.79 ± 0.11 (7.22)
T2013	**3.20**	3.29 + 0.09 (2.82)	3.48 ± 0.05 (8.60)
T2014	**3.40**	3.20 ± 0.06(-6.02)	3.22 ± 0.09 (-5.32)

b) **Wall Thickness (WT)**

Tube No.	**Ref (mm)**	**IIB**	**FWHM**
		Mean ± SD (mm) (%)	
T2001	**0.15**	0.15 ± 0.05 (1.32)	0.66 ± 0.20 (336.57)
T2002	**0.20**	0.22 ± 0.04 (13.54)	0.44 ± 0.12 (123.09)
T2003	**0.30**	0.36 ± 0.04 (20.95)	0.46 ± 0.06 (54.50)
T2004	**0.45**	0.46 ± 0.04 (2.43)	0.26 ± 0.09 (-43.29)
T2005	**1.58**	1.52 ± 0.04 (-3.44)	1.32 ± 0.13 (-16.38)
T2006	**0.60**	0.62 ± 0.07 (3.48)	0.57 ± 0.15 (-4.32)
T2007	**0.25**	0.27 ± 0.05 (7.80)	0.80 ± 0.07 (219.86)
T2008	**0.40**	0.48 ± 0.02 (20.99)	0.82 ± 0.08 (106.84)
T2009	**0.80**	0.89 ± 0.06 (11.93)	0.90 ± 0.08 (12.50)
T2010	**1.60**	1.50 ± 0.02 (-6.54)	1.41 ± 0.03 (-11.73)
T2011	**0.60**	0.72 ± 0.05 (19.82)	0.86 ± 0.08 (43.84)
T2012	**1.15**	1.07 ± 0.03 (-6.82)	1.04 ± 0.08 (-8.99)
T2013	**1.60**	1.44 ± 0.03 (-9.59)	1.43 ± 0.03 (-10.24)
T2014	**0.60**	0.71 ± 0.04(19.13)	0.86 ± 0.08 (45.32)

Note.— Comparisons of CT measured dimensions using IIB and FWHM methods. The reference inner diameter and wall thickness (Ref) were listed in the manufacturer's manual. Images included were acquired at six tube potential/current combinations and reconstructed with six reconstruction mode/kernel combinations.

CT imaging

The QRM-Thorax phantom was scanned using a 320-slice CT scanner (Aquilion One, Canon American Medical Systems, Tustin, CA) with a 320 × 0.5 mm collimator, 350-ms rotation time, 220-mm scan field-of-view (FOV), and each combination of the following parameters: three tube potentials (120, 100, and 80 kV) and two tube currents (200 and 50 mA). The center of the cylindrical phantom was placed in the isocenter of the scanner. The phantom was positioned at 0 or 30-degree angles between the CT z-axis and the phantom z-axis to assess circular and elliptical 2D cross-sectional images on small airway dimensions. The CT images were reconstructed in a 220 mm reconstructed FOV using a 512 × 512 matrix (0.43 x 0.43 x 0.50 mm) with two reconstruction algorithms: the filtered back projection (FBP) and an adaptive iterative dose reduction (AIDR 3D) algorithm. Three different reconstruction kernels (FC30, FC52, and FC56) were investigated, where the FC30 reconstruction kernel corresponds to a smooth reconstruction kernel, the FC52 reconstruction kernel corresponds to a standard lung reconstruction kernel, and the FC56 reconstruction kernel corresponds to a sharp lung reconstruction kernel. The $CTDI_{vol}$ values were recorded and calculated from the dose report sheet.

Integrated-HU Based technique (IIB)

The proposed integrated technique does not directly depend on the spatial resolution since the lumen area is used for measurement rather than lumen edge detection. The basic assumption of the integrated HU method is that although the partial volume effects influence a single voxel that contains the fractional amount of different materials, the overall integrated HU signal within the measured region-of-interest (ROI) is conserved. The concept behind this technique is explained in **Figure 8.3**. **Figure 8.3a** shows the airway tube phantom inside a chest phantom with three materials: the air (S_o), the airway wall material (S_W), and the background lung parenchymal material (S_{bg}). Before the measurement, three ROIs are obtained to calibrate each material signal on a large tube, as shown in **Figures 8.3b** and **8.3c**:

1) A circular ROI is placed at the airway center that all pixels are not affected by the partial volume effect to measure the pure air signal (S_o).
2) A ring ROI is placed on the airway wall that all pixels are not affected by the partial volume effect to measure the wall material signal (S_w).
3) A background ROI is placed outside the tube to measure the background signal (S_{bg}).

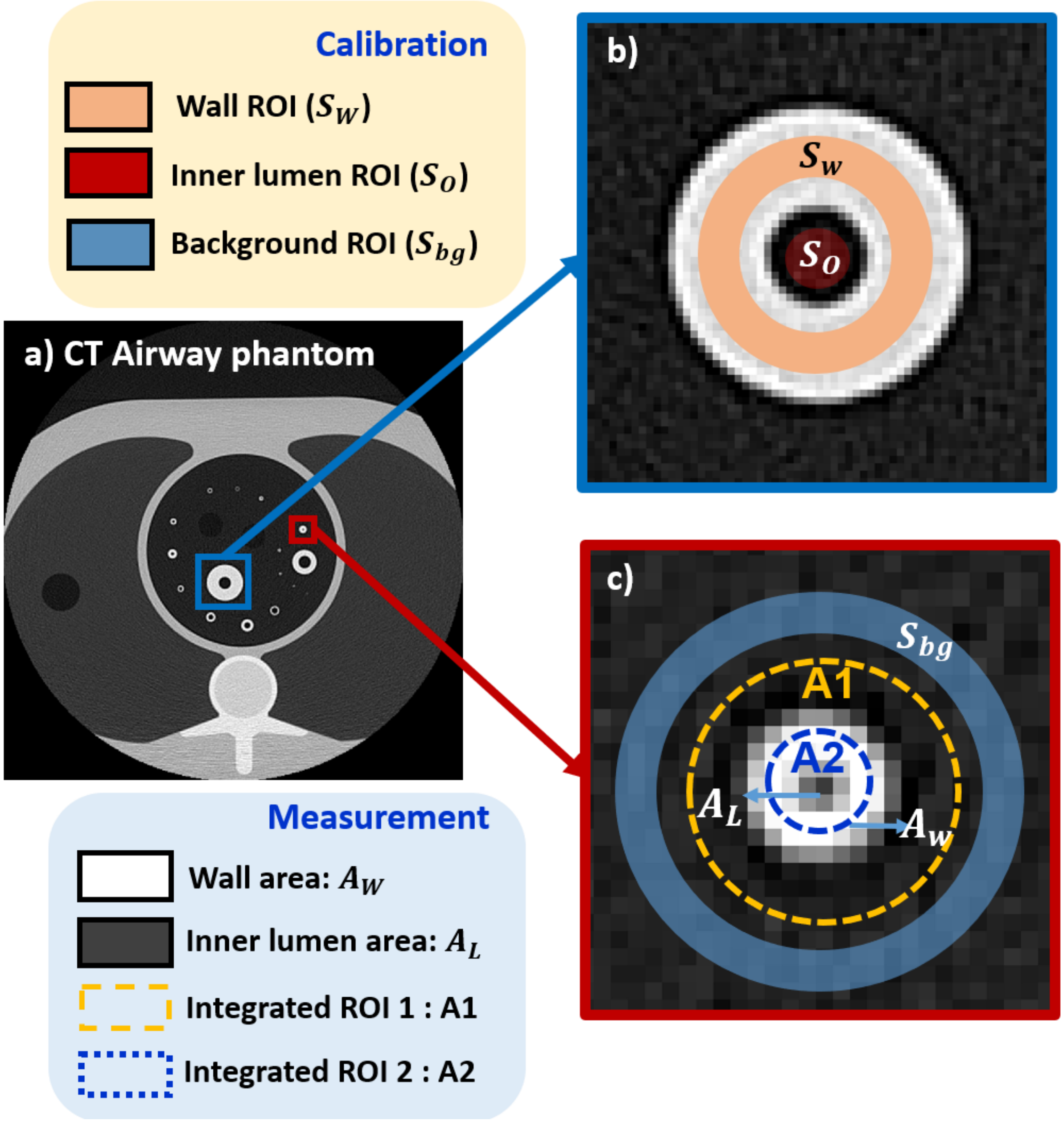

Figure 8.3 Representative phantom image and the integrated-based technique.

a) Raw CT image of the airway phantom. b) An expansion of one tubing for material calibration. S_o: pure air HU; S_W: pure wall material HU. c) An expansion of the measuring tubing with two region-of-interests (A_1, A_2) for airway dimension measurements. S_{bg}: background HU. A_L: inner lumen area; A_W: wall area.

Two more ROIs were used to measure the wall area and the inner lumen area, as shown in **Figure 8.3c**. Specifically, to measure the wall area (A_W), a circular ROI (A1) is placed outside the outer airway wall to include the signal of the tube object. Based on the signal conservation assumption, the integrated HU (I_1) within the A1 is given by:

$$I_1 = A_L\, S_o + A_W S_w + (A_1 - A_L - A_W)\, S_{bg} \qquad (8.1)$$

where A_W is the actual wall area, A_L is the actual inner lumen area.

Then, Eq.1 can be rearranged as:

$$A_W = \frac{I_1 - A_1 S_{bg}}{S_w - S_{bg}} + \frac{(S_o - S_{bg}) A_L}{S_w - S_{bg}} \qquad (8.2)$$

As the signal of lung parenchyma and the air are relatively close compared to the wall material, we assume that $S_{bg} \approx S_o$. Hence, the wall area (A_W) is estimated by:

$$A_W = \frac{I_1 - A_1 S_{bg}}{S_w - S_{bg}} \qquad (8.3)$$

Similarly, to measure the inner lumen area (A_L), another circular ROI (A2) is placed on the tube wall to include the signal of the airway lumen. Then, integrated HU (I_2) within the A2 is:

$$I_2 = A_L\, S_o + (A_2 - A_L)\, S_w \qquad (8.4)$$

Hence, the inner lumen area (A_L) is given by:

$$A_L = \frac{I_2 - A_2 S_w}{S_o - S_w} \qquad (8.5)$$

The inner diameter and the wall thickness are then derived by the area. The proposed integrated HU technique allows for small airway dimension measurements by calibrating the wall material on the larger airway, regardless of the partial volume effect on small airways (**Figure 8.2**).

Full-width Half Maximum Method (FWHM)

The FWHM algorithm was implemented using in-house software developed in MATLAB® (R2019a; MathWorks Inc.). The airway measurement was accomplished using the following four steps:

1) Convert the native Cartesian coordinates (x, y) to polar coordinates (r, θ) for each interpolated cross-sectional image (186,205).
2) Generate radial bins along each angular bin and calculate the average value for each bin.
3) Cast the density spectrum curve along each theta and apply the standard full-width half-maximum method on the ID and WT measurements.
4) Calculate the average ID and WT from six continuous cross-sectional images.

Image pre-processing

A commercial software (VITAL Images, Pulmonary Analysis Workflow; Canon Medical Systems) was used to segment each airway from the chest phantom. The segmentation was accomplished semi-automatically by using a vessel selection tool based on a region growing algorithm and followed by the manual correction on the borders of the airway segments. Next, an in-house software developed in MATLAB® (R2019a; MathWorks Inc.) was used to generate the cross-sectional images for each airway. Specifically, the centerline of each airway was extracted from the airway segments using a 3-dimensional skeletonized algorithm (183). Then, a 3D curved planer reformation (CPR) was performed along its centerline to generate longitudinal cross-sectional images that are perpendicular to the centerline (**Figure 8.2**). The cross-sectional images were then up-sampled by a factor of five using a bi-cubic interpolation algorithm. Finally, interpolated cross-sectional images were used for the airway measurement using both IIB and FWHM methods.

Statistical Analysis

The mean and standard deviation (SD) of the ID and WT for each tube were calculated across six contiguous cross-sectional images along the centerline. The mean error was calculated as the relative difference between the CT measurement sizes and the known tube sizes ($\% Err = \frac{CT\_Measurement - Actual}{Actual} \times 100\%$). The averaged measurements of all imaging and reconstruction parameters were quantitatively compared to the actual dimensions through linear regression. The measurements from each scan and reconstruction parameter were compared with the known tube sizes using the Mann-Whitney U test (SPSS, version 22, IBM, Armonk, NY). In addition, the root-mean-square error (RMSE) with respect to the known tube dimensions and the root-mean-square deviation (RMSD) with respect to the linear fit were determined to evaluate the accuracy and precision of the two methods. Lastly, to assess the reliability of the measurement, the coefficient of variation (CV) was calculated as a ratio of SD and mean from six independent realizations of each airway measurement ($CV = \frac{SD}{Mean} \times 100\%$).

Results

Evaluation of Overall Performance

The ID and WT measurements were evaluated for all fourteen airway phantoms using both integrated-HU based (IIB) and the FWHM algorithms and compared with the known tube dimensions as a reference. The examples of cross-sectional images and the density spectrum curve in four representative tubes (T2001, T2004, T2005, and T2014) are shown in **Figure 8.2**. Due to the partial volume effects, the airways in T2001 and T2004 are barely visible, and the airway walls are blurred in all four tubes.

Figure 8.4 shows the mean measurement and the mean error of each simulated airway dimension with the CT images acquired at various tube currents, CTDI dose level, reconstruction algorithms/kernels, and tube tilted-angles. The mean, standard deviation, and mean error of each tube dimension measurements are summarized in **Table 8.1**. For ID measurements, both IIB and FWHM regression lines show a slope close to unity and negligible intercept, while larger mean errors were found using the FHWM method when IDs were less than 2 mm due to the partial volume effect. The overall RMSE (mean error %) for IIB and FWHM were 0.12mm (-0.24%) and 0.27mm (-2.63%), respectively. For WT measurements, the IIB measurements were related to the known measurements by WIIB = 0.89WK + 0.09 (r=0.99), with a RMSE of 0.08mm, a RMSD of 0.06mm, and a mean error of 6.61%. The FWHM measurements were related to known WT measurements by WFWHM = 0.60WK + 0.60 (r=0.88), with a RMSE of 0.29mm, a RMSD of 0.17mm and a mean error of 60.55%. Further detailed linear regression parameters are listed in **Table 2**. Significant differences are found between the FHWM measured WT and the known WT (p = 0.003), while no significant differences between the IIB measured WT and the known WT (p = 0.93) (Table II). The WT measurement using the IIB mode yielded a factor of two improvements in the accuracy (RMSE, RMSD and mean error) as compared to the FHWM method.

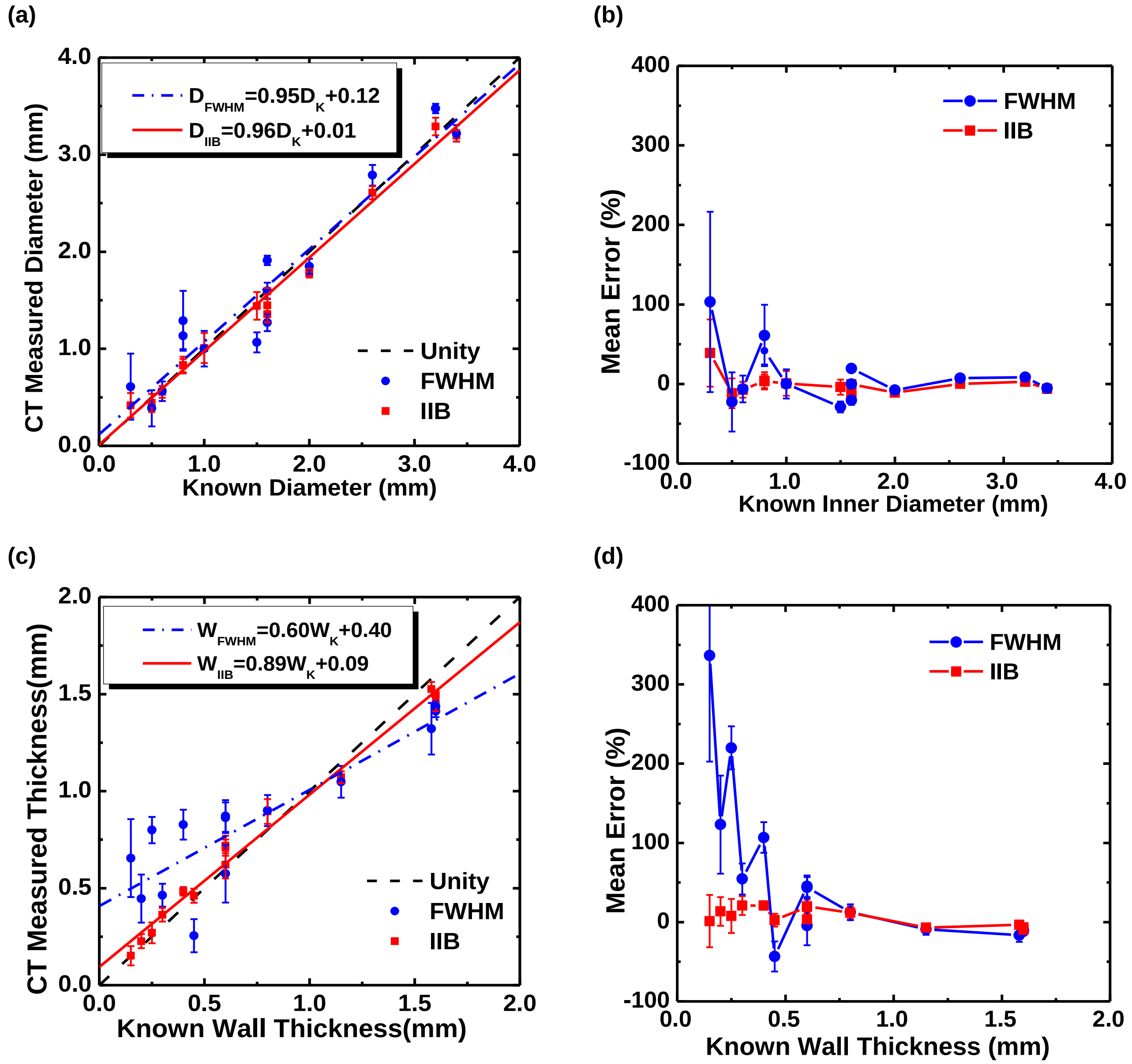

Figure 8.4 The linear regression and mean error analyses for CT-measured dimensions using the Integrated Intensity-Based Method (IIB) and Full-Width Half Maximum Method (FWHM).

a), b): Inner diameter; c), d): Wall thickness. Images were acquired at all combinations of tube voltages, currents and tilted-degree angles and reconstructed all combinations of reconstruction kernels and algorithms. Each point represents the average CT-measured dimension of all measurements.

Table 8.2 Linear regression of CT measured airway dimensions using the integrated-based method (IIB) and FWHM (N = 12).

Technique	IIB		FWHM	
	ID	**WT**	**ID**	**WT**
Slope	0.96 [0.94,0.99]	0.91 [0.89,0.93]	0.96 [0.91, 1.01]	0.61 [0.55, 0.68]
Intercept (mm)	0.02 [-0.02, 0.05]	0.06 [0.04,0.07]	0.07 [-0.02, 0.17]	0.40 [0.35,0.46]
Pearson’s r	0.99	0.99	0.940	0.831
Error (%)	1.40	6.61	3.88	56.57
RMSE (mm)	0.12	0.08	0.30	0.39
RMSD (mm)	0.11	0.06	0.30	0.17
P-value	0.31	0.93	0.82	**0.003**

Note.— 95% Confidence Intervals are presented in the bracket. ID: inner diameter; WT: wall thickness; RMSE: root-mean-square error; RMSD: root-mean-square deviation. P-value less than 0.05 indicates significant difference. Images included were acquired at 200 mA, 120 kV, 70mAs and 9.1 mGy and reconstructed with six reconstruction mode/kernel combinations. The linear regression equation: $\boldsymbol{Y_{measure}} = \boldsymbol{a} + \boldsymbol{bX_{true}}$, where the CT measured ID and WT (dependent variables) are related to the true ID and WT (explanatory variable), respectively.

To evaluate the precision of the measurement, coefficient of variations of each independent measurement of ID and WT using the two methods are shown in **Figure 8.5**. The variability of the measurements is significantly higher using the FWHM method compared to the IIB method, where the CV values are more dispersed in ID less than 2 mm and WT less than 0.8 mm. The results indicate that the methods are less reliable in small airway measurements due to the increasing partial volume effects and decreasing signal to noise for the small tubes. Also, it is noticeable that the CV values of ID were 50% higher than WT using the FWHM method for the same tube dimensions. The underlying reason is that the inner lumen disappears due to the partial volume effects as no signal change can be detected between the air and wall material from the density spectrum curve of small airways, as shown in **Figures 8.2c** and **8.2d**.

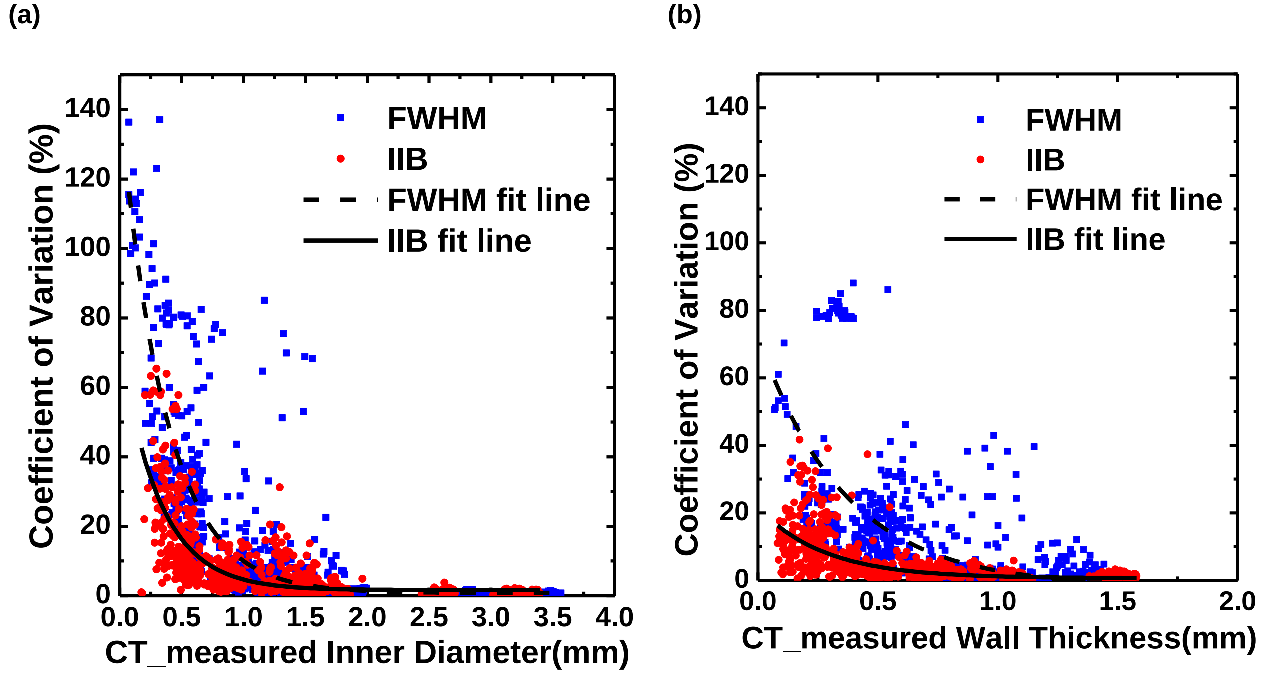

Figure 8.5 Reliability of tube dimension measurements for the IIB and FWHM using the coefficient of variation (CV).

CV is calculated from independent realizations of each tube dimension by dividing the mean to the standard deviation. Images were acquired at all combinations of tube voltages, currents and tilted-degree angles and reconstructed using all combinations of reconstruction kernels and algorithms.

Evaluation of CT Parameters

Figure 8.6 exhibits box plots of the mean measurement error for the ID and WT using both methods for different dose levels, tube potentials, reconstruction kernels, and tube tilted angles. **Figures 8.6a** and **8.6b** show that the mean error of the FWHM method was at least two times greater than the IIB method for both ID and WT measurements, while the measurement error for each method remained stable for all dose levels. **Figures 8.6c** and **8.6d** compare the FWHM and IIB performances for images acquired at 200 mA and three different tube potentials. For each method, the mean error differences are less than 10 % between any two ID or WT measurements using different tube potentials. **Figures 8.6e** and **8.6f** compare the mean error for AIDR3D and FBP reconstruction algorithms with three different kernels. The overall mean error using the AIDR3D is slightly lower than FBP in both ID and WT airway phantom measurements for the IIB method. In the FWHM measurement, the FBP algorithm slightly reduces ID measurement errors by approximately 5% but increases the WT measurement errors by approximately 5% compared to the AIDR 3D algorithm. Among all measurements, the AIDR3D algorithm with FC30 can provide the lowest error in airway measurement using the IIB method. **Figures 8.6g** and **8.6h** compare the mean error between the two tube-tilt angles at 0 and 30 degrees. For the IIB method, the differences in mean error were small (< 2%) in both ID and WT measurements, indicating that the measurements are robust to airway branches with a tilt angle from 0 to 30 degrees.

The supplementary results on CT parameter effects are provided in **Tables 8.3, 8.4**, and **8.5**

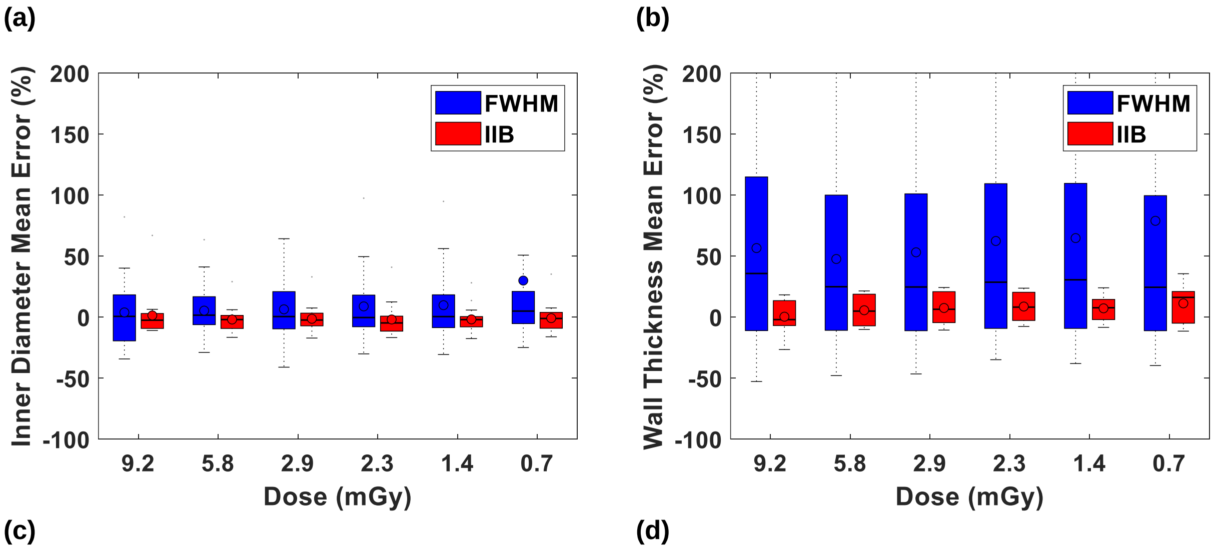

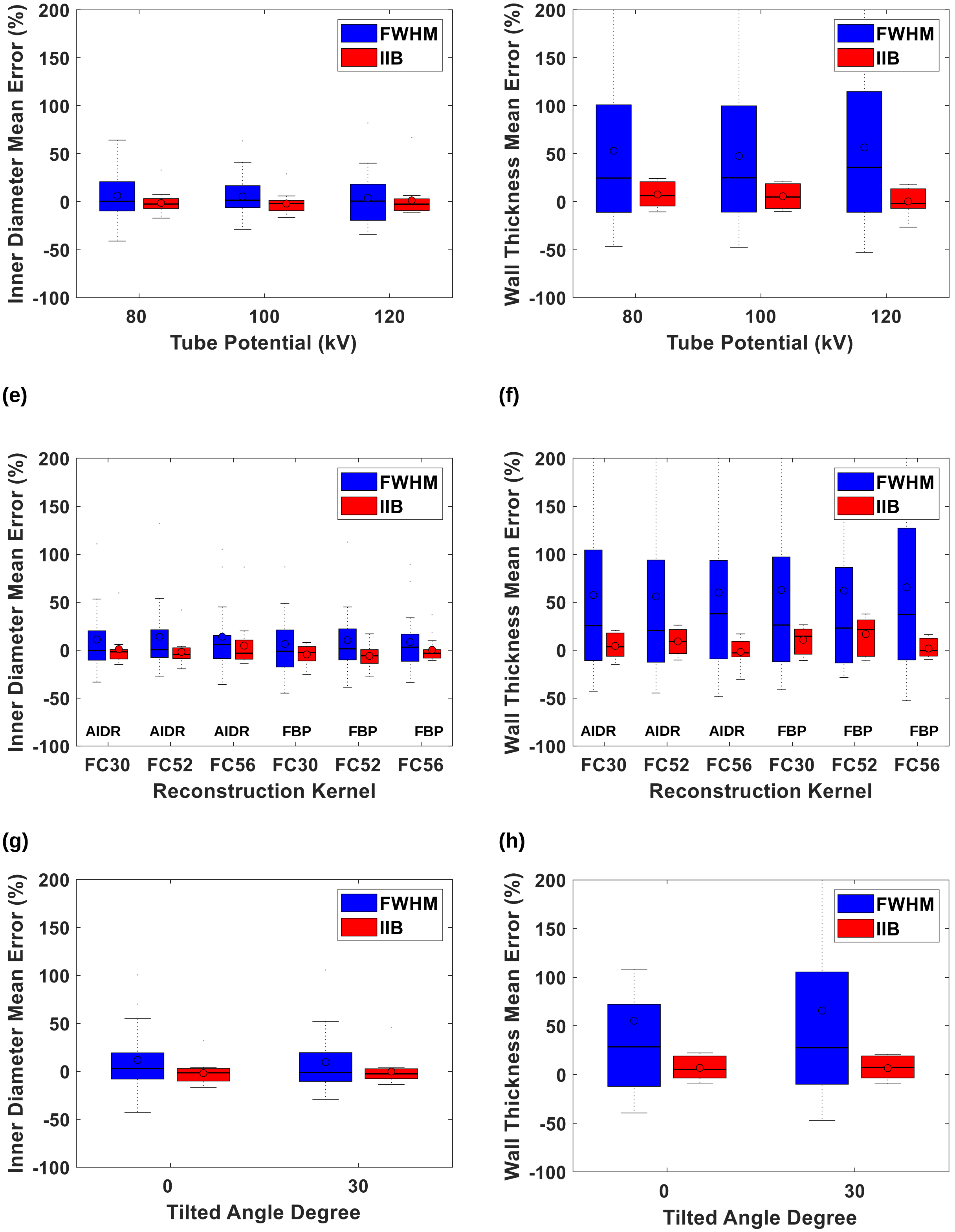

Figure 8.6 Comparisons of the mean error using IIB and FWHM methods with various radiation doses (a, b), tube potentials (c, d), reconstruction mode/kernel combinations (e, f), and tilt angels (g, h).

The variations in the inner diameter (a,c,e,g) and wall thickness (b,d,f,h) were both assessed. Note-(a,b,e,f,g,h) were images acquired at six tube potential/current combinations, two tilt angles, and reconstructed with six reconstruction mode/kernel combinations; (c,d) images were acquired at three tube potentials, 200 mA, two tilt angles, and reconstructed with six reconstruction mode/kernel combinations.

Table 8.3 Effect of the radiation dose using the IIB and FWHM methods on ID and WT measurements.

Tube Current (mA)			**200 (N = 36)**			**50 (N = 36)**		
Tube Voltage (kV)			**120 (N = 12)**	**100 (N =12)**	**80 (N =12)**	**120 (N =12)**	**100 (N = 12)**	**80 (N = 12)**
CTDI Dose Level (mGy)			**9.6**	**5.8**	**2.9**	**2.3**	**1.4**	**0.7**
Inner diameter	**IIB**	Error (%)	**1.40**	**-1.94**	**-1.36**	**-1.90**	**-1.83**	**-0.83**
		RMSE (mm)	**0.12**	**0.11**	**0.12**	**0.14**	**0.15**	**0.12**
		RMSD (mm)	**0.11**	**0.10**	**0.11**	**0.11**	**0.11**	**0.11**
	FWHM	Error (%)	**3.88**	**5.33%**	**6.41%**	**8.82**	**9.77**	**29.95**
		RMSE (mm)	**0.30**	**0.26**	**0.26**	**0.26**	**0.27**	**0.36**
		RMSD (mm)	**0.30**	**0.25**	**0.25**	**0.25**	**0.27**	**0.32**
Wall Thickness	**IIB**	Error (%)	**0.35**	**5.64**	**7.49**	**8.69**	**7.24**	**11.29**
		RMSE (mm)	**0.07**	**0.08**	**0.09**	**0.08**	**0.08**	**0.10**
		RMSD (mm)	**0.05**	**0.06**	**0.06**	**0.05**	**0.06**	**0.05**
	FWHM	Error (%)	**56.57**	**47.6**	**53.11**	**62.37**	**64.74**	**78.88**
		RMSE (mm)	**0.30**	**0.26**	**0.26**	**0.29**	**0.30**	**0.34**
		RMSD (mm)	**0.19**	**0.16**	**0.16**	**0.16**	**0.22**	**0.19**

Note.—Images included were acquired at six tube potential/current combinations, two tilt angles and reconstructed with six reconstruction mode/kernel combinations. RMSE: root-mean-square error; RMSD: root-mean-square deviation.

Table 8.4 Effect of the reconstruction algorithms and kernels using the IIB and FWHM methods on ID and WT measurements.

Reconstruction Algorithms			**AIDR 3D (N = 36)**			**FBP (N = 36)**		
Reconstruction Kernels			**FC30 (N = 12)**	**FC52 (N =12)**	**FC56 (N = 12)**	**FC30 (N =12)**	**FC52 (N =12)**	**FC56 (N = 12)**
Inner diameter	**IIB**	Error (%)	**1.06**	**-1.84 %**	**4.64 %**	**-4.56 %**	**-6.06 %**	**0.30 %**
		RMSE (mm)	**0.13**	**0.14**	**0.15**	**0.13**	**0.16**	**0.12**

		RMSD (mm)	**0.11**	**0.12**	**0.11**	**0.12**	**0.14**	**0.10**
	FWHM	Error (%)	**11.09**	**13.94**	**13.99**	**6.47**	**10.32**	**8.35**
		RMSE (mm)	**0.28**	**0.27**	**0.32**	**0.25**	**0.24**	**0.30**
		RMSD (mm)	**0.27**	**0.26**	**0.30**	**0.25**	**0.23**	**0.30**
Wall Thickness	**IIB**	Error (%)	**4.38**	**9.06**	**-1.83**	**10.77**	**16.65**	**1.69**
		RMSE (mm)	**0.08**	**0.10**	**0.06**	**0.10**	**0.12**	**0.06**
		RMSD (mm)	**0.06**	**0.07**	**0.05**	**0.06**	**0.06**	**0.05**
	FWHM	Error (%)	**57.34**	**55.86**	**59.97**	**62.64**	**61.96**	**65.52**
		RMSE (mm)	**0.29**	**0.27**	**0.32**	**0.28**	**0.27**	**0.32**
		RMSD (mm)	**0.17**	**0.15**	**0.22**	**0.15**	**0.18**	**0.21**

Note.— Images included were acquired at six tube potential/current combinations, two tilt angles and reconstructed with six reconstruction mode/kernel combinations. RMSE: root-mean-square error; RMSD: root-mean-square deviation.

Table 8.5 Effect of tilted angel using the IIB and FWHM methods on ID and WT measurements.

Tilted angle (degree)			**0 (N =12)**	**30 (N=12)**
Inner diameter	**IIB**	**Error (%)**	-1.91 %	-0.24 %
		RMSE (mm)	0.12	0.12
		RMSD (mm)	0.11	0.10
	FWHM	**Error (%)**	11.81	9.57
		RMSE (mm)	0.29	0.25
		RMSD (mm)	0.28	0.25
Wall Thickness	**IIB**	**Error (%)**	6.96	6.61
		RMSE (mm)	0.08	0.08
		RMSD (mm)	0.06	0.06
	FWHM	**Error (%)**	55.37	65.73
		RMSE (mm)	0.29	0.29
		RMSD (mm)	0.18	0.16

Note.— Images included were acquired at six tube potential/current combinations, two tilt angles and reconstructed with six reconstruction mode/kernel combinations. RMSE: root-mean-square error; RMSD: root-mean-square deviation.

Discussion

Our study results show that the proposed integrated-HU based method can provide improved accuracy and precision for both inner diameter and wall thickness measurements compared to the FWHM method using a chest phantom fitted with airways. Although strong positive correlations were observed between the FWHM measurements and known tube dimensions, the measurement errors were at least two times larger than the IIB method (**Figure 8.5**). In this study, quantitative assessment focused on small airway dimensions with lumen diameters ranging from 0.3 to 2 mm. A mean error less than 15% can be achieved for ID greater than 0.5 mm and 2.0 mm using the IIB and FHWM methods, respectively. Moreover, the mean error of all WT measurements was 6.96% and 55.36% using IIB and FHWM methods, respectively. A mean error less than 15% can be achieved for WTs greater than 0.8 mm and 1.6 mm using the IIB and FHWM methods, respectively. Additionally, a substantial reduction in coefficient of variation was demonstrated in ID and WT measurements using the IIB method, particularly for small airways (ID<1 mm, WT<1 mm). Hence, the IIB method can potentially improve quantification of small airway dimensions for patients with obstructive disease.

Both histological and CT quantification results have shown that the critical sites of airway alteration in patients with obstructive lung diseases are small airways, which are defined as the inner diameter less than 2-3 mm (181,206–208). Due to spatial resolution limitations, efforts have been devoted to addressing the partial volume effect in the small airway dimension measurement. Several model-based approaches have used hypothetical point spread functions of a CT system to generate synthetic attenuation profiles of an airway, and the measurements were based on the full-width-half-maximum principle (170,174). Later, to be independent of a specific model and the point spread function, the model-free airway detection approach was developed based on the phase congruency principle for better localization of the airway inner/outer wall boundaries (209). Further, the integral of intensity profiles across the airway wall was added to the FWHM analysis to improve the robustness and accuracy of the airway wall thickness measurement (202). Unfortunately, all of these approaches require precise boundary detection to apply the FWHM principle, leading to a measurement bias towards an overestimation of the wall thickness (210). On the other hand, our proposed integrated technique is independent of the intensity profile and edge detection, as it only relies on the integrated HU signal measurement over an airway ROI. This study demonstrated the feasibility of overcoming the limitations of partial volume effect by calibrating the HUs for air, tissue, and wall material in the non-affected areas, thus allowing accurate measurements of small airway dimensions.

It is also worth mentioning that the determination of the CT values of the inner lumen (air), airway wall material, and the outer lumen (background parenchyma) plays a vital role in the measurement accuracy using the integrated-based technique. Such calibration of the CT values can be implemented by measuring the mean HU within a pure material ROI, which is not affected by the partial volume effect. For instance, to calibrate the air, an ROI should be placed within the lumen where the boundary should be about 5 pixels away from the airway wall. Nevertheless, for small airway measurements, all pixels of lumen and wall within the measurement ROI may be affected by the partial volume effects (**Figures 8.3a and 8.3b**). Instead, the calibration of the mean CT values may be accomplished in a nearby larger airway or other lower generation airways to eliminate the partial volume effect. This calibration step will make the integrated-intensity based method more feasible for clinical implementation.

Further, we evaluated the performance in terms of robustness against varying scanning and reconstruction parameters and accuracy in determining airway dimensions for both IIB and FWHM methods. Our proposed IIB method consistently exhibited high accuracy over FWHM for various scan parameters, including six radiation dose levels, three reconstruction kernels, two reconstruction algorithms, and two gantry tilt angles. No significant variabilities and biases were found using different reconstruction kernels and radiation dose levels for the IIB method, indicating the robustness of the IIB method that can suppress the image noise by integrating the HU signal in a region of interest. The consistent underestimation of ID and overestimation of WT were found using the FHWM in all dose levels, indicating that the spatial resolution limits the

FWHM performance. Regarding the reconstruction modes, our results found that the images reconstructed with the AIDR3D algorithm perform slightly better than the FBP algorithm for both IIB and FWHM methods. Lastly, the IIB method can provide adequate accuracy using low-dose CT on airway phantom measurements. The error in WT was reduced by a factor of two using the IIB method, even at the lowest dose level (0.7 mGy).

Limitations. This study has several limitations. First, a standard chest phantom (30 cm) was used in this study, which is smaller than the average patient size. Although the image quality will degrade with a larger phantom size, the measurement accuracy is not expected to be affected using the integrated-based method. Nevertheless, future studies will need to assess the IIB method using larger phantoms or patients with airway obstructive diseases. Second, the chest phantom contains no cardiac and respiratory motion, which may not reflect the human airway measurements *in vivo*. However, a phantom validation study with known airway (tube) dimensions is important before its clinical implementation. Indeed, the placement of the calibration ROI will be more challenging with motion artifacts; however, the measurement accuracy is expected to be maintained as larger airways can be used for calibration purposes. Third, all the airway phantoms are silicone tubes, resulting in a higher CT value (~300 HU) than the actual airway wall material (~100HU). Fortunately, as long as the CT value of the wall material is measured with no partial volume effect, the IIB measurement accuracy is expected to be unaffected by the material of the wall. Fourth, the proposed method was only evaluated with a Canon scanner using either FBP or AIDR3D reconstruction algorithms. Our results indicate that the AIDR3D algorithm has slightly improved performance on the airway measurement, so it would be interesting to compare the effects of other iterative reconstruction algorithms such as the iDose from Philips, ADMIRE from Siemens, and the forward-projected model-based iterative reconstruction algorithm (FIRST) from Canon using the IIB method in future work. Finally, the IIB method was only compared to the conventional FWHM algorithm; other airway measurement algorithms such as the maximum-likelihood algorithms, deep learning methods will need to be further assessed.

Conclusion

This study proposed and validated a semi-automatic, integrated-intensity based approach for quantification of small airway dimensions. The proposed IIB method shows a factor of two improvement in accuracy and precision as compared to the standard FWHM method in the determination of airway lumen diameter and wall thickness. The IIB method with AIDR3D reconstruction using the FC30 kernel resulted in the most accurate measurement of airway dimensions. This quantitative technique can potentially provide a better understanding of small airway remodeling in patients with COPD and asthma.

Chapter 9 Clinical Translation and Future Work

In this dissertation, the accuracy of regional perfusion measurement was first retrospectively validated in a swine animal model as compared to the quantitative microsphere perfusion measurement. With the optimal timing protocol, the accuracy and the reproducibility of the prospective two-volume perfusion technique was validated against the retrospective perfusion measurement on the whole lung and lobar-basis regional perfusion territories. In combination, the findings indicated that accurate whole-lung and vessel-specific lobar perfusion measurement (in ml/min/g) is feasible with the comprehensive pulmonary CT technique at a significantly reduced radiation and contrast dose, as compared to current dynamic CT perfusion techniques. In addition, small airway dimensions can be accurately assessed using an integrated-based quantification method in a phantom study.

Given these findings, the next step and future direction of the low-dose comprehensive pulmonary CT technique is clinical implementation in human subjects with pulmonary disease. The current study data was acquired at a single center using our Aquilion One Canon CT scanner. A further multi-center and multi-scanner perfusion study needs to be carried out to verify the proposed dynamic CT technique.

<u>Future clinical implementation</u>

Small PE detection

A preliminary study was performed in a swine model to detect small PEs in distal segmental and sub-segmental arteries using the proposed two-volume, comprehensive CT pulmonary technique. The CTPA can be used as the standard diagnostic tool in the examination of PE. Within a single contrast injection, quantitative assessment of pulmonary perfusion can be compared to the CTPA to determine whether it can bring additional clinical value in detection of small PE.

Procedures: Under the fluoroscopy, an 8-Fr Pigtail catheter was placed in the distal left pulmonary artery (left caudal lobe) via right jugular vein (11-F) for induction of PE. After confirming the location of the catheter's tip, two or three gelatin sponge plugs with a 2-mm diameter were injected to produce small PEs in peripheral pulmonary arteries. Thereafter, followed by the contrast injection, the two-volume dynamic CT perfusion was performed prospectively using a helical scan mode. After 15-minute delay for the contrast clearance, two to three more gelatin sponges were injected to gradually increase the degree of PE severity and CT acquisition was repeated. Perfusion measurement was made with the comprehensive CT pulmonary technique under each PE condition (**Figure 9.1**).

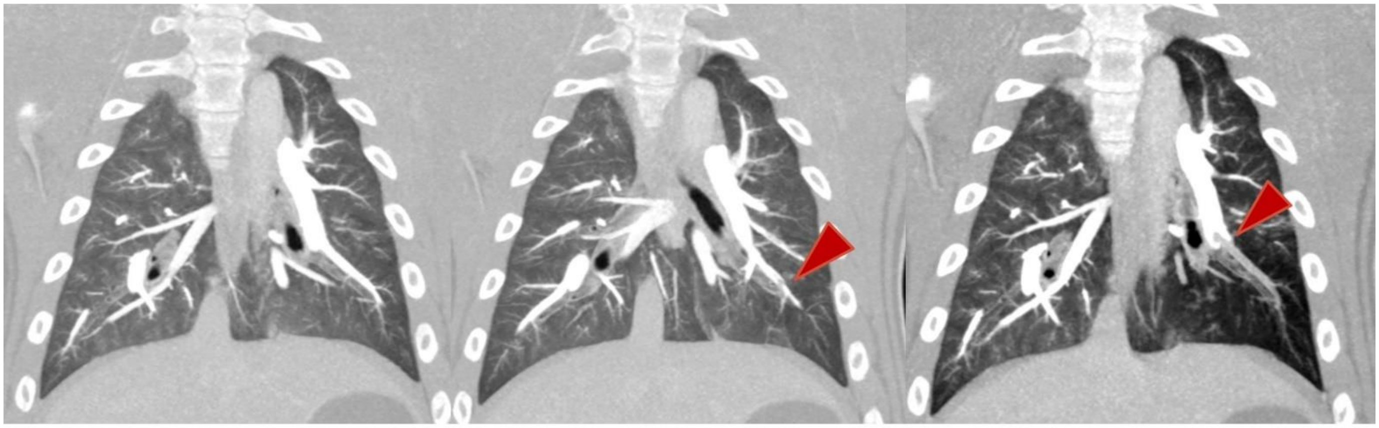

Figure 9.1 CT pulmonary angiography with the presence of small embolus.

An example of the morphological assessment by the CTPA and physiological assessment by the dynamic perfusion is shown in **Figure 9.2**.

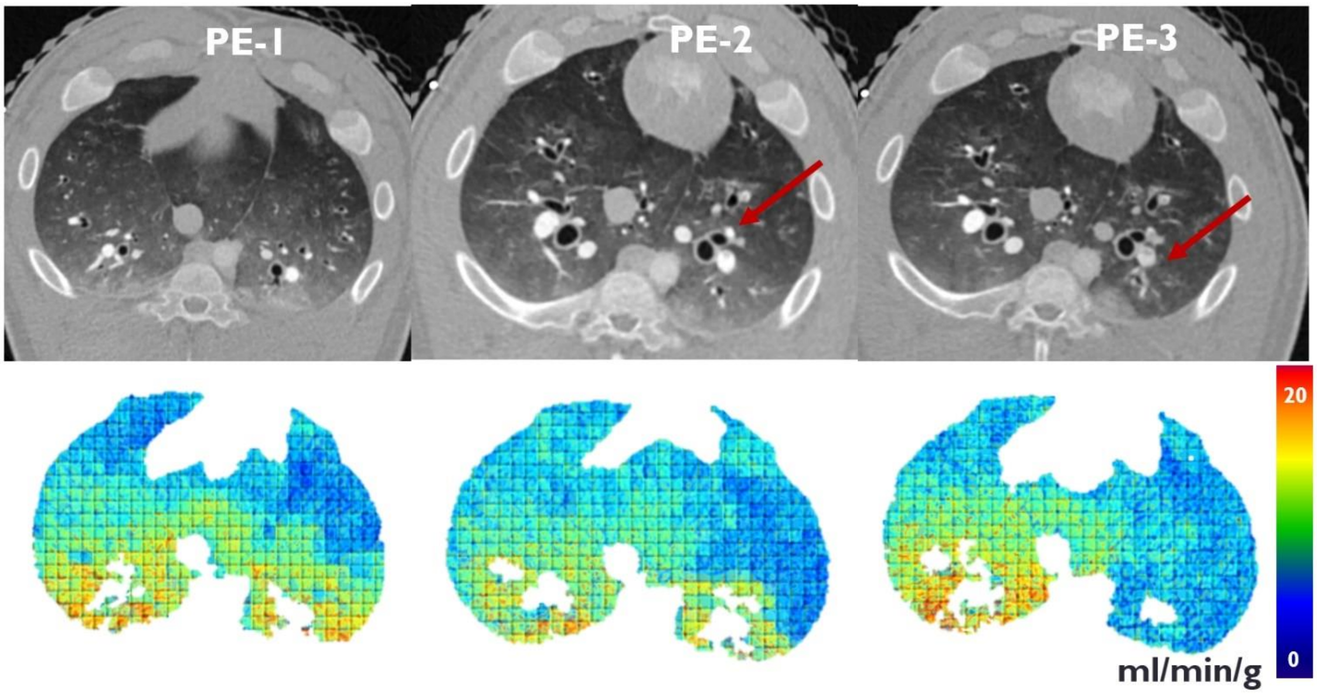

Figure 9.2 Two-volume, whole-lung CT perfusion distribution map with the presence of PE.

PE risk stratification with MCP technique

In Chapter 4, MCP technique was validated for quantifying the PE-distal territory with the perfusion defect territory as the reference standard. The mass and spatial correspondences showed that the MCP technique can accurately quantify the subtended lung tissue distal to a PE using the CTPA image. While the amount of subtended lung tissue at-risk can be quantitatively measured, it is clinically important to relate the subtended mass to the PE severity as other pulmonary arterial obstruction indices and indicators. Subsequently, the diagnostic performance of the MCP technique needs to be assessed in patients with suspected PE in future studies.

Experimental and imaging studies also suggest that the heterogeneity of the distribution of ventilation and perfusion can be observed in various lung diseases, including pulmonary embolism, chronic obstructive pulmonary disease, and lung cancer (137–141,150). The influence of gravity on the measured distribution of blood flow in the lung is largely through the deformation of the parenchymal tissue(211). Also, as previously discussed, the lungs are anatomically and functionally separated into different lobes by lobar fissures; many diseases preferentially impact a particular lobe (150,151). Hence, it is clinically essential to provide perfusion and airway obstruction assessment on specific regions. The vessel-specific MCP technique determines the lobar territories by assigning each voxel to its supplying vessel based on the shortest spatial distance, which does not rely on visualization and manual segmentation of the fissures. Such a technique can be implemented to study the regional perfusion in the presence of tissue deformation and potentially be translated to other perfusion image modalities such as SPECT, PET, and MRI, enabling the cross-validation of regional ventilation/perfusion between different modalities and techniques.

Quantitative assessment of airway alteration

In chapter 8, a semi-automatic and quantitative technique based on the integrated-HU method was validated for the quantification of small airway dimensions. The airway dimensions, including the inner lumen diameter (ID) and the wall thickness (WT), can be accurately measured down to 0.5mm in lumen diameter with an acceptable error using physical airway phantoms as the gold standard. With such high accuracy in small airways, the integrated-HU technique can be implemented to quantify airway dimensions in both healthy human subjects and patients with asthma or COPD. Due to the complexity of the lung anatomy, future works will need to be concentrated on the intensity calibration for airway wall material and the background lung parenchyma, and the selection of measurement regions-of-interest with the presence of nearby airways and vessels.

Differentiation of Pulmonary Nodule Malignancy

The lung has a dual vascular supply by the pulmonary circulation and bronchial circulation, with a trend that malignant nodules have higher portion of bronchial circulation. A first-pass technique may be implemented with four volume scans to assess both pulmonary and bronchial blood flow (**Figures 9.3 and 9.4**). Future studies can aim to assess diagnostic capability of the whole-nodule, first-pass CT technique for the classification pulmonary nodules using low-dose CT perfusion.

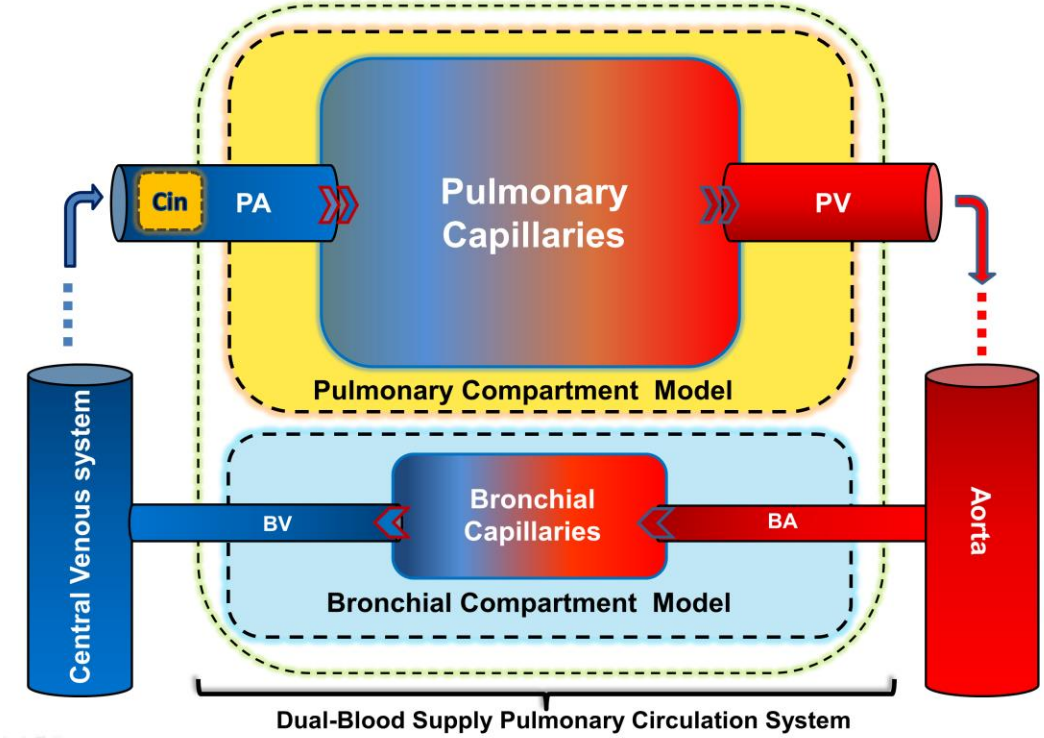

Figure 9.3 Dual-supply pulmonary circulation.

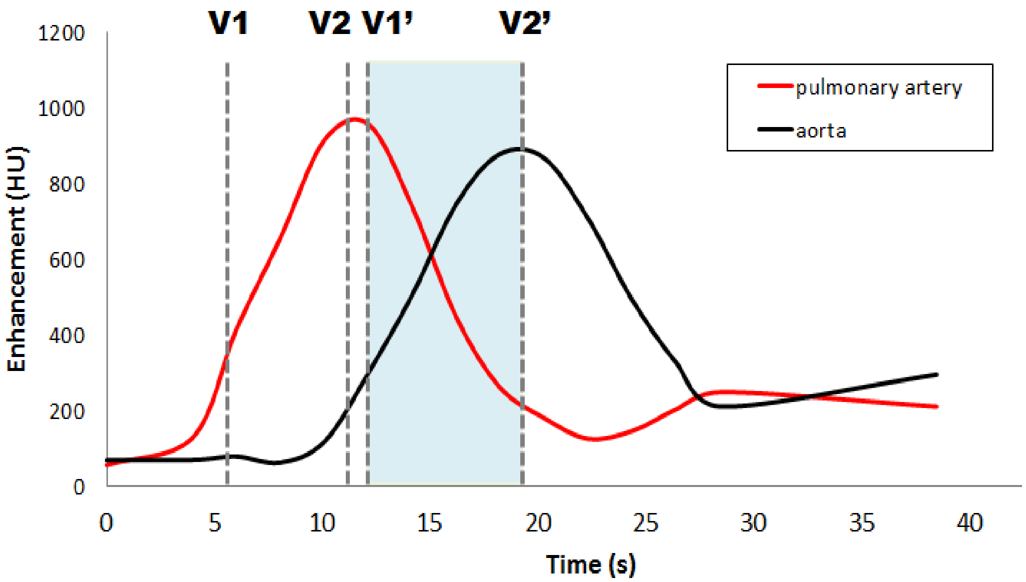

Figure 9.4 Contrast-enhanced arterial input functions for pulmonary artery and descending aorta.

A preliminary study was conducted in nineteen patients (8 males, 11 females; mean age of 61 years) with pulmonary nodules where patients underwent low-dose dynamic CT perfusion scan and histopathological diagnosis. A total of 20 volume scans were acquired using a 320-detector CT scanner for duration of 90 seconds after 40 mL of contrast followed by a 40 mL saline chaser at an injection rate of 5 ml/sec. Pulmonary arterial perfusion (PAP) and bronchial arterial perfusion (BAP) in ml/min/100ml and Perfusion Index (PI = PAP/(PAP+BAP)) were assessed using all 20 volume scans for dual-input maximum slope model (MSM) perfusion using standard 2D technique. For the novel, dual-input, whole nodule first-pass analysis (FPA) measurement, only four volume scans were used to obtain absolute PAP, BAP (both in ml/min/g) and PI. Average perfusion values within the entire tumor were compared with the biopsy results as the reference standard.

By using the perfusion index with a cutoff threshold of 0.6 for MSM technique and 0.5 for the FPA technique, the overall accuracy, sensitivity, and specificity were 0.47, 0.46, 0.50 and 0.68, 0.73, 0.63, respectively. The effective radiation dose for the MSM and the FPA technique were estimated to be 26 and 2.4 mSv, respectively. Representative perfusion maps of both malignant and benign cases are shown in **Figure 9.5**. The preliminary results indicate that the whole-nodule, first-pass analysis perfusion technique was more accurate in detecting malignant pulmonary nodules using the perfusion index as an imaging biomarker, while simultaneously lowering the radiation dose by a factor of 10 when compared to standard maximum slope low-dose CT perfusion techniques. Whole nodule first-pass technique can be prospectively implemented to substantially reduce patient dose while accurately detecting malignant pulmonary nodules.

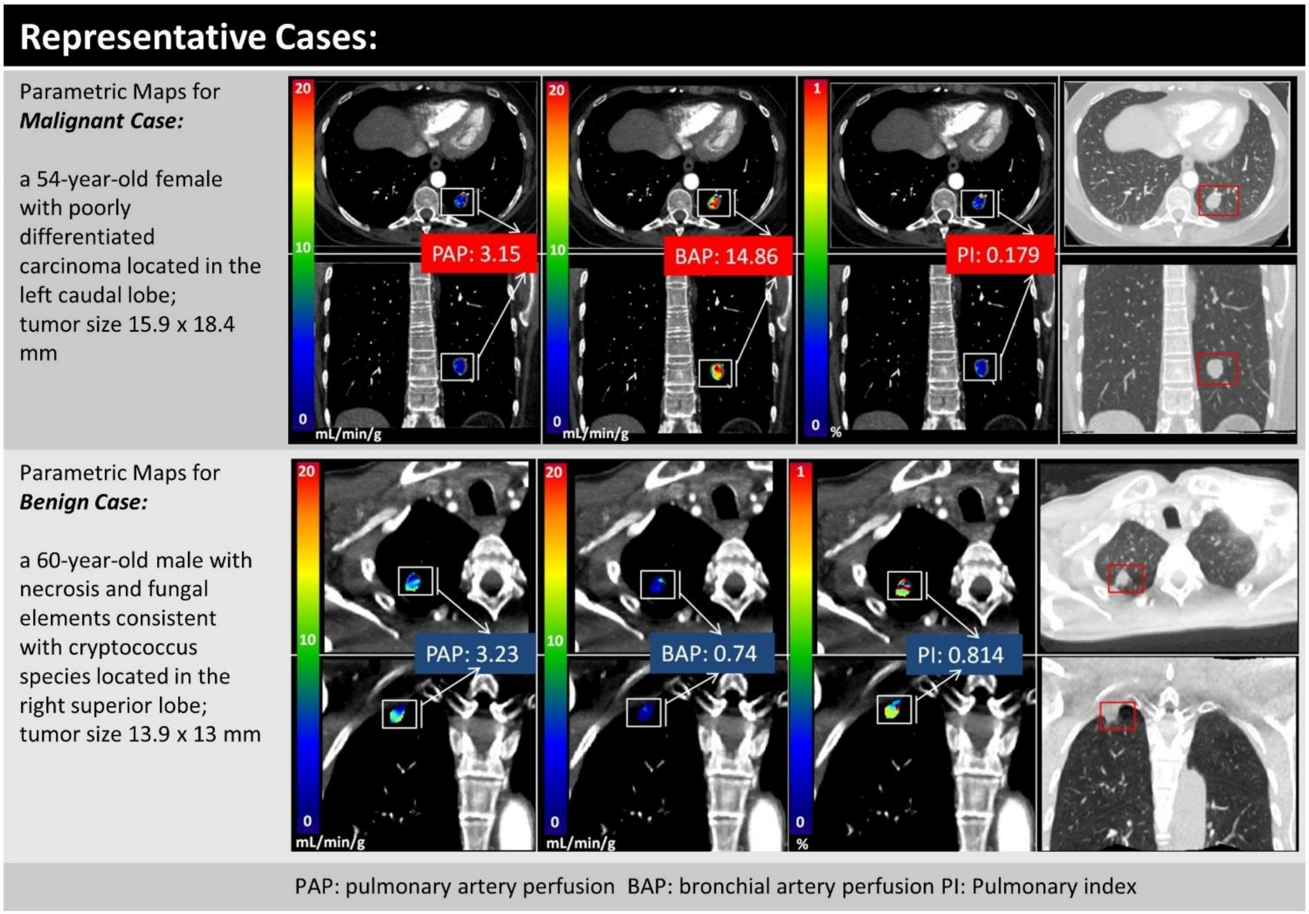
Representative Cases:

Parametric Maps for ***Malignant Case:***

a 54-year-old female with poorly differentiated carcinoma located in the left caudal lobe; tumor size 15.9 x 18.4 mm

Parametric Maps for ***Benign Case:***

a 60-year-old male with necrosis and fungal elements consistent with cryptococcus species located in the right superior lobe; tumor size 13.9 x 13 mm

PAP: pulmonary artery perfusion BAP: bronchial artery perfusion PI: Pulmonary index

Figure 9.5 Representative cases of lung nodule malignance differentiation.

Conclusion

The research as part of this dissertation addresses the unmet clinical need through the development, validation, and preliminary clinical translation of an accurate, low-dose, comprehensive pulmonary CT technique based on first-pass analysis. A comprehensive CT technique can provide the morphological and physiological assessments of pulmonary disease by a single low-dose CT examination at a substantially reduced radiation dose. In addition, a semi-automatic, integrated-intensity based approach was validated for quantification of small airway dimensions, enabling a better understanding of small airway remodeling in patients with COPD and asthma. The proposed CT-based techniques make the quantitative assessment of pulmonary diseases more reliable, accessible, and impactful to patients in need.

REFERENCES

1. Giuntini C, Di Ricco G, Marini C, Melillo E, Palla A. Pulmonary embolism: epidemiology. Chest. 1995 Jan;107(1 Suppl):3S-9S.

2. Doğan H, de Roos A, Geleijins J, Huisman MV, Kroft LJM. The role of computed tomography in the diagnosis of acute and chronic pulmonary embolism. Diagn Interv Radiol. 2015;21(4):307–16.

3. Nielsen JD. The incidence of pulmonary embolism during deep vein thrombosis. Phlebology. 2013 Mar;28 Suppl 1:29–33.

4. Essien E-O, Rali P, Mathai SC. Pulmonary Embolism. Medical Clinics of North America. 2019 May;103(3):549–64.

5. Wiener R, Schwartz L, Woloshin S. Time Trends In Pulmonary Embolism In The United States: Evidence Of Overdiagnosis? In: D14 INNOVATIVE HEALTH SERVICES RESEARCH TO IMPROVE OUTCOMES [Internet]. American Thoracic Society; 2010 [cited 2021 Jul 16]. p. A5348–A5348. Available from: http://www.atsjournals.org/doi/abs/10.1164/ajrccm-conference.2010.181.1_MeetingAbstracts.A5348

6. Beckman MG, Hooper WC, Critchley SE, Ortel TL. Venous Thromboembolism: A Public Health Concern. American Journal of Preventive Medicine. 2010 Apr 1;38(4, Supplement):S495–501.

7. Fedullo PF, Yung GL. Pulmonary Thromboembolic Disease. In: Grippi MA, Elias JA, Fishman JA, Kotloff RM, Pack AI, Senior RM, et al., editors. Fishman's Pulmonary Diseases and Disorders [Internet]. 5th ed. New York, NY: McGraw-Hill Education; 2015 [cited 2021 Aug 4]. Available from: accessmedicine.mhmedical.com/content.aspx?aid=1122362776

8. Goldhaber SZ. Epidemiology of Pulmonary Embolism. Semin Vasc Med. 2001;01(2):139–46.

9. Toplis E, Mortimore G. The diagnosis and management of pulmonary embolism. Br J Nurs. 2020 Jan 9;29(1):22–6.

10. Kruger PC, Eikelboom JW, Douketis JD, Hankey GJ. Pulmonary embolism: update on diagnosis and management. Med J Aust. 2019 Jul;211(2):82–7.

11. Corrigan D, Prucnal C, Kabrhel C. Pulmonary embolism: the diagnosis, risk-stratification, treatment and disposition of emergency department patients. Clin Exp Emerg Med. 2016 Sep 30;3(3):117–25.

12. Lan NSH, Massam BD, Kulkarni SS, Lang CC. Pulmonary Arterial Hypertension: Pathophysiology and Treatment. Diseases. 2018 May 16;6(2):38.

13. Badesch DB, Raskob GE, Elliott CG, Krichman AM, Farber HW, Frost AE, et al. Pulmonary arterial hypertension: baseline characteristics from the REVEAL Registry. Chest. 2010 Feb;137(2):376–87.

14. Frost AE, Badesch DB, Barst RJ, Benza RL, Elliott CG, Farber HW, et al. The Changing Picture of Patients With Pulmonary Arterial Hypertension in the United States: How REVEAL Differs From Historic and Non-US Contemporary Registries. Chest. 2011 Jan 1;139(1):128–37.

15. Badesch DB, Abman SH, Ahearn GS, Barst RJ, McCrory DC, Simonneau G, et al. Medical therapy for pulmonary arterial hypertension: ACCP evidence-based clinical practice guidelines. Chest. 2004 Jul;126(1 Suppl):35S-62S.

16. Wright JL, Churg A. Pathology of Chronic Obstructive Pulmonary Disease: Diagnostic Features and Differential Diagnosis. In: Grippi MA, Elias JA, Fishman JA, Kotloff RM, Pack AI, Senior RM, et al., editors. Fishman’s Pulmonary Diseases and Disorders [Internet]. 5th ed. New York, NY: McGraw-Hill Education; 2015 [cited 2021 Aug 9]. Available from: accessmedicine.mhmedical.com/content.aspx?aid=1122358638

17. Rabe KF, Watz H. Chronic obstructive pulmonary disease. The Lancet. 2017 May 13;389(10082):1931–40.

18. Mannino DM, Buist AS. Global burden of COPD: risk factors, prevalence, and future trends. The Lancet. 2007 Sep;370(9589):765–73.

19. Welte T, Vogelmeier C, Papi A. COPD: early diagnosis and treatment to slow disease progression. Int J Clin Pract. 2015 Mar;69(3):336–49.

20. Fishman’s Pulmonary Diseases and Disorders, 5e | AccessMedicine | McGraw Hill Medical [Internet]. [cited 2021 Aug 3]. Available from: https://accessmedicine.mhmedical.com/book.aspx?bookid=1344#72095619

21. Johns CS, Swift AJ, Hughes PJC, Ohno Y, Schiebler M, Wild JM. Pulmonary MR angiography and perfusion imaging—A review of methods and applications. European Journal of Radiology. 2017 Jan 1;86:361–70.

22. Pistolesi M, Miniati M, Di Ricco G, Marini C, Giuntini C. Perfusion lung imaging in the adult respiratory distress syndrome. Journal of Thoracic Imaging. 1986 Jul;1(3):11–24.

23. Ohno Y, Koyama H, Lee HY, Miura S, Yoshikawa T, Sugimura K. Contrast-enhanced CT- and MRI-based perfusion assessment for pulmonary diseases: basics and clinical applications. Diagn Interv Radiol. 2016 Sep;22(5):407–21.

24. Reinartz P, Wildberger JE, Schaefer W, Nowak B, Mahnken AH, Buell U. Tomographic Imaging in the Diagnosis of Pulmonary Embolism: A Comparison Between V/Q Lung Scintigraphy in SPECT Technique and Multislice Spiral CT. :8.

25. Imaging lung perfusion | Journal of Applied Physiology [Internet]. [cited 2021 Aug 4]. Available from: https://journals.physiology.org/doi/full/10.1152/japplphysiol.00320.2012

26. Uematsu H, Ohno Y, Hatabu H. Recent advances in magnetic resonance perfusion imaging of the lung. Top Magn Reson Imaging. 2003 Jun;14(3):245–51.

27. Pedersen MR, Fisher MT, van Beek EJR. MR imaging of the pulmonary vasculature--an update. Eur Radiol. 2006 Jun;16(6):1374–86.

28. Hatabu H, Gaa J, Kim D, Li W, Prasad PV, Edelman RR. Pulmonary perfusion and angiography: evaluation with breath-hold enhanced three-dimensional fast imaging steady-state precession MR imaging with short TR and TE. American Journal of Roentgenology. 1996 Sep;167(3):653–5.

29. Hatabu H, Gaa J, Kim D, Li W, Prasad PV, Edelman RR. Pulmonary perfusion: Qualitative assessment with dynamic contrast-enhanced MRI using ultra-short TE and inversion recovery turbo FLASH. Magnetic Resonance in Medicine. 1996;36(4):503–8.

30. Wild JM, Marshall H, Bock M, Schad LR, Jakob PM, Puderbach M, et al. MRI of the lung (1/3): methods. Insights Imaging. 2012 Aug 1;3(4):345–53.

31. Lee CW, Seo JB, Song JW, Kim MY, Lee HY, Park YS, et al. Evaluation of computer-aided detection and dual energy software in detection of peripheral pulmonary embolism on dual-energy pulmonary CT angiography. European radiology. 2011;21(1):54–62.

32. Pontana F, Faivre JB, Remy-Jardin M, Flohr T, Schmidt B, Tacelli N, et al. Lung perfusion with dual-energy multidetector-row CT (MDCT): feasibility for the evaluation of acute pulmonary embolism in 117 consecutive patients. Academic radiology. 2008;15(12):1494–504.

33. Ohno Y, Koyama H, Matsumoto K, Onishi Y, Takenaka D, Fujisawa Y, et al. Differentiation of Malignant and Benign Pulmonary Nodules with Quantitative First-Pass 320-Detector Row Perfusion CT versus FDG PET/CT. Radiology Radiology. 2011;258(2):599–609.

34. Yuan X, Zhang J, Quan C, Cao J, Ao G, Tian Y, et al. Differentiation of malignant and benign pulmonary nodules with first-pass dual-input perfusion CT. European Radiology. 2013;23(9):2469–74.

35. Shan F, Zhang Z, Xing W, Qiu J, Yang S, Wang J, et al. Differentiation between malignant and benign solitary pulmonary nodules: Use of volume first-pass perfusion and combined with routine computed tomography. European Journal of Radiology. 2012 Nov 1;81(11):3598–605.

36. Ng Q-S, Goh V, Fichte H, Klotz E, Fernie P, Saunders MI, et al. Lung cancer perfusion at multi-detector row CT: reproducibility of whole tumor quantitative measurements. Radiology. 2006 May;239(2):547–53.

37. Hoffman EA, Chon D. Computed tomography studies of lung ventilation and perfusion. Proc Am Thorac Soc. 2005;2(6):492–8, 506.

38. Herzog P, Wildberger JE, Niethammer M, Schaller S, Schoepf UJ. CT perfusion imaging of the lung in pulmonary embolism. Acad Radiol. 2003 Oct;10(10):1132–46.

39. Hwang HJ, Hoffman EA, Lee CH, Goo JM, Levin DL, Kauczor H-U, et al. The role of dual-energy computed tomography in the assessment of pulmonary function. European Journal of Radiology. 2017;86:320–34.

40. Ferda J, Ferdova E, Mirka H, Baxa J, Bednarova A, Flohr T, et al. Pulmonary imaging using dual-energy CT, a role of the assessment of iodine and air distribution. European journal of radiology. 2011;77(2):287–93.

41. Millner MR, McDavid WD, Waggener RG, Dennis MJ, Payne WH, Sank VJ. Extraction of information from CT scans at different energies. Med Phys. 1979 Feb;6(1):70–1.

42. Kim HS, Jeong ES, Yang MH, Yang S-O. Bone mineral density assessment for research purpose using dual energy X-ray absorptiometry. Osteoporos Sarcopenia. 2018 Sep;4(3):79–85.

43. Chiro GD, Brooks RA, Kessler RM, Johnston GS, Jones AE, Herdt JR, et al. Tissue signatures with dual-energy computed tomography. Radiology. 1979 May;131(2):521–3.

44. Johnson TRC, Krauss B, Sedlmair M, Grasruck M, Bruder H, Morhard D, et al. Material differentiation by dual energy CT: initial experience. Eur Radiol. 2007 Jun;17(6):1510–7.

45. Thieme SF, Johnson TR, Lee C, McWilliams J, Becker CR, Reiser MF, et al. Dual-energy CT for the assessment of contrast material distribution in the pulmonary parenchyma. AJR Am J Roentgenol. 2009;193(1):144–9.

46. Geyer LL, Scherr M, Körner M, Wirth S, Deak P, Reiser MF, et al. Imaging of acute pulmonary embolism using a dual energy CT system with rapid kVp switching: initial results. Eur J Radiol. 2012 Dec;81(12):3711–8.

47. Nance JW, Henzler T, Meyer M, Apfaltrer P, Braunagel M, Krissak R, et al. Optimization of contrast material delivery for dual-energy computed tomography pulmonary angiography in patients with suspected pulmonary embolism. Invest Radiol. 2012 Jan;47(1):78–84.

48. Thieme SF, Johnson TRC, Lee C, McWilliams J, Becker CR, Reiser MF, et al. Dual-energy CT for the assessment of contrast material distribution in the pulmonary parenchyma. AJR Am J Roentgenol. 2009 Jul;193(1):144–9.

49. Doğan H, de Roos A, Geleijins J, Huisman MV, Kroft LJM. The role of computed tomography in the diagnosis of acute and chronic pulmonary embolism. Diagn Interv Radiol. 2015;21(4):307–16.

50. van der Hulle T, Cheung WY, Kooij S, Beenen LFM, van Bemmel T, van Es J, et al. Simplified diagnostic management of suspected pulmonary embolism (the YEARS study): a prospective, multicentre, cohort study. The Lancet. 2017 Jul 15;390(10091):289–97.

51. Wiener RS, Schwartz LM, Woloshin S. Time Trends in Pulmonary Embolism in the United States: Evidence of Overdiagnosis. Arch Intern Med. 2011 May 9;171(9):831–7.

52. Hoffman EA, Simon BA, McLennan G. State of the Art. A structural and functional assessment of the lung via multidetector-row computed tomography: phenotyping chronic obstructive pulmonary disease. Proceedings of the American Thoracic Society. 2006;3(6):519–32.

53. Hoffman EA, Reinhardt JM, Sonka M, Simon BA, Guo J, Saba O, et al. Characterization of the interstitial lung diseases via density-based and texture-based analysis of computed tomography images of lung structure and function. Academic radiology. 2003;10(10):1104–18.

54. Hopkins SR, Wielpütz MO, Kauczor H-U. Imaging lung perfusion. Journal of Applied Physiology. 2012;113(2):328–39.

55. Chon D, Beck KC, Larsen RL, Shikata H, Hoffman EA. Regional pulmonary blood flow in dogs by 4D-X-ray CT. Journal of applied physiology (Bethesda, Md : 1985). 2006;101(5):1451–65.

56. Dakin JH, Evans TW, Hansell DM, Hoffman EA. Regional Pulmonary Blood Flow in Humans and Dogs by 4D Computed Tomography. Academic Radiology. 2008;15(7):844–52.

57. Fuld MK, Halaweish AF, Haynes SE, Divekar AA, Guo J, Hoffman EA. Pulmonary perfused blood volume with dual-energy CT as surrogate for pulmonary perfusion assessed with dynamic multidetector CT. Radiology. 2013;267(3):747–56.

58. Larici AR, Calandriello L, Amato M, Silvestri R, del Ciello A, Molinari F, et al. First-pass perfusion of non-small-cell lung cancer (NSCLC) with 64-detector-row CT: a study of technique repeatability and intra- and interobserver variability. La radiologia medica. 2014;119(1):4–12.

59. Ohno Y, Nishio M, Koyama H, Seki S, Tsubakimoto M, Fujisawa Y, et al. Solitary pulmonary nodules: Comparison of dynamic first-pass contrast-enhanced perfusion area-detector CT, dynamic first-pass contrast-enhanced MR imaging, and FDG PET/CT. Radiology. 2015;274(2):563–75.

60. Lossnitzer D, Baumann S, Henzler T. Dynamic four-dimensional CT angiography for the assessment of pulmonary perfusion in an adult patient with pulmonary artery occlusion and major aortopulmonary collateral after multistage repair of Fallot’s Pentalogy. Cardiology in the young. 2017;27(6):1212–3.

61. Nguyen-Kim TD, Frauenfelder T, Strobel K, Veit-Haibach P, Huellner MW. Assessment of bronchial and pulmonary blood supply in non-small cell lung cancer subtypes using computed tomography perfusion. Investigative radiology. 2015;50(3):179–86.

62. Molloi S, Qian YJ, Ersahin A. Absolute volumetric blood flow measurements using dual-energy digital subtraction angiography. Med Phys. 1993;20(1):85–91.

63. Molloi S, Zhou Y, Kassab GS. Regional volumetric coronary blood flow measurement by digital angiography: in vivo validation. Acad Radiol. 2004;11(7):757–66.

64. Ziemer BP, Hubbard L, Lipinski J, Molloi S. Dynamic CT perfusion measurement in a cardiac phantom. Int J Cardiovas Imag Int J Cardiovas Imag. 2015;31(7):1451–9.

65. Hubbard L, Ziemer B, Lipinski J, Sadeghi B, Javan H, Groves EM, et al. Functional Assessment of Coronary Artery Disease Using Whole-Heart Dynamic Computed Tomographic Perfusion. Circulation Cardiovascular imaging. 2016;9(12).

66. Hubbard L, Lipinski J, Ziemer B, Malkasian S, Sadeghi B, Javan H, et al. Comprehensive Assessment of Coronary Artery Disease by Using First-Pass Analysis Dynamic CT Perfusion: Validation in a Swine Model. Radiology. 2018;286(1):93–102.

67. Glenny R, Bernard S, Brinkley M. Validation of fluorescent-labeled microspheres for measurement of regional organ perfusion. Journal of Applied Physiology. 1993;74(5):2585–97.

68. Molloi S, Bednarz G, Tang J, Zhou Y, Mathur T. Absolute volumetric coronary blood flow measurement with digital subtraction angiography. Int J Card Imaging. 1998;14(3):137–45.

69. Busse N, Erwin W, Pan T. Evaluation of a semiautomated lung mass calculation technique for internal dosimetry applications. Medical physics. 2013;40(12):122503.

70. Boone J, Strauss K, Cody D, McCollough C, McNitt-Gray M, Toth T, et al. Size-specific dose estimates (SSDE) in pediatric and adult body CT examinations: report of AAPM task group 204. College Park, Md: American Association of Physicists in Medicine. 2011;

71. McCollough C, Bakalyar DM, Bostani M, Brady S, Boedeker K, Boone JM, et al. Use of Water Equivalent Diameter for Calculating Patient Size and Size-Specific Dose Estimates (SSDE) in CT: The Report of AAPM Task Group 220. AAPM Rep. 2014;2014:6–23.

72. McCollough C CD Edyvean S, Geise R, et al. The Measurement, Reporting, and Management of Radiation Dose in CT. 2008.

73. Modat M, Ridgway GR, Taylor ZA, Lehmann M, Barnes J, Hawkes DJ, et al. Fast free-form deformation using graphics processing units. Comput Methods Programs Biomed. 2010;98(3):278–84.

74. Shikata H, Hoffman EA, Sonka M. Automated segmentation of pulmonary vascular tree from 3D CT images. In: Medical Imaging 2004. SPIE; 2004. p. 10.

75. Lin LI. A concordance correlation coefficient to evaluate reproducibility. Biometrics. 1989;45(1):255–68.

76. Eldridge SM, Ukoumunne OC, Carlin JB. The intra-cluster correlation coefficient in cluster randomized trials: a review of definitions. Int Stat Rev. 2009;77(3):378–94.

77. Kerry SM, Bland JM. The intracluster correlation coefficient in cluster randomisation. BMJ. 1998;316(7142):1455.

78. Nabavi DG, Cenic A, Dool J, Smith RM, Espinosa F, Craen RA, et al. Quantitative assessment of cerebral hemodynamics using CT: stability, accuracy, and precision studies in dogs. J Comput Assist Tomogr. 1999;23(4):506–15.

79. van Elmpt W, Das M, Hullner M, Sharifi H, Zegers K, Reymen B, et al. Characterization of tumor heterogeneity using dynamic contrast enhanced CT and FDG-PET in non-small cell lung cancer. Radiotherapy and Oncology. 2013;109(1):65–70.

80. Hubbard L, Malkasian S, Zhao Y, Abbona P, Molloi S. Timing optimization of low-dose first-pass analysis dynamic CT myocardial perfusion measurement: validation in a swine model. Eur Radiol Exp. 2019;3(1):16.

81. Hubbard L, Malkasian S, Zhao Y, Abbona P, Molloi S. Contrast-to-Noise Ratio Optimization in Coronary Computed Tomography Angiography: Validation in a Swine Model. Acad Radiol [Internet]. 2018; Available from: http://www.ncbi.nlm.nih.gov/pubmed/30172714

82. Venkat B, Sharma S, Sharma D, Sood S, Aggarwal N, Sarkar M, et al. CT perfusion in non-small cell lung cancers for assessing treatment response, monitoring treatment and predicting prognosis. The Egyptian Journal of Radiology and Nuclear Medicine. 2018;49(2):338–45.

83. Stenner P, Schmidt B, Allmendinger T, Flohr T, Kachelrie M. Dynamic iterative beam hardening correction (DIBHC) in myocardial perfusion imaging using contrast-enhanced computed tomography. Investigative Radiology. 2010;45(6):314–23.

84. Kitagawa K, George RT, Arbab-Zadeh A, Lima JA, Lardo AC. Characterization and correction of beam-hardening artifacts during dynamic volume CT assessment of myocardial perfusion. Radiology. 2010;256(1):111–8.

85. Ippolito D, Capraro C, Guerra L, De Ponti E, Messa C, Sironi S. Feasibility of perfusion CT technique integrated into conventional 18FDG/PET-CT studies in lung cancer patients: clinical staging and functional information in a single study. Eur J Nucl Med Mol Imaging. 2013;40(2):156–65.

86. Moradi F, Morris TA, Hoh CK. Perfusion Scintigraphy in Diagnosis and Management of Thromboembolic Pulmonary Hypertension. Radiographics. 2019;39(1):169–85.

87. Mirsadraee S, Reid JH, Connell M, MacNee W, Hirani N, Murchison JT, et al. Dynamic (4D) CT perfusion offers simultaneous functional and anatomical insights into pulmonary embolism resolution. European Journal of Radiology. 2016;85(10):1883–90.

88. Hubbard L, Malkasian S, Zhao Y, Abbona P, Kwon J, Molloi S. Low-Radiation-Dose Stress Myocardial Perfusion Measurement Using First-Pass Analysis Dynamic Computed Tomography: A Preliminary Investigation in a Swine Model. Invest Radiol. 2019;54(12):774–80.

89. Kay FU, Beraldo MA, Nakamura MAM, De Santis Santiago R, Torsani V, Gomes S, et al. Quantitative Dual-Energy Computed Tomography Predicts Regional Perfusion Heterogeneity in a Model of Acute Lung Injury. J Comput Assist Tomogr. 2018;42(6):866–72.

90. Grob D, Smit E, Prince J, Kist J, Stoger L, Geurts B, et al. Iodine Maps from Subtraction CT or Dual-Energy CT to Detect Pulmonary Emboli with CT Angiography: A Multiple-Observer Study. Radiology. 2019;292(1):197–205.

91. Hoey ET, Mirsadraee S, Pepke-Zaba J, Jenkins DP, Gopalan D, Screaton NJ. Dual-energy CT angiography for assessment of regional pulmonary perfusion in patients with chronic thromboembolic pulmonary hypertension: initial experience. AJR American journal of roentgenology. 2011;196(3):524–32.

92. Koike H, Sueyoshi E, Sakamoto I, Uetani M, Nakata T, Maemura K. Quantification of lung perfusion blood volume (lung PBV) by dual-energy CT in patients with chronic thromboembolic pulmonary hypertension (CTEPH) before and after balloon pulmonary angioplasty (BPA): Preliminary results. European Journal of Radiology. 2016;85(9):1607–12.

93. Zhao Y, Hubbard L, Malkasian S, Abbona P, Molloi S. Dynamic pulmonary CT perfusion using first-pass analysis technique with only two volume scans: Validation in a swine model. Plos One. 2020;15(2):e0228110.

94. Bae KT. Intravenous contrast medium administration and scan timing at CT: considerations and approaches. Radiology. 2010;256(1):32–61.

95. Bae KT, Seeck BA, Hildebolt CF, Tao C, Zhu F, Kanematsu M, et al. Contrast Enhancement in Cardiovascular MDCT: Effect of Body Weight, Height, Body Surface Area, Body Mass Index, and Obesity. American Journal of Roentgenology. 2008 Mar 1;190(3):777–84.

96. Awai K, Hiraishi K, Hori S. Effect of Contrast Material Injection Duration and Rate on Aortic Peak Time and Peak Enhancement at Dynamic CT Involving Injection Protocol with Dose Tailored to Patient Weight. Radiology. 2004 Jan 1;230(1):142–50.

97. Higaki T, Nakaura T, Kidoh M, Yuki H, Yamashita Y, Nakamura Y, et al. Effect of contrast material injection duration on arterial enhancement at CT in patients with various cardiac indices: Analysis using computer simulation. Plos One. 2018;13(2):e0191347.

98. Cademartiri F, Van Der Lugt A, Luccichenti G, Pavone P, Krestin GP. Parameters affecting bolus geometry in CTA: a review. J Comput Assist Tomogr. 2002;26(4):598–607.

99. Garcia P, Genin G, Bret PM, Bonaldi VM, Reinhold C, Atri M. Hepatic CT enhancement: effect of the rate and volume of contrast medium injection in an animal model. Abdominal Imaging. 1999;24(6):597–603.

100. Han JK, Kim AY, Lee KY, Seo JB, Kim TK, Choi BI, et al. Factors influencing vascular and hepatic enhancement at CT: experimental study on injection protocol using a canine model. J Comput Assist Tomogr. 2000;24(3):400–6.

101. Ng CS, Chandler AG, Wei W, Anderson EF, Herron DH, Kurzrock R, et al. Effect of Sampling Frequency on Perfusion Values in Perfusion CT of Lung Tumors. American Journal of Roentgenology. 2013;200(2):W155–62.

102. Kong WF, Wang YT, Yin LL, Pu H, Tao KY. Clinical risk stratification of acute pulmonary embolism: comparing the usefulness of CTA obstruction score and pulmonary perfusion defect score with dual-energy CT. Int J Cardiovasc Imaging. 2017;33(12):2039–47.

103. Schoepf UJ, Costello P. CT Angiography for Diagnosis of Pulmonary Embolism: State of the Art. Radiology. 2004;230(2):329–37.

104. Remy-Jardin M, Pistolesi M, Goodman LR, Gefter WB, Gottschalk A, Mayo JR, et al. Management of Suspected Acute Pulmonary Embolism in the Era of CT Angiography: A Statement from the Fleischner Society. Radiology. 2007;245(2):315–29.

105. Sauter A, Koehler T, Fingerle AA, Brendel B, Richter V, Rasper M, et al. Ultra Low Dose CT Pulmonary Angiography with Iterative Reconstruction. Plos One. 2016;11(9):e0162716.

106. Sharma S, Lucas CD. Increasing use of CTPA for the investigation of suspected pulmonary embolism. Postgrad Med. 2017;129(2):193–7.

107. Moore AJE, Wachsmann J, Chamarthy MR, Panjikaran L, Tanabe Y, Rajiah P. Imaging of acute pulmonary embolism: an update. Cardiovasc Diagn Ther. 2018;8(3):225–43.

108. van Es J, Douma RA, Schreuder SM, Middeldorp S, Kamphuisen PW, Gerdes VEA, et al. Clinical impact of findings supporting an alternative diagnosis on CT pulmonary angiography in patients with suspected pulmonary embolism. Chest. 2013;144(6):1893–9.

109. Hinzpeter R, Eberhard M, Gutjahr R, Reeve K, Pfammatter T, Lachat M, et al. CT Angiography of the Aorta: Contrast Timing by Using a Fixed versus a Patient-specific Trigger Delay. Radiology. 2019;291(2):531–8.

110. Fleischmann D, Kamaya A. Optimal vascular and parenchymal contrast enhancement: the current state of the art. Radiol Clin North Am. 2009;47(1):13–26.

111. Higashigaito K, Schmid T, Puippe G, Morsbach F, Lachat M, Seifert B, et al. CT Angiography of the Aorta: Prospective Evaluation of Individualized Low-Volume Contrast Media Protocols. Radiology. 2016 Sep;280(3):960–8.

112. Brenner DJ. Should We be Concerned About the Rapid Increase in CT Usage? Reviews on Environmental Health. 2010;25(1, Sp. Iss. SI):63–7.

113. Patel S, Kazerooni EA, Cascade PN. Pulmonary embolism: optimization of small pulmonary artery visualization at multi-detector row CT. Radiology. 2003;227(2):455–60.

114. Schoellnast H, Deutschmann HA, Fritz GA, Stessel U, Schaffler GJ, Tillich M. MDCT angiography of the pulmonary arteries: influence of iodine flow concentration on vessel attenuation and visualization. AJR Am J Roentgenol. 2005;184(6):1935–9.

115. Nijhof WH, Jansen MM, Jager GJ, Slump CH, Rutten MJ. Feasibility of a low concentration test bolus in CT angiography. Clin Radiol. 2016;71(12):1313 e1-1313 e4.

116. Moradi M, Khalili B. Qualitative indices and enhancement rate of CT pulmonary angiography in patients with suspected pulmonary embolism: Comparison between test bolus and bolus-tracking methods. Adv Biomed Res. 2016;5:113.

117. Wang M, Li W, Lun-Hou D, Li J, Zhai R. Optimizing computed tomography pulmonary angiography using right atrium bolus monitoring combined with spontaneous respiration. European Radiology. 2015;25(9):2541–6.

118. Kai N, Oda S, Utsunomiya D, Nakaura T, Funama Y, Kidoh M, et al. Dual-region-of-interest bolus-tracking technique for coronary computed tomographic angiography on a 320-row scanner: reduction in the interpatient variability of arterial contrast enhancement. Br J Radiol. 2018;91(1081):20170541.

119. Cao L, Liu X, Li J, Liang W, Qu T, Li Y, et al. Improving the Degree and Uniformity of Enhancement in Coronary CT Angiography with a New Bolus Tracking Method Enabled By Free Breathing. Acad Radiol. 2019;26(12):1591–6.

120. Yoshida M, Matsumoto Y, Masuda T, Kikuhara Y, Kobayashi Y, Yoshiura T, et al. [Comparison of Contrast Enhancement between Bolus-tracking and Test-bolus Methods on Coronary CT Angiography]. Nihon Hoshasen Gijutsu Gakkai Zasshi. 2020;76(6):579–85.

121. Cademartiri F, Nieman K, van der Lugt A, Raaijmakers RH, Mollet N, Pattynama PM, et al. Intravenous contrast material administration at 16-detector row helical CT coronary angiography: test bolus versus bolus-tracking technique. Radiology. 2004;233(3):817–23.

122. McHugh ML. Interrater reliability: the kappa statistic. Biochem Med (Zagreb). 2012 Oct 15;22(3):276–82.

123. Rodrigues JC, Mathias H, Negus IS, Manghat NE, Hamilton MC. Intravenous contrast medium administration at 128 multidetector row CT pulmonary angiography: bolus tracking versus test bolus and the implications for diagnostic quality and effective dose. Clin Radiol. 2012;67(11):1053–60.

124. Rodrigues JC, Joshi D, Lyen SM, Negus IS, Manghat NE, Hamilton MC. Tube potential can be lowered to 80 kVp in test bolus phase of CT coronary angiography (CTCA) and CT pulmonary angiography (CTPA) to save dose without compromising diagnostic quality. European Radiology. 2014;24(10):2458–66.

125. Stein PD, Kayali F, Olson RE. Trends in the use of diagnostic imaging in patients hospitalized with acute pulmonary embolism. The American Journal of Cardiology. 2004 May 15;93(10):1316–7.

126. Weiss CR, Scatarige JC, Diette GB, Haponik EF, Merriman B, Fishman EK. CT Pulmonary Angiography is the First-Line Imaging Test for Acute Pulmonary Embolism: A Survey of US Clinicians. Academic Radiology. 2006 Apr 1;13(4):434–46.

127. Corrigan D, Prucnal C, Kabrhel C. Pulmonary embolism: the diagnosis, risk-stratification, treatment and disposition of emergency department patients. Clin Exp Emerg Med. 2016 Sep 30;3(3):117–25.

128. Quantification of pulmonary embolism by conventional and CT angiography. In: Pulmonary Embolism [Internet]. Chichester, UK: John Wiley & Sons, Ltd; 2016 [cited 2021 Jul 21]. p. 440–1. Available from: https://onlinelibrary.wiley.com/doi/10.1002/9781119039112.ch89

129. Miller GAH, Sutton GC, Kerr IH, Gibson RV, Honey M. Comparison of Streptokinase and Heparin in Treatment of Isolated Acute Massive Pulmonary Embolism. Br Med J. 1971 Jun 19;2(5763):681–4.

130. Wu AS, Pezzullo JA, Cronan JJ, Hou DD, Mayo-Smith WW. CT Pulmonary Angiography: Quantification of Pulmonary Embolus as a Predictor of Patient Outcome—Initial Experience. Radiology. 2004 Mar 1;230(3):831–5.

131. Qanadli SD, El Hajjam M, Vieillard-Baron A, Joseph T, Mesurolle B, Oliva VL, et al. New CT Index to Quantify Arterial Obstruction in Pulmonary Embolism. American Journal of Roentgenology. 2001 Jun 1;176(6):1415–20.

132. Ustabaşıoğlu FE, Solak S, Kula O, Gunay B, Serez B, Tunçbilek N. The relationship between computed tomographic obstruction index and pulmonary vein cross-sectional area in acute pulmonary embolism. Radiol Med. 2020 Mar;125(3):265–71.

133. Çildag MB, Gok M, Karaman CZ. Pulmonary Artery Obstruction Index and Right Ventricular Dysfunction Signs in Initial and Follow up Pulmonary Computed Tomography Angiography in Acute Pulmonary Embolism. J Clin Diagn Res. 2017 Jul;11(7):TC21–5.

134. Kjaergaard J, Schaadt BK, Lund JO, Hassager C. Quantification of right ventricular function in acute pulmonary embolism: relation to extent of pulmonary perfusion defects. Eur J Echocardiogr. 2008 Sep;9(5):641–5.

135. Yu T, Yuan M, Zhang Q, Shi H, Wang D. Evaluation of computed tomography obstruction index in guiding therapeutic decisions and monitoring percutanous catheter

fragmentation in massive pulmonary embolism. Journal of Biomedical Research. 2011 Nov 1;25(6):431–7.

136. Yu T, Yuan M, Zhang Q, Shi H, Wang D. Evaluation of computed tomography obstruction index in guiding therapeutic decisions and monitoring percutanous catheter fragmentation in massive pulmonary embolism. Journal of Biomedical Research. 2011 Nov 1;25(6):431–7.

137. Park J, Yun J, Kim N, Park B, Cho Y, Park HJ, et al. Fully Automated Lung Lobe Segmentation in Volumetric Chest CT with 3D U-Net: Validation with Intra- and Extra-Datasets. J Digit Imaging. 2020 Feb 1;33(1):221–30.

138. Singh R, Nie RZ, Homayounieh F, Schmidt B, Flohr T, Kalra MK. Quantitative lobar pulmonary perfusion assessment on dual-energy CT pulmonary angiography: applications in pulmonary embolism. Eur Radiol. 2020 May 1;30(5):2535–42.

139. Provost K, Leblond A, Gauthier-Lemire A, Filion É, Bahig H, Lord M. Reproducibility of Lobar Perfusion and Ventilation Quantification Using SPECT/CT Segmentation Software in Lung Cancer Patients. Journal of Nuclear Medicine Technology. 2017 Sep 1;45(3):185–92.

140. Borges JB, Suarez-Sipmann F, Bohm SH, Tusman G, Melo A, Maripuu E, et al. Regional lung perfusion estimated by electrical impedance tomography in a piglet model of lung collapse. Journal of Applied Physiology. 2012 Jan 1;112(1):225–36.

141. Shen M, Tenda ED, McNulty W, Garner J, Robbie H, Luzzi V, et al. Quantitative Evaluation of Lobar Pulmonary Function of Emphysema Patients with Endobronchial Coils. Respiration. 2019;98(1):70–81.

142. Yuan SY, Rigor RR. Regulation of Endothelial Barrier Function. San Rafael CA: © 2011 by Morgan & Claypool Life Sciences.; 2010.

143. Malkasian S, Hubbard L, Dertli B, Kwon J, Molloi S. Quantification of vessel-specific coronary perfusion territories using minimum-cost path assignment and computed tomography angiography: Validation in a swine model. Journal of cardiovascular computed tomography. 2018;12(5):425–35.

144. Malkasian S, Hubbard L, Abbona P, Dertli B, Kwon J, Molloi S. Vessel-specific coronary perfusion territories using a CT angiogram with a minimum cost path technique and its direct comparison to the American Heart Association 17-segment model. Eur Radiol. 2020;30(6):3334–45.

145. Sethian JA. A fast marching level set method for monotonically advancing fronts. Proc Natl Acad Sci U S A. 1996;93(4):1591–5.

146. Taha AA, Hanbury A. Metrics for evaluating 3D medical image segmentation: analysis, selection, and tool. BMC Medical Imaging. 2015 Aug 12;15(1):29.

147. Fenster A, Chiu B. Evaluation of Segmentation algorithms for Medical Imaging. In: 2005 IEEE Engineering in Medicine and Biology 27th Annual Conference. 2005. p. 7186–9.

148. Zou KH, Warfield SK, Bharatha A, Tempany CM, Kaus MR, Haker SJ, et al. Statistical validation of image segmentation quality based on a spatial overlap index. Acad Radiol. 2004;11(2):178–89.

149. Cárdenes R, de Luis-García R, Bach-Cuadra M. A multidimensional segmentation evaluation for medical image data. Comput Methods Programs Biomed. 2009 Nov 1;96(2):108–24.

150. Doel T, Gavaghan DJ, Grau V. Review of automatic pulmonary lobe segmentation methods from CT. Comput Med Imaging Graph. 2015 Mar;40:13–29.

151. American Thoracic Society, European Respiratory Society. American Thoracic Society/European Respiratory Society International Multidisciplinary Consensus Classification of the Idiopathic Interstitial Pneumonias. This joint statement of the American Thoracic Society (ATS), and the European Respiratory Society (ERS) was adopted by the ATS board of directors, June 2001 and by the ERS Executive Committee, June 2001. Am J Respir Crit Care Med. 2002 Jan 15;165(2):277–304.

152. Zhang L, Hoffman EA, Reinhardt JM. Atlas-driven lung lobe segmentation in volumetric X-ray CT images. IEEE Transactions on Medical Imaging. 2006 Jan;25(1):1–16.

153. van Rikxoort EM, Prokop M, de Hoop B, Viergever MA, Pluim JPW, van Ginneken B. Automatic segmentation of pulmonary lobes robust against incomplete fissures. IEEE Trans Med Imaging. 2010 Jun;29(6):1286–96.

154. Lassen B, van Rikxoort EM, Schmidt M, Kerkstra S, van Ginneken B, Kuhnigk J-M. Automatic segmentation of the pulmonary lobes from chest CT scans based on fissures, vessels, and bronchi. IEEE Trans Med Imaging. 2013 Feb;32(2):210–22.

155. Park J, Yun J, Kim N, Park B, Cho Y, Park HJ, et al. Fully Automated Lung Lobe Segmentation in Volumetric Chest CT with 3D U-Net: Validation with Intra- and Extra-Datasets. J Digit Imaging. 2020 Feb 1;33(1):221–30.

156. Dandy WE. Incomplete Pulmonary Interlobar Fissure Sign. Radiology. 1978 Jul 1;128(1):21–5.

157. Thapa P, Desai S. Morphological variation of human lung fissures and lobes: An anatomical cadaveric study in North Karnataka, India. Indian j health sci. 2016;9(3):284.

158. Moradi F, Morris TA, Hoh CK. Perfusion Scintigraphy in Diagnosis and Management of Thromboembolic Pulmonary Hypertension. RadioGraphics. 2019 Jan;39(1):169–85.

159. Ohno Y, Fujisawa Y, Sugihara N, Kishida Y, Seki S, Koyama H, et al. Dynamic Contrast-Enhanced Perfusion Area-Detector CT: Preliminary Comparison of Diagnostic Performance for

N Stage Assessment With FDG PET/CT in Non–Small Cell Lung Cancer. American Journal of Roentgenology. 2017 Nov 1;209(5):W253–62.

160. Jimenez-Juan L, Mehrez H, Dey C, Homampour S, Salazar-Ferrer P, Granton JT, et al. Quantitative assessment of pulmonary artery occlusion using lung dynamic perfusion CT. Sci Rep. 2021 Jan 12;11:483.

161. Grob D, Oostveen LJ, Prokop M, Schaefer-Prokop CM, Sechopoulos I, Brink M. Imaging of pulmonary perfusion using subtraction CT angiography is feasible in clinical practice. Eur Radiol. 2019;29(3):1408–14.

162. Dissaux B, Le Floch P-Y, Robin P, Bourhis D, Couturaud F, Salaun P-Y, et al. Pulmonary perfusion by iodine subtraction maps CT angiography in acute pulmonary embolism: comparison with pulmonary perfusion SPECT (PASEP trial). Eur Radiol. 2020 Sep;30(9):4857–64.

163. Culver BH, Glenny RW. Chapter 4 - Pulmonary Circulation. In: Spiro SG, Silvestri GA, Agustí A, editors. Clinical Respiratory Medicine (Fourth Edition) [Internet]. Philadelphia: W.B. Saunders; 2012 [cited 2021 Jul 28]. p. 29–36. Available from: https://www.sciencedirect.com/science/article/pii/B9781455707928000040

164. Cho H, Ding H, Masaki F, Barber W, Iwanczyk J, Molloi S. TH-A-103-08: System Optimization of Spectral Breast CT Based On An Energy-Resolved Photon-Counting Si Strip Detector: A Simulation Study. In AAPM; 2013. p. 000527. Available from: http://link.aip.org/link/?MPH/40/000527/2 http://dx.doi.org/10.1118/1.4815725

165. Nakano Y, Muro S, Sakai H, Hirai T, Chin K, Tsukino M, et al. Computed tomographic measurements of airway dimensions and emphysema in smokers. Correlation with lung function. Am J Respir Crit Care Med. 2000;162(3 Pt 1):1102–8.

166. Baron RL, Oliver JH, Dodd GD, Nalesnik M, Holbert BL, Carr B. Hepatocellular carcinoma: Evaluation with biphasic, contrast-enhanced, helical CT. Radiology. 1996;199(2):505–11.

167. Montaudon M, Lederlin M, Reich S, Begueret H, Tunon-de-Lara JM, Marthan R, et al. Bronchial measurements in patients with asthma: comparison of quantitative thin-section CT findings with those in healthy subjects and correlation with pathologic findings. Radiology. 2009;253(3):844–53.

168. Berger P, Perot V, Desbarats P, Tunon-de-Lara JM, Marthan R, Laurent F. Airway wall thickness in cigarette smokers: quantitative thin-section CT assessment. Radiology. 2005;235(3):1055–64.

169. Gono H, Fujimoto K, Kawakami S, Kubo K. Evaluation of airway wall thickness and air trapping by HRCT in asymptomatic asthma. European Respiratory Journal. 2003;22(6):965–71.

170. Saba OI, Hoffman EA, Reinhardt JM. Maximizing quantitative accuracy of lung airway lumen and wall measures obtained from X-ray CT imaging. J Appl Physiol (1985). 2003;95(3):1063–75.

171. Lutey BA, Conradi SH, Atkinson JJ, Zheng J, Schechtman KB, Senior RM, et al. Accurate measurement of small airways on low-dose thoracic CT scans in smokers. Chest. 2013;143(5):1321–9.

172. Dijkstra AE, Postma DS, ten Hacken N, Vonk JM, Oudkerk M, van Ooijen PM, et al. Low-dose CT measurements of airway dimensions and emphysema associated with airflow limitation in heavy smokers: a cross sectional study. Respir Res. 2013;14:11.

173. Telenga ED, Oudkerk M, van Ooijen PMA, Vliegenthart R, ten Hacken NHT, Postma DS, et al. Airway wall thickness on HRCT scans decreases with age and increases with smoking. BMC Pulmonary Medicine. 2017;17(1):27.

174. Yang Z, Jin H, Kim JH. Attenuation profile matching: An accurate and scan parameter-robust measurement method for small airway dimensions in low-dose CT scans. Med Phys. 2018;

175. Little SA, Sproule MW, Cowan MD, Macleod KJ, Robertson M, Love JG, et al. High resolution computed tomographic assessment of airway wall thickness in chronic asthma: reproducibility and relationship with lung function and severity. Thorax. 2002;57(3):247–53.

176. Washko GR, Dransfield MT, Estépar RSJ, Diaz A, Matsuoka S, Yamashiro T, et al. Airway wall attenuation: a biomarker of airway disease in subjects with COPD. J Appl Physiol (1985). 2009 Jul;107(1):185–91.

177. Kosciuch J, Przybylowski T, Gorska K, Krenke R, Baran W, Kujawa M, et al. [Relationship between airway basement membrane thickness and lung function tests in patients with asthma]. Pneumonol Alergol Pol. 2009;77(3):256–63.

178. Oguma T, Hirai T, Niimi A, Matsumoto H, Muro S, Shigematsu M, et al. Limitations of airway dimension measurement on images obtained using multi-detector row computed tomography. Plos One. 2013;8(10):e76381.

179. Galban CJ, Han MK, Boes JL, Chughtai KA, Meyer CR, Johnson TD, et al. Computed tomography-based biomarker provides unique signature for diagnosis of COPD phenotypes and disease progression. Nat Med. 2012;18(11):1711–5.

180. J.M. HAMWPMMSJHB. Location and direction dependence in the 3D MTF for a high-resolution CT system. Med Phys. 2020;

181. Tanabe N, Oguma T, Sato S, Kubo T, Kozawa S, Shima H, et al. Quantitative measurement of airway dimensions using ultra-high resolution computed tomography. Respir Investig. 2018;56(6):489–96.

182. Hlastala MP, Berger AJ. Physiology of Respiration [Internet]. Oxford University Press, USA; 2001. Available from: https://books.google.com/books?id=4Gr43yYwauMC

183. Lee TC, Kashyap RL, Chu CN. Building Skeleton Models via 3-D Medial Surface Axis Thinning Algorithms. CVGIP: Graphical Models and Image Processing. 1994;56(6):462–78.

184. Kim N, Seo JB, Song KS, Chae EJ, Kang SH. Semi-automatic measurement of the airway dimension by computed tomography using the full-width-half-maximum method: a study on the measurement accuracy according to the CT parameters and size of the airway. Korean Journal of Radiology. 2008;9(3):226–35.

185. Friedman SN, Fung GS, Siewerdsen JH, Tsui BM. A simple approach to measure computed tomography (CT) modulation transfer function (MTF) and noise-power spectrum (NPS) using the American College of Radiology (ACR) accreditation phantom. Med Phys. 2013;40(5):051907.

186. Hernandez AM, Abbey CK, Ghazi P, Burkett G, Boone JM. Effects of kV, filtration, dose, and object size on soft tissue and iodine contrast in dedicated breast CT. Medical Physics. 2020;47(7):2869–80.

187. Robinson TE, Long FR, Raman P, Saha P, Emond MJ, Reinhardt JM, et al. An airway phantom to standardize CT acquisition in multicenter clinical trials. Acad Radiol. 2009;16(9):1134–41.

188. Hackx M, Gyssels E, Severo Garcia T, De Meulder I, Alard S, Bruyneel M, et al. Chronic Obstructive Pulmonary Disease: CT Quantification of Airway Dimensions, Numbers of Airways to Measure, and Effect of Bronchodilation. Radiology. 2015;277(3):853–62.

189. Achenbach T, Weinheimer O, Dueber C, Heussel CP. Influence of Pixel Size on Quantification of Airway Wall Thickness in Computed Tomography. Journal of Computer Assisted Tomography. 2009;33(5):725–30.

190. Bartlett DJ, Koo CW, Bartholmai BJ, Rajendran K, Weaver JM, Halaweish AF, et al. High-Resolution Chest Computed Tomography Imaging of the Lungs: Impact of 1024 Matrix Reconstruction and Photon-Counting Detector Computed Tomography. Invest Radiol. 2019;54(3):129–37.

191. CMS. Decision memo for screening for lung cancer with low-dose computed tomography (LDCT) (CAG-00439N). https://www.cms.gov/medicare-coverage-database/details/nca-decision-memo.aspx?NCAId=274. 2015.

192. Singh D, Long G, Cancado JED, Higham A. Small airway disease in chronic obstructive pulmonary disease: insights and implications for the clinician. Curr Opin Pulm Med. 2019;

193. Tiddens HA, Paré PD, Hogg JC, Hop WC, Lambert R, de Jongste JC. Cartilaginous airway dimensions and airflow obstruction in human lungs. Am J Respir Crit Care Med. 1995 Jul 1;152(1):260–6.

194. Vignola AM, Kips J, Bousquet J. Tissue remodeling as a feature of persistent asthma. Journal of Allergy and Clinical Immunology. 2000 Jun 1;105(6, Part 1):1041–53.

195. Barnes PJ. Inflammatory mechanisms in patients with chronic obstructive pulmonary disease. J Allergy Clin Immunol. 2016;138(1):16–27.

196. Nakano Y, Muro S, Sakai H, Hirai T, Chin K, Tsukino M, et al. Computed Tomographic Measurements of Airway Dimensions and Emphysema in Smokers: Correlation with Lung Function. Am J Respir Crit Care Med. 2000 Sep;162(3):1102–8.

197. Hasegawa M, Nasuhara Y, Onodera Y, Makita H, Nagai K, Fuke S, et al. Airflow Limitation and Airway Dimensions in Chronic Obstructive Pulmonary Disease. Am J Respir Crit Care Med. 2006 Jun 15;173(12):1309–15.

198. Saba OI, Hoffman EA, Reinhardt JM. Maximizing quantitative accuracy of lung airway lumen and wall measures obtained from X-ray CT imaging. Journal of Applied Physiology. 2003 Sep 1;95(3):1063–75.

199. Hackx M, Bankier AA, Gevenois PA. Chronic obstructive pulmonary disease: CT quantification of airways disease. Radiology. 2012;265(1):34–48.

200. Mohamed Hoesein FA, de Jong PA, Lammers JW, Mali WP, Mets OM, Schmidt M, et al. Contribution of CT quantified emphysema, air trapping and airway wall thickness on pulmonary function in male smokers with and without COPD. COPD. 2014;11(5):503–9.

201. Washko GR, Dransfield MT, Estepar RS, Diaz A, Matsuoka S, Yamashiro T, et al. Airway wall attenuation: a biomarker of airway disease in subjects with COPD. J Appl Physiol (1985). 2009;107(1):185–91.

202. Weinheimer O, Achenbach T, Bletz C, Duber C, Kauczor HU, Heussel CP. About objective 3-d analysis of airway geometry in computerized tomography. IEEE Trans Med Imaging. 2008;27(1):64–74.

203. Molloi S, Johnson T, Ding H, Lipinski J. Accurate quantification of vessel cross-sectional area using CT angiography: a simulation study. Int J Cardiovasc Imaging. 2017 Mar;33(3):411–9.

204. Molloi S, Johnson T, Lipinski J, Ding H, Hubbard L. A phantom based evaluation of vessel lumen area quantification for coronary CT angiography. Int J Cardiovasc Imaging. 2019;35(3):551–7.

205. Friedman SN, Fung GSK, Siewerdsen JH, Tsui BMW. A simple approach to measure computed tomography (CT) modulation transfer function (MTF) and noise-power spectrum (NPS) using the American College of Radiology (ACR) accreditation phantom. Med Phys. 2013 May;40(5):051907.

206. Hamid Q, Song Y, Kotsimbos TC, Minshall E, Bai TR, Hegele RG, et al. Inflammation of small airways in asthma. J Allergy Clin Immunol. 1997;100(1):44–51.

207. Tanabe N, Vasilescu DM, McDonough JE, Kinose D, Suzuki M, Cooper JD, et al. Micro–Computed Tomography Comparison of Preterminal Bronchioles in Centrilobular and Panlobular Emphysema. Am J Respir Crit Care Med. 2017 Mar 1;195(5):630–8.

208. Hogg JC, Chu F, Utokaparch S, Woods R, Elliott WM, Buzatu L, et al. The nature of small-airway obstruction in chronic obstructive pulmonary disease. N Engl J Med. 2004;350(26):2645–53.

209. Estépar RSJ, Washko GG, Silverman EK, Reilly JJ, Kikinis R, Westin C-F. Accurate airway wall estimation using phase congruency. Med Image Comput Comput Assist Interv. 2006;9(Pt 2):125–34.

210. Reinhardt JM, Souza ND, Hoffman EA. Accurate measurement of intrathoracic airways. Ieee Transactions on Medical Imaging. 1997;16(6):820–7.

211. Clark AR, Tawhai MH, Hoffman EA, Burrowes KS. The interdependent contributions of gravitational and structural features to perfusion distribution in a multiscale model of the pulmonary circulation. Journal of Applied Physiology. 2011 Apr 1;110(4):943–55.